Bazaka, Kateryna (2011) ***Fabrication and characterization of plasma polymer thin films from monoterpene alcohols for applications in organic electronics and biotechnology.*** **PhD Thesis, James Cook University.**

https://doi.org/10.25903/v0d4%2Db519

Bazaka, Kateryna (2011) ***Fabrication and characterization of plasma polymer thin films from monoterpene alcohols for applications in organic electronics and biotechnology*****. PhD thesis, James Cook University.**

IV.1 SURFACE ARCHITECTURE AND MECHANICAL PROPERTIES OF POLYTERPENOL THIN COATINGS

Abstract

Organic plasma polymers are currently attracting significant interest for their potential in the areas of flexible optoelectronics and biotechnology. Thin films of plasma polymerised polyterpenol fabricated under varied deposition conditions were studied using nanoindentation and nanoscratch analyses. Coatings fabricated at higher deposition power were characterised by improved hardness, from 0.33 GPa for 10 W to 0.51 GPa for 100 W at 500 μN load, and enhanced wear resistance. The elastic recovery was estimated to be between 0.1 and 0.14. Coatings deposited at higher RF powers also showed less mechanical deformation and improved quality of adhesion. The average (R_a) and RMS (R_q) surface roughness parameters decreased, from 0.44 nm and 0.56 nm for 10 W to 0.33 nm and 0.42 nm for 100 W, respectively.

Keywords: hardness; plasma-enhanced CVD (PECVD) (deposition); nano-indentation; thin film

As published in: Bazaka, K., Jacob, M. V., Nanotribological and nanomechanical properties of plasma polymerised polyterpenol thin films. *Journal Materials Research 2011, 26, 2952-2961*.

IV.1.1 Introduction

Polymer thin films fabricated using low-temperature non-equilibrium plasma techniques are actively studied for their physical and chemical stability, and low cost, uncomplicated production [319]. From one precursor, polymers of significantly different chemical and physical structures or films with property gradient can be obtained by controlling deposition conditions of polymerisation. Such conditions include the energy delivered into the reaction chamber, monomer flow, geometry of the reactor, addition of gas and so on [89]. Furthermore, compounds not amenable to conventional thermo-chemical polymerisation pathways can be polymerised using plasma techniques. Given their high adhesion to the substrate and smooth, defect free and uniform surfaces, plasma polymers have already found their application as anti scratch barriers and protective coatings. These include corrosion protective barrier coatings on reflectors and metallic surfaces, coupling and corrosion prevention layers on steel, adhesion promotion pre-treatments on aluminium, gas permeation barrier coatings in packaging, and resist in microfabrication processing [348]. Organic plasma polymers are currently attracting significant interest for their potential in the areas of mechanics, flexible electronics, and optics. The ability to retain certain functionalities of the organic precursor in the polymer film also renders these materials attractive to the field of biotechnology. Here, organic plasma polymers can take role of biomaterials, tissue scaffolds, hydrophobic antifouling coatings, and as antireflective coatings on polymeric ophthalmic lenses.

Whether within an electronic device or as a bioactive coating, the mechanical and morphological properties of these films influence the nature of application, performance and longevity of these materials. Furthermore, the morphology of the surface is known to influence the wetting behaviour of the solid films, the latter being an important consideration with regard to biomedical prospect of these materials. Hence, to determine potential applications of such organic polymer thin films, and to optimise such a material for specific applications, an understanding of the relationship between the fabrication parameters and the resultant mechanical properties of the plasma polymer is required.

Techniques such as microhardness and tensile testing are commonly employed to study the mechanical characteristics of a wide range of bulk amorphous polymers. They provide useful information with regard to materials' elastic modulus and microstructure, as well as the effect of molecular weight and composition on the mechanical behaviour of these materials. Whilst functional for bulk polymers, these techniques have limited characterization capacity when it comes to investigations on thin plasma polymer film structures and coatings, since many of the above mentioned applications require thin films of below 100 nm in thickness. Relatively large loads and penetration depths required to image the indent lead to results being dominated by substrate contribution. Furthermore, the technique does not offer information on the elastic properties of the thin films. Depth-sensing indentation (or nanoindentation), on the other hand, was initially developed for studies on plastic-elastic materials. It applies very low loads and small depths and therefore can be successfully used for characterization of plasma polymerised thin films [349]. Similarly, the adhesion and fracture strength of ultrathin or soft plasma polymer films can be evaluated using a nanoscratch test that allows for high-resolution application of ultralow scratch loads and acquisition of displacement data as films deform and fail.

Here, we study the nanotribological and nanomechanical properties and surface morphology of the plasma polymerised terpinen-4-ol (polyterpenol) thin films fabricated under various deposition conditions [350]. Polyterpenol is a transparent insulating material with refractive index just above that of glass [336,351]. It is characterised by sound physical and chemical stability, and its tunable onset degradation temperature and low post-annealing retention rates suggest polyterpenol as a potential sacrificial material for fabrication of air gaps and sealed nano-channels [347]. Polyterpenol films fabricated at low power conditions have been shown to prevent adhesion and propagation of selected human pathogenic bacteria, *S. aureus* and *P. aeruginosa*, indicating the material can be applied as an antibacterial and antifouling coating for indwelling medical devices [200,352]. Polyterpenol films implemented as a surface modification of the gate insulator in pentacene based organic field effect transistor (OFET) significantly shifted the threshold voltage, improved the effective mobility and the switching property of the polyterpenol containing OFET [337,353].

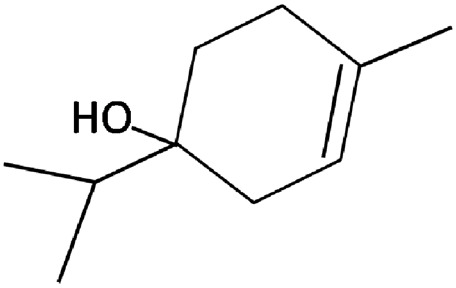

Figure IV.1.1. Chemical structure of terpinen-4-ol.

IV.1.2 Experimental

Plasma enhanced chemical vapor deposition was used to fabricate thin polyterpenol films from non-synthetic monoterpene alcohol precursor (Australian Botanical Products Ltd) according to an experimental procedure described elsewhere [336]. External copper electrodes were employed to capacitively couple the RF (13.56 MHz) power supply to the deposition chamber. Films were manufactured at room temperature and pressure of 100 mTorr under varied deposition conditions, such as time and input power, on pre-cleaned glass substrates. The polymer films used in this study were deposited at 10, 15, 25, 50, 75 and 100 W RF power. Spectroscopic ellipsometer (model M-2000D, J.A. Woollam Co. Inc.) was used to estimate optical thickness and roughness of the deposited films.

A NT-MDT atomic force microscope (AFM) was employed in nanoindentation analysis, with the standard head replaced with a Triboscope indenter system manufactured by Hysitron Inc. (Minneapolis, MN), which allows for application of a desired load on the indenter with an electrostatic force taking a role of a transducer. Berkovich indenter (70.3° equivalent semi-opening angle) was used in indentations and instrument compliance was calibrated using fused silica. Preliminary images of the samples under investigations were collected in order to evaluate the roughness of the area to be indented. The indentation profile consisted of loading, holding and unloading. Typical loads used in the indentation ranged from 100 μN to 700 μN with fixed loading time and hold time of between 2 and 5 s. The loading and unloading rates, and the time associated with each segment were varied to investigate the effect of these parameters on the resultant hardness and modulus values. In the load−partial unload experiment, several cycles of loading to gradually increasing depth and unloading to 10% of the maximum load for that cycle are performed with the tip of the indenter remaining in contact with the sample. The loading/unloading rate and holding time was kept constant at 100 μN/s and 20 s, respectively, with 50–800 nm depth range. The technique is another tool to capture the variation in mechanical properties of the thin film-substrate system as a function of indentation depth.

The indentation process was monitored continuously during loading and unloading phases with respect to displacement, force, and time. The contact area for each indent was calculated from the stiffness vales and the known modulus for quartz. Contact parameters and mechanical properties of the films are derived from the contact area and load displacement curve as proposed by Oliver and Pharr [354]. In the case of polyterpenol, the unloading stiffness was calculated after polynomial fitting of 90% of the unloading curve. The contact depth h_c is established using elastic analysis developed by Sneddon for the penetration of a flat elastic half space by probes of axisymmetric shapes as $h_c = h_{max} - \varepsilon(P_{max}/S)$, where h_{max} is maximum depth, ε is a constant dependant on the pressure distribution established after the plastic deformation and is a function of the geometry of the indenter, P_{max} is maximum force, and S is contact stiffness. For Berkovich indenter, ε is usually assumed to take value of 0.75. The contact stiffness S is defined as $S = \frac{dP}{dh}$, and $S = 2aE_r = \frac{2\beta}{\sqrt{\pi}} E_r \sqrt{A}$, where P is the indenter load, h is the depth of penetration by the indenter, a is the contact radius, β is a correction factor that depends on the material properties, the geometry of the indenter and the penetration depth [355], E_r is the reduced modulus, and A is the projected (cross-sectional) contact area. Recently, Abbes *et al* demonstrated the dependence of β on the penetration depth and tip for elastic−plastic materials, and the consequent effect on hardness and elastic modulus measurements [355]. In this study, the correction factor β of 1.034 was used in the calculations to account for the tip geometry of Berkovich indenter; the dependence of β on the material properties of the fused quartz and polyterpenol samples was not investigated, thus limiting the quantitative merit of the results obtained. However, qualitative assessment of the evolution of sample hardness with RF power can still take place assuming that not taking into account the material-related β factor correction produces a systematic bias of the same order of magnitude for the different polyterpenol samples. The hardness of the film sample H is derived from the peak force applied to the sample P_{max} and the projected contact area A, as $H = \frac{P_{max}}{A}$, where $A = f(h_c)$. The reduced elastic modulus accounts for the deformation of both the indenter and the thin polymer film, and can be expressed through $\frac{1}{E_r} = \frac{(1-\nu^2)}{E} + \frac{(1-\nu_i^2)}{E_i}$, where E is the elastic modulus of the sample, ν is related to Poisson's ratio of the specimen under investigation, and E_i and ν_i are the elastic modulus and Poisson's ratio pertinent to the material of the indenter.

In nanoscratch experiment, the samples were subjected to a ramp force profile, with a maximum force of 2000 μN, a scratch length of 20 nm, over 30 sec. As with indentation experiments, Berkovich probe was used for scratching, with orientation of the Berkovich tip being between the face forward and edge forward relative to scanning direction [356]. A two-dimensional force transducer of the nanoindentation probe allows for force measurements in the lateral and vertical directions, from which the friction coefficient of a material can be determined as the ratio between the lateral force and the normal (applied) force [357,358]. Multiple measurements collected for each sample were plotted as normal displacement vs normal force to estimate adhesion between the polymer thin film and the glass substrate. Visual examination of the surface in response to the deformation was conducted using post-scratch topographical scans. The cross hatch test using the Elcometer 107 kit was also performed to obtain a standardised (ASTM D3359) qualitative assessment of the adhesion between polyterpenol films and glass substrate.

IV.1.3 Results and Discussion

IV.1.3.1 Surface morphology

The surface morphology of polyterpenol thin films fabricated under different RF power conditions was studied using AFM in semi-contact mode. When comparing to AFM contact mode, where the high tip–to–surface forces can mechanically deform the surface under the investigation, the short intermittent contacts between the tip and the sample surface characteristic of AFM tapping mode reduce the inelastic deformations to the surface of the sample. Furthermore, the effective forces applied to the surface are smaller than those of the contact mode.

Table IV.1.1. Roughness of polyterpenol thin films deposited at different input RF power.

	10 W	15 W	25 W	50 W	75 W	100 W
Maximum peak height R_{max}, nm	5.29	4.50	4.50	3.60	3.52	2.93
Average Roughness R_a, nm	0.44	0.43	0.40	0.40	0.35	0.33
Root Mean Square R_q, nm	0.56	0.55	0.54	0.51	0.44	0.42
Surface skewness R_{sk}	0.11	0.07	0.39	0.20	0.13	0.05
Coefficient of kurtosis R_{kur}	1.47	0.13	1.56	0.29	0.20	0.20

Scanned images representative of the samples are presented in Figure IV.1.2 and roughness parameters for the films are summarized in Table IV.1.1. The surface of unmodified glass substrate was also scanned and used as a reference. Independent of deposition power, polyterpenol coatings were smooth, uniform and defect free, lacking comparatively prominent features (maximum peak height of 15.1 nm) present on the surface of unmodified substrate. Smooth surface of polyterpenol films indicates that the polymerization reactions took place predominantly on the surface of the glass substrate rather than in the gas phase [326]. The maximum peak height (R_{max}) decreased for films deposited at higher RF power, from 5.29 nm for 10 W to 2.93 nm for 100 W. The average (R_{a}) and RMS (R_{q}) surface roughness parameters also decreased, from 0.44 nm and 0.56 nm for 10 W to 0.33 nm and 0.42 nm for 100 W, respectively. These roughness estimates were in agreement with previously reported roughness values for polyterpenol established by means of spectroscopic ellipsometry [336]. All polymer thin films displayed a surface skewness (R_{skw}) greater than 0 and coefficient of kurtosis (R_{kur}) less than 3, i.e. the R_{skw} values describe a disproportionate number of peaks pertaining to the polyterpenol surfaces; and the R_{kur} values signify the surfaces with well spread out height distribution [359,360]. There was no observed dependency of the surface skewness (R_{skw}) and coefficient of kurtosis (R_{kur}) values on the deposition power used during polyterpenol film fabrication.

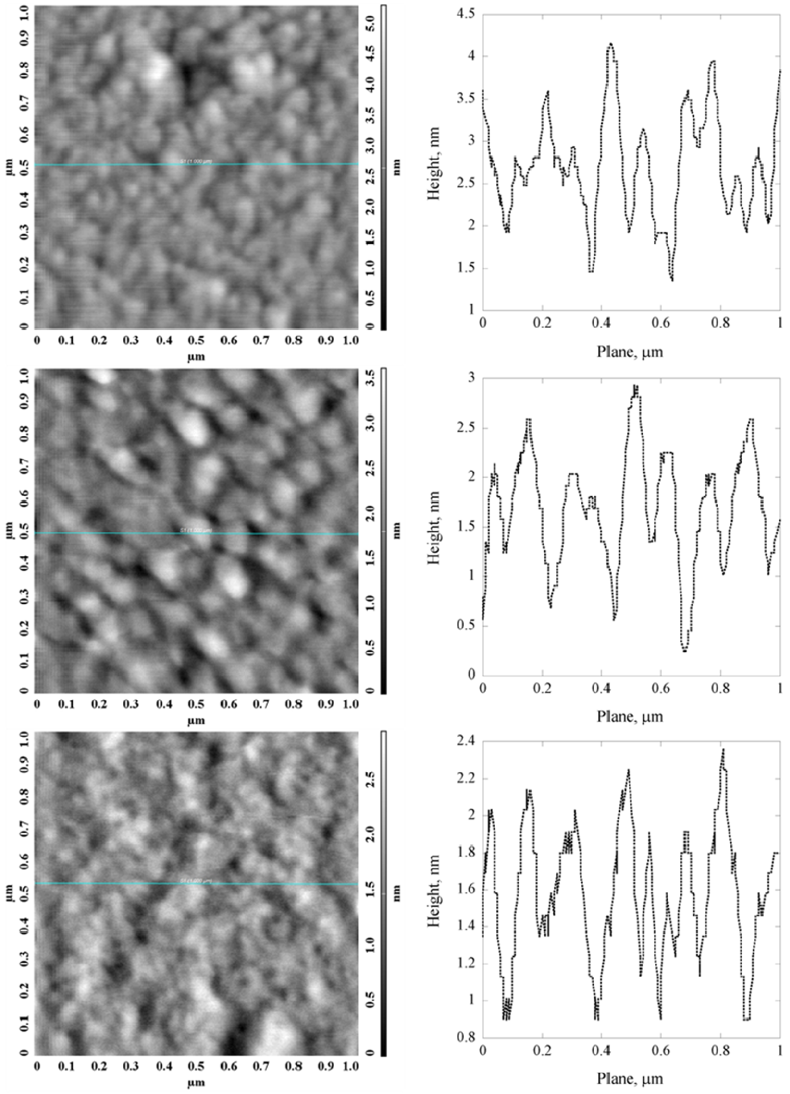

Figure IV.1.2. Typical two-dimensional (2D) AFM images and surface profiles of polyterpenol thin film surfaces deposited at 10 W (top), 50 W (middle), and 100 W (bottom) from approximately 1 µm × 1 µm scanned areas.

According to Pelliccione and Lu, there are multiple factors that would influence the formation of a complex morphology on the surface of a thin film grown via plasma assisted chemical vapour deposition [361]. Therefore, the roughness parameters of polyterpenol films were also investigated as a function of film thickness and deposition rate. Thinner films (below 100 nm) were characterised by a slightly lower R_q compared to films of thickness between 300 and 2000 nm fabricated under similar deposition conditions. A similar trend for plasma polymerised trans-2-butene was reported, where overall increase in RMS roughness was attributed to the increase in low frequency contributions [362]. Higher deposition rate (1 μm/h vs 0.2 μm/h) also resulted in the increase in the surface roughness of the film due to the particles in the growth region unable to relax fast enough before the next layer of the film is assembled [87]. The degree of surface roughness has also been demonstrated to depend on the deposition temperature, with higher temperatures resulting in the increased surface relaxation rate that allows the short wavelength roughness amplitudes to relax towards longer wavelength more quickly, resulting in a smoother surface of the plasma film.

Surface morphology is known to influence the wetting behaviour of the solid films, namely the hysteresis and the mean contact angle of the liquid drop placed on the surface. It has been demonstrated that for hydrophilic surfaces, where $cos\ \theta > 0$, the effective contact angle on rough surface is smaller than the Young's angle of chemically comparable smooth surface. Previous water contact angles studies on polyterpenol films fabricated under varied RF power showed an increase in θ with deposition power, the increased hydrophobicity predominantly attributed to a decrease in oxygen containing functionalities present at the surface of the polymer. For films deposited at 100 W, water contact angle was determined to be approximately 75°, compared to approximately 60° estimated for 10 W films. Given that hydrophilicity is amplified by roughness of the surface, as described by Wenzel [363], the decrease in surface roughness with deposition power is also likely to contribute to increased hydrophobicity of the surface.

IV.1.3.2 Nanoindentation

Many factors, including the mechanical strength and thickness of plasma polymer thin films, residual stress, and chemical bonds at the interface, are thought to affect the adhesive or cohesive strength of the material. Mechanical failure can take form of delamination at the interface due to lower adhesive strength; the other form of mechanical failure of the coating is cracking or brittle failure in the thin film due to lower cohesive strength. Determination of adhesive or cohesive strength in combination with identification of the critical failure sites can be used to determine factors that may contribute to de-bonding of the coating and potential failure of the device. The effect of experimental conditions at which the nanoindentation and nanoscratch test are performed, such as the indentation load, loading rate, and hold time in the case of nanoindentation, and the scratching speed, loading rate, and probe radius should also be accounted for to ensure the correct interpretation of the results.

Mechanical properties of plasma polymerised polyterpenol deposited under different RF power conditions were investigated using a single indentation method and a load-partial-unload technique. Illustrative single indentation curves from 2000 nm thick polyterpenol film fabricated at 10 W and 100 W are presented in Figure IV.1.3. It is not uncommon that the tip would continue to move into the surface of the sample during the holding time as a result of viscous creep of the material. The observed divergence between the unloading and loading curves is a reflection of a residual plastic deformation within the indented film. As can be seen from polyterpenol material response to the indentation, the film deposited at 10 W is softer than one fabricated at 100 W, with less elastic recovery observed during unloading for the former. Furthermore, the softer 10 W film displays more extensive creep deformation occurring during the hold period at maximum load. Single indentations under similar load conditions performed at randomly chosen locations on the surface of the samples confirmed lateral homogeneity of the indentation behaviour of the films.

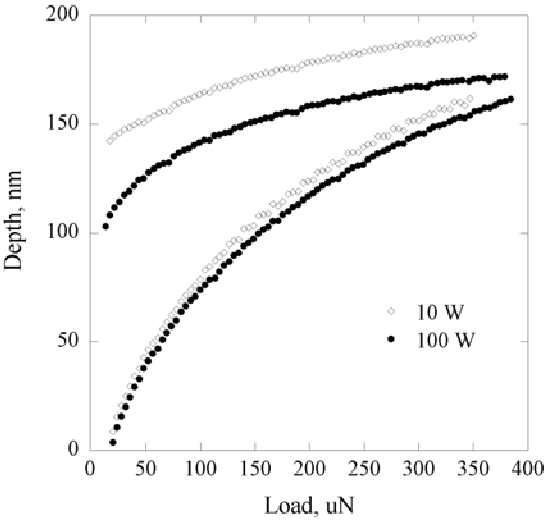

Figure IV.1.3. Typical single indentation curves force-displacement collected for polyterpenol thin films deposited at 10 and 100 W, film thickness 2000 nm.

Figure IV.1.4 shows typical repeat single indentation profiles under increasing indentation load of polyterpenol film deposited at 75 W. In order to collect thin film only plastic response, indentation depths of no more than one tenth of the overall thickness of the film were employed, so that the stress field remains within the film and the measurement is not influenced by the substrate. The variation in hardness with indentation depth was determined from repeated single indentations on films fabricated under different RF power conditions. It is possible that polyterpenol thin films examined in this study are slightly harder at the surface of the samples, at indentation depth below 130 nm. More likely, however, is that the chain molecular mobility is being restricted in the confined region of mechanical contact adjacent to the probe, with shallower indents resulting in a more profound expansion impediment due to intrinsic length scales of the material such as the polymer chain length [364]. Tweedie *et al* proposed that the superposed contact stress shifts T_g at the probe–amorphous polymer interface, resulting in a mechanically distinct region confined between the polymer and the diamond probe [365]. Such a region may be characterised by a combination of unique structural and physical properties, with an apparent stiffness that exceeds the elastic response of the bulk polymer. Furthermore, the choice of the probe material may influence the attraction toward and repulsion from the probe, consequently affecting the molecular mobility within the contact region via intermolecular interactions or via stretching or alignment of polymer chains with regard to the surface of the probe.

It is difficult to determine a definite trend in the hardness of the polyterpenol thin films with indentation depth due to multiple sources of error. These include the relative non-uniformity of the indent, such as pile-up and sink-in phenomena observed on some samples, and associated with it difficulties in precise estimation of the indent area (possible overestimation in the case of pile-up and underestimation due to sink-in features), respective influences of material properties and sample thicknesses, creep, to name but a few. In addition, as the indent is imaged with the same tip that was employed in the actual indentation process, there is a possibility of imaging artefacts and tip effects affecting the precision of the measurement. Hence, the values presented in Table IV.1.2 are indicative of the evolution of the hardness properties of polyterpenol under changing fabrication conditions, and may quantitatively differ from the actual material properties due to aforementioned measurement constrains.

Table IV.1.2. Mechanical properties of plasma polymerised thin films (at 500 μN load).

Sample	Hardness ± SE, GPa	Elastic recovery parameter
10 W	0.33 ± 0.02	0.11
15 W	0.35 ± 0.02	0.12
25 W	0.38 ± 0.03	0.10
50 W	0.42 ± 0.02	0.14
75 W	0.49 ± 0.01	0.13
100 W	0.51 ± 0.01	0.13

Above the plastic depth of 130 nm for films deposited at 10, 15, and 25 W, and above 100 nm for films fabricated at 50, 75, and 100 W, hardness levels off to an approximately constant value, indicating there is no significant variation in the structure of polyterpenol coating across its thickness. The variation in the mechanical properties of polyterpenol thin films with indentation depth examined using load−partial unload technique revealed that at depths below

200 nm, the depth profile of the hardness follows a trend similar to that determined using the single indentation approach. Above the plastic depth of approximately 200 nm, the hardness of the system gradually increases due to the stress field no longer being contained within the body of the coating. As the influence of the mechanical properties of the substrate on the elastoplastic response of the film-substrate system becomes more prominent, such data becomes less representative of the coating itself.

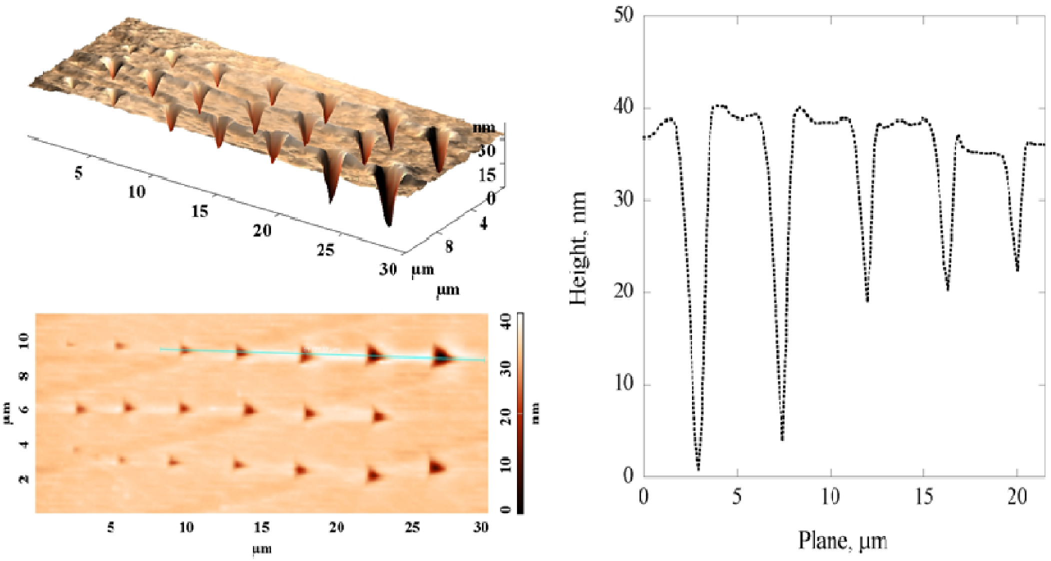

Figure IV.1.4. Typical AFM image of plastic impressions remaining in polyterpenol sample fabricated at 75 W after indented under different load conditions.

In order to evaluate the effect such parameters as loading time and dwell time have on the indentation behaviour of polyterpenol films, additional single indentations were performed on samples deposited at 50 W. At constant load of 700 µN, increasing loading and unloading time, with rates (*r*) ranging from 0.5 to 20 nm/s, decreased calculated hardness value from 0.44 GPa to 0.40 GPa. As the contact depth at maximum load is influenced by creep deformation taking place during the holding time, the hardness values obtained using these maximum contact depth estimates will also be affected. Calculated from the tangent of the slope of the unloading curve, the modulus will also be directly impacted by the choice of the holding time. Where holding time is absent or insufficiently low, the film will continue to deform viscoplastically during unloading leading to distortions in the shape of the unloading curve. In the case of polyterpenol thin films, increasing the hold time from 3 s to 25 s at constant load of 400 µN resulted in a decrease in the calculated hardness from 0.43 GPa to 0.39 GPa. A logarithmic creep expression $h = A \ln (Bt + 1)$, where h is increase in depth at P_{max}, t is the holding time, and A and B are fitting parameters, can be used to describe the creep data for polyterpenol, as it has been previously used to illustrate the indentation induced time dependent part of the plastic deformation of a number of polymers, ceramics and glasses [348]. Parameters A and B which relate to the general susceptibility to creep and the rate of the exponential creep process, respectively, did not change significantly under varied holding time conditions, with A at approximately 3.55. To compare, Beake and co-workers estimated that fused silica has A of approximately 2.2 whilst the value for poly(ethylene terephthalate) (PET) is in the vicinity of 10.1. This indicates that in their creep behaviour, polyterpenol films resemble fused silica more than they do traditional polymers, due to the high degree of cross linking characteristic of plasma films. The presence of covalent bonds that connect polymer chains results in restricted chain movement within the polymer film, and hence the better creep resistance of polyterpenol. Creep constant k can be estimated from the plot of the plastic deformation as a function of holding time using $H=H_0 t^{-k}$, where H is hardness, H_0 is the hardness at t =1 min and t is the holding time. For polyterpenol thin films fabricated at 50 W, the creep constant was determined to be approximately 0.05, similar to that reported k of 0.07 for plasma polymerised hexane films, and k values of approximately 0.04 and 0.09 for such conventional thermoplastics as PET and poly(ethylene oxide), respectively [348].

Regression analyses of the force curves collected for the polyterpenol samples indicated the hardness increased with the deposition power, from 0.33 GPa for 10 W to 0.51 GPa for 100 W at 500 μN load, as presented in Table IV.1.2. The elastic recovery was calculated as $(h_{max} - h_c)/h_c$, where h_{max} is the maximum indent depth and h_c is the contact depth. For polyterpenol films, the elastic recovery parameter was estimated to be between 0.1 and 0.14. The increase in hardness is attributed to the increase in the degree of cross-linking within the polymer thin film as a direct consequence of the increased RF power delivered into the deposition chamber [366], which is in agreement with previously reported FTIR and XPS results. Highly cross-linked polymers are significantly more rigid and compact compared to conventional amorphous or crystalline polymeric structures as the vibrational movement of the carbon backbone of the polymer is restricted by the presence of a multiple covalent bonds between polymer chains, conferring improved mechanical properties to this three-dimensional structure compared to a linear thermoplastic polymer [367,368]. Studies conducted on hexamethyldisiloxane and acetylene films demonstrated further improvement of the hardness and wear resistance of these plasma polymerised coatings can be achieved by applications of such post deposition treatments as an oxygen plasma treatment and ion implantation, respectively [368,369]. The modification is generally localised to the surface region of the film.

IV.1.3.3 Nanoscratch

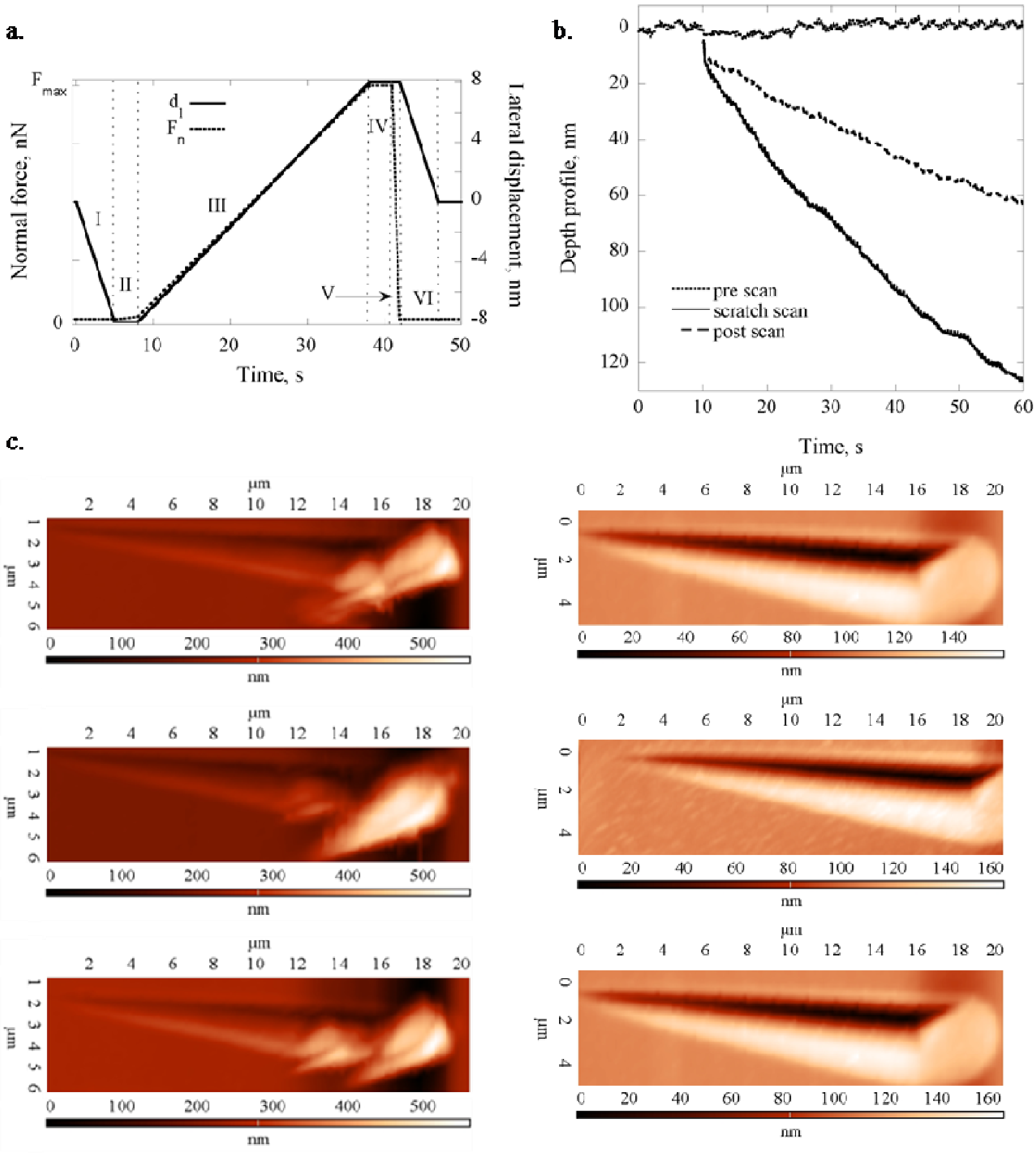

Figure IV.1.5. a) Nanoscratch normal force F_n and lateral displacement d_l curves. b) Nanoscratch depth profile for the polyterpenol thing film coating tested with ramping normal load of 20−2000 µN. c) AFM images of scratches performed on polyterpenol thin films fabricated at (a) 10 W, and (b) 100 W under varied normal load; top panel 1000 µN, middle panel 1500 µN, bottom panel 2000 µN.

Figure IV.1.5 presents the nanoscratch depth profiles for polyterpenol thin films for a maximum normal load of 2000 µN. The initial state of the surface preceding the scratch is reflected in pre-scratch curve, the scratch scan curve corresponds to the actual tip penetration into the sample in the course of the testing, whilst the post-scan curve is a representation of residual deformation of the sample coating as a result of scratching, that is the plastic deformation of the probed coating after unloading the tip. In the case of polyterpenol thin films, the deviation between scratch and post scan curve indicates partial elastic recovery of the film sample. The residual plastic deformation was also confirmed by AFM scans, as presented in Figure IV.1.5(c). Pile-up along the scratch trace and at the point of maximum applied normal load is noticeable on the AFM images of polyterpenol films deposited at lower RF power (depicted by the lighter shading of the AFM image), indicating different mechanism of mechanical deformation for these coatings. Upon loading, the constant slope of the scratch scan indicates a homogenous mechanical response of the material. Application of similar maximum normal loads resulted in higher scratch depths in the case of samples fabricated at lower RF powers, indicating these coatings are softer compared to polyterpenol films deposited at increased RF power levels.

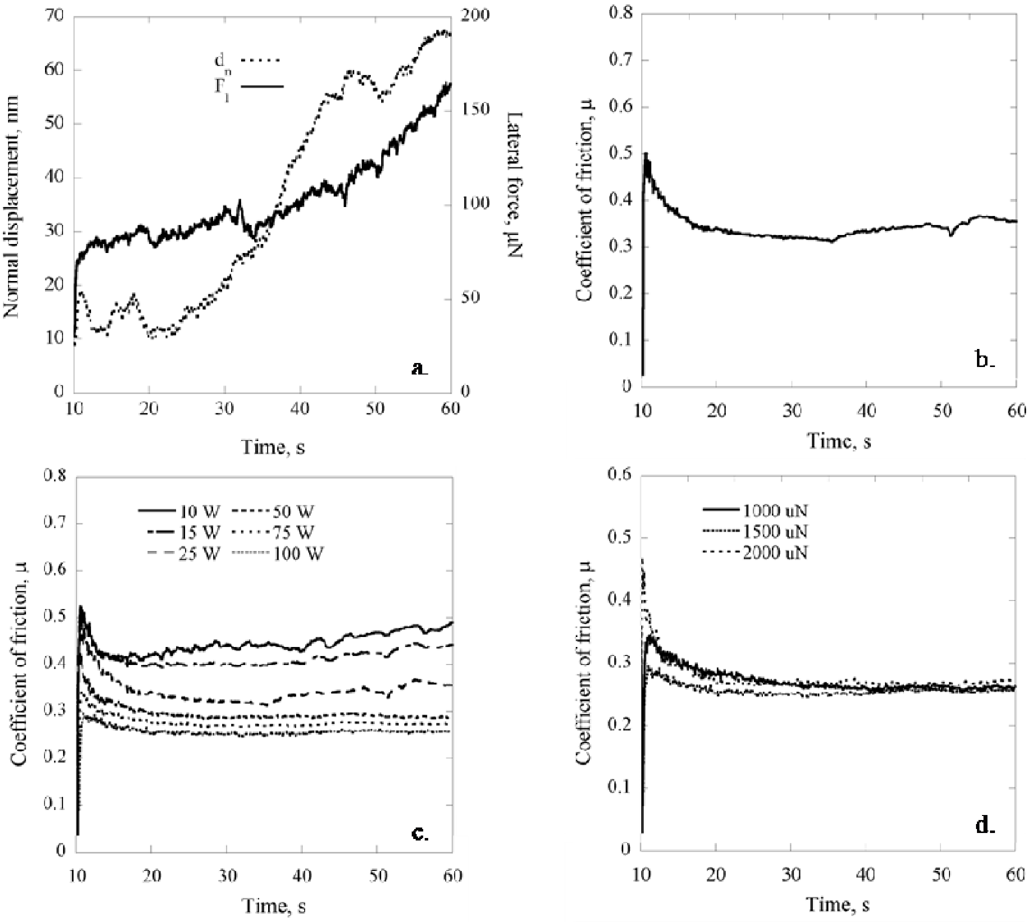

Figure IV.1.6. Nanoscratch data for polyterpenol thin films fabricated at 25 W: (a) lateral force F_1 and normal displacement d_n, and (b) friction coefficient μ_s as a function of time. Coefficient of friction profiles of the polyterpenol thin film (c) as a function of deposition RF power, and (d) under varied ramping normal load (film fabricated at 100 W).

In Figure IV.1.6, the nanoscratch data for polyterpenol thin films are presented as a plot of lateral force F_1 and normal displacement d_n, and friction coefficient μ_s as a function of time. As the normal load increases, the evolution of the coefficient of friction for all the films show an increase to a stable value, with films deposited at higher RF power being characterised by lower values of the coefficient of friction. Figure IV.1.6(c) shows coefficient of friction profiles for polyterpenol as a function of deposition power and as a function of applied maximum normal load. Absence of significant fluctuations in the friction coefficient indicates no considerable damage, cracking or delamination of the coating occurred. Coatings deposited at higher RF powers showed less mechanical deformation and hence are likely to be more stable and less susceptible to wear. Overall, all polyterpenol films were characterised by sound adhesion to the substrate. The friction coefficient was also found to be independent of the normal load applied during the nanoscratch test.

IV.1.3.3 Cross-hatch testing

Potential for damage and delamination of polyterpenol coatings was also assessed using a cross hatch test that provides a standardised (ASTM D3359) qualitative assessment of the adhesion of the coating to the substrate. The adhesion behaviour of polyterpenol thin films deposited on glass, PET and polystyrene (PS) is summarised in Figure IV.1.7. Independent of the substrate, the quality of adhesion is improved for samples deposited at higher RF power. Sample fabricated at 10 W was characterised the least favourable adhesion response, with delamination affecting between 15% and 25% of the surface area, whilst samples deposited at 20 W and 50 W displayed minimal (less than 5 %) damage to the sample surface, and no delamination was detected for 75 W and 100 W polyterpenol films. Such improved performance of the latter two film types is associated with enhanced interfacial bonding as a result of increased ion bombardment during plasma aided deposition. For films deposited at lower powers, surface modifications of the substrate prior to film deposition can be used to improve the quality of adhesion. Plasma-assisted surface cross-linking, surface activation using argon or argon-nitrogen gas mixture, or addition of adhesion layers are some of the methods to enhance the bonding within polymer thin film-substrate system. Examination of the optical images for the scratched samples also suggests a difference in the hardness of the polyterpenol coatings deposited under varied RF power conditions. Thin films deposited at an RF power of 10 W appear to be softer, with visible damage to the surface of the coating other than adhesion failure as a result of tape application and removal. These results are consistent with hardness evaluation performed using nanoindentation system.

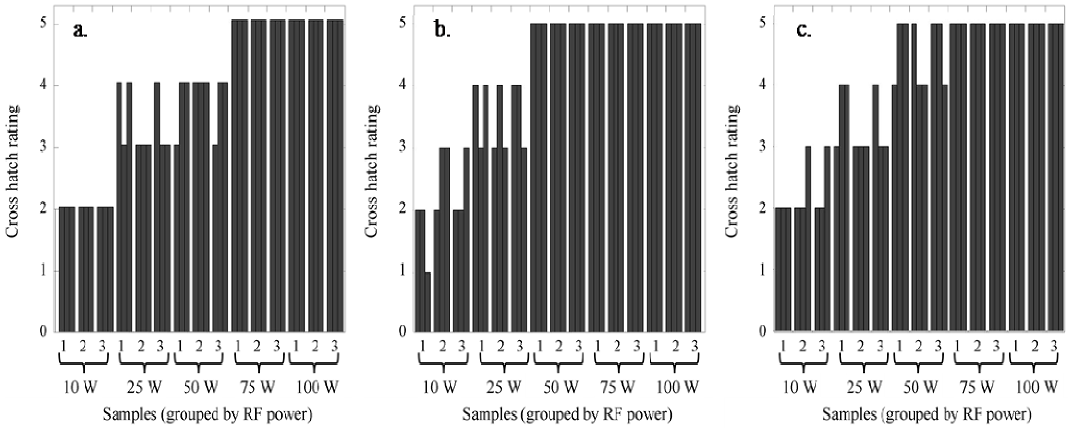

Figure IV.1.7. Adhesion behaviours of polyterpenol thin films fabricated on (a) glass, (b) PET, and (c) PS at various RF power levels.

IV.1.4 Conclusions

Thin films of polyterpenol were fabricated using RF plasma polymerisation under varied RF deposition power levels and their mechanical and tribological properties were examined using nanoindentation and nanoscratch analyses. Independent of deposition power, polyterpenol coatings were smooth, uniform, and defect free. Smooth surface of polyterpenol films indicates that the polymerization reactions took place predominantly on the surface of the glass substrate rather than in the gas phase. The average (R_a) and RMS (R_q) surface roughness parameters also decreased, from 0.44 nm and 0.56 nm for 10 W to 0.33 nm and 0.42 nm for 100 W, respectively. Coatings fabricated at higher deposition power were characterised by improved hardness and enhanced wear resistance. The hardness increased from 0.33 GPa for 10 W to 0.51 GPa for 100 W at 500 μN load. The elastic recovery was estimated to be between 0.1 and 0.14. Absence of significant fluctuations in the friction coefficient indicates no considerable damage, cracking or delamination of the coating occurred. Coatings deposited at higher RF powers showed less mechanical deformation attributed to increased degree of cross-linking associated with higher input power and hence are likely to be more stable and less susceptible to wear. Potential for damage and delamination of polyterpenol coatings was also qualitatively assessed using a standardised cross-hatch test. Independent of the substrate, the quality of adhesion is improved for samples deposited at higher RF power; the results consistent with those obtained using nanoindentation system. This study substantiate that the polyterpenol, which adheres well to many commonly used substrates, is a potential candidate for thin film applications which require smooth and uniform surfaces.

CHAPTER V

CHEMICAL AND PHYSICAL STABILITY UNDER VARIED ENVIRONMENTAL CONDITIONS

In this chapter, stability of polyterpenol under ambient and extreme environmental condition is investigated.

In Section V.1, chemical and physical properties are observed over prolonged periods of time, providing crucial information regarding the feasibility of employing the polyterpenol thin films. Considering that certain applications require the materials to maintain their properties after being exposed to high temperatures, such as during some stages of the IC fabrication, whereas others favour those materials that can thermally disintegrate living minimal residue, thermal degradation of polyterpenol is investigated. The results of this study are published as *Bazaka, K., Jacob, M. V., Post-deposition ageing reactions of plasma derived polyterpenol thin films. Polymer Degradation and Stability 2010, 95, 1123-1128*.

Understanding of the interactions that take place upon exposure of the polyterpenol material to common solvents are fundamental in determining the stability and degradation profile of these films. As discussed in Section V.2, this information is essential in ascertaining solubilisation potential of polyterpenol when exposed to solvents used for wet processing in IC fabrication. Similarly, ability to withstand or degrade upon contact with physiological fluids will predetermine biomaterial applicability of the polyterpenol coatings. Surface tension, wettability and solubility properties of polyterpenol are presented in *Bazaka, K., Jacob, M. V., Solubility and surface interactions of RF plasma polymerized polyterpenol thin films*.

V.1 POST-DEPOSITION AGEING REACTIONS AND THERMAL STABILITY OF POLYTERPENOL

Abstract

Owing to the structural flexibility, uncomplicated processing and manufacturing capabilities, plasma polymers are the subject of active academic as well as industrial research. Polymer thin films prepared from non-synthetic monomers combine desirable optical and physical properties with biocompatibility and environmental sustainability. However, the ultimate expediency and implementation of such materials will dependent on the stability of these properties under varied environmental conditions. Polyterpenol thin films were manufactured at different deposition powers. Under ambient conditions, the bulk of ageing occurred within first 150 h after deposition and was attributed to oxidation and volumetric relaxation. Films observed for further 12 months showed no significant changes in thickness or refractive index. Thermal degradation behavior indicated thermal stability increased for the films manufactured at higher RF powers. Annealing the films to 405 °C resulted in full degradation, with retention between 0.29 and 0.99 %, indicating films' potential as sacrificial material.

Keywords: Ageing; ellipsometry; encapsulating layer; thermal degradation;

As published in: Bazaka, K., Jacob, M. V., Post-deposition ageing reactions of plasma derived polyterpenol thin films. *Polymer Degradation and Stability* 2010, 95, 1123-1128.

V.1.1 Introduction

Organic polymer thin films deposited by means of plasma polymerisation hold the prospects of combining advantageous properties of the precursor, such as biocompatibility, with the attractive features offered by plasma polymerized thin films, such as high adhesion to substrate and surface uniformity, and have been discussed by many authors [77,216,320,340,370]. Actual and potential applications for such polymer films include areas such as semiconductor technology, protective and biocompatible coatings, permselective membranes, sacrificial materials and as adhesion promoters [87,90,371]. The implementation of plasma polymer materials will be influenced by the extent to which a polymer film's properties deteriorate or change under ambient environment or when subjected to extreme environmental conditions, such as annealing. High material stability is essential for applications where the original properties are to be maintained during the intended lifetime of the device. On the other hand, a low point of thermal decomposition and low retention rate are a critical characteristic for sacrificial materials, which are used for closed cavity nanometer scale air gap structures in photonics and in semiconductor devices [372-374].

Recently, a novel organic polymer material was reported [336]. Films were fabricated from non-synthetic terpinen-4-ol by means of radio frequency plasma polymerisation. With the refractive index and extinction coefficient values at 500 nm of 1.55 and 0.0007 respectively, optical band gap of 2.67 eV, and smooth defect free surface, these films have prospective applications in optics and electronics. As an optically transparent film, polyterpenol film can also be implemented as an encapsulating (protective) layer for the circuit boards. Manufactured from an environmentally friendly natural source, these films are potentially biocompatible and therefore can be utilized as coatings where biocompatibility is essential, e.g. organ implants. Yet, the ultimate expediency of polyterpenol material is dependent on the stability of the films.

In this study, the stability and thermal degradation of polymer thin films derived from organic terpinen-4-ol monomer is examined. The effect of deposition RF on the stability of the polymer films is scrutinized.

V.1.2 Experimental

Amorphous polyterpenol thin films were prepared using capacitively coupled 13.56 MHz radio frequency plasma deposition with detailed description of the experimental arrangement outlined elsewhere [336]. Samples were fabricated at RF power levels of 10 to 100 W. Films of approximately equal thickness were achieved by gradual increase of deposition time for higher RF power. As substrate materials, glass slides, ultra-flat Si wafers (100) and KBr windows were employed to be used for ellipsometric, x-ray reflectometry (XRR) and Fourier transform infrared spectroscopy (FTIR) studies respectively. Prior to plasma deposition, the Si wafers and glass slides were washed in solution of Extran and distilled water, ultrasonically cleaned for 30 min and rinsed with ethanol to remove any inorganic contaminants. The wafers were further treated with piranha solution (20% H_2SO_4 in concentrated H_2O_2) for 3 h to destroy residual organic contaminants. The wafers and glass slides were thoroughly rinsed with double distilled water and blown dry. The cleaning protocol produced a hydrophilic surface, leaving a relatively dense layer of Si-OH groups on a silicon oxide layer, without notably roughening the surface.

Samples of approximately ~700 nm thickness were stored in ambient conditions (23 °C) and their material properties were observed for 1128 h. Optical properties and film thickness were monitored using variable angle spectroscopic ellipsometer (model M-2000, J. A. Woollam Co., Inc.). Images were taken by means of NT-MDT atomic force microscope (AFM) to estimate the alteration in the surface of the film. Scans were obtained using Nicolet Maxim FTIR spectrometer immediately after deposition and after 1000 h of ageing to determine the change in the chemical structure of the films. Samples of ~ 45 nm thickness were examined using XRR after 150 hours and after 12 months of storage to ascertain changes in atomic thickness (*d*), interfacial roughness (σ) and scattering length density (*SLD*) of the films. The XRR measurements were acquired as a function of incident angle (θ) in air using a Panalytical X’Pert Pro reflectometer with Cu Kα ($\lambda = 1.54056$ Å) radiation.

Films of ~ 600 nm thicknesses were first kept in ambient conditions for the material to stabilise. Then, thermal stage option of the ellipsometer was used to collect *in-situ* dynamic Ψ and Δ parameters (at fixed $\varphi = 70°$) for the samples while they were annealed up to 405 °C. Temperature was applied to the stage in 10 °C steps with 5 min intervals to maintain thermal equilibrium between the sample and the stage. FTIR scans were performed before and after annealing samples to 200 and 300 °C.

V.1.3 Results and Discussion

V.1.3.1 Surface properties

AFM examination of the films immediately after the deposition and subsequently after 1128 h in ambient environment showed no visible change had taken place (Figure V.1.1). As deposited, all polymer films were found to be smooth and defect free, suggesting the polymerization occurred predominantly on the surface of the glass substrate rather than in the gas phase. Irrespective of deposition power, exposure to ambient environment for 1128 h did not visibly change the surface topography of the polyterpenol samples. Statistical analyses of films as-deposited and post-exposure were performed against such surface descriptors as average roughness (R_a), RMS roughness (R_q), maximum peak height (R_{max}), surface skewness (R_{skw}) and coefficient of kurtosis (R_{kur}). Roughness parameters such as R_a, R_q, and R_{max} were not statistically different ($p > 0.05$) from the respective as-deposited values. Average roughness R_a for the films was around 0.3 nm. All polymer surfaces displayed the surface skewness (R_{skw}) > 0 and coefficient of kurtosis (R_{kur}) < 3. Such values for R_{skw} and R_{kur} indicate a disproportionate number of peaks pertinent to the polyterpenol surfaces and a well spread out height distribution, respectively. Minor variations in these values were attributed to the inherent properties of the area of the polymer film being scanned. They were also found not to be significantly different ($p > 0.05$) for samples as-deposited and after 1128 h of exposure. Thus, the polyterpenol films are stable under ambient conditions and therefore can be applied as transparent encapsulating layers in electronic circuitry.

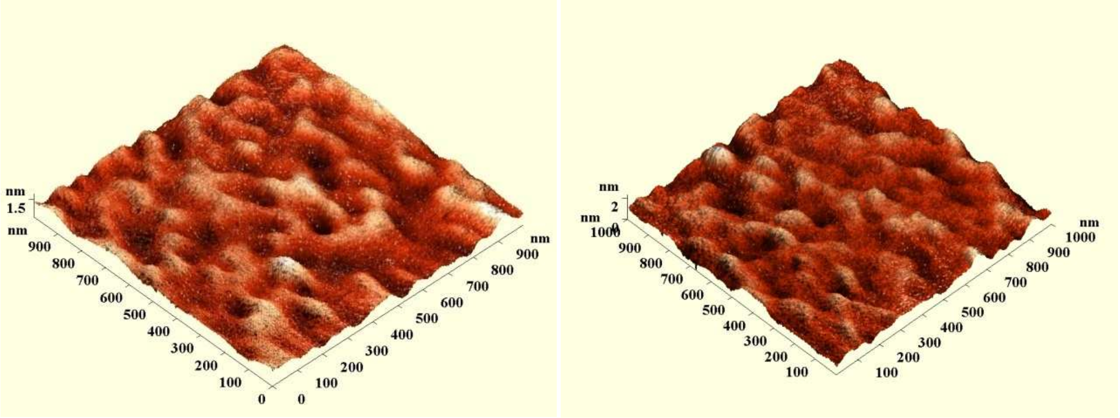

Figure V.1.1. AFM image of 25 W polyterpenol films as deposited and after 1128 h.

V.1.3.2 Film thickness and roughness

Film thickness was monitored through ellipsometric parameters Ψ and Δ and transmission data collected over a wavelength range of 200–1000 nm at angles of incidence φ= 55°, 60°, and 65°. Data was obtained near the Brewster angle for the material to minimise noise and systematic error [375]. The position of the glass slide in relation to the ellipsometry stage was recorded and used for subsequent measurement to reduce sampling error. Sample thicknesses remained approximately constant over the observation period (Table V.1.1). Minor thickness reduction observed in samples fabricated at 25, 50, 75 and 100 W can be explained by molecular relaxation and gradual increase in density during an extended ageing process. Comparable ageing behaviour has been previously noted for glassy polymers like polysulfone, with 0.8 % thickness reduction over 250 days of observation [376]. Minor thickness increase detected in samples deposited at 10 and 15 W was likely due to the oxygen uptake into the chemical structure of the material through alkyl radical termination [377].

Table V.1.1. Change in thickness and refractive index (at 300, 600 and 900 nm) of Polyterpenol films subjected to 1128 h in ambient environment.

Power	Refractive index change, %			Thickness change, %
	300 nm	600 nm	900 nm	
10 W	0.02	0.08	0.02	0.28
15 W	0.08	0.08	0.14	0.32
25 W	0.34	0.23	0.05	-0.12
50 W	0.49	0.28	0.07	-0.11
75 W	0.58	0.32	0.14	-0.36
100 W	0.49	0.41	0.18	-0.37

The effect of deposition power on thermal stability of polyterpenol films was examined using dynamic ellipsometric data (Ψ and Δ) from annealing samples to 405 °C. Preliminary examination of Ψ and Δ data indicated all samples were relatively stable up to approximately 245 °C, with the degradation onset shifting to higher temperatures for samples deposited at increased power levels. Greater thermal stability for this temperature range can be ascribed to higher degree of cross-linking in polymers fabricated at 50, 75 and 100 W. Prior to the onset of bulk degradation, 10, 15 and 25 W samples underwent insignificant thermal decomposition attributed to desorption of low molecular weight species, similar to α-methylstyrene . Above 245 °C, notable alterations in Ψ and Δ parameters suggested the materials were undergoing a phase change, with concurring rapid reduction in thickness, as demonstrated in Figure V.1.2, and significant increase in refractive index.

Annealing to 405 °C resulted in complete decomposition of the films with residue levels ranging between 0.29 and 0.99 %, compared to 0.8 to 5.8 % residue reported for plasma polymerized poly(methyl methacrylate) [340,378]. This is a favourable result if the material to be considered for use as a sacrificial layer in air gap fabrication that requires low onset degradation temperature and least residue [377]. Furthermore, by varying deposition conditions, RF power in this case, a range of onset decomposition temperatures can be achieved, an important factor if the material to be considered for integration in multi-component structures.

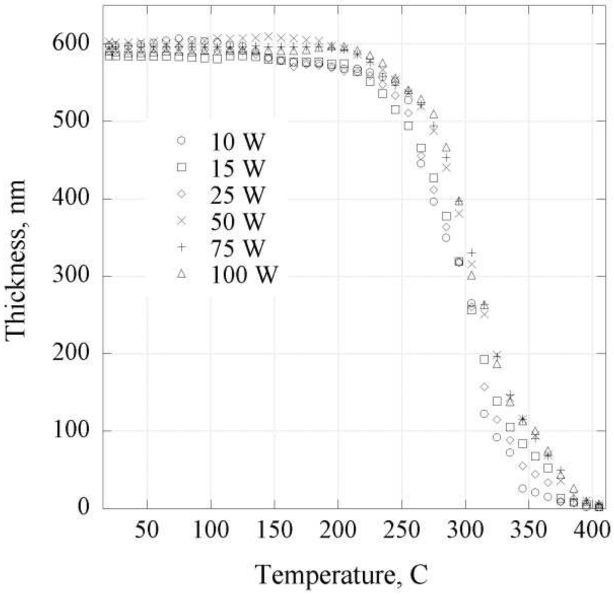

Figure V.1.2. Film thicknesses as a function of temperature for polyterpenol films (to 405 °C).

XRR studies of films of approximately 45 nm in thickness were conducted to ascertain changes in atomic thickness (*d*), surface roughness and scattering length density (*SLD*) of the films subject to long term exposure to the ambient environment. Reflectometry probes the structure of a thin film normal to the surface by measuring the specularly reflected beam as a function of the momentum change perpendicular to the surface (Q_z). Similarly to spectroscopic ellipsometry, where reflection of light off a thin uniform layer deposited on a surface of a substrate results in interference fringes the period of which is directly proportionate to the layer's thickness and the magnitude of which is closely related with layer's refractive index, x-ray reflection leads to oscillations (Kiessig fringes) from which the thickness of the layer can be determined by $d \approx 2\pi/\Delta Q_z$. Using the Parratt formalism, reflectivity data were fitted as log(*R*) vs *Q*, with corrections for a linear background, resolution smearing, and Gaussian roughness at each interface [379]. The *SLD* value of 20.1 10^{-6} Å^{-2} was assumed for Si and native oxide layer.

The air-solid reflectivity measurement from the polyterpenol film deposited at 25 W is shown in Figure V.1.3, where symbols represent the observed reflectivity data and a solid line is the calculated reflectivity profile derived from the single layer structural model. Films were found to be of uniform density and high smoothness, latter being confirmed by a large number of Kiessig fringes persisting to high Q_z, where instrumental background commonly dominates. Surface roughness was calculated to be in a range of 0.35 nm compared to 0.3 nm obtained from AFM studies. A discrepancy between roughness values obtained from AFM and reflectivity data stems from the difference in measurement areas between these techniques – 10 μm × 10 μm and 1 cm × 1 cm for AFM and XRR respectively.

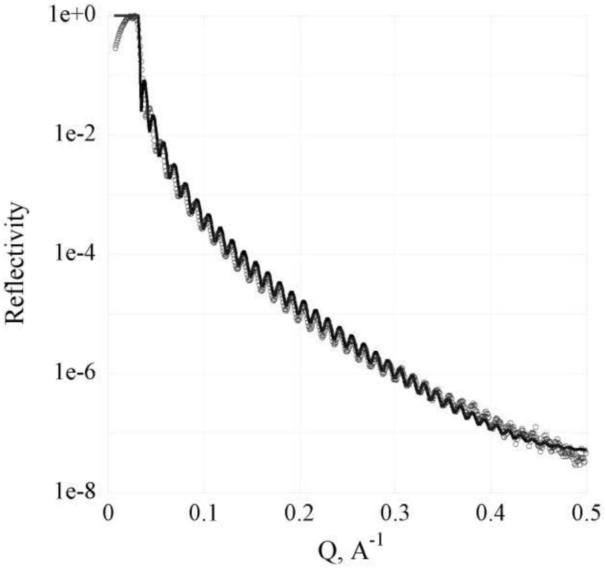

Figure V.1.3. X-ray reflectivity data and fit for Polyterpenol film deposited at 25 W.

Refined structural parameters for polyterpenol films, such as SLD, thickness and surface roughness, were determined from reflectivity data collected after 150 h and 12 months of exposure to ambient environment. The difference between the values was negligible, frequently below the modelling error value for the respective fitted parameter. In addition, although care was taken to conduct measurements in the exactly the same location, such error could have attributed to the discrepancy between the before and after values. Deposition power was found to have no significant effect on the long term stability of the polymer. Therefore, under ambient conditions, the polyterpenol films are stable in terms of their atomic thickness, roughness and scattering length density, latter being a factor of polymer density and composition.

V.1.3.3 Optical properties

The optical properties of the polyterpenol films as-deposited and approximately 1128 h post-deposition are presented in Table V.1.1. The change in refractive index (at 300, 600 and 900 nm) over the duration of the measurement period is demonstrated in Figure V.1.4. Within the first 150 h after the deposition, the refractive index increased for all the samples independent of deposition power. Rapid deterioration of films’ optical properties (first 150 h) was followed by a slowdown in the rate of change as the materials approached their thermodynamic equilibrium state. The index remains stable thereafter indicating the bulk of the degradation of Polyterpenol films occurred within the first 150 h after deposition, irrespective of the power level at which the samples were deposited.

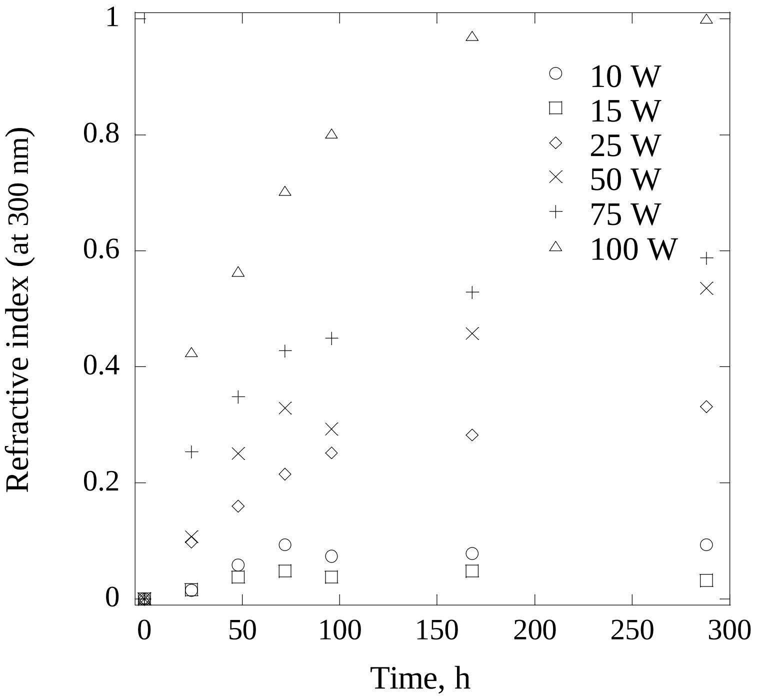

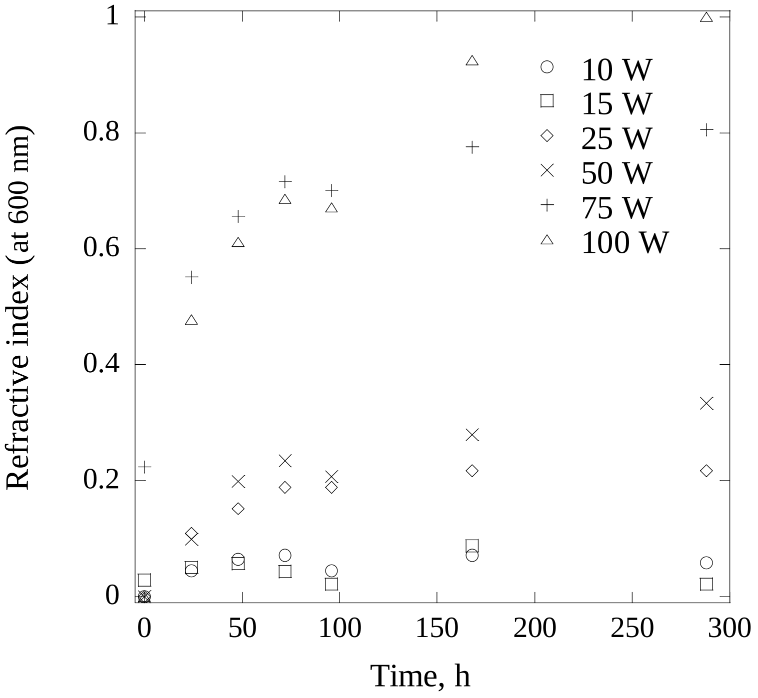

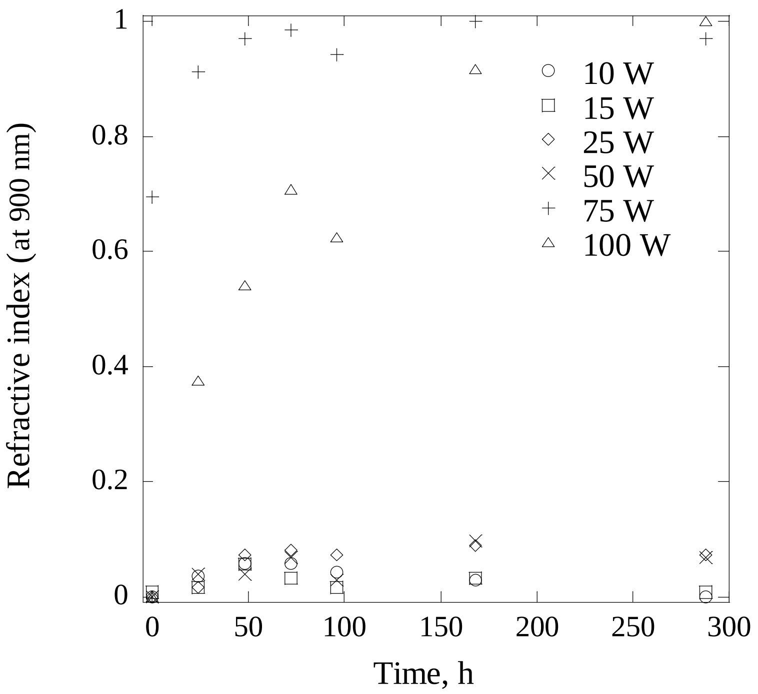

Figure V.1.4. Refractive index at 300, 600 and 900 nm as a function of time for Polyterpenol thin films deposited at RF power of 10, 15, 25, 50, 75 and 100 W.

Absorption spectra of samples were collected as-deposited and after 12 months of exposure to ambient environment using UV-Vis Spectroscope to ascertain if films retained their optical transparency over the visible part of the light spectrum. Unlike other studies where increase in deposition power resulted in broadening and/or shifting of position of the absorption peak [96], polyterpenol films deposited at different power levels possessed similar absorption profile with the main absorption peak around 295 nm which was attributed to pi–pi* transitions. Figure V.1.5 demonstrates the UV-Vis absorption behaviour of the polyterpenol thin film deposited at 25 W prior to and after 12 months of storage. As can be seen from the graph, exposing the polyterpenol sample to ambient environmental conditions had no significant effect on the absorbance spectrum of the film irrespective of the deposition power. This is a favourable result if the material is to be considered for applications where optical transparency is essential, such as an encapsulating (protective) layer for the circuit boards.

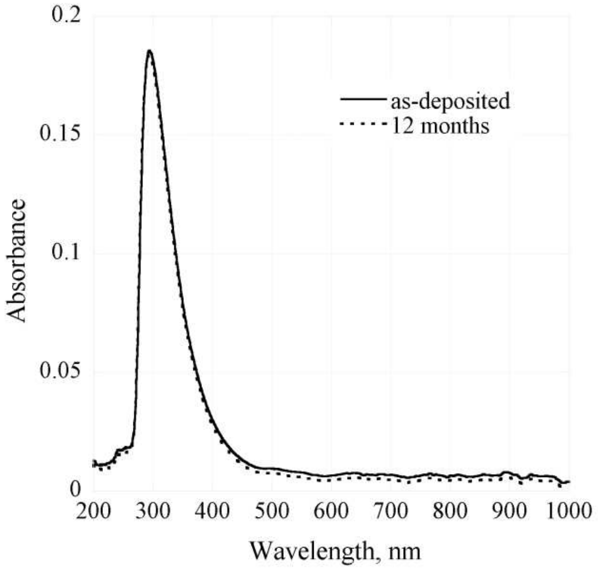

Figure V.1.5. UV-Vis absorption spectrum of Polyterpenol film deposited at 25 W.

Annealing samples to 245 °C did not result in any significant change in the refractive index of the material, with films deposited at 50, 75 and 100 W showing higher degradation onset temperature compared to ones deposited at 10, 15 and 25 W, due to lower degree of cross-linking for the latter. Above 245 °C, all materials were undergoing a phase change, with significant increase in refractive index, as shown in Figure V.1.6.

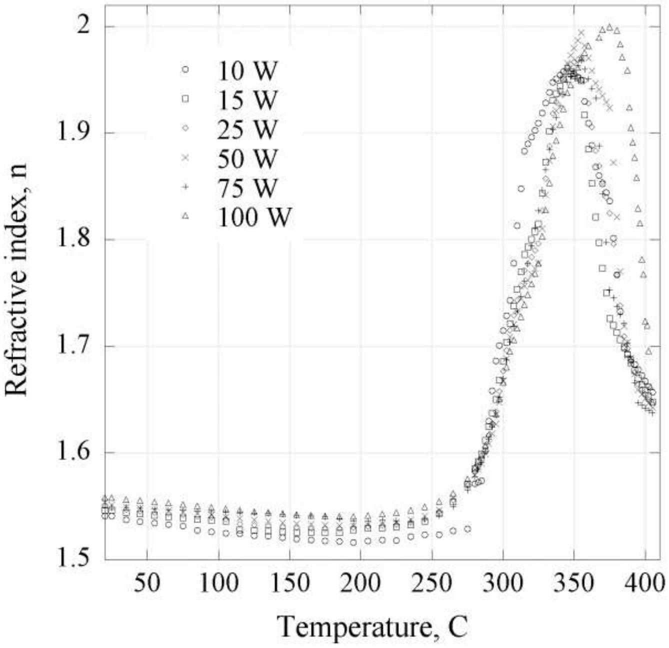

Figure V.1.6. Dynamic refractive index for Polyterpenol films as a function of annealing temperature.

V.1.3.4 Chemical properties

FTIR spectra of samples fabricated at 10, 15, 25, 50, 75 and 100 W as-deposited and after 1128 h of exposure to ambient conditions were compared to understand the nature of the degradation process taking place. Absorption bands were assigned based on reference infrared group frequencies and a previous study [336]. From previous study, IR spectra of the films deposited at varying power levels primarily differed in magnitude of the spectra peaks, the behaviour that was confirmed during this study. Therefore, it can be assumed that samples deposited at different powers are likely to exhibit similar degradation behaviour. After 1128 h for samples deposited at 10 and 15 W, there was no significant change in the spectra other than a small (in the region of 1%) increase in intensity of the broad peak at 3450 cm^{-1} that can be attributed to an uptake of oxygen into the chemical structure of the material typically observed in plasma polymers. However, the oxidation taking place in these polyterpenol films was less pronounced compared to other plasma polymer films under similar ageing conditions, such as poly(α-methylstyrene), where the inclusions of additional oxygen containing groups (such as C–O and C=O) were reported [377].

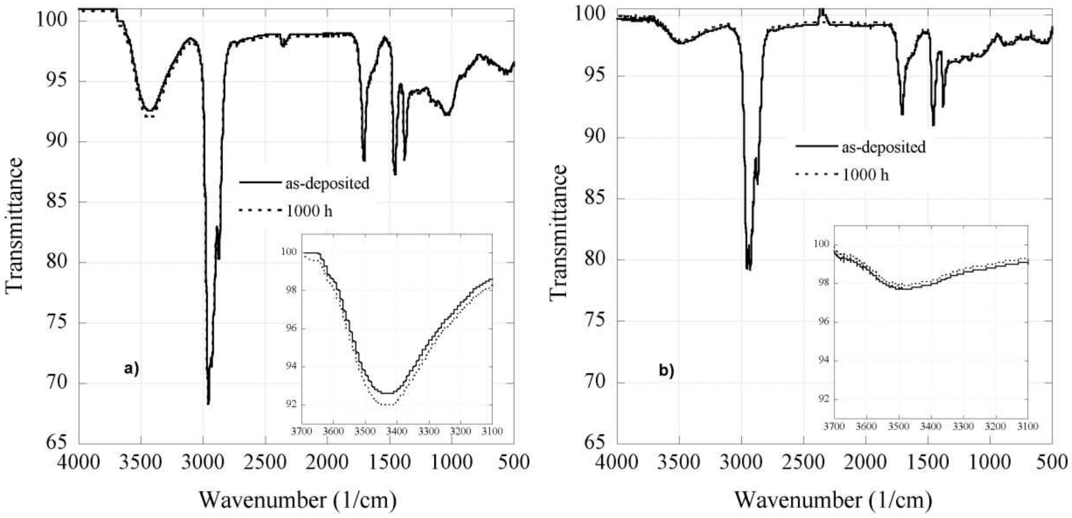

Figure V.1.7. FTIR spectra for Polyterpenol thin films deposited at a) 10 W and b) 100 W as deposited and after 1128 h in ambient environment.

Figure V.1.7 demonstrates the FTIR spectra for polyterpenol thin films deposited at 10 and 100 W. There was no observable difference (less than 0.05%) between as-deposited and post-1128 h spectra for samples deposited at 25, 50, 75 and 100 W confirming the respective change in refractive indices was attributable to material relaxation [380]. Interestingly, in the case of poly (α–methylstyrene), samples deposited at higher power showed higher levels of oxygen incorporation due to the presence of higher concentration of radical sites, while polyterpenol films demonstrated a reverse trend, with polymers deposited at 100 W being incorporating less oxygen compared to 10 W samples. Other experiments (results not shown here), including surface energy calculations, Raman and XPS, confirmed that polymers deposited at higher RF powers were more chemically and physically stable than the films fabricated at lower powers due to the higher degree of cross-linking and reduced oxygen content.

FTIR spectra for polyterpenol films as-deposited and post-annealing were compared to gain further insight into thermal stability of the material (Figure V.1.8). In general, thermal treatment up to a certain temperature increases the mobility of the cross linked polymer chains in the bulk of the film, hence favouring the recombination of free trapped radicals, and is often used to improve the stability of the plasma polymer, although it also results in a notable weight loss. As evidenced by the change in thickness (Figure V.1.2), samples fabricated at 10, 15 and 25 W display two distinct regimes of decomposition, which is not the case for films fabricated at higher RF powers. For these films, the first regime is commencing at approximately 100 °C and is largely driven by desorption of low molecular weight species prior to the onset of bulk decomposition; the less cross linked nature of these films is thought to be the likely cause, similar to poly(α–methylstyrene). The second phase of decomposition begins at approximately 200 °C. Films fabricated at 50, 75 and 100 W begin to thermally decompose at significantly higher temperatures, 175, 195 and 205 °C respectively, the shift to higher onset degradation temperature is attributed to the increasing degree of cross linking pertinent to these polymers. Furthermore, as demonstrated in Figure V.1.7, polymers fabricated at lower RF power contain higher amounts of oxygen containing moieties, such as hydroxyl and carboxyl groups, that are characterized by weaker bonds with lower dissociation energy compared to most C–H bonds. As C–O bonds are more polar than hydrocarbon bonds, new reaction pathways are generated as the lone electron pairs undergo acid/base interactions. FTIR spectrum for 200 °C was almost identical to one for as-deposited film confirming that the thermal degradation over this temperature range was principally due to weight loss [377]. Between 200 and 250 °C, the rate of weight loss increases, particularly for samples deposited at lower powers, however the refractive index remains relatively stable. Above approximately 250 °C, all polyterpenol films undergo a phase change which is reflected in a rapid increase in refractive index and concomitant reduction in film thickness (Figures V.1.2 and V.1.6). Side groups that are weakly bonded to the carbon backbone and that form stable small molecules, such as hydroxyl moiety, have been demonstrated to split off the polymer molecule easily. Polyvinyl alcohol and polyvinyl acetate have been shown to undergo non-radical depolymerization process of hydrogen abstraction via elimination of water [381]. Similarly, hydrogen abstraction is believed to be the likely process to transform the original polyterpenol film into a less hydrocarbon dense structure. A spectrum for 300 °C confirms hydrogen abstraction, with significant reduction in intensity of peaks assigned to stretching (ν) and bending (δ) of C–H bonds [2955 cm^{-1} (ν_a(C–H)), 2930 cm^{-1} (ν_a(C–H)), 2875 cm^{-1} (ν_s(C–H)), 1459 cm^{-1} (δ_a(C–H)) and 1380 cm^{-1} (δ_s(C–H))], hydroxy group [3460 cm^{-1} (ν(–OH))], and increase in intensity for peaks associated with carbon-oxygen stretching [1707 cm^{-1} (ν(C=O)), 1150 cm^{-1} (ν(C–O)), 1050 cm^{-1} (ν(C–O))]. Furthermore, the peaks widened indicating a loss in homogeneity in bonding environments [377]. Absent from the original spectrum, a new peak indicative of unsaturation appeared [1608 cm^{-1} (ν(C=C))], although it might have been previously obscured by the relatively strong carbonyl peak. Due to the cross linked nature of polyterpenol, the scission of weaker C–H bonds is also likely to takes place, with the hydrogen at tertiary carbon atoms being the likely initiation site. For brunched and cross linked hydrocarbon polymers, thermal degradation via radical transfer to the tertiary carbon atom followed by the scission of a C–C bond in the β–position is another common degradation pathway.

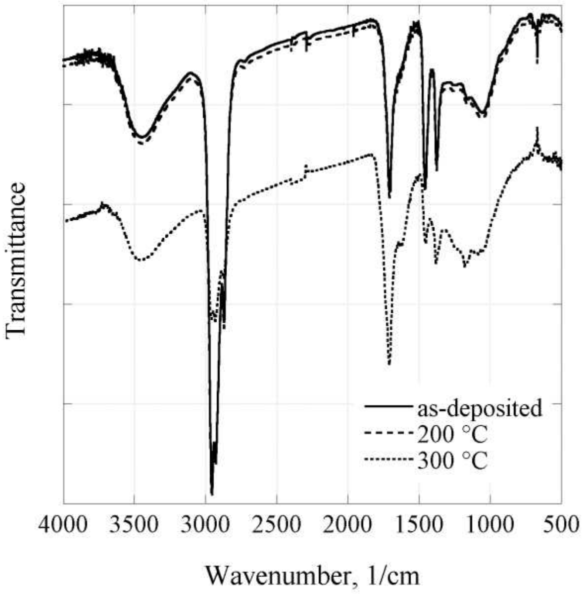

Figure V.1.8. FTIR spectra of samples fabricated at 25 W as-deposited and after successive annealing to 200 and 300 °C.

V.1.4 Conclusion

Optical parameters, thickness and chemical structure of polyterpenol thin films prepared by radio-frequency plasma deposition from organic terpinen-4-ol monomer at different deposition powers were observed over the period of 1128 h. Under ambient conditions, the bulk of ageing occurred within first 150 h after deposition and was attributed to oxidation and volumetric relaxation. Changes of under 0.58 and 0.37 % in refractive index and thickness respectively were insignificant confirming the Polyterpenol films were stable when in contact with ambient environment and therefore can potentially be used as an encapsulating layer in circuitry. Thermal ageing studies indicated thermal stability increased for the films manufactured at higher RF powers. Annealing the films to 405 °C resulted in full degradation, with retention between 0.29 and 0.99 %. Films deposited at lower RF powers showed most promising decomposition outcomes due to their less cross-linked structure compared to the films fabricated at higher RF power. Polyterpenol films are therefore believed to have great potential for use as sacrificial material in air gap fabrication due to their controllable degradation onset temperature and minimal residue levels.

V.2 SOLUBILITY AND SURFACE INTERACTIONS OF POLYTERPENOL THIN FILMS

Abstract

Organic thin films have myriad of applications in biological interfaces, micro-electromechanical systems and organic electronics. Polyterpenol thin films fabricated via RF plasma polymerization have been substantiated as a promising gate insulating and encapsulating layer for organic optoelectronics, sacrificial place-holders for air gap fabrication as well as antibacterial coatings for medical implants. This study aims to understand the wettability and solubility behavior of the nonsynthetic polymer thin film, polyterpenol. Polyterpenol exhibited monopolar behavior, manifesting mostly electron donor properties, and was not water soluble due to the extensive intermolecular and intramolecular hydrogen bonds present. Hydrophobicity of polyterpenol surfaces increased for films fabricated at higher RF power attributed to reduction in oxygen containing functional groups and increased cross linking. The studies carried out under various deposition conditions vindicate that we could tailor the properties of the polyterpenol thin film for a given application.

Keywords: biomaterials; coatings; contact angle; optical coatings; organic semiconductors;

As submitted to: Bazaka, K., Jacob, M. V., Solubility and surface interactions of RF plasma polymerized polyterpenol thin films (in review).

V.2.1 Introduction

Organic thin films have a wide variety of current and potential applications in biological interfaces and sensors, in micro-electromechanical systems, and in organic electronics, including protective coatings, waveguides and component materials [85,86,319]. Thin films can be produced from organic precursors using a variety of techniques, including spin-coating and plasma-enhanced chemical vapor deposition [89,90,96]. Non equilibrium plasmas have been gaining popularity for the fabrication of polymer thin films as the method allows for deposition of smooth, defect free and uniform films from organic composites that may not necessarily polymerize through conventional thermo chemical pathways [87,88,98]. Polymers produced at different RF powers exhibit different chemical and physical properties, including structures with property gradient. The RF polymerization conditions include the geometry of the reaction chamber, the magnitude of the excitation signal or the manner the energy is delivered into the chamber. For instance, low energy, pulsed plasma, off-glow deposition and lower substrate temperatures are conditions likely to enhance the retention of the original monomer constituents in the polymer [322,339,382]. Plasma techniques are also widely used for surface modifications of polymer materials, altering the surface energy, roughness and chemical functionality of the material, improving adhesion of photoresists and developers in lithographic processes [383,384].

An organic polymer thin film material fabricated from non-synthetic monomer terpene-4-ol using radio frequency polymerization exhibited some interesting properties [336]. The key features of the polyterpenol thin films were transparency, optical comparable to glass, insulating electrical properties [337,350,353]. Relatively high degradation temperature and low post-annealing retention rates indicated polyterpenol is a potential sacrificial material. The developed material can be used in microelectronics field for air gap fabrication to replace low-k materials and to produce sealed nano-channels for biomedical testing applications [347,385]. Terpinen-4-ol is known for its antibacterial, antifungal, antiviral, and anti-inflammatory properties [386]. Manufactured from an environmentally friendly natural source, these films are potentially biocompatible and therefore are considered for applications as coatings in situations where biocompatibility is essential, such as in organ implants. Surface modification of biomaterials using plasma enhanced techniques have been recognized as an economical and effective method by which biocompatibility and biofunctionality can be achieved, while preserving the favorable bulk characteristics of the biomaterial, such as strength and inertness [200,283,352]. Plasma deposition of organic polymers, such as films of polyterpenol, affords device manufacturers a flexible and environmentally friendly process that enables tailoring of the surface morphology, structure, composition, and properties of the material to a specific need. Polyterpenol thin film coatings deposited on glass substrates at low power conditions, i.e. 10 W, have been shown to retain the antibacterial properties of its precursor against selected human pathogenic bacteria and prevent adhesion and proliferation of the bacterial cells on the film surface.

Surface free energy provides valuable information about the type of interactions that occur at the interface between the solid and the liquid [182]. Should a material be chosen as a sacrificial layer for air-gap fabrication, it is essential that such material retains its original dimension in the presence of a variety of acids, bases and organic solvents commonly used in IC processing, until it is thermally decomposed as one of the latter stages of IC fabrication. Where a wet etching procedure is chosen to remove the placeholding material, such sacrificial material should display selective solubility to the chosen solvent [387]. For polymer material to be considered as an appropriate coating for implantable medical devices, such coating should be biocompatible, yet prevent biofilm formation on its surface. Wettability of the surface has been shown to greatly influence the events that take place upon implantation of the material into the host body. Wetting by physiological liquids predetermines the subsequent adsorption of proteins and cells to the surface of the implanted materials [188], and therefore is detrimental to blood/cell/ tissue compatibility [189-191]. A correlative relationship has been demonstrated between surface wettability and blood/ cell/tissue compatibility, with higher degree of wettability linked to a higher level of cell attachment and ensuing spreading rates [192]. The tribological (friction) behavior of an implantable medical device is highly dependent on the surface wettability, with more wettable surfaces being generally better tolerated by the body [193].

The goal of this paper is to undertake a detailed study of the surface energy, wettability and solubility characteristics of polyterpenol when in contact with common processing solvents. In this paper we examine, by means of a sessile drop contact angle measurement, the wettability of a wide range of practically relevant solvents on polyterpenol thin films fabricated at a range of RF deposition powers. The wettability is correlated with the elemental composition of the film's surface determined using XPS analysis. From these data, surface energies and solubility behaviors are extracted.

V.2.2 Experimental

A detailed description of the experimental arrangements is outlined elsewhere [336]. In order to obtain consistency constant monomer flow is maintained under a constant pressure of 150 mTorr. The amorphous polyterpenol thin films of approximately same thickness of 500nm were fabricated under various RF input powers of 10, 25, 50 and 100 W. Chemical compositional analysis on polyterpenol thin films was carried out by X-ray Photoelectron spectroscopy (XPS) using an Axis Ultra spectrometer (Kratos Analytical Ltd., UK), equipped with a monochromatic X-ray source (Al Kα, hν = 1486.6 eV) operating at 150 W. The energy scale of the instrument was calibrated by measuring the binding energies for pure metal foils, Au $4f_{7/2}$ (E_b = 84.0 eV), Ag $3d_{5/2}$ (E_b = 368.3 eV), and Cu $2p_{3/2}$ (E_b = 932.7 eV). In the course of the analysis, polymer thin film samples were bombarded with low-energy electrons to offset surface charging, with the hydrocarbon C 1s peak component (E_b = 285.0 eV) used as reference for charge correction. Energies of 160 eV and 20 eV were used to analyze photoelectrons emitted at 90° to the surface from an area of 700 × 300 μm^2 for survey and region spectra respectively, recorded at corresponding steps of 1 eV and 0.1 eV. Kratos Vision II software was employed to remove linear background and fit synthetic Gaussian-Lorentzian components to the peaks in the high-resolution regions of spectra.

Contact angle studies were performed using a KSV 101 system. First, the experimental procedure was verified by conducting several water contact angle measurements on PTFE. A linear fit to water contact angle measurements on PTFE performed to validate the experimental procedure yielded $y=-0.02t+119$ and $R^2=0.98$ which was comparable to the results in literature [342]. Images were taken for 30 s at 1 s interval and image processing software was employed to establish the contact angle, θ, by fitting the Young-Laplace equation to the measured drop profile. For every solvent-sample combination, a contact angle was measured 10 times and the average was taken as the result. The obtained values of θ were used to calculate the surface tension (also referred to as surface energy with the corresponding units mJm^{-2} and mNm^{-1} being dimensionally equivalent) using three different methods, namely the Owens, Wendt, Rabel and Kaelble (OWRK) [388-390], Van Oss, Chaudhury, and Good (VCG) [391-393], and Neumann's [394] approaches. The interaction between two molecules within substance 1(in this case, the polymer), immersed or dissolved in substance 2 (the solvent) was determined from their interfacial tension γ_{12} using Equation 1 [395,396]:

$$\Delta G_{121} = -2\gamma_{12} \tag{1}$$

where ΔG_{121} is the free energy change and γ_{12} can be calculated using the following two equations:

$$\gamma_{12} = (\sqrt{\gamma_1^{LW}} - \sqrt{\gamma_2^{LW}})^2 + 2(\sqrt{\gamma_1^+\gamma_1^-} + \sqrt{\gamma_2^+\gamma_2^-} - \sqrt{\gamma_1^+\gamma_2^-} - \sqrt{\gamma_1^-\gamma_2^+}) \tag{2}$$

in the case of two completely miscible substances, where the interfacial tension cannot be directly measured but instead is calculated from the substances' individual surface tension components; and

$$\gamma_{sl} = \gamma_s - \gamma_l cos\theta \tag{3}$$

for two completely immiscible substances (or any given solid-liquid system), where the interfacial tension can be derived directly from the measured contact angle θ.

OWRK approach assumes the total surface tension of any liquid or solid phase i can be expressed as a sum of its polar γ^p and disperse γ^d fractions of the surface tension as follows [388,390]:

$$\gamma_i = \gamma_i^p + \gamma_i^d \tag{4}$$

The polar and disperse fractions of the surface tension of a solid is derived from the contact angle data of various liquids with known dispersive and polar fractions by transposition of the following equation to the general equation for a straight line $y = mx + b$:

$$y = \sqrt{\gamma_s^p} x + \sqrt{\gamma_s^d} \tag{5}$$

where $y = (1 + cos\theta) \cdot \gamma_l / 2\sqrt{\gamma_l^d}$, and $x = \sqrt{\gamma_l^p / \gamma_l^d}$. In a linear regression of the plot of y against x for at least two solvents, γ_s^p is obtained from the square of the slope of the curve m and γ_s^d from the square of the ordinate intercept b. Neumann's method of deriving the surface tension is based on the equation of state theory [394], where the contact angle between the solid and liquid is given as follows:

$$cos\theta = -1 + 2\sqrt{\frac{\gamma_s}{\gamma_l}} e^{-\beta(\gamma_s - \gamma_l)^2} \tag{6}$$

where γ_s and γ_l represent solid and liquid total surface tensions, respectively, and β is the empirically set coefficient related to a specific solid surface ($\beta \approx 0.0001247$). VCG approach postulates the total surface tension of a nonionic surface i consists of two contributions [393]: the γ_i^{LW} component that corresponds to Lifshitz-van der Waals interactions, comprising dispersion, dipolar, and induction forces, and the γ_i^{AB} component describing an acid-base interaction, comprising all of the electron-donor γ_i^- and electron-accepter γ_i^+ interactions, such as hydrogen bonding:

$$\gamma_i = \gamma_i^{LW} + \gamma_i^{AB} = \gamma_i^{LW} + 2\sqrt{\gamma_i^{+}\gamma_i^{-}} \qquad (7)$$

Therefore, for a given solid-liquid system, a complete Young-Dupre equation can be used as follows:

$$(1 + cos\theta)\gamma_l = 2(\sqrt{\gamma_s^{LW}\gamma_l^{LW}} + \sqrt{\gamma_s^{+}\gamma_l^{-}} + \sqrt{\gamma_s^{-}\gamma_l^{+}}) \qquad (8)$$

where three parameters for a solid γ_s^{LW}, γ_s^{+}, and γ_s^{-} can be determined by solving the equation for three liquids for which the surface tension parameters γ_l^{LW}, γ_l^{-}, γ_l^{+} and contact angle with the solid θ are known. These liquids should be either polar with different parameters, or a combination of one apolar (such as diiodomethane, with γ_l^{-}= γ_l^{+}=0) and two polar solvents.

V.2.3 Results and discussion

V.2.3.1 Elemental composition

Elemental analysis of the polyterpenol thin films deposited at different RF power levels was performed using XPS, and the results are presented in Figure V.2.1 and Table V.2.1.

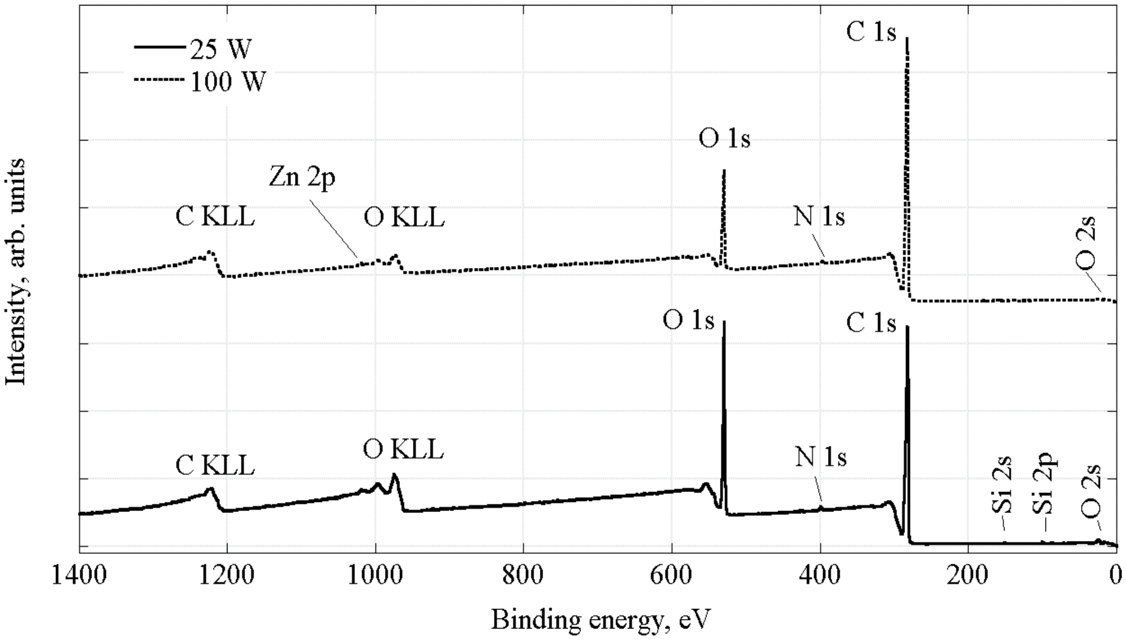

Figure V.2.1. XPS spectra of polyterpenol thin films fabricated at 25 and 100 W RF power.

Table V.2.1. Elemental composition of polyterpenol thin films deposited at 25 and 100 W RF power.

Peaks	25 W		100 W	
	Binding Energy eV	Atomic fraction %	Binding Energy eV	Atomic fraction %
Zn 2p	1022	-	1022	0.1
O 1s	533	22.8	533	12.2
N 1s	400	0.9	400	0.6
C 1s	286	76.0	286	87.1
Si 2p	102	0.3	102	-

Carbon and oxygen dominate the surface of both films (up to 99 at. %), with Si, Zn and N present in trace amounts (below 1%) and regarded as negligible. Glass substrate and ambient air were determined to be the most likely contributors of Si and Zn, and N respectively. The oxygen content significantly decreases from 22.8 to 12.2 % while the carbon fraction increases from 76.0 to 87.1 % with RF deposition power increased from 25 to 100 W. This result is in agreement with FTIR and Raman studies of polyterpenol that showed a substantial reduction in magnitude of the H-bonded O–H stretch related band for polymers fabricated under higher RF power conditions [200].

The high-resolution XPS spectra for the film deposited under 25 W RF power conditions is presented in Figure V.2.2. C1s spectrum encompasses contributions from carbon atoms in at least four chemical states, with peaks assigned to hydrocarbon species (BE = 285.0 eV) and functional groups with increasing bonding to oxygen (BE= 286.4, 287.7, and 289.1 eV for C – O, C = O and O – C = O species respectively). The N1s spectrum has been fitted to two bonding environments, nitrogen bonded to carbon (BE = 400.0 eV, C – N) and N bonded to a single oxygen atom (BE= 402.1 eV). The peak for oxygen O1s could not be fitted to particular chemical states due to a lack of fine structure although the width of the peak suggests it consists of more than one bonding environment, most likely originating from functional groups containing O bonded to C. The Si2p spectrum contains contributions from a single Si species (BE = 102.0 eV) indicating Si atoms bonded to O. Hence, polyterpenol is mostly hydrocarbon, with oxygen containing groups being present in the form of hydroxyl and carboxylic acid.

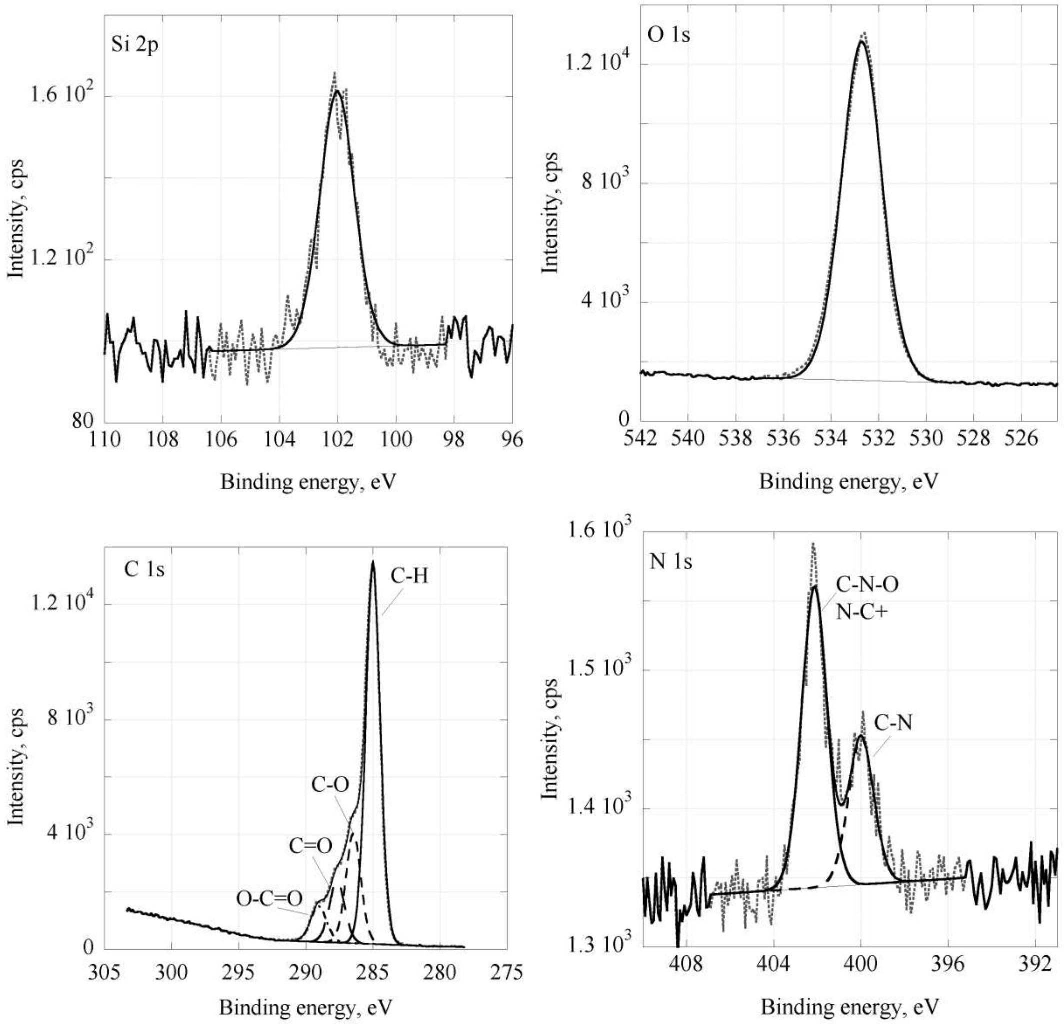

Figure V.2.2. XPS spectra of C 1s, O 1s, N 1s and Si 2p of polyterpenol thin films fabricated at 25 W RF power.

V.2.3.2 Contact angle and wettability

Any change in the shape of the drop may reflect such solvent/solid interactions as penetration of the liquid into the solid, swelling of the solid by the liquid, and chemical reactions that may take place at the liquid/solid interface, and can therefore have an effect on the values of γ_{sl}, and the apparent contact angle, θ. Examination of raw contact angle data (Figure V.2.3) for glycerol as a solvent revealed an initial rapid drop in contact angle for all samples independent of their deposition power and was attributed to the absorption of the solvent into the sample. For solvents such as ethylene glycol, formamide, and DMSO, the initial rapid drop in contact angle was also present, however it was more profound for the samples deposited at lower RF powers and decreased in magnitude with increased deposition power.

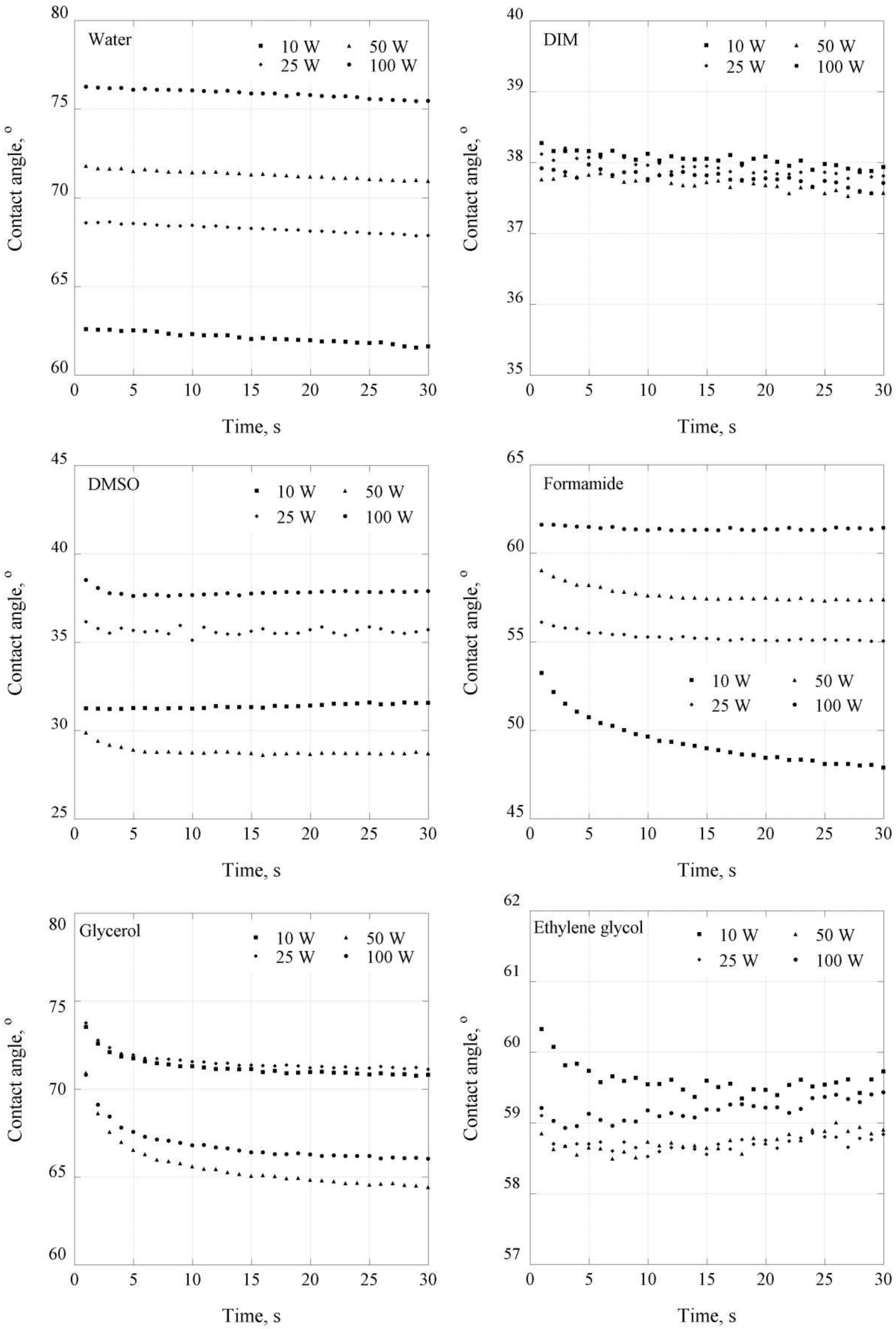

Figure V.2.3. Representative contact angle curves for polyterpenol thin films fabricated at different RF input power.

An initial rapid decrease in the contact angle indicates the absorption of the solvent into the sample is taking place, while a comparatively high rate of change signifies the reorientation of functionalities at the solid-solvent interface. Polyterpenol thin films deposited at higher RF power were found to be more hydrophobic compared to the films fabricated at lower RF power, with water contact angles of 63° and 76° for 10 and 100 W samples, respectively, and was attributed to the reduction in availability of hydrophilic moieties at the top surface of the polymer. Improved stability was expected for polyterpenol films fabricated at higher RF powers due to the increased degree of cross linking and the decrease in the oxygen content associated with the higher deposition power. Consequently, the polymers deposited at higher RF fabrication power displayed lower rate of change. Calculated contact angles for polyterpenol films deposited at varied RF power levels are summarized in Table V.2.2.

Table V.2.2. Surface tension parameters and corresponding contact angles θ for polyterpenol films deposited at varied RF powers.

Solvent	γ	γ^{LW}	γ^{AB}	γ^{+}	γ^{-}	Initial contact angle θ °			
						10 W	25 W	50 W	100 W
Water	72.8	21.8	51.0	25.5	25.5	62.7	68.7	71.7	76.3
Ethylene glycol	48.0	29.0	19.0	1.9	47.0	60.1	58.8	58.6	59.0
Glycerol	64.0	34.0	30.0	3.9	57.4	73.0	73.1	69.5	69.8
DIM	50.8	50.8	0.0	0.0	0.0	38.2	38.1	37.8	37.9
Formamide	57.5	38.5	19.0	2.3	39.6	53.2	56.1	58.9	61.6
DMSO	43.6	35.6	8.0	0.5	32.0	31.2	35.8	29.5	38.0
Hexane	18.4	-	-	-	-	-	-	-	-
Chloroform	27.3	-	-	-	-	-	-	-	-
Ethanol	22.4	-	-	-	-	-	-	-	-
Acetone	24.0	-	-	-	-	-	-	-	-

For solvents such as water, glycerol, DIM, and formamide, the contact angle decreased with time from its observed value at *t=0*, which is due to the reactions between the solid-liquid interface and/or evaporation are taking place [342]. Drops of different volume were used to determine if evaporation was the cause of the decrease in contact angle; drop volume was found not to influence the measured contact angle significantly. Therefore, absorption of the liquid by the polymer is the likely reason behind the observed decrease in contact angle. In the case of ethylene glycol and DMSO, the initial drop is followed by subsequent increase in contact angle over time, and is attributed to reorientation of functionalities occurring at the solid-liquid interface. Wettability is known to be strongly influenced by the morphological architecture and chemical composition of the surface [397-400]. The difference in the morphology of the sample under investigation was insignificant and thus, the decrease in oxygen containing functional groups was the likely driver of the increase in the hydrophobicity of the polymer surface [343].

V.2.3.3 Surface tension parameters

Surface tension parameters for polyterpenol thin films deposited at different power levels were derived using the OWRK, VCG and Neumann's approaches and the results are presented in Table V.2.3, V.2.4, and V.2.5, respectively. Total surface tension parameters determined via the three methods were comparable. The OWRK method was expected to be more accurate compared to VCG or Neumann's approaches as multiple contact angle measurements for a range of solvents are employed to determine the solid surface tension value. As a single liquid method, Neumann's approach is profoundly affected by the choice of the test liquid and neither the dispersion nor the polar component can be evaluated. VCG is also greatly affected by the choice of three solvents.

Table V.2.3. Surface tension parameters of polyterpenol films deposited at different RF powers (calculated using OWRK approach).

	γ^{LW}	γ^{AB}	γ_S
10 W	28.5	9.4	37.9
25 W	30.0	7.1	37.0
50 W	31.9	5.9	37.7
100 W	32.2	4.5	36.7

Table V.2.4. Surface tension parameters of polyterpenol thin films deposited at various power levels (determined using Neumann's approach).

	10 W	25 W	50 W	100 W
Water	46.23	42.54	40.64	37.79
Ethylene glycol	29.38	29.99	30.07	29.88
Glycerol	33.65	33.56	35.62	35.48
DIM	41.41	41.44	41.57	41.53
Formamide	39.73	38.27	36.77	35.27
DMSO	35.43	36.21	38.37	35.43

In OWRK method, disperse γ^{LW} and polar γ^{AB} fractions of the surface tension of polyterpenol samples were determined by plotting the measured contact angles for all liquids and fitting a straight line to the plotted values. The linear fit improved for samples deposited at higher RF powers, indicating a higher degree of accuracy between contact angle measurements for different liquids and improved stability of the films fabricated under increased RF power conditions. The results summarized in Table V.2.3 show the increase in RF deposition power did not affect the total surface energy of the polyterpenol film. However, a clear trend was present for the dispersive fraction γ^{LW} and acid-base fraction γ^{AB} as a function of fabrication power. Lower power samples were characterized by lower γ^{LW} and higher γ^{AB} values compared to films fabricated at higher RF power levels, as surfaces of the latter contained less of polar moieties (such as –OH). Neumann's approach for calculation of surface tension produced a unique value γ_S per solvent-sample combination; the results are summarized in Table V.2.4. The surface tension parameters calculated from water, formamide, and DMSO contact angles decrease for increasing RF fabrication power, while the surface tension parameters calculated from respective contact angles for glycerol show the reverse trend. Surface tension values obtained from ethylene glycol and DIM contact angle data remain approximately the same for all samples irrespective of RF power.

Table V.2.5. Surface tension parameters of polyterpenol films deposited at different RF powers (calculated using VCG method).

Sample	Liquid combination	γ^{LW}	γ^{+}	γ^{-}	γ_S
10 W	DIM:W:EG	40.50	0.75	30.24	31.00
	DIM:W:G	40.50	0.77	30.39	30.83
	DIM:W:F	40.50	0.01	22.53	39.45
	DIM:W:DMSO	40.50	0.03	23.03	38.93
25 W	DIM:W:EG	40.55	0.37	20.68	35.05
	DIM:W:G	40.55	0.42	21.10	34.57
	DIM:W:F	40.55	0.02	16.67	39.41
	DIM:W:DMSO	40.55	0.07	17.71	38.32
50 W	DIM:W:EG	40.70	0.26	16.65	36.53
	DIM:W:G	40.70	0.04	14.16	39.24
	DIM:W:F	40.70	0.08	14.89	38.46
	DIM:W:DMSO	40.70	0.00	12.48	40.96
100 W	DIM:W:EG	40.65	0.16	11.66	37.95
	DIM:W:G	40.65	0.01	9.23	40.54
	DIM:W:F	40.65	0.12	11.38	38.27
	DIM:W:DMSO	40.65	0.06	10.64	39.07

For surface tension calculations using the VCG approach, 10 solvent combinations (apolar liquid, DIM, and two polar liquids) were used for each type of sample and the results are presented in Table V.2.5. As mentioned earlier, the VCG method is highly affected by the choice of test solvents, the observation which was confirmed by our results. Certain solvent combinations produced large negative surface tension results, e.g. diiodomethane−glycerol−formamide in the case of all sample types (Table V.2.6). Electron-donor γ^- and electron-acceptor γ^+ parameters calculated using liquid combinations containing water as one of the solvents showed highest consistency.

Table V.2.6. Surface tension parameters of polyterpenol films deposited at different RF powers for other solvent combinations (calculated using VCG method).

Sample	Liquid combination	γ^{LW}	γ^+	γ^-	γ_S
10 W	DIM:EG:G	40.50	0.69	28.36	31.68
	DIM:EG:F	40.50	15.36	425.00	-121.08
	DIM:EG:DMSO	40.50	0.55	5.96	36.88
	DIM:G:F	40.50	38.96	472.28	-230.81
	DIM:G:DMSO	40.50	0.10	0.87	41.10
	DIM:F:DMSO	40.50	0.04	26.49	38.37
25 W	DIM:EG:G	40.55	0.24	15.76	36.67
	DIM:EG:F	40.55	6.22	192.90	-28.70
	DIM:EG:DMSO	40.55	0.03	0.48	40.79
	DIM:G:F	40.55	16.80	184.49	-70.79
	DIM:G:DMSO	40.55	0.00	4.49	40.53
	DIM:F:DMSO	40.55	0.14	25.38	36.83
50 W	DIM:EG:G	40.70	1.72	64.71	19.58
	DIM:EG:F	40.70	1.99	72.83	16.61
	DIM:EG:DMSO	40.70	0.55	4.55	37.52
	DIM:G:F	40.70	1.18	51.53	25.10
	DIM:G:DMSO	40.70	0.04	5.23	41.58
	DIM:F:DMSO	40.70	0.09	1.90	41.54
100 W	DIM:EG:G	40.65	1.81	66.01	18.77
	DIM:EG:F	40.65	0.32	18.06	35.86
	DIM:EG:DMSO	40.65	0.00	2.81	40.50
	DIM:G:F	40.65	9.85	224.45	-53.39
	DIM:G:DMSO	40.65	0.15	20.04	37.13
	DIM:F:DMSO	40.65	0.02	6.37	39.90

V.2.3.4 Monopolar nature and solubility

For all polymer samples, the electron-donor fraction γ^- of the surface tension was significantly lower than the electron-acceptor γ^+ component, indicating the monopolar nature of the polyterpenol material. Similar to poly(methyl methacrylate) and poly(vinyl alcohol) [392], polyterpenol films manifested mostly electron donor properties with hardly any electron acceptor properties. Molecules of strongly monopolar material tend to repel each other when immersed in polar liquids, such as water, which allows the liquid to penetrate into the monopolar substance resulting in pronounced solubility or dispersibility. The interfacial tension between strongly monopolar surfaces and water has a negative value. As previously shown by van Oss et al [392], for a given solute 1 (monopolar) – solvent 2 (bipolar) combination, it is possible to determine the minimum value for γ_1^- parameter for which the solubility of the solute 1 in solvent 2 will occur:

$$\gamma_{12}^{TOT} = (\sqrt{\gamma_1^{LW}} - \sqrt{\gamma_2^{LW}})^2 + 2(\sqrt{\gamma_2^+\gamma_2^-} - \sqrt{\gamma_1^-\gamma_2^+}) \qquad (4)$$

Assuming $\gamma_1^{LW} \approx 40.6$ mJ/m^2 for polyterpenol material and $\gamma_2^{LW}, \gamma_2^+, \gamma_2^-$ literature values for water (Table V.2.2), the polymer will become water-soluble at $\gamma_1^- > 28.48$ mJ/m^2. For samples deposited at 10 W, calculations using VCG method for two out of four solvent combinations produced $\gamma_1^- > 28.48$ mJ/m^2 indicating the sample might be soluble in water. In the case of samples fabricated at 10 W, there was a significant degree of variance between electron-donor parameters calculated using different solvent combinations (Table V.2.5). Examination of raw water contact angle and drop volume dynamics (data not shown here) for the 10 W sample indicated the films were stable when in contact with this solvent. The γ_1^- decreased significantly for polymers deposited at higher RF power, with all polymers deposited at 25 W or above having $\gamma_1^- < 28.48$ mJ/m^2, and as such the materials were determined to be not water soluble. Extensive intermolecular and intramolecular hydrogen bonds and dominating presence of hydrophobic moieties on the surface of the films could be responsible for the insolubility of polyterpenol in water.

Surface tension parameters obtained using the three methods were then used to calculate the solubility ΔG_{121} of polyterpenol films in the test liquids, as well as common processing solvents such as hexane, chloroform, acetone, and ethanol. Respective surface tensions of the latter four solvent are significantly lower than γ^{LW} of 40.6mJ/m^2 for the polymer, making it impossible to obtain meaningful contact angle data for these liquids; hence, the contact angle of 0° was used. Solubility ΔG_{121} of polyterpenol films in various solvents is presented in Table V.2.7. The polymer material was found to be solvophobic for all solvents ($\Delta G_{121} > 0$) except for DIM for which the calculations produced a mixed result. The solvophobicity of polyterpenol material increased with applied RF fabrication power for all solvents. Acetone is frequently used to remove photoresist, and since polyterpenol films are not soluble in acetone, they are suitable for use as thermally degradable sacrificial materials in IC fabrication where wet etching procedure is employed. In biomedical applications, sterilization with ethanol prior to an experiment or implantation is routine. $\Delta G_{121} > 0$ confirms that ethanol could be used as sterilization agent for polyterpenol thin films.

Table V.2.7. Solubility ΔG_{121} of polyterpenol films in various solvents based on surface tension components from VCG; OWRK; and Neumann approaches.

Solvent	γ_S method of acquisition	10 W		25 W		50 W		100 W	
		A[1]	B[2]	A	B	A	B	A	B
Water	DIM:W:EG	4.9	4.9	-17.1	-17.1	-27.4	-27.4	-41.4	-41.4
	DIM:W:G	5.2	5.2	-16.2	-16.2	-32.9	-32.9	-46.6	-46.6
	DIM:W:F	-12.0	-12.0	-25.9	-25.9	-31.3	-31.3	-42.1	-42.1
	DIM:W:DMS	-11.0	-11.0	-23.8	-23.7	-36.3	-36.3	-43. 7	-43.7
	Owens	-8.9		-21.1		-29.8		-39.0	
	Neumann	-25.6		-32.1		-35.7		-41.1	
Ethylene glycol	DIM:W:EG	-14.2	-14.1	-20.4	-20.3	-23.1	-23.0	-26.5	-26.5
	DIM:W:G	-13.8	-14.1	-19.4	-20.4	-28.5	-21.5	-31.7	-23.4
	DIM:W:F	-31.1	-14.6	-29.1	-18.9	-26.9	-22.1	-27.1	-26.2
	DIM:W:DMS	-30.0	-14.7	-26.9	-19.4	-31.9	-19.9	-28.7	-25.4
	Owens	-28.0		-24.3		-25.5		-24.1	
	Neumann	-44.6		-35.4		-31.3		-26.2	
Glycerol	DIM:W:EG	-24.6	-24.2	-32. 9	-31.9	-28.2	-35.4	-31.7	-40.1
	DIM:W:G	-24.2	-24.2	-31.9	-32.0	-33.7	-33.8	-36.9	-36.9
	DIM:W:F	-41.5	-24.2	-41.6	-30.2	-32.1	-34.4	-32.3	-39.8
	DIM:W:DMS	-40.4	-24.4	-39.4	-30.8	-37.1	-32.0	-34.0	-38.9
	Owens	-38.4		-36.8		-30.6		-29.3	
	Neumann	-55.0		-47.9		-36.6		-31.4	

Solvent	γ_S method of	10 W	25 W	50 W	100 W

	acquisition								
Formamide	DIM:W:EG	6.9	-7.6	-6.0	-14.8	-13.7	-18.0	-21.2	-22.0
	DIM:W:G	7.2	-7.5	-5.0	-14.7	-19.1	-17.3	-26.4	-20.0
	DIM:W:F	-10.0	-10.1	-14.7	-14.6	-17.5	-17.6	-21.9	-21.8
	DIM:W:DMS	-9.0	-10.1	-12.5	-14.9	-22.5	-16.3	-23.5	-21.3
	Owens	-6.9		-9.9		-16.1		-18.8	
	Neumann	-23.6		-21.0		-21.9		-20.9	
DMSO	DIM:W:EG	12.6	-1.3	0.6	-6.2	2.8	-8.0	-7.2	-10.2
	DIM:W:G	12.9	-1.2	1.6	-6.1	-2.6	-7.2	-12.4	-7.9
	DIM:W:F	-4.3	-3.3	-8.1	-5.7	-1.1	-7.5	-7.9	-10.0
	DIM:W:DMS	-3.3	-3.3	-6.0	-6.0	-6.1	-6.0	-9.5	-9.4
	Owens	-1.3		-3.4		0.4		-4.8	
	Neumann	-17.9		-14.4		-5.4		-6.9	
DIM	DIM:W:EG	17.8	17.8	9.9	9.9	7.2	7.2	4.3	4.3
	DIM:W:G	18.2	18.2	10.8	10.8	1.8	1.8	-0.9	-0.9
	DIM:W:F	1.0	1.0	1.1	1.1	3.4	3.4	3.6	3.6
	DIM:W:DMS	2.0	2.0	3.3	3.3	-1.6	-1.6	2.0	2.0
	Owens	4.0		5.9		4.8		6.7	
	Neumann	-12.6		-5.1		-1.0		4.6	
Hexane	DIM:W:EG	-25.2		-33.3		-36.3		-39.1	
	DIM:W:G	-24.9		-32.3		-41.7		-44.3	
	DIM:W:F	-42.1		-42.0		-40.1		-39.7	
	DIM:W:DMS	-41.1		-39.8		-45.1		-41.4	
	Owens	-39.0		-37.3		-38.7		-36.7	
	Neumann	-55.7		-48.3		-44.5		-38.8	
Chloroform	DIM:W:EG	-7.4		-15.5		-18.4		-21.2	
	DIM:W:G	-7.0		-14.5		-23.8		-26.5	
	DIM:W:F	-24.3		-24.2		-22.3		-21.9	
	DIM:W:DMS	-23.2		-22.0		-27.3		-23.5	
	Owens	-21.2		-19.4		-20.8		-18.9	
	Neumann	-37.8		-30.4		-26.6		-20.9	

Solvent	γ_S method of acquisition	10 W	25 W	50 W	100 W
Ethanol	DIM:W:EG	-17.2	-25.3	-28.3	-31.1
	DIM:W:G	-16.9	-24.4	-33.7	-36.3

	DIM:W:F	-34.1	-34.0	-32.2	-31.8
	DIM:W:DMS	-33.1	-31.9	-37.1	-33.4
	Owens	-31.0	-29.3	-30.7	-28.7
	Neumann	-47.7	-40.3	-36.5	-30.8
Acetone	DIM:W:EG	-14.0	-22.1	-25.0	-27.9
	DIM:W:G	-13.6	-21.1	-30.4	-33.1
	DIM:W:F	-30.9	-30.8	-28. 9	-28.5
	DIM:W:DMS	-29.8	-28.6	-33.9	-30.1
	Owens	-27.8	-26.0	-27.4	-25.5
	Neumann	-44.4	-37.0	-33.2	-27.5

[1, 2] Derived using interfacial tension values for a completely immiscible system (A) and a completely miscible system (B).

V.2.4 Conclusion

Surface tension and solubility parameters of polyterpenol thin films as a function of the deposition RF power were examined. Contact angle values obtained for six different solvents were employed in the calculations. For solvents such as water, glycerol, DIM and formamide, reactions between the solid-liquid interface and evaporation were taking place; in the case of ethylene glycol and DMSO, the reorientation of functionalities at the solid-liquid interface occurred. Improved stability was observed for films fabricated at higher RF powers due to the increased degree of cross linking and the decrease in the oxygen content associated with the higher deposition power; the decrease in oxygen containing functional groups was responsible for the increased hydrophobicity of the polymer surface, from 62.7° for the 10 W samples to 76.3° for the films deposited at 100 W. Polyterpenol films manifested mostly electron donor properties with hardly any electron acceptor properties. In the case of 10 W samples, it was not clear from the calculations whether such polymers are water soluble or not as there was a significant degree of variance between electron-donor parameters calculated using different solvent combinations. Polymers deposited at higher RF power were determined to be not water soluble due to the extensive intermolecular and intramolecular hydrogen bonds present. Polyterpenol films fabricated at higher RF powers were less soluble for all test liquids as well as other solvents commonly used in electronics and biomedical processing, namely hexane, chloroform, acetone and ethanol, except for DIM. Solubility and wettability results obtained for polyterpenol confirmed that thin films deposited from terpinen-4-ol using RF plasma deposition can be used for applications where the polymer must resist solubilisation, i.e. if it is used as a protective coating; a thermally degradable sacrificial material in IC fabrication where wet etching procedure is used; or an antifouling coating for implantable medical devices.

Furthermore, the solubility and wetting behaviour of polyterpenol can be influenced by controlling such deposition condition as RF power.

CHAPTER VI

ELECTRICAL AND DIELECTRIC PROPERTIES

This chapter presents an overview of the electromagnetic characterisation of the polyterpenol based polymer films fabricated at different input power conditions. Comprehensive characterisation of insulating property at different frequencies is paramount if this materials to be used as an insulating gate modification in organic electronic devices.

In Section VI.1, the values of dielectric constant are attained at optical and microwave frequencies using spectroscopic ellipsometry and split−post dielectric resonators, respectively. The results are published as *Bazaka, K., Jacob, M. V., Complex permittivity measurements of RF plasma polymerized polyterpenol organic thin films employing split post dielectric resonator. Journal of Polymer Engineering 2011, 31, 73-75*.

In Section VI.2, the insulating nature of polyterpenol thin films is confirmed at lower frequencies, based on impedance data obtained using Al−polyterpenol−Al structures. DC conduction mechanism in films fabricated under varied RF power is investigated using current−voltage characteristics of the aforementioned metal−insulator−metal device. The conductivity of polyterpenol thin films is also determined from current−voltage characteristics. A manuscript outlining the finding of this study are communicated as *Bazaka, K., Jacob, M. V., Investigation of electrical conduction in plasma polymerised polyterpenol thin films*.

Section VI.3 investigates *in situ* iodine doping as a potential method to enhance conductivity and lower the band gap of polyterpenol thin films. The effect of doping onto bulk and surface properties of polyterpenol is also reviewed, as unfavourable changes in stability or surface chemistry may negate the improvement in electrical conductivity. The results of this study are published in part as *Bazaka, K., Jacob, M. V., Effect of iodine doping on surface and optical properties of polyterpenol thin films. Material Science Forum 2010, 654-656, 1764-1767*, with an expanded work communicated as *Bazaka, K., Jacob, M. V., Effects of iodine doping on optoelectronic and chemical properties of polyterpenol thin films*.

VI.1 COMPLEX PERMITTIVITY OF POLYTERPENOL AT MICROWAVE AND OPTICAL FREQUENCIES

Abstract

In the fields of organic electronics and biotechnology, applications for organic polymer thin films fabricated using low-temperature non-equilibrium plasma techniques are gaining significant attention because of the films' physical and chemical stability, smooth, defect free and uniform surfaces, high adhesion to the substrate and low cost of production. To determine potential applications of such organic polymer thin films in devices, a complex permittivity measurement of is necessary to ascertain their dielectric properties. Polymer thin films were fabricated from non-synthetic terpinen-4-ol by means of radio frequency polymerisation (13.56 MHz) on low loss dielectric substrates. Real and imaginary parts of permittivity as a function of frequency were measured using the variable angle spectroscopic ellipsometer. The real part of permittivity (*k*) was found to be between 2.34 and 2.65 in the wavelength region 400 nm to 1100 nm indicating a potential low-*k* material. These permittivity values were confirmed at microwave frequencies. Dielectric properties of polyterpenol films were measured by means of split post dielectric resonators (SPDR) operating at frequencies of 10 GHz and 20 GHz. Employing full wave electromagnetic theory, permittivity and dielectric loss tangent can be derived from the observed shift in measured resonant frequency and Q-factor of SPDR with bare substrate and of SPDR with coated substrate. Permittivity increased for samples deposited at higher RF energy − from 2.65 (25 W) to 2.83 (75 W) measured by 20 GHz SPDR and from 2.32 (25 W) to 2.53 (100 W) obtained using 10 GHz SPDR. The error in permittivity measurement was predominantly attributed to the uncertainty in film thickness measurement.

As published in: Bazaka, K., Jacob, M. V., Complex permittivity measurements of RF plasma polymerized polyterpenol organic thin films employing split post dielectric resonator. *Journal of Polymer Engineering* 2011, 31, 73-75.

VI.1.1 Introduction

In the fields of organic electronics and biotechnology, applications for organic polymer thin films fabricated using low-temperature non-equilibrium plasma techniques are gaining significant attention because of the thin films' physical and chemical stability, smooth, defect free and uniform surfaces, high adhesion to the substrate and low cost of production [319]. Furthermore, from one precursor, polymers of significantly different chemical and physical structures or films with property gradient can be obtained by controlling deposition conditions of plasma polymerisation, such as the energy delivered into the reaction chamber, monomer flow or position of the substrate within the reactor [89]. To determine potential applications of such organic polymer thin films in devices, particularly high frequency and electrical devices, a complex permittivity measurement is necessary to ascertain their dielectric properties.

Split post dielectric resonators (SPDR) are widely used for measurements of permittivity of laminar dielectric materials and substrates [401]. However, accurate measurements on thin dielectric films deposited on a dielectric substrate can be difficult due to a number of issues, including the non-uniform thickness of the substrate, and relatively low film thickness and low permittivity of the material [402]. In this paper we discuss applications of SPDRs for complex permittivity measurements and estimate the permittivity of thin organic film, namely polyterpenol, fabricated on low loss dielectric substrates using RF plasma polymerisation technique. Polyterpenol films are optically transparent amorphous polymers with promising optical and electrical properties [336].

VI.1.2 Exeprimental

Polymer thin films were fabricated from non-synthetic terpinen-4-ol by means of radio frequency polymerisation (13.56 MHz) on low loss dielectric substrates. The substrates made from the GE-type 124 quartz with a dielectric constant of 3.75 (at 20 °C, 1 MHz) were masked so that only half of the substrate was deposited to allow for the reference to be measured after the deposition is performed and hence reduce the possibility of deviation between the reference and coated substrate. Deposition was performed at room temperature and pressure of 150 mTorr under varied deposition power and time conditions. Thickness and real and imaginary parts of permittivity as a function of frequency were determined from the Ψ, and Δ ellipsometric data collected for $\varphi = 55^\circ, 60^\circ$, and 65° angles of incidence over the 200 – 1000 nm wavelength range using variable angle spectroscopic ellipsometer (model M-2000, J. A. Woollam Co., Inc.). Uncertainties of thickness were taken as the ratio of the standard deviation of thickness divided by the mean thickness value.

Films' permittivity values were estimated at microwave frequencies with SPDRs operating at frequencies of 10 GHz and 20 GHz. The resonant frequencies and unloaded Q-factors of SPDRs containing the samples were measured by 8364B network analyser at the room temperature (23 °C). To mitigate the experimental error associated with changes in humidity and account for possible resonant frequency drift with temperature or time, the resonant frequency and Q-factor of the empty resonator is taken at the beginning and end of a set of measurements whilst reference and coated substrate measurements are taken consecutively. Employing full wave electromagnetic theory, permittivity and dielectric loss tangent can be derived from the observed shift in measured resonant frequency and Q-factor of SPDR with bare substrate and of SPDR with coated substrate.

VI.1.3 Results and discussion

From ellipsometric studies, the real part of permittivity (*k*) was found to be between 2.34 and 2.65 in the wavelength region 200 nm to 1000 nm, indicating potential of polyterpenol as a low-k material, with lower permittivity values corresponding to films deposited at lower RF power (Figure VI.1.1).

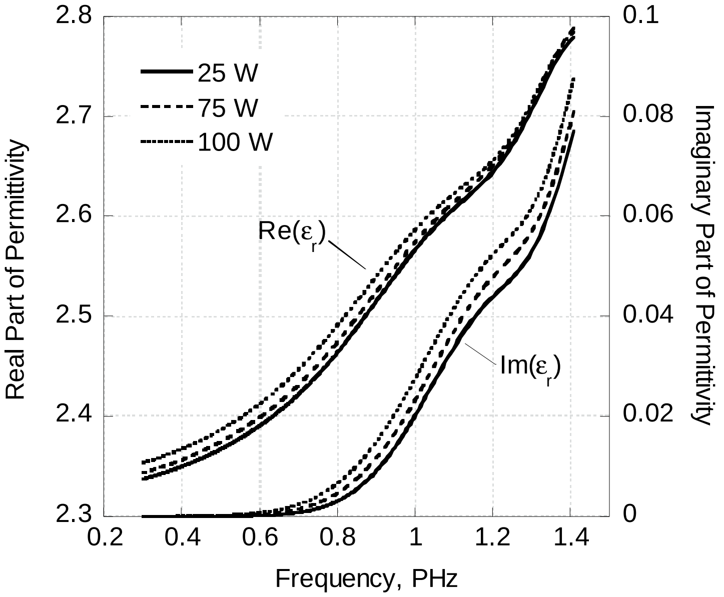

Figure VI.1.1. Real and imaginary part of permittivity as a function of frequency measured using the ellipsometric technique for polyterpenol films fabricated at different RF deposition powers.

In microwave studies, the real part of the complex permittivity is derived from measured resonant frequencies of the resonator using the equation (1) where h_f is sample thickness, f_S and

f_f resonant frequencies of the SPDR with bare and coated substrates respectively, K_s is a parameter evaluated for a number of ε_f and h_f using the Rayleigh–Ritz technique.

$$\varepsilon_f = 1 + \frac{f_s - f_f}{h_f f_s K_s(\varepsilon_f, h_f)} \qquad (1)$$

Results of measurements of the resonant frequencies, Q-factors and thicknesses of films and substrates are demonstrated in Table VI.1.1. Irrespective of deposition power, all measured samples possessed relatively large dielectric losses. However, as for most known dielectrics loss tangent increases almost linearly with frequency, at frequency of 2 GHz losses can be one order of magnitude smaller. Permittivity increased for samples deposited at higher RF energy - from 2.65 (25 W) to 2.83 (75 W) measured by 20 GHz SPDR and from 2.32 (25 W) to 2.53 (100 W) obtained using 10 GHz SPDR. Compared to 10 GHz SPDR, greater accuracy is expected from the measurement using the 20 GHz resonator; however, the influence of such external factors as humidity and thermal drift of the network analyzer is also greater and so a larger frequency shift (and hence film thickness) is needed.

Table V.1.1. Split-post dielectric resonator 10 GHz and 20 GHz measurements at 23 °C for Polyterpenol samples deposited on quartz.

Material	Thickness (µm)	Frequency 10 GHz		Frequency 20 GHz	
		Permittivity (ε_f)	Loss tangent (tan δ_f)	Permittivity (ε_f)	Loss tangent (tan δ_f)
Quartz	190	3.69	8.28 × 10−5	3.82	2.10 × 10−4
Polymer on quartz					
25 W	4.91	2.32	2.48 × 10−2	2.65	2.54 × 10−2
75 W	5.02			2.83	9.19 × 10−3
100 W	4.78	2.53	5.02 × 10−3		

The numerical electromagnetic analysis of a SPDR structure for thin films deposited on such low permittivity substrates as quartz indicates that variation of coefficients *K* is smaller than 1% and relative uncertainties of resonant frequency measurements are smaller than 0.001%. With thickness measurements, results from ellipsometric studies were compared to those from other spectroscopic techniques with the uncertainty found to be in the region of 10%. Detailed study (reported elsewhere [402]) was conducted to ascertain the most significant source of error in permittivity measurements on organic thin films, which was found to be predominantly attributed to the uncertainty in film thickness measurement (Figure VI.1.2). Therefore, higher accuracy can be attained by precisely measuring the thickness and measuring the permittivity at higher frequencies.

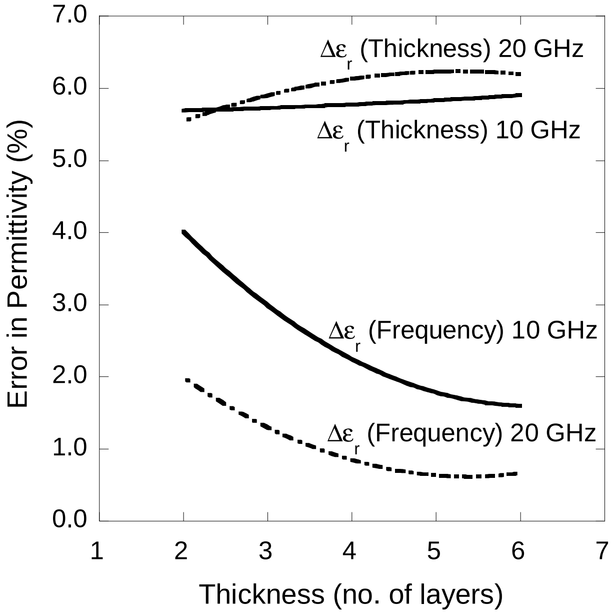

Figure VI.1.2. Estimated error in permittivity due to the uncertainty in thickness and resonant frequency measurement (one layer is approximately 1 μm in thickness) [402].

VI.1.4 Conclusions

It has been show that SPDRs operating at 10 and 20 GHz are appropriate and precise tools for measurement of permittivity and dielectric loss tangent of thin organic films deposited on low loss dielectric substrates. The technique was used to evaluate the permittivity of polyterpenol thin films. The estimated permittivity values (~2.6) and relatively lower transmission losses substantiated that polyterpenol is a potential low-k material.

VI.2 INSULATING PROPERTIES AND ELECTRICAL CONDUCTION MECHANISM OF POLYTERPENOL

Abstract

Polyterpenol thin films were fabricated using RF plasma polymerisation and their electrical properties studied using Al−polyterpenol−Al structures. At a frequency of 1 kHz, the dielectric constant varied with input RF power, from 3.86 (10 W) to 4.42 (100 W) at 1 kHz. The current density–voltage characteristics of polyterpenol films of different thickness were investigated at room temperature. At higher applied voltage region, DC conduction was dominated by Schottky conduction mechanism. The resistivity of the polyterpenol were found to decrease for films deposited at higher RF power, attributed to the change in the chemical composition and structure of the polymer.

As submitted to: Bazaka, K., Jacob, M. V., Investigation of electrical conduction in plasma polymerised polyterpenol thin films.

VI.2.1 Introduction

Organic gate insulating materials are attracting increasing attention , with significant efforts devoted to not only finding a suitable substitute to the SiO_2 insulating layer but also to designing materials capable of supporting the development of flexible, large scale electronics. For years, advancements in the performance of ultra large scale integrated circuits have been hindered by propagation delay, cross-talk noise, and power dissipation due to resistance–capacitance coupling associated with the increased wiring capacitance, particularly interline capacitance between the metal lines on the same level [403]. Whereas the resistance is affected by the nature of the conducting material, capacitance is chiefly controlled by the choice of the dielectric material [324]. Hence, thin film insulating materials with a relatively low dielectric constant ($k < 3$) are under concentrated investigation for their potential as interlayer dielectrics. Organic gate insulators with high dielectric constant have also made significant progress for their role in the advancement of high-performance organic thin film transistors, where introduction of high−k gate dielectric greatly reduces device operational voltage [404]. Plasma−assisted fabrication is one of the deposition techniques suitable for fabrication of both low− and high−k dielectric polymer thin films through an appropriate choice of monomer and fabrication process conditions. Being a low−temperature process, non−equilibrium plasma polymerisation is particularly suited for fabrication of thin film structures and use of temperature−sensitive substrates. Plasma polymerised films are smooth and pin−hole free, and their chemical, physical and optoelectronic properties can be tailored to suit a desired application by controlling the retention of original monomer functionality, degree of cross−linking , and branching [405].

This low−cost ‘green’ process has been used to fabricate environmentally friendly insulating thin films from a number of naturally occurring non−synthetic monomers, such as terpinen-4-ol and linalyl acetate [337,406]. The former, polyterpenol, has been demonstrated to enhance the performance of pentacene−based organic field effect transistor when incorporated as a gate insulating layer [337]. Using electric field induced second harmonic generation, the carrier−blocking property of polyterpenol was demonstrated [353]. Since the performance of an organic device relies on the charge carrier injection and transport in the active material, adequate understanding of the nature of the carrier transport within the polymer thin films is significant for microelectronic and optoelectronic applications alike. As such, this paper investigates the charge carrier transport properties of polyterpenol thin films in order to determine the dominant charge transport mechanism of these plasma polymers.

VI.2.2 Experimental

For *J–V* measurements, structures consisted of a single polyterpenol thin layer sandwiched between two metal electrodes. Metal−insulator−metal (MIM) structures were deposited onto glass substrates, previously ultrasonically cleaned in Extran solution, rinsed in distilled water, acetone, and isopropanol, and blown dry. Devices were prepared by first depositing aluminium electrodes (99.99% pure) via thermal evaporation at a pressure of 10^{-6} Torr using a custom made shadow mask. Then, polyterpenol thin films were fabricated using RF plasma polymerisation set up, where an ENI RF generator delivers 13.56 MHz RF energy into the chamber via capacitively coupled copper electrodes. Terpinen-4-ol (Australian Botanical Products Pty. Ltd., Australia, used without further purification) vapours were introduced into the chamber via monomer inlet and deposition took place at 10, 15, 25, 50, and 100 W RF power. Time of deposition was varied to obtain films of desired thickness. Top electrodes were then evaporated using the aforementioned thermal evaporation technique. Once fabricated, samples were kept under controlled conditions.

Variable Angle Spectroscopic Ellipsometry (VASE) was used to determine polyterpenol film thickness. Hioki 3522-50 LCR HiTESTER meter (Hioki) was used to measure device capacitance at frequencies between 1 Hz to 100 kHz. The measured values, together with the geometry of the device, were then used to estimate the dielectric constant, ε_r, of the polyterpenol thin films. DC *I–V* measurements were performed on the MIM structures with an effective area of 2.5×10^{-5} m^2 using a Keithley 2636A source meter (Keithley Instruments, Inc., Cleveland, Ohio). Measurements were taken 0−6 V, 0−30V, and 0−150 V, collecting 1000 data points within each range.

VI.2.3 Results and discussion

Representative capacitance curves of polyterpenol fabricated at different RF input power are depicted in Figure VI.2.1, with corresponding average relative permittivity values summarized in Table VI.2.1. These permittivity values are similar to those reported for plasma polymerised multistacked bipolar allylamine and vinyl acetic thin films [404]. Relative permittivity increased slightly for polymers fabricated at higher input power, in agreement with previously reported findings [350]. However, the difference was not statistically significant. Independent of the power of deposition, the dielectric constant decreased with increasing frequency, a behaviour characteristic of polymer insulating materials. Previous studies determined the dielectric constant values of polyterpenol to be around 2.6 at microwave and optical frequencies. Jacob et al [337] reported relative dielectric constants of 3.4 and 5.2 for polyterpenol thin films deposited at 25 W, as determined from DC I−V and impedance spectroscopy measurements, respectively. The discrepancy in dielectric constants is attributed to the frequency dependence of the material parameter, including parasitic capacitance.

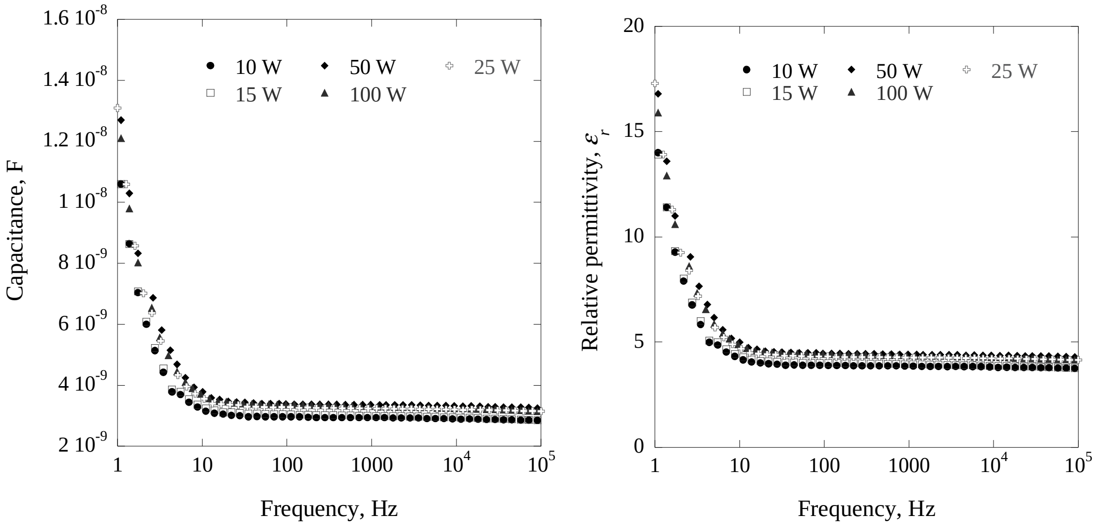

Figure VI.2.1. a. Frequency dependence of capacitance of the polyterpenol containing MIM device at room temperature (polyterpenol film thickness ~ 350 nm, area 30 mm^2). b. Relative permittivity as a function of frequency.

Table VI.2.1. Relative permittivity of polyterpenol fabricated at varied input power conditions.

Sample	Relative permittivity ε_r					
	1 Hz	10 Hz	100 Hz	1 kHz	10 kHz	100 kHz
10 W	15.23	4.21	3.90	3.86	3.83	3.75
15 W	15.21	4.34	4.01	3.95	3.88	3.76
25 W	17.31	4.69	4.32	4.27	4.23	4.15
50W	18.39	4.98	4.42	4.36	4.26	4.15
100W	17.33	4.76	4.47	4.42	4.37	4.30

Conduction mechanisms were investigated for polyterpenol thin films of different thickness (100 – 500 nm) by measuring standard $I-V$ characteristics of these films in the voltage range 0.1−6V. No breakdown in the device occurred up to 50V, with some samples withstanding higher applied electric fields (up to 4.2 10^8 V/m). For all tested devices, the measured $I–V$ dependence of polyterpenol demonstrated low current over a wide range of applied voltage. The observed $J-V$ characteristics of the polyterpenol devices at room temperature are depicted in Figure VI.2.2. Independent of polyterpenol deposition conditions, the $J-V$ curves approximate the same shape. Each curve implies two different conduction processes, according to the power law $J \propto V^n$, n being the power law index, with different slopes n evident in the lower and higher voltage regions [407]. In the low voltage region, the current density J exhibits an approximately ohmic dependence with the applied voltage V, with slopes of $0.80<n<0.94$. As the applied potential exceeds 2.5 V, the slope of the graph n is found to lie in 2.27−2.38, indicating a non-ohmic conducting mechanism.

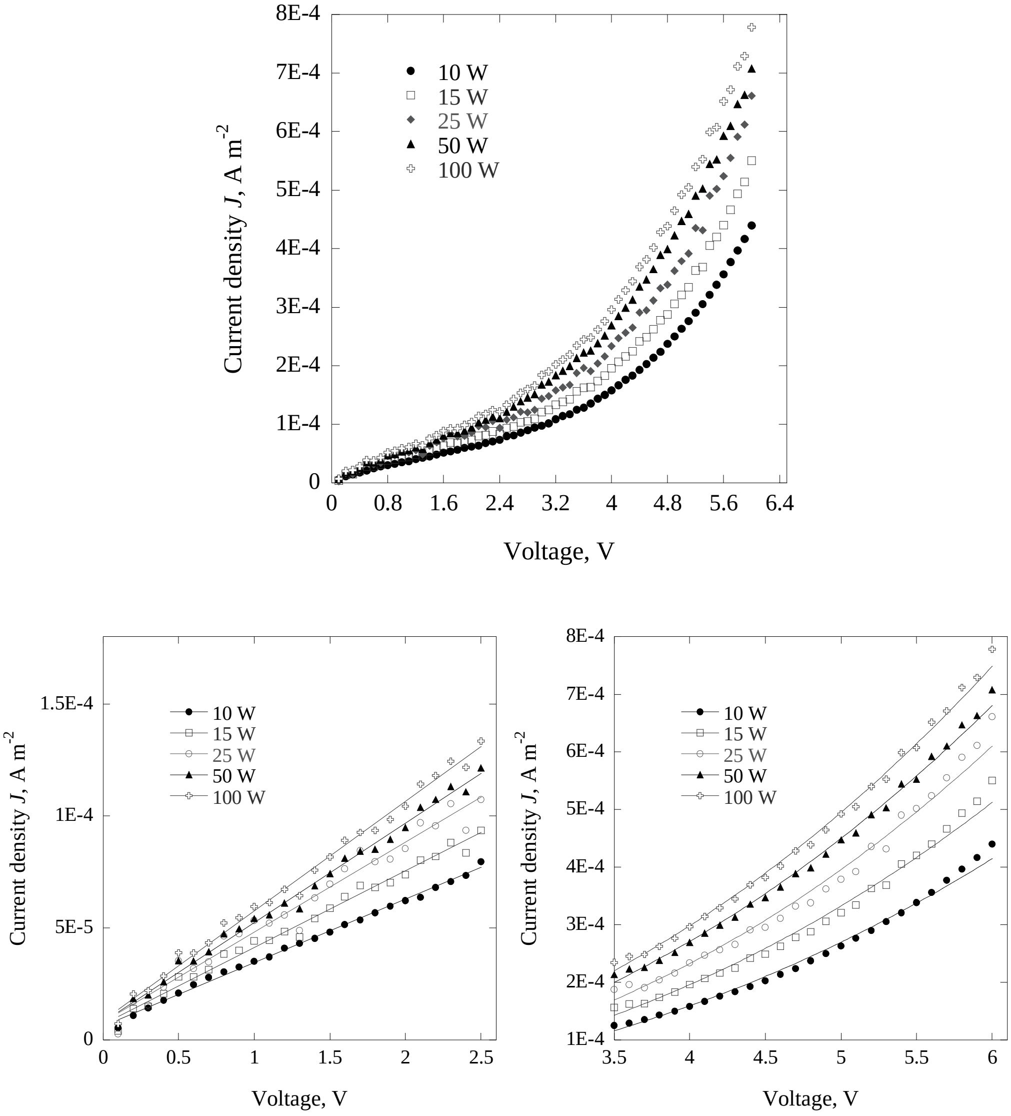

Figure VI.2.2. Current density (J) −Voltage (V) relationship for polyterpenol films with approximate thickness of 120 nm (a). Power law fit in the lower (b) and higher (c) applied voltage regions.

While discussing the transport phenomena in plasma polymer thin films in the high (non-ohmic) field region, space charge limited conduction, Schottky conduction, and Poole–Frenkel conduction have been reported as most likely for polymerized thin films [408,409]. The space charge limited conduction illustrates a process where the current conducted through the material is limited by a distribution of trapping sites within the bulk of the polymer. Schottky conduction, on the other hand, is a barrier limited conduction mechanism, where the potential barrier is lowered as a result of interaction of an electric field at a metal–insulator interface and the image force. A bulk limited conduction process, the Poole–Frenkel mechanism accounts for the case where the application of a sufficiently high electric field induces a lowering of the trap barrier of the polymer material.

In order to determine which of the aforementioned mechanisms most adequately accounts for the charge transport of polyterpenol, two distinct plots of (J –V) in the forward direction are analysed. For space charge limited conduction, double log plot of the form ln J−ln V should provide a linear characteristic, whereas Schottky and Poole–Frenkel mechanisms will be indicated by a linear dependence with a positive slope of ln J – $V^{0.5}$ plot. Furthermore, the dependence of current density J on film thickness d for the samples of different thickness at a constant voltage can aid in differentiation between the types of the electronic conduction. The dependence of J on d is described by the relation $J \propto d^{-l}$, with l being a parameter dependent on the trap distribution within the material. A slope $l < 3$ is indicative of Schottky or Poole–Frenkel conduction, whereas $l \geq 3$ signifies the possibility of space charge limited conduction.

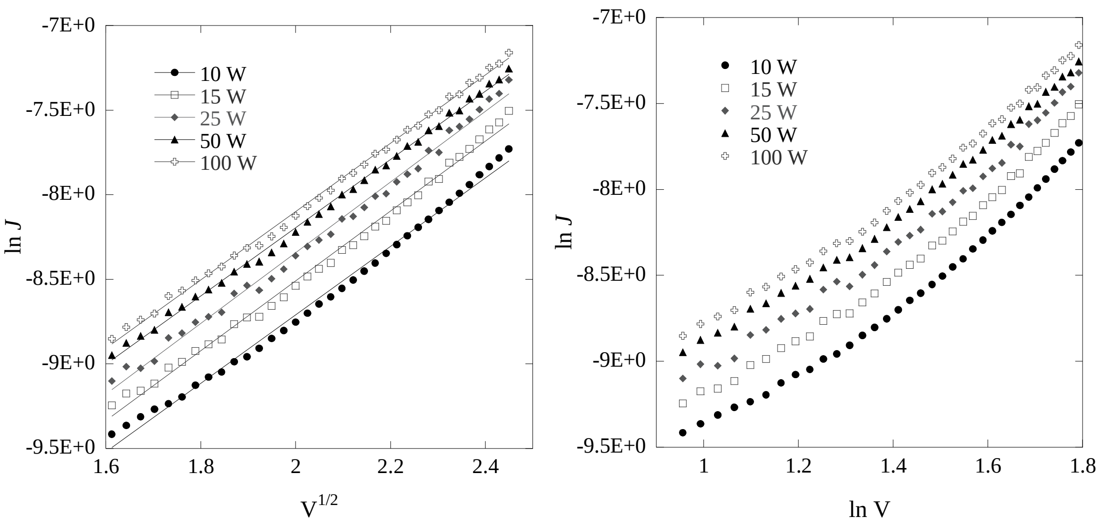

Figure VI.2.3. Variation of ln J with square root of applied voltage V (a) and ln V (b) for polyterpenol thin films (thickness d = 350 nm). In (a), linear fitting produces slope of approximately 2.05 and R > 0.997.

In the present case, the ln $J - V^{0.5}$ plot graph is evidently more linear compared to ln J−ln V, as presented in Figure VI.2.3, suggesting the possibility that Schottky or Poole–Frenkel conduction may dominate in this region. Furthermore, no clear dependence of the current density J on the film thickness was found, further ruling out the possibility of the space charge limited conduction being the dominant charge transport process. Therefore, the type of conduction mechanism in polyterpenol most probably is Schottky or Poole–Frenkel conduction.

The general expression for both Schottky and Poole–Frenkel type conductions can be expressed as [410]:

$$J = J_0 \exp\left(\frac{\beta F^{1/2} - \phi}{kT}\right) \tag{1}$$

where J_0 is the low field current density, F the applied electric field, k the Boltzmann constant, T the absolute temperature, β the coefficient of the static electric field, and ϕ the ionization energy of localized centres and Coulomb barrier height of the electrode polymer interface in the case of Poole–Frenkel and Schottky mechanisms, respectively. The field lowering coefficient β are known as β_S and β_{PF} in the case of Schottky and Poole–Frenkel conductions, respectively, and can be defined as [411]:

$$\beta_{\mathrm{PF}} = 2\beta_{\mathrm{S}} = 2\left(\frac{e^3}{4\pi\varepsilon_0\varepsilon_r}\right)^{1/2} \tag{2}$$

where e is the electronic charge, ε_0 the permittivity of free space, ε_r the dielectric constant of the bulk polymer material at high frequencies. Calculated theoretically, β_S and β_{PF} can facilitate differentiation between the Schottky and Poole–Frenkel mechanisms by comparing these values to experimentally determined β coefficient. The following relation was used to determine β_{exp}:

$$\beta_{\mathrm{exp}} = skTd^{1/2} \tag{3}$$

where s is the slope of the linear section of ln $J - V^{1/2}$ characteristic:

$$s = \frac{\Delta \ln J}{\Delta \ln V^{1/2}} \tag{4}$$

The experimental values for β and the theoretical values of the coefficients calculated from Equation 2 using average dielectric constant calculated from capacitance measurement, and are presented in Table VI.2.2. For different RF power levels, the value of β_{exp} does not change significantly, thus confirming previous findings of small variability in ε_r with deposition power. It is also evident that the experimental values closely match the theoretically calculated

Schottky coefficient β_S. Hence, in the higher field region Schottky mechanism is likely to dominate charge transport. This finding agrees well to that reported by Jacob [337], where Schottky conduction was also identified as the prevailing conduction mechanism. Similar conduction behaviour has been reported for plasma polymerised vinylene carbonate and 2,6,termdiethylaniline thin films [410,412].

Table VI.2.2. Comparison between the theoretical and experimental β coefficients (film thickness $d \approx 120$ nm)

	Slope s	β_{exp}	β_S,	β_{PF}
10 W	2.02	1.72×10^{-5}	2.25×10^{-5}	4.51×10^{-5}
15 W	2.08	1.75×10^{-5}	2.27×10^{-5}	4.54×10^{-5}
25 W	2.12	1.75×10^{-5}	2.27×10^{-5}	4.54×10^{-5}
50 W	2.02	1.82×10^{-5}	2.27×10^{-5}	4.53×10^{-5}
100 W	2.03	1.76×10^{-5}	2.26×10^{-5}	4.53×10^{-5}

The resistivity of the samples was also determined using the expression:

$$\rho = \frac{\left(\frac{V}{I}\right)A}{d} \tag{5}$$

where ρ is the resistivity of the material, A the device surface area, d the thin film thickness, V measured voltage, and I measured current. The resistivity for all samples are in the order of 10^8−10^9 Ωm (calculated at 6 V), confirming the insulating nature of polyterpenol material. The resistivity of the sample decreases slightly with RF power, associated with changes in chemical structure, such as loss of polar functional groups, and the degree of cross−linking [350]. The conductivity σ values for each sample type calculated at 6 V are presented in Table VI.2.3, and are comparable to those of other plasma polymers. The conductivity can be potentially increased by introducing doping agents, such as iodine [413].

Table VI.2.3. Summary of electrical properties of polyterpenol.

	ε_r	β_{exp}	σ, S/cm
10 W	3.84	1.716×10^{-5}	8.21×10^{-10}
15 W	3.90	1.746×10^{-5}	10.0×10^{-10}
25 W	4.24	1.750×10^{-5}	1.12×10^{-9}
50 W	4.20	1.819×10^{-5}	1.47×10^{-9}
100 W	4.39	1.760×10^{-5}	1.52×10^{-9}

VI.2.4 Conclusion

The electrical properties of polyterpenol thin films were investigated using AC and DC current−voltage characterization. The dielectric constant, ε_r, was found to vary slightly with RF power, increasing from 3.75 (10 W) to 4.30 (100 W) at 100 kHz. The conduction mechanism was identified as ohmic in the lower applied voltage region, whereas Schottky conduction mechanism dominated at the higher voltage region. Variations in RF deposition power did not influence the conduction process, while the conductivity of the material increased slightly for polyterpenol thin films deposited at higher input power. Low permittivity combined with high resistivity of polyterpenol substantiates the material’s potential as an insulating and blocking layer for fabrication of organic electronic devices.

VI.3 ENHANCEMENT OF CONDUCTIVITY VIA DOPING: EFFECT ON ELECTRICAL, PHYSICOCHEMICAL AND SURFACE PROPERTIES AND STABILITY

Abstract

Polyterpenol thin films were manufactures using RF plasma polymerisation. Iodine doping was carried out *in* situ, which led to significant change in the chemical structure of the film. Iodine was being incorporated into the backbone of the polymer, with associated notable reduction in the methyl and methylene functional groups and appearance of C=C bond. Higher levels of doping notably increased the refractive index of the thin films, from 1.54 to 1.70 at 500 nm wavelength, and significantly reduced the transparency of films. The band gap of polyterpenol was also reduced by doping, by extending the density of states more into the visible region. Conductivity also increased from 5.05×10^{-8} S/cm to 7.74×10^{-7} S/cm and 1.20×10^{-6} S/cm (at 20 V) for increasing doping levels. Doping was found not to affect surface morphology but increased hydrophilicity of surfaces.

Keywords: doping ; iodine; plasma polymer; semiconducting thin films;

Published in part as: Bazaka, K., Jacob, M. V., Effect of iodine doping on surface and optical properties of polyterpenol thin films. *Material Science Forum* 2010, 654-656, 1764-1767.

VI.3.1Introduction

The employment of plasma polymerization techniques for synthesis of high performance organic thin film materials has been investigated by many authors because these techniques allow the polymerisation of a range of organic compounds that may not necessarily polymerise through conventional thermo chemical pathways [85,86,88,89]. Polymers, fabricated using RF plasma polymerisation, are smooth, pinhole free and uniform, with chemical and physical properties that can be tailored by controlling such deposition parameters as pressure, RF power, monomer flow rate and time of fabrication [322,339,382]. Owing to their high-resistivity and high dielectric breakdown strength, organic polymer materials have found numerous applications, such as thin film insulators and capacitors for integrated microelectronics, passivation layers in IC, and protective coatings [414]. Polymer materials manufactured from renewable natural sources, such as essential oils, offer an additional advantage of being environmentally sustainable compared to polymer materials derived from fossil fuels [325,415,416]. Much research has been devoted to enhance the electrical conductivity of organic polymers, primarily through doping them with appropriate electron donors (such as alkali metals) or acceptors (such as iodine or arsenic pentafluoride) [417]. Iodine doping has been studied principally because of the significant effect an introduction of this doping agent has on the electrical and dielectric properties of polymer thin films, including an increase in electrical conductivity due to oxidation of the polymer and a change in polymer charge storing capacity [418].

In this paper we report on the effect in situ iodine doping has on optoelectronic and chemical properties of the plasma polymerized terpinen-4-ol thin films, herein called polyterpenol. Polyterpenol is fabricated from non-synthetic mono terpene alcohol, a major constituent of *Melaleuca alternifolia* oil, by way of radio frequency polymerisation [336]. With refractive index slightly above that of glass, transparency to the visible region, very smooth surface and high chemical inertness and thermal stability, polyterpenol films have prospective applications in organic optoelectronics as encapsulating layers for the organic circuitry [347,350,419,420]. Polyterpenol has also been demonstrated as an appropriate insulating material to improve the OFET output characteristics and is a prospective candidate for full flexible organic electronic circuits [337,353,421].

VI.3.2 Experimental

Pristine and iodine doped polyterpenol thin films were fabricated from non-synthetic terpinen-4-ol monomer (distilled by Australian Botanical Products) using the experimental setup depicted in Figure VI.3.1. RF energy (13.56 MHz) was delivered into the deposition chamber by means of capacitively coupled copper electrodes. Substrates (superwhite glass slides and KBr pallets) were cleaned according to the procedure detailed elsewhere [336]. The cleaned glass substrates were then placed into the deposition chamber and flushed with argon for 1 minute to produce an oxygen-free surface. 1 ml of Terpinen-4-ol monomer was used for every deposition. The films were fabricated at room temperature, pressure of 100 mTorr and RF power of 25 W. *In situ* doping was performed by releasing the iodine vapours into the deposition chamber using the dopant inlet along with the monomer. Thickness, roughness and optical properties of the doped and pristine samples deposited on glass substrates were examined through variable angle spectroscopic ellipsometry (model M-2000D, J.A. Woollam Co. Inc.) and UV-Vis spectroscopy (Avantes Avaspec-2048 spectrometer, Avalight-DHc light source). FTIR spectra of samples deposited onto KBr pallets were recorded at room temperature using a single beam FTIR spectrometer (Nicolet Maxim). X-ray photoelectron spectroscopy (XPS) survey spectra were collected using an Axis Ultra spectrometer (Kratos Analytical Ltd., UK), equipped with a monochromatic X-ray source (Al Kα, hν = 1486.6 eV) operating at 150 W. The surfaces of the thin film samples were scanned using an atomic force microscope (AFM) (NT-MDT) in semi-contact mode to observe the surface topography and to quantitatively estimate the surface roughness. Surface wettability studies were performed using a contact angle system (KSV 101, CCD camera) employing the sessile drop method. An average of ten measurements per sample was obtained using sterilized nanopure H_2O (18.2 M Ω cm^{-1}), diiodomethane (Sigma Aldrich) and ethylene glycol (Sigma Aldrich). The average contact angle for each liquid was used to calculate the surface free energy and its components, based on the Lewis acid/base method [393]. For *J–V* measurements, MIM structures were prepared by depositing aluminium electrodes via thermal evaporation using a custom made shadow mask placed beneath the samples.

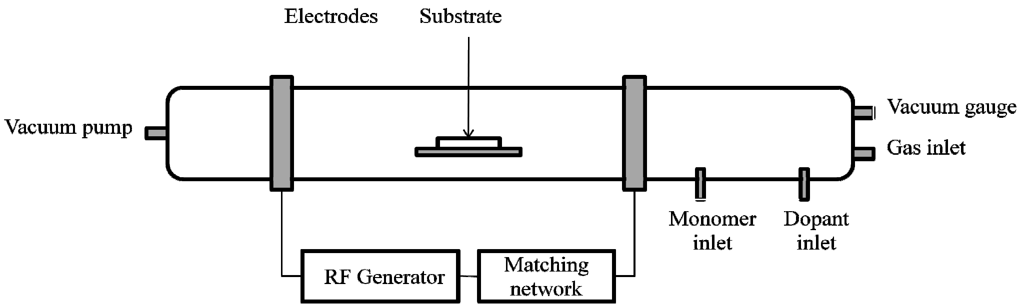

Figure VI.3.1. Plasma polymerisation setup.

VI.3.3 Results and discussion

VI.3.3.1 Chemical composition

FTIR and XPS spectroscopy was used to analyze the changes in chemical structure of polyterpenol films as a consequence of doping. XPS survey spectra collected for pristine and iodine doped polyterpenol samples deposited under the same conditions are depicted in Figure VI.3.2, and the atomic fractions of elements present in the films are summarized in Table VI.3.1. Similar to pristine polyterpenol film, the iodine doped polymers are hydrocarbon in nature, with low iodine concentration. Si and N atoms detected by the XPS are likely the contaminations that have originated from glass and air respectively. In the doped film, there is a significant reduction in the oxygen to carbon ratio compared to pristine polyterpenol. Such change is likely to be associated with the introduction of impurity into the polymer structure via elimination of oxygen, possibly through formation of highly oxidizing iodine compounds.

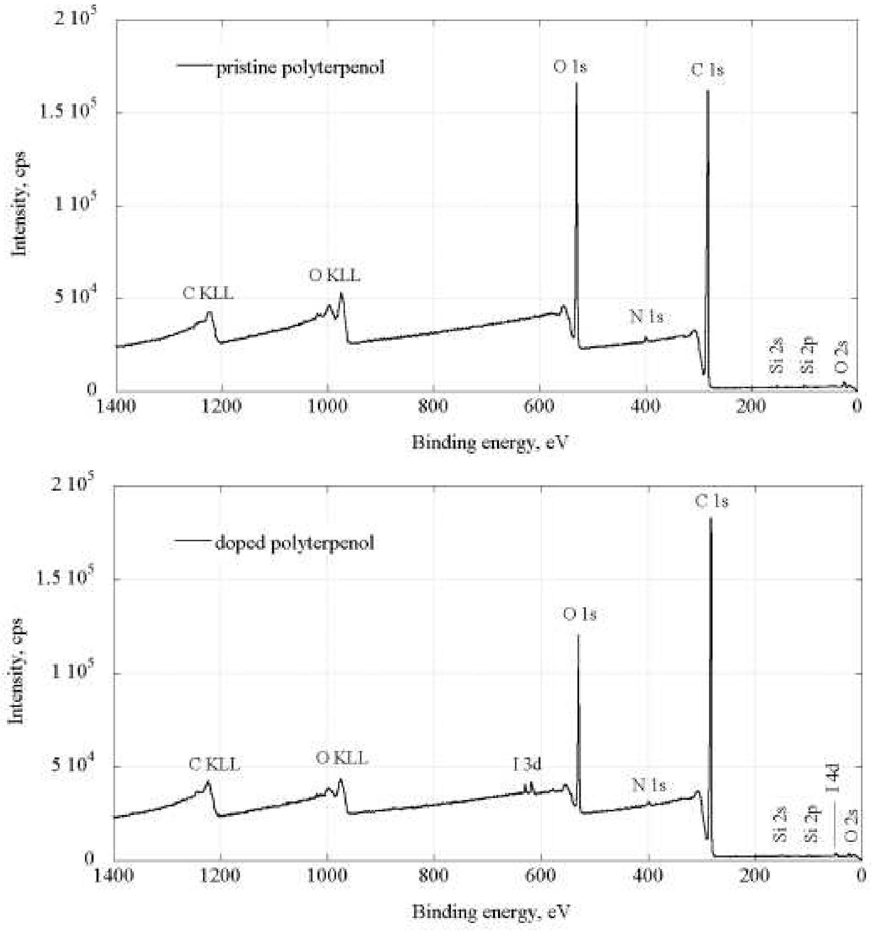

Figure VI.3.2. XPS spectra for (a) pristine and (b) iodine doped polyterpenol samples.

Table VI.3.1. Atomic fractions (%) of elements detected on the surfaces of pristine and iodine doped polyterpenol samples using XPS.

	Atomic fractions, %				
	I	O	N	C	Si
pristine		22.8	0.9	76.0	0.3
doped	0.1	15.2	0.6	83.9	0.2

In the FTIR spectra of the monomer and pristine polymer sample (Figure VI.3.3) the previously reported peaks were observed [347,350]. The FTIR absorption bands and the suggested groups for pure and iodine doped polyterpenol are presented in Table VI.3.2. Introduction of iodine resulted in the significant reductions in the intensity of bands associated with methyl and methylene functional groups. The relationship between intensities of methyl (1380 cm^{-1}) and methylene/methyl (1450 cm^{-1}) bands indicates chain branching and suggests that similar to pristine polyterpenol, iodine doped film is comprised mostly of short polymer chains rather than long linear backbone structures [422]. Presence of several peaks in 600-500 cm^{-1} region of the doped spectrum which correspond to aliphatic C-I stretch implies incorporation of iodine atoms into the backbone of the polymer.

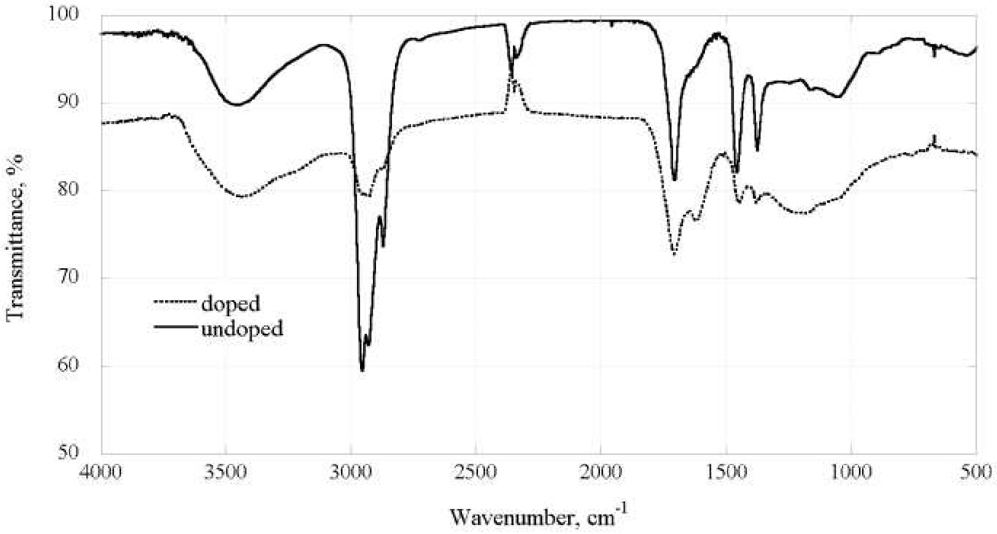

Figure VI.3.3. FTIR spectra of pristine and iodine doped plasma polymerized terpinen-4-ol.

The shifts observed in C-H frequencies and skeletal C-C vibration bands can be attributed to high electronegativity of iodine atoms that can have marked effect on the spectrum of neighbouring group frequencies. Integration of iodine into the polyterpenol molecular structure, most likely by abstraction of H, is further supported by the presence of the group frequency associated with conjugated C=C bond. Considering the complex chemical structure of polyterpenol thin film and presence of a large number of residual radicals commonly observed in plasma polymers, several different reactions with iodine are likely to occur. Formation of iodine oxidants during polymerisation can lead to oxidation of alcohol moieties to ketones. Furthermore, light-induced homolytic dissociation of iodine may lead to formation of additional iodine radicals that can in turn initiate hydrogen abstraction. Therefore, *in situ* iodine doping results in a change in structure of plasma polymerized terpinen-4-ol thin film samples.

Table VI.3.2. Assignments of FTIR bands of pristine and iodine doped polyterpenol films.

Group frequency, wavenumber (cm^{-1})		Assignment
pristine	iodine doped	
~3460	3438	Hydroxy group, H-bonded OH stretch
2955	2958	Methyl asymmetric C-H stretch
2930	2932	Methylene asymmetric C-H stretch
2875	2874	Methyl symmetric C-H stretch
1708	1708	Ketone
	1619	Alkenyl C=C stretch
1457	1450	Methylene C-H bend
1377	1379	Methyl symmetric C-H bend
~1020	~1180	Skeletal C-C vibrations
	600-500	Aliphatic C-I stretch

VI.3.3.2 Optoelectrical properties

Spectroscopic ellipsometry and UV-vis studies were carried out on the polyterpenol thin films deposited on glass substrates to elucidate the effect of iodine doping on the thickness and optical properties of the thin polymer films. Spectroscopic ellipsometry measures functions of the Fresnel reflection coefficients (Ψ, Δ) which are then parameterized as a function of wavelength in order to obtain thin film parameters such as film thickness, surface roughness, refractive index and extinction coefficient spectral dependencies, dielectric functions etc [329,423]. The relationship between R_p and R_s Fresnel coefficients (for the *p*- and *s*- polarizations respectively) and the complex reflection coefficient (ρ) can be expressed through:

$$\rho = \frac{R_p}{R_s} = \tan(\Psi)\, e^{i\Delta} = \frac{|r_p|}{|r_s|} e^{i\Delta} \qquad (1)$$

where r_p and r_s are complex Fresnel coefficients, Δ a phase shift between s and p polarized waves [328]. Gaussian (harmonic) oscillators are suggested for fitting conjugated polymer data in order to obtain the values for the film optical constants [329,330]. Mean-square error values of below 2 were achieved in the modelling process. Comparison between refractive index, extinction coefficient and transmission profiles of the pristine and iodine doped polyterpenol thin films are presented in Figure VI.3.4. Higher levels of doping notably increased the refractive index of the thin films, from 1.54 to 1.70 at 500 nm wavelength, and significantly reduced the transparency of films, owing to the strong absorption of visible light.

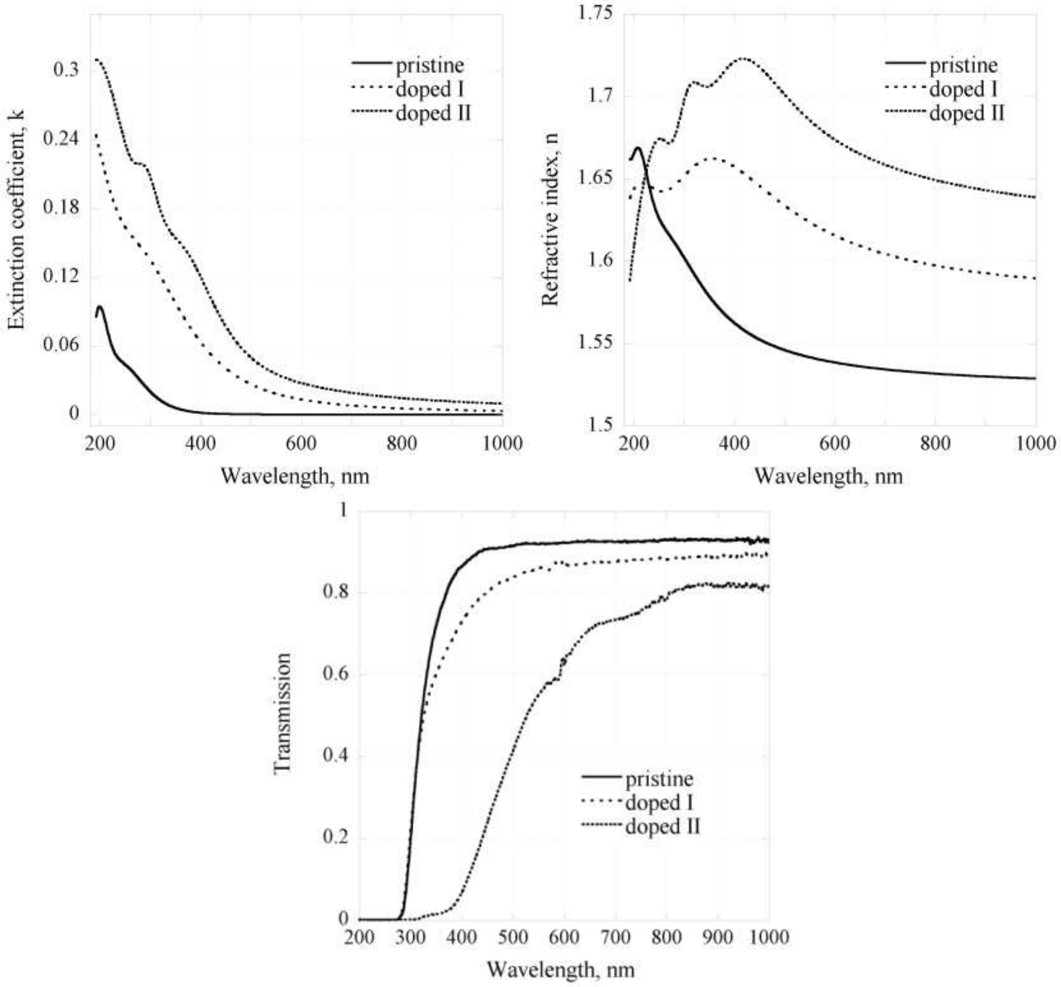

Figure VI.3.4. Refractive index, extinction coefficient, and transmission of polyterpenol thin films as a function of iodine doping level.

For the dielectric function, the real and imaginary terms can be expressed as follows:

$$\varepsilon_2(E) = Ae^{-\left(\frac{E-En}{\sigma}\right)^2} - Ae^{-\left(\frac{E+En}{\sigma}\right)} \quad (2)$$

$$\varepsilon_1(E) = \frac{2}{\pi} P \int_{E_g}^{\infty} \frac{\xi \varepsilon_2(\xi)}{\xi^2 - E^2} d\xi \qquad (3)$$

where A is the amplitude, σ the full width at half maximum, and E_n the peak position [331]. From ellipsometric studies, in the wavelength region 200 nm to 1000 nm the real part of permittivity (k) was found to be between 2.34 and 2.78 for pristine and between 2.52 and 2.97 for iodine doped polyterpenol samples. For pristine polyterpenol thin films, the results were in accord with previously reported complex permittivity studies that found polyterpenol as a potential low-k material.

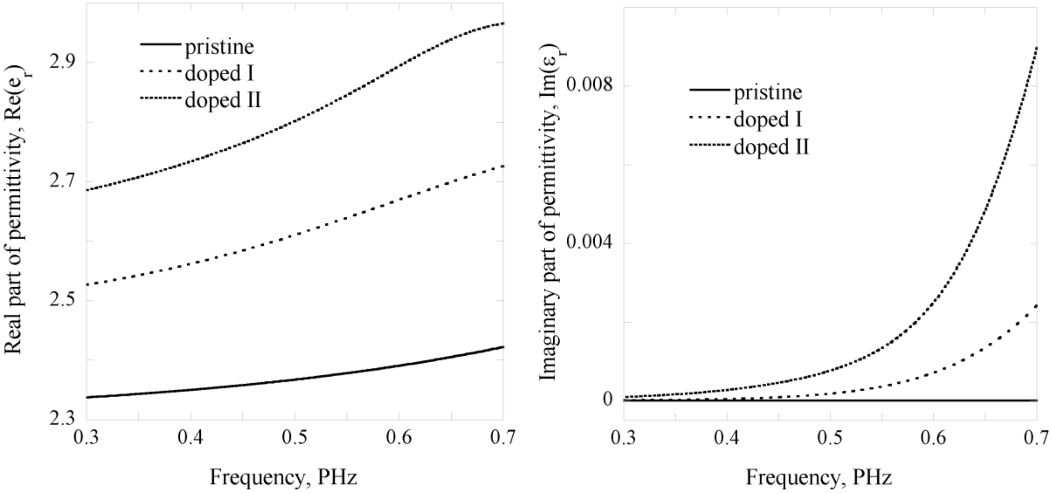

Figure VI.3.5. Real and imaginary part of permittivity as a function of frequency measured using the ellipsometric technique for polyterpenol films fabricated at different RF deposition powers.

The optical band gap of the polymer thin films were determined from absorption data obtained using UV-vis spectroscopy and ellipsometry, and also by fitting a Tauc-Lorenz oscillator model to the ellipsometric data collected for the film samples. In amorphous semiconductors, the photon absorption follows the Tauc relation [332]:

$$\alpha h\nu = B(h\nu - E_g)^n \qquad (4)$$

where α is the absorption coefficient, $h\nu$ the photon energy, B a constant dependant on the length of localized state tails, and n is determined by the nature of the electronic structure of the material, and E_g the optical band gap [98]. Parameter n can take values of ½ for direct and 2 for indirect transition; the n value of 2 is frequently chosen for amorphous materials and indicates a parabolic function for the density of states distribution in the band tails [333,335]. Due to high degree of disorder pertinent to the structure of plasma polymers, the value of the optical gap will diverge from the energy gap value by the width of the range of localized states in the valence and conduction band [334,345]. Absorption coefficient data which resulted from the modelling of optical constants (*n, k*) was used to estimate the optical band gap values for pristine and iodine doped polyterpenol. As shown in Figure VI.3.6, transition energies were estimated by plotting $(\alpha h\nu)^2$ and $(\alpha h\nu)^{1/2}$ as a function of photon energy ($h\nu$) and extrapolating the linear section of the curve to the abscissa, with the intercept denoting the values for the direct and indirect transition energy gaps. UV-Vis absorbance data was treated in a similar fashion to confirm the results (data not shown here). The results showed consistency between estimation methods and are outlined in Table VI.3.3. Introduction of iodine reduced the indirect transition band gap of polyterpenol from 2.82 to 1.64 eV, the reduction attributed to the incorporation of iodine into polymer chain, as confirmed by FTIR and XPS studies, and in so doing extending the density of states more into the visible region of the electromagnetic spectrum. In addition, the increased absorption can be attributed to an increase in C=C bonds in the iodine doped polyterpenol film layers compared to pristine polyterpenol.

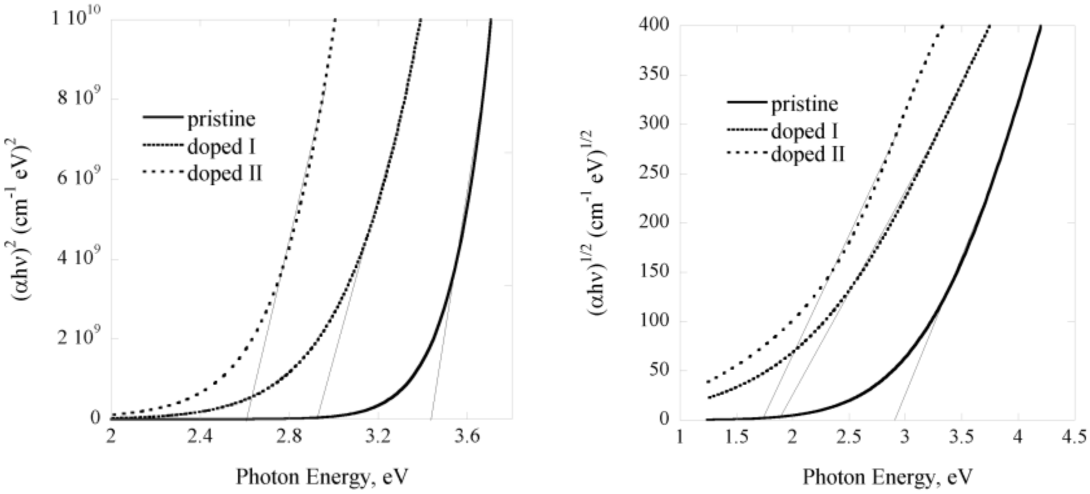

Figure VI.3.6. Direct and indirect allowed transition energies of pristine and iodine doped polyterpenol films.

Polyterpenol has a low electrical conductivity due to the weak van der Waals forces, with the variable-range hopping as the dominant charge transport mechanism due to strong localization of the charge carriers typical for the amorphous organic polymer [424]. Changes in electrical properties of doped amorphous materials, such as plasma polymers, are primarily related to the change in the gap-state occupation, rather than an increase in the band state electron or hole density characteristic of doped crystalline materials. In its doped state, the electrical activity of iodine atoms stems from a complex reaction with both dangling bonds D^0 and hydrogen atoms of polyterpenol chain, and the generation of an additional dangling bond state D^+ [335]. Hence, as well as free charge carriers, iodine doping generates relatively deep localized states in the polyterpenol, in addition to the intrinsic density of states distribution [425]. Such changes in the gap-state density cause the shift in Fermi level and hence the electrical conductivity of polyterpenol thin films.

Table VI.3.3. Band gap, direct allowed and indirect allowed transition energy gap of polyterpenol thin films.

Sample type	Band gap, eV	Direct allowed transition energy gap, eV	Indirect allowed transition energy gap, eV
Pristine polyterpenol	3.33	3.44	2.81
Iodine doped I	2.51	2.93	1.85
Iodine doped II	2.29	2.61	1.64
Iodine doped II annealed to 100 °C for 5 h	2.48	2.82	1.74

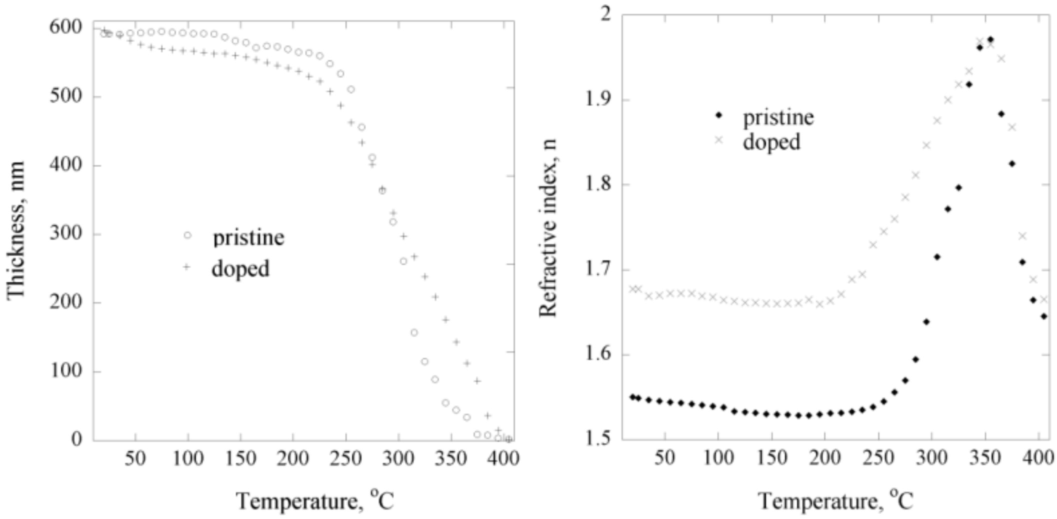

Figure VI.3.7. Film thickness (a) and dynamic refractive index (b) of pristine and iodine doped polyterpenol film as a function of annealing temperature.

Spectroscopic ellipsometry was used to investigate the stability of the iodine doped polyterpenol thin films. Changes in thickness and optical properties of the samples were monitored as the films were annealed to 405 °C in 10 °C steps with 5 min intervals to maintain thermal equilibrium between the sample and the stage. Previous studies have shown that pristine polyterpenol films fabricated under similar RF power conditions possess two distinct regimes of thermal decomposition, with the first regime commencing at approximately 100 °C and characterized by minor thickness reduction attributed to desorption of low molecular weight species and recombination of free trapped radicals [347]. Iodine doped samples revealed a slightly more pronounced weight loss over the same temperature range, as demonstrated in Figure VI.3.7a. Doped polyterpenol were subjected to 5 hours of annealing at 100 °C and their absorption spectrum recorded, as presented in Figure VI.3.8. It was found that the indirect allowed transition band gap increased slightly, from 1.64 eV pre-treatment to 1.74 eV post-annealing, the increase was attributed to desorption of loosely bonded iodine atoms from the surface of the film, similar to *in situ* iodine doped plasma polymerised polyaniline [426]. Subsequent heat treatment at 100°C of these samples did not result in any further change in the band gap, an indication that the change in the optical properties of iodine doped polyterpenol was stable and permanent, and is the result of iodine atoms being incorporated into the structure of the polymer.

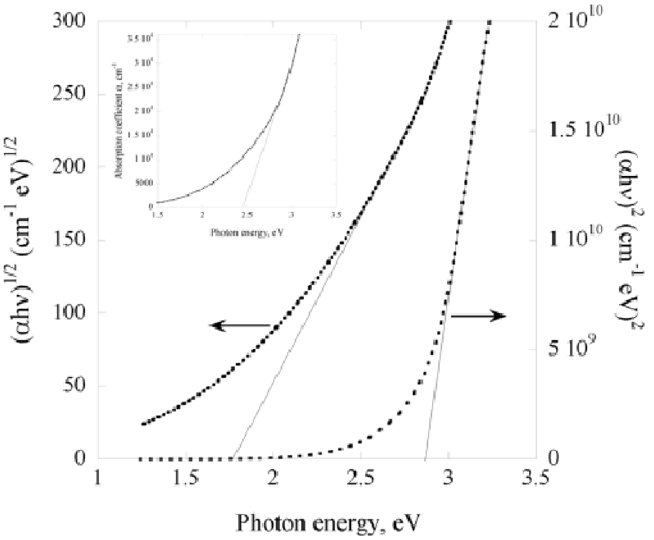

Figure VI.3.8. Band gap, direct allowed and indirect allowed transition energies of iodine doped polyterpenol thin films heat treated at 100 °C for 5 hours.

Unlike pristine polyterpenol films that remain relatively stable in terms of their optical properties up to 250 °C, iodine doped samples commence second regime of decomposition at around 200 °C with a significant increase in refractive index, as shown in Figure VI.3.7b. As discussed earlier, integration of iodine into the polyterpenol structure was likely to involve H abstraction and formation of highly reactive iodine oxidants. Increased temperature combined with light-induced homolytic dissociation of iodine would enhance the mobility and reactivity of such species, with new reaction pathways being initiated. In addition, pristine polyterpenol films contain a significantly larger proportion of C-H bonds which have higher dissociation energy compared to oxygen containing moieties, and hence would contribute to thermal stability of the films. Over the temperature range of 200 °C to 405 °C, doped films undergo a phase change which is reflected in a rapid increase in refractive index and significant reduction in film thickness. Similar to polyvinyl alcohol and polyvinyl acetate, polyterpenol samples are believed to experience non-radical depolymerization via hydrogen abstraction [381], and scission of weaker C-H bonds via radical transfer to the tertiary carbon atom followed by the scission of a C-C bond in the β-position which is a common thermal degradation pathway in cross-linked and branched plasma polymers.

VI.3.3.3 Electrical studies

Current density – voltage relationships of the pristine and doped thin films of approximately 350 nm in thickness sandwiched between Al as electrodes are shown in Figure VI.3.9. While the *J–V* curves of doped samples are approximately the same shape, having two sections of different gradient in the low and high voltage regions, the *J–V* curve for the device containing pristine polyterpenol is distinct.

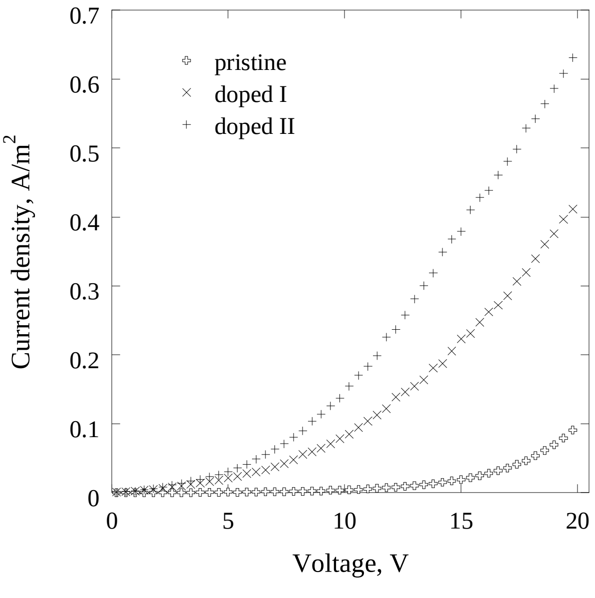

Figure VI.3.9. Current density, *J*, of devices containing pristine and iodine doped polyterpenol with an applied voltage between 0 V and 20 V.

Ability to determine a predominant mechanism of conduction in insulating polymer thin films relies on the dependence of the current density on such parameters as applied voltage, film thickness, temperature, and so on. For instance, $n \geq 2$ generally indicates a possibility of space charge limited conduction mechanism. A linear dependence of ln $J-\ln V$ also suggests this mechanism, whereas a linear dependence of ln $J-V^{0.5}$ indicates a possibility of Schottky or Poole–Frenkel conduction. Furthermore, for space charge limited conduction mechanism, a thickness dependence of conductivity should be satisfied in the form $J \propto d^{-l}$, where l is a parameter associated with the trap distribution and should be $l \geq 3$ in the presence of traps. On the other hand, if Poole-Frenkel conduction or Schottky emission is assumed, the current density should obey log $J \sim d^{-1/2}$ at a fixed voltage. The general expression for both Schottky and Poole–Frenkel type conductions is [410]:

$$J = J_0 \exp\left(\frac{\beta F^{1/2} - \phi}{kT}\right) \tag{1}$$

where J_0 is the low field current density, F the applied electric field, k the Boltzmann constant, T the absolute temperature, β the coefficient of the static electric field, and ϕ the ionization energy of localized centres and Coulomb barrier height of the electrode polymer interface in the case of Poole–Frenkel and Schottky mechanisms, respectively. The field lowering coefficient β are known as β_S and β_{PF} in the case of Schottky and Poole–Frenkel conductions, respectively, and can be expressed as [411]:

$$\beta_{\mathrm{PF}} = 2\beta_{\mathrm{S}} = 2\left(\frac{e^3}{4\pi\varepsilon_0\varepsilon_r}\right)^{1/2} \tag{2}$$

where e is the electronic charge, ε_0 the permittivity of free space, ε_r the dielectric constant of the bulk polymer material at high frequencies. By comparing theoretical β_S and β_{PF} with experimentally attained β coefficient, Schottky and Poole–Frenkel mechanisms can be differentiated. The following relation was used to determine $\beta_{\exp}$:

$$\beta_{\exp} = skTd^{1/2} \tag{3}$$

where s is the slope of the linear section of ln $J-V^{1/2}$ characteristic:

$$s = \frac{\Delta \ln J}{\Delta \ln V^{1/2}} \tag{4}$$

In the low field region of 0–2.5 V, the J–V characteristic of pristine polyterpenol can be described by a power law relation, where $J \propto V^n$, and $n = 0.94$. Such value of n indicates an approximately Ohmic conduction mechanism. Exceeding 2.5 V, the value of n is 2.05 and 4.68 for 2.5−10 V and 10−20 V applied voltage, respectively, indicating non-Ohmic charge transport for these regions. Although $n > 2$ suggests a possibility of space charge limited conduction, fitting the J-V data, the relationship is more linear in ln $J-V^{0.5}$ plot, suggesting Schottky or

Poole-Frenkel conduction. This agrees well with previous studies that demonstrated an approximately Ohmic conduction in the lower applied field region, and Schottky emission in 2.5−6 V region for pristine polyterpenol. Deposited in the glow region, plasma polymers may contain a significant concentration of trapping sites. However, the value of parameter *l* of less than 3 required in space charge limited conduction eliminates this possibility.

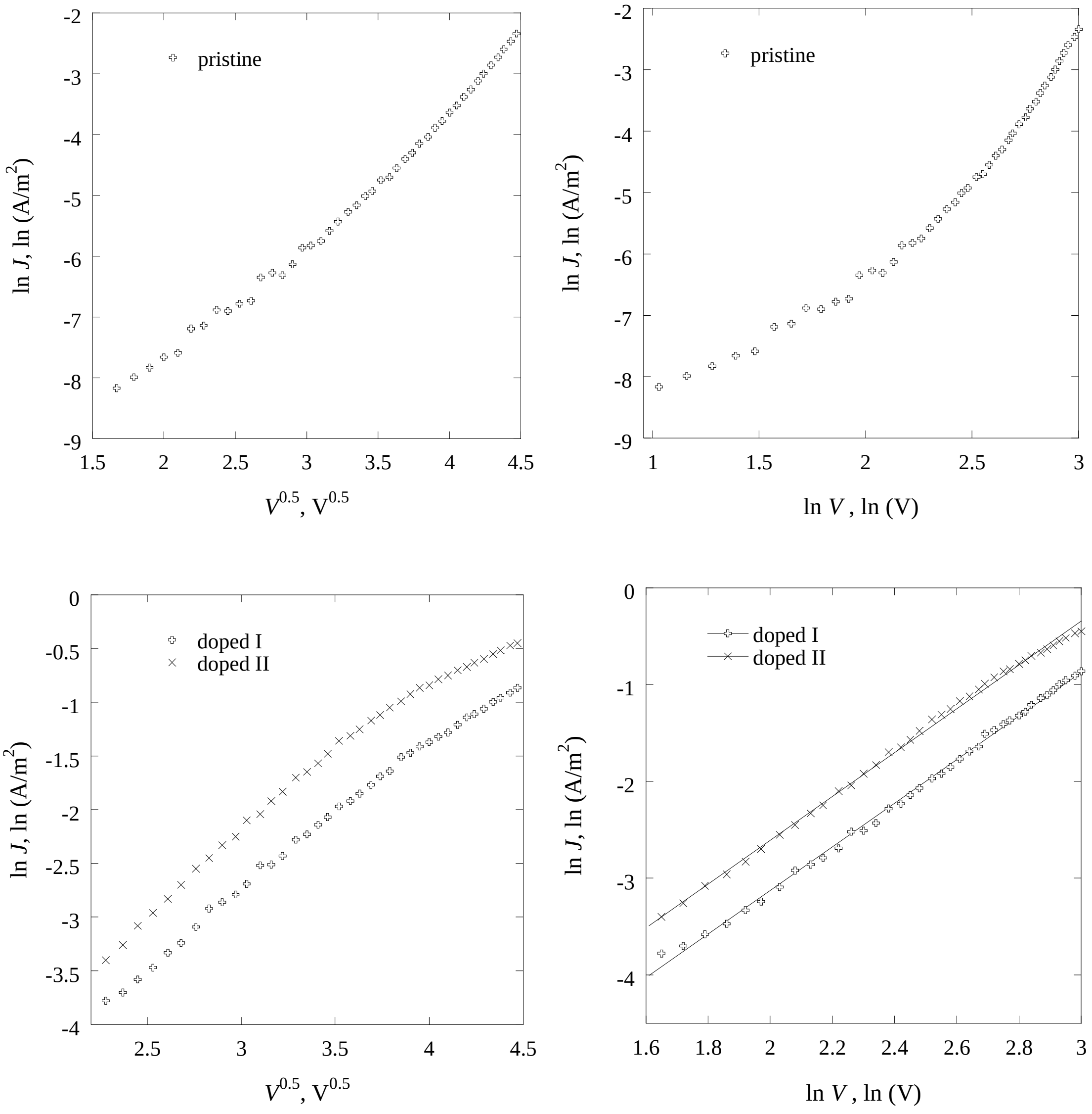

Figure VI.3.10. Schottky/ Poole–Frenkel (a) and space charge limited (b) conduction mechanism fits to *J*–*V* curves in the high field region for pristine and iodine doped polyterpenol.

Then, the experimental values for β_{exp} were determined as 1.44×10^{-5} and 4.32×10^{-5} eV $\text{m}^{1/2}\,\text{V}^{-1/2}$ for 2.5−10 V and 10−20 V, respectively. Using the dielectric value $\varepsilon_r = 2.8$ obtained at high frequencies using spectroscopic ellipsometry, β_S and β_{PF} were calculated as 2.27×10^{-5} and 4.54×10^{-5} eV $\text{m}^{1/2}\,\text{V}^{-1/2}$, respectively. It is likely that in 2.5−10 V region, the dominant transport is Schottky emission, whereas in 10−20 V applied field region, Poole–Frenkel mechanism may dominate. Similar to pristine polyterpenol, the J-V curves of lightly doped samples were also described by the power law relation $J \propto V^n$ in the lower power region, 0−5 V, with n of 1.08, suggesting an Ohmic conduction mechanism. In the same region, strongly doped samples were described by $J \propto V^n$, with $n = 1.33$, indicating Schottky/ Poole–Frenkel mechanisms as likely. In the higher applied voltage region, doped samples had n of 2.25 and 2.27 for lower and higher doping levels, indicating a possibility of space charge limited mechanism. A plot of ln J−ln V in this region is more linear compared to ln $J - V^{0.5}$, advocating in favour of space charge limited conduction.

The conductivity of the samples was also determined as a reciprocal of resistivity ρ calculated as:

$$\rho = \frac{\left(\frac{V}{I}\right)A}{d} \quad (5)$$

where ρ is the resistivity of the material, A the device surface area, d the thin film thickness, V measured voltage, and I measured current. Doping increased the conductivity from 5.05×10^{-8} S/cm to 7.74×10^{-7} S/cm and 1.20×10^{-6} S/cm for increasing doping levels (calculated at 20 V).

VI.3.3.3 Surface properties

Atomic force microscopy and nanoindentation analyses were executed to highlight the changes in physical and surface properties of the polymer films while contact angle measurements are conducted to evaluate wettability of the polymer samples. Examination of the surface topography of the pristine and iodine doped polyterpenol thin films showed that the surfaces were smooth, defect free and uniform. The maximum peak height (R_{max}), surface skewness (R_{skw}) and coefficient of kurtosis (R_{kur}) increased from 5.4 nm, 0.22, 1.65 for pristine to 6.8 nm, 0.76, 2.51 for iodine doped polyterpenol, respectively. Such values of R_{skw} and R_{kur} indicate a disproportionate number of peaks and a well spread out height distribution for the surface. The average roughness (R_a) and RMS (R_q) parameters of iodine doped films were found to be similar to the values for pristine polyterpenol, 0.42 nm and 0.56 nm for R_a and R_q respectively.

Surface wettability studies were performed using water, diiodomethane and ethylene glycol. The average contact angle reduced from 68.7° to 61.6° for water, 71.63° to 47.1° for glycerol, and from 38.1° to 28.4° for diiodomethane, for pristine and iodine doped films respectively. Increased hydrophilicity of doped samples was attributed to a significantly larger number of polar functional groups exposed to the top of the polymer surface. Contact angle measurements were also conducted on a number of iodine doped samples stored for 60 days in ambient environment, with noted an approximately 10% increase in respective contact angles for water and glycerol compared to those pertaining to freshly deposited doped surfaces. Plasma polymerized thin films are frequently characterized by a significant number of radicals trapped within the bulk of the polymer. After the deposition, these radicals continue to react with one another, the polymer molecules, and the ambient environment. Rapid oxidation of polymer upon exposure to the air is common for plasma polymers, and results in the formation of oxygen containing groups on the surface of the films, rendering the film more hydrophilic. Overtime, however, the polar moieties have a propensity to migrate into or re-orientate themselves toward the bulk of the film in an attempt to minimize the interfacial tension at the polymer/air interface. Such change in surface configuration can account for the change in the contact angle behaviour of doped polymer films with time. Under similar exposure conditions, the surface configuration of pristine polyterpenol remains relatively constant, due to initially lower surface tension and consequent lower interfacial tension between the surface of polyterpenol and ambient air.

Table VI.3.4. Contact angle and surface tension for pristine and doped polyterpenol thin film.

Sample	Contact angle, [°]			Surface tension fractions, [mJ m^{-2}]			
	Water	Glycerol	DIM	γ^{LW}	γ^{+}	γ^{-}	γ_S
pristine	68.67	71.63	38.12	40.54	0.26	19.82	45.08
doped	61.59	47.05	28.42	23.87	5.56	14.15	41.24

The average contact angle for each liquid was used to calculate the surface free energy and its components, based on the Lewis acid/base method [427], and the results are summarized in Table Vi.3.4. As is the case with pristine polyterpenol films, iodine doped samples were found to be monopolar in nature, largely manifesting electron-donor properties. However, the electron-acceptor fraction of the surface tension for iodine doped samples was significantly higher than that of pristine polyterpenol, due to the presence of iodine atoms. As a monopolar solid, the iodine polyterpenol is likely to interact with polar solvents, such as water. Over time, the polar components of surface tension and the total surface tension of the film surface decrease, hence lowering the solvophilic response of the surface to polar solvents.

VI.3.4 Conclusion

Polyterpenol thin films were manufactures using RF plasma polymerisation. Iodine doping was carried out *in* situ, which led to significant change in the chemical structure of the film. FTIR studies revealed that iodine was being incorporated into the backbone of the polymer, and that such incorporation resulted in the notable reduction in the methyl and methylene functional groups and appearance of C=C bond. Reduction in oxygen and increase in carbon atomic fractions as determined by XPS studies further indicated that abstraction of H, most probably by elimination of water, was one of the likely reaction pathways to take place during co-polymerisation. Higher levels of doping notably increased the refractive index of the thin films, from 1.54 to 1.70 at 500 nm wavelength, and significantly reduced the transparency of films, owing to the strong absorption of light characteristic of iodine species. Introduction of iodine impurity reduced the band gap of polyterpenol, by extending the density of states more into the visible region of the electromagnetic spectrum and an increase in C=C bonds in the iodine doped film layers compared to pristine polyterpenol. Doping increased the conductivity from 5.05×10^{-8} S/cm to 7.74×10^{-7} S/cm and 1.20×10^{-6} S/cm (at 20 V) for increasing doping levels. When subjected to annealing to 100 °C for 5 hours, the band gap of doped polyterpenol increased slightly, the increase was attributed to desorption of loosely bonded iodine atoms from the surface of the film, and remained stable thereafter. Doping was found not to affect surface morphology of the film. All films were smooth, defect free and uniform. Increased hydrophilicity of doped samples was attributed to a significantly larger number of polar functional groups exposed to the top of the polymer surface. Iodine doped samples were found to be monopolar in nature, largely manifesting electron-donor properties, although the electron-acceptor fraction of the surface tension for iodine doped samples was significantly higher than that of pristine polyterpenol, due to the presence of iodine atoms.

CHAPTER VII

POTENTIAL APPLICATIONS IN ORGANIC ELECTRONICS

The feasibility of polyterpenol as an insulating layer in electronics applications is tested.

In Section VII.1, performance of polyterpenol-incorporated pentacene-based organic field effect transistors is compared against a non-modified counterpart. The changes in device performance and characteristics are measured with respect to device mobility, threshold voltage and switching ratio. The results of this work are published as *Jacob, M. V., Bazaka et al., Fabrication and characterization of polyterpenol as an insulating layer and incorporated organic field effect transistor. Thin Solid Films 2010, 518, 6123-6129.*

Subsequent sections investigate the carrier transport in double-layer p- and n-type metal-insulator-metal devices using electric field induced second harmonic generation. In these experiments, polyterpenol is used as an insulating blocking layer that facilitates visualisation of single-species carriers within a multilayer device or a device containing an ambipolar semiconducting material, such as pentacene. In Section VII.2, the active material is pentacene and, and time−resolved measurement is used to demonstrated carrier injection, transport and accumulation under forward and reverse bias conditions. The blocking property of polyterpenol is reported in *Bazaka, K. et al., Investigation of interfacial charging and discharging in double-layer pentacene-based metal-insulator-metal device with polyterpenol blocking layer using electric field induced second harmonic generation. Chemical Physics Letters 2011, 503, 105-111.*

In Section VII.3, the effect of polyterpenol deposition conditions on the blocking performance of the layer are also investigated using the aforementioned technique, with results outlined in *Bazaka, K. et al., Effect of organic gate dielectric material properties on interfacial charging and discharging of pentacene MIM device. Physics Procedia 2011, 14, 62-66.*

In Section VII.4, the charge transport mechanism across plasma polymerised polyterpenol is investigated by employing fullerene organic semiconductor on the polyterpenol thin film and Al top electrodes. Electron blocking property suggested by the results of this experiment is further substantiated using an electroluminescence spectrum measurement on Al/C_{60}/Alq3/polyterpenol/IZO structures. The outcomes of this investigation is summarised in *Jacob, M. V., Bazaka, K. et al., Electron−blocking hole−transport polyterpenol thin films. Chemical Physics Letters*.

VII.1 POLYTERPENOL AS A GATE MODIFICATION LAYER IN PENTACENE-BASED OFET

Abstract

A non-synthetic polymer material, polyterpenol, was fabricated using a dry polymerization process namely RF plasma polymerization from an environmentally friendly monomer and its surface, optical and electrical properties investigated. Polyterpenol films were found to be transparent over the visible wavelength range, with a smooth surface with an average roughness of less than 0.4 nm and hardness of 0.4 GPa. The dielectric constant of 3.4 for polyterpenol was higher than that of the conventional polymer materials used in the organic electronic devices. The non-synthetic polymer material was then implemented as a surface modification of the gate insulator in field effect transistor (OFET) and the properties of the device were examined. In comparison to the similar device without the polymer insulating layer, the polyterpenol based OFET device showed significant improvements. The addition of the polyterpenol interlayer in the OFET shifted the threshold voltage significantly; + 20 V to –3 V. The presence of trapped charge was not observed in the polyterpenol interlayer. This assisted in the improvement of effective mobility from 0.012 to 0.021 cm^2/Vs. The switching property of the polyterpenol based OFET was also improved; 10^7 compared to 10^4. The results showed that the non-synthetic polyterpenol polymer film is a promising candidate of insulators in electronic devices.

Keywords: Gate insulator; OFET; pentacene; polyterpenol; surface modification

As published in: Jacob, M. V., Bazaka, K., Weis, M., Taguchi, D., et al., Fabrication and characterization of polyterpenol as an insulating layer and incorporated organic field effect transistor. *Thin Solid Films* 2010, 518, 6123-6129.

VII.1.1 Introduction

A significant industrial growth in the area of organic semiconductors over the past few years has been well recognized by the scientific community [16,17]. The advancement is especially noticeable in organic electronic systems such as flexible electronic displays, organic field effect transistors (OFETs) and thin-film organic photovoltaic devices. In spite of numerous advantages to the organic circuits and devices, the efficiency of such systems is yet to be comparable to that of silicon based devices. This necessitates the development of advanced, high-performance organic materials with properties comparable to those of conventional electronics materials [85,86,89,319,336]. In the last few years, a considerable effort has been directed to the development of organic thin-film transistors due to their potential of being used in organic electronics, particularly in flexible screens and other printed electronic devices. Amongst a variety of organic semiconducting materials evaluated, pentacene was found to be one of the most promising candidates for the fabrication of organic transistor, since it offers higher mobility, better on/off ratio, improved environmental stability, and better reliability than most other organic materials. Along with the development of preparation method of pentacene as an active layer in OFET, much effort has been made to improve the OFET performance by controlling the semiconductor/dielectric interfacial properties, and using an additional layer such as polymer thin-film, self-assembled monolayer, high-*k* metal oxide, thin polymer/thick high-*k* oxide hybrid layer, etc [428-431]. Despite these efforts, the need for further improvements remains. In this paper, we focus on organic materials fabricated from non-synthetic renewable sources using environmentally responsible techniques, making these materials suitable for the demands of sustainable human life of the 21st century.

Recently, the fabrication of a non-synthetic polymer thin-film material namely *polyterpenol* was reported [336]. Polyterpenol is an environmentally friendly material fabricated from a non-synthetic source, i.e. terpinen-4-ol (Figure VII.1.1a), with properties that are stable and reproducible under similar fabrication conditions [347]. Plasma techniques such as DC, AC or RF polymerization [96,325,393,432,433] that can be used to manufacture polyterpenol thin-films are a clean and dry process and hence electronic circuit modifications can be carried out without altering the device properties. Furthermore, a wide range of low-cost substrates including glass, plastic, and metal foils can be used to fabricate polymer thin-films [86,319]. The typical characteristics of plasma polymerised thin-films are a smooth homogenous surface, pinhole free layer and high adhesion to the substrate [96]. Considering the above mentioned properties of the material, in this work we studied the electrical insulating properties of the non-synthetic polyterpenol polymer film, and examined the performance of this polymer as a gate insulating layer in OFET. First, polyterpenol thin-films of various thicknesses were fabricated and their surface potential was evaluated using Kelvin probe technique. The current–voltage (*I*–*V*) characteristics were studied using a metal-insulator-metal (MIM) structure. Finally, polyterpenol thin-films were incorporated as an insulating layer of the pentacene based FET and the performances of the OFETs with and without the polymer layer were compared. In the device, the polymer insulating layer was introduced between the SiO_2 layer and pentacene layers. The experiments suggested that the polyterpenol thin-films used here is a possible candidate of insulators in electronic organic devices.

VII.1.2 Experiments

VII.1.2.1 Polymer thin-film fabrication

RF plasma polymerization technique was used to fabricate polymer thin-films from non-synthetic terpinen-4-ol monomer distilled by Australian Botanical Products. The chemical structure of the terpinen-4-ol is shown in Figure VII.1.1a. RF signal of 13.56 MHz with input power of 25 W was used to generate the glow discharge. RF energy was delivered into a custom-manufactured glass deposition chamber [325] by means of capacitive coupled copper electrodes. Non-synthetic terpinen-4-ol was slowly released into the glass discharge chamber which was kept under a vacuum of 40 Pa and at ambient temperature. The deposition time was varied to obtain samples of various thicknesses. Polymer thin-films with thicknesses of 30, 50, 100 and 500 nm were fabricated on different substrates, such as ITO/Al/Au coated glass and Si wafers with 100 nm silicon dioxide (SiO_2) layer. Si substrate pre-coated with gold thin-film on one side and 100 nm SiO_2 on the other side was used for the fabrication of 100 nm thick polymer thin-film. In this instance, the heavily-doped Si wafer was to serve as the gate for the OFET circuit.

A UV–vis spectrometer (Avantes 2048) was used to collect the absorbance profile for each of the polyterpenol samples, and also as a tool for preliminary estimation of the thickness of the thin-film. Optical properties of the films were determined from the ellipsometric data collected at three different angles of incidence (φ = 55°, 60°, and 65°) over the wavelength range of 200 – 1000 nm (6.2– 1.2 eV) by means of regression analysis (WVASE32 software package). First, Cauchy dispersion was applied to data within 500–1000 nm range assuming the films are optically transparent within this region (*k* approximates 0) and the film is homogenous, and using the thickness estimated obtained by means of UV–vis spectrometer as an initial input parameter. Roughness layer (50% material/50% void) was also employed in the modeling process. Then, Gaussian oscillators were employed as harmonic oscillators. The surface architecture of polyterpenol films was investigated using atomic force microscope (AFM) (NT-MDT NTEGRA Prima) to evaluate the topographical properties of the surfaces over scales ranging from angstroms to microns. The non-destructive semi-contact AFM mode was used in order to minimize the damage to the surface of the films. Multiple scans of randomly chosen areas were performed on each sample to ensure the accuracy of characterizations. The fabricated samples exhibited very smooth surface with average surface roughness of 0.4 nm, as described in section 3.1.

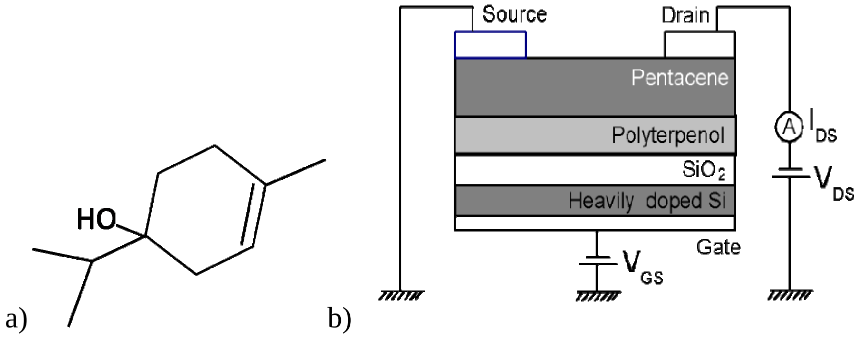

Figure VII.1.1. (a) Molecular structure of terpinen-4-ol, and (b) schematic view of OFET with polyterpenol interlayer.

VII.1.2.2 MIM and OFET fabrication

MIM structure was fabricated using the polymer thin-film. For the MIM structure, a 300 nm thick polymer thin-film was sandwiched between ITO and 8 nm thick gold electrodes. In addition to the MIM structure, for the electrical characterization top-contact pentacene OFETs were fabricated, as shown in Figure VII.1.1(b). Heavily-doped Si wafers with a 100 nm thick thermally prepared SiO_2 insulating layer were used as the base substrate for fabricating the OFET structures. Polyterpenol thin-film with a thickness of 100nm was deposited onto the silicon dioxide surface. Pentacene (Tokyo Kasei Kogyo Co., Japan) without further purification was used as the source for the thin-film of thickness 100 nm deposited on top of the polyterpenol film. During the deposition of pentacene, the pressure was kept at less than 10^{-4} Pa and the deposition rate was fixed at 3 nm/min, monitored using a quartz crystal microbalance. Gold electrodes (source and drain electrodes) with a thickness of 100 nm were deposited on the pentacene thin-film surface using a custom made mask so that a channel length (L) of 50 μm and width (W) of 3 mm were obtained. Keithley 2400 Source Meter was used for the I–V measurements of the MIM or the OFET structures. The DC bias voltage was varied from 40 V to –40 V. The impedance measurements were carried out using Solartron 1260 Impedance Analyzer. MIM samples were tested in the range of 1 MHz to 1 Hz with 10 points per decade with AC signal amplitude of 0.5 V. In order to avoid unexpected carrier injection, sample charging or electric breakdown, the exposure of sample to the high electric field was minimized by applying opposite bias voltages in the next frequency sweep.

VII.1.3 Results and discussion

VII.1.3.1 Fundamental properties

Polyterpenol thin-films of different thicknesses with refractive index of 1.55 (at wavelength of 450 nm) were deposited onto a range of substrates. The film thicknesses were measured using ellipsometry and the thicknesses were estimated to be 30, 50, 100, 200 and 500 nm. The surface properties of polyterpenol were examined to reveal a smooth, defect free surafce commonly reported for plasma polymerised thin-films [336].

a. The optical band gap:

The UV–Vis absorption spectrum was measured using a spectrometer. The absorption coefficient data were used to estimate the optical band gap of the material using the Tauc equation $\alpha h\nu = B\,(h\nu - E_g)^{n}$, where α is the optical absorbance, ν is the frequency of light, and n and B are factors dependent on the type of transition and the length of localized state tails, respectively. For n value of 2, the E_g was estimated to be 2.65 eV, which is in agreement with [336].

b. Refractive index:

The refractive of the sample was measured using the spectroscopic ellipsometric method over the wavelength region 200–1000 nm. The refractive index of the films was estimated from the ellipsometric data collected at three different angles of incidence (φ = 55°, 60°, and 65°). Transmission data were appended to enhance the accuracy of the model used to determine optical constants of the material and understand the transparency range of the polymer films under investigation. For modelling, Cauchy dispersion was initially applied over the wavelength region where k approximates zero. Subsequently, harmonic oscillators, in this case two Gaussian oscillators, were implemented. Figure VII.1.2 shows the refractive index and extinction coefficient values over the wavelength region of 200 to 1000 nm.

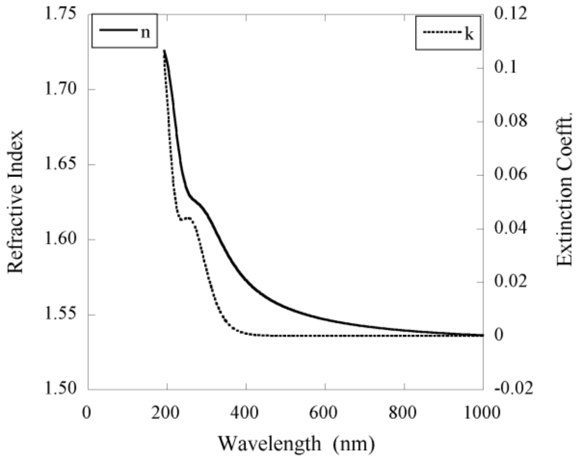

Figure VII.1.2. The refractive index and extinction coefficient of 100 nm thick polyterpenol thin-film.

c. Surface potential:

The Kelvin probe is a non-contact, non-destructive measurement device based on a vibrating capacitor and is used to investigate surface and bulk properties of materials. It measures the work function difference, or for non-metals, the surface potential, between a conducting specimen and a vibrating tip. The work function is an extremely sensitive indicator of surface condition and is affected by adsorbed or evaporated layers, surface reconstruction, surface charging, oxide layer imperfections, and surface and bulk contamination.

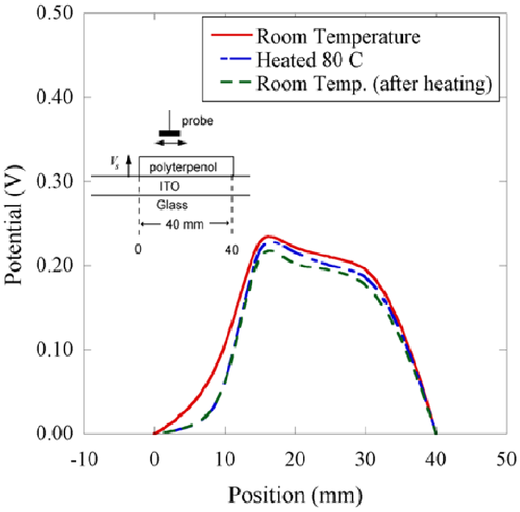

Figure VII.1.3. The surface potential of polyterpenol thin-film deposited on ITO coated glass substrate; and the schematic view of the measurement setup (inset).

We have measured the surface potential of a 100 nm thick polyterpenol sample deposited ITO. Figure VII.1.3(a) shows the surface potential of the polyterpenol measured at room temperature under vacuum, then heated to 80 °C and then cooled down to room temperature. The difference between these three measurements is very small which substantiates stable operation of the polyterpenol incorporated device under varying temperatures. These results also suggest that as-deposited polyterpenol film adheres well to the surface of ITO and is very stable.

d. Surface morphology and surface energy:

Figure VII.1.4 shows the surface profile of the polymer thin-film investigated using atomic force microscope (AFM). The surface is very smooth, without any pinholes, and the average roughness R_a is less than 0.4 nm. The roughness parameters obtained for polyterpenol thin-films are summarised in Table VII.1.1. The hardness was measured using the Hysterion nanoindentation probe used in conjunction with AFM. The estimated hardness value of polyterpenol is 0.4 GPa.

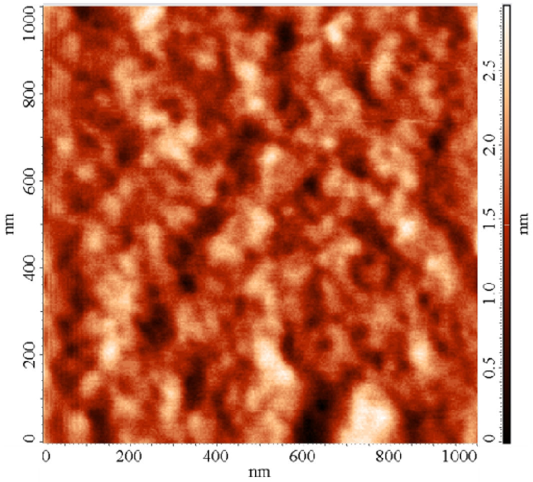

Figure VII.1.4. The surface profile of the polyterpenol thin-film (AFM).

Table VII.1.1. Surface energy fractions and roughness parameters of polyterpenol thin-films.

Surface free energy fractions (mJ/m^2)					Roughness parameters				
γ^{LW}	γ^{AB}	γ^{+}	γ^{-}	γ_{TOT}	R_a, nm	R_q, nm	R_{max}, nm	R_{skw}	R_{kur}
40.5	5.4	0.4	20.6	45.9	0.42	0.52	5.3	0.6	0.71

Contact angle data collected for 6 different liquids was then used to calculate surface energy fractions for polyterpenol films using Van Oss, Chaudhury, and Good method [393]. The results were in agreement with previous studies that found polyterpenol to be strongly monopolar, with significantly larger electron-donor fraction γ^- compared to electron-acceptor fraction γ^+. A contact angle of 68 ° indicated that the polyterpenol thin-films were moderately hydrophilic. Previous studies have shown that higher RF input power during deposition can be used to increase the hydrophobicity of polyterpenol samples [347].

VII.1.3.2 The DC I–V characteristics as an insulating layer of MIM elements

Standard I–V measurement can be used to illustrate steady-state carrier injection and transport phenomena in solids. The measured I–V dependence (see Figure VII.1.5(a)) of polyterpenol MIM structure exhibits low current over a wide range of applied external fields, but it clearly shows the applied electric field dependence.

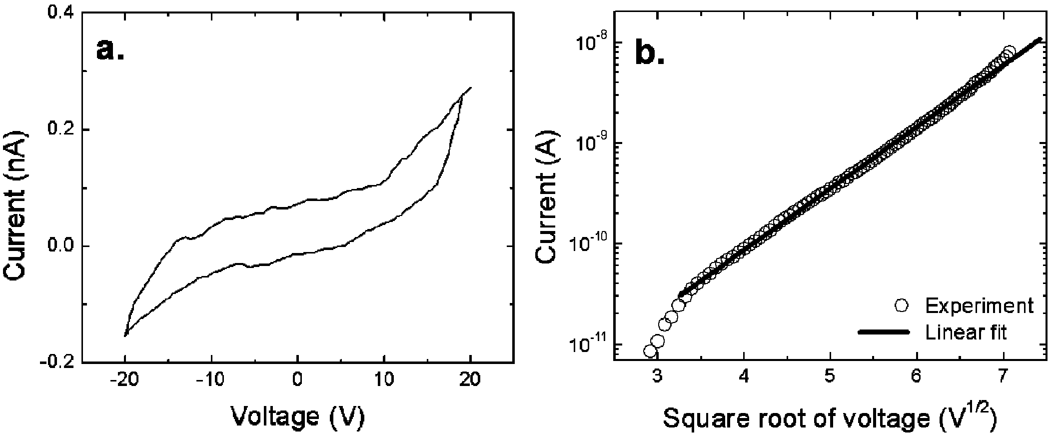

Figure VII.1.5. (a) Current voltage measurement on MIM structure and (b) its analysis as a Schottky injection.

When the MIM device is exposed to the electric field, carriers are injected into the polyterpenol film from the metal electrode. The thermionic emission (or Schottky injection) [16] process accounts for the I–V characteristics, as plotted in Figure VII.1.5(b) by a linear line using semi-log scale. In more detail, the electrode-film interface can be described by a carrier injection potential barrier energy ΔΦ (difference between Fermi energy of the electrode metal and highest occupied molecular orbital level of the film). The thermionic emission (or Schottky injection) [16] and the current density on the metal-organic interface J_0 can be described by the relation:

$$J_0 = AT^2 \exp\left(-\frac{\Delta\Phi - \beta\sqrt{E}}{k_B T} \right) \tag{1}$$

where β, A, T, and k_B are the Schottky parameter ($\beta = \sqrt{e^3 / 4\pi\varepsilon_0\varepsilon_r}$), the Richardson constant, temperature, and the Boltzmann constant, respectively. The I–V characteristics of the MIM device satisfy the relation of Eq. (1), and we obtain the relative dielectric constant of polyterpenol of 3.4 from the slope. This value is comparable with other polymers, such as poly(methyl methacrylate) [433,434] of 2.2 to 3. The polyterpenol keeps its insulating properties up to electric field of 1.3 MV/cm, this value is also comparable with other polymers [435].

VII.1.3.3 The AC I–V characteristics as an insulating layer of MIM elements

Steady-state I–V measurements exemplified the fundamental insulating behavior of polyterpenol thin-film. Hence, further detailed study of the dielectric properties of the material was carried out employing impedance spectroscopy as shown in Figure VII.1.6(a). Although polyterpenol film was investigated in the range of applied electric fields up to 1MV/cm, recorded impedance was kept unchanged (not shown here). This confirms that almost no charge was present in the bulk of the polyterpenol film and therefore verifies insulating nature of the polyterpenol thin-film. Based on the results of impedance spectroscopy experiments, an appropriate equivalent electric circuit was designed (see inset of Figure VII.1.6(a)) consisting of parallel polyterpenol film resistance and capacitance and a small parasite resistance in series. The resistance and capacitance of the polyterpenol thin-film was obtained by fitting the experimental data as illustrated in of Figure VII.1.6(a) and corresponding values are 404 MΩ and 0.31 nF respectively. These results correspond to resistivity of 2700 MΩm and relative dielectric constant of 5.2. The discrepancy in dielectric constants between the I–V and IS experiment attributes to the frequency dependence of the material parameter including parasitic capacitance.

Without employing the equivalent circuit it is also possible to evaluate charge propagation through the polyterpenol film on the basis of frequency dependence of impedance phase shown in Figure VII.1.6(b). Single peak corresponding to single relaxation process is observed and its maximum value represents the reciprocal value of relaxation time. In this case relaxation time τ is identical with the transit time of the injected charge carrier across the film. Hence, in accordance with the time-of-flight method we can evaluate effective mobility μ, using the transit time τdefined as $\tau = \frac{d^2}{\mu V}$, where d is the film thickness, and V is the applied voltage. We obtained the mobility of ~10^{-8} cm^2/Vs, which is in agreement with the already identified insulating behaviour of the polyterpenol film.

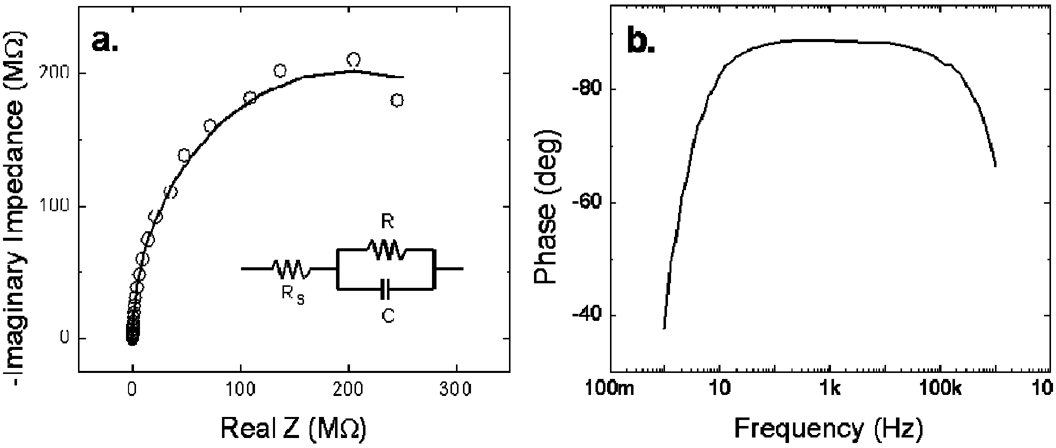

Figure VII.1.6. (a) Z-plot of the impedance spectroscopy for bias voltage +20 V with appropriate fit and (b) frequency dependence of impedance phase. Inset in (a) shows equivalent circuit used for data fitting.

VII.1.3.4 Insulating layers as an OFET gate insulator

VII.1.3.4.1 Transport properties

In order to understand the feasibility of employing the polyterpenol in organic devices we have manufactured an OFET as described in section 2.2, and investigated its transfer and output characteristics. From the transfer characteristics the threshold voltage V_t was determined. For the comparison purposes we have fabricated two OFETs, one with SiO_2 as the insulating layer and the second one with polyterpenol as the insulating layer. As Figure VII.1.7(a) shows, for SiO_2–pentacene OFET, the threshold voltage value estimated from the transfer characteristic was 26 V. Significant shift in the threshold voltage was observed for the pentacene OFET with polyterpenol interlayer. The threshold voltage value is estimated as –3 V. This observation gives us circumstantial evidence about the presence of internal electric field due to polyterpenol interlayer. The surface potential measurements suggest that the polymer on metallic surface is positively charged of about 0.2 V on ITO coated surface for 100 nm polymer thin-film thickness (see Figure VII.1.3). Due to the internal field generation at the polymer-semiconductor interface the positive charges accumulated and assisted the threshold voltage shift. Switching between ON and OFF state of the electronics device can be expressed by the sub-threshold slope and the ON/OFF ratio. As is shown in Figure VII.1.7(b), on/off ratio for the OFET with pentacene on the bare SiO_2 surface and polyterpenol surface reached a value of 10^4 and 10^7 respectively. This improvement of off state is usually related to repulsive electrostatic fields which have an origin in electrostatic charge or permanent electric dipoles (spontaneous polarization).

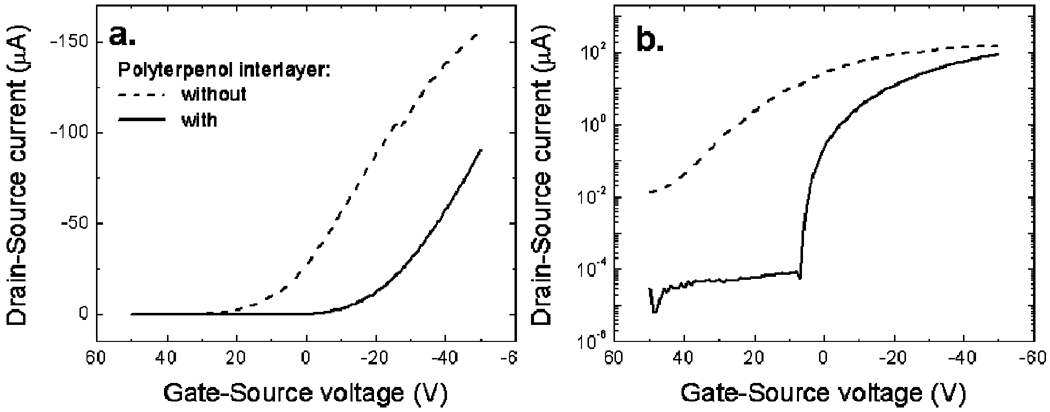

Figure VII.1.7. Transfer characteristics of OFET with and without polyterpenol interlayer in (a) linear and (b) semi-log scale for estimation of threshold and sub-threshold slope respectively.

In order to study the effect of the polyterpenol interlayer, the output characteristics of the OFETs were recorded for the comparable applied voltage (V_{gs}–V_t) in the range of –10 to –50 V and some of the selected results are shown in Figure VII.1.8.

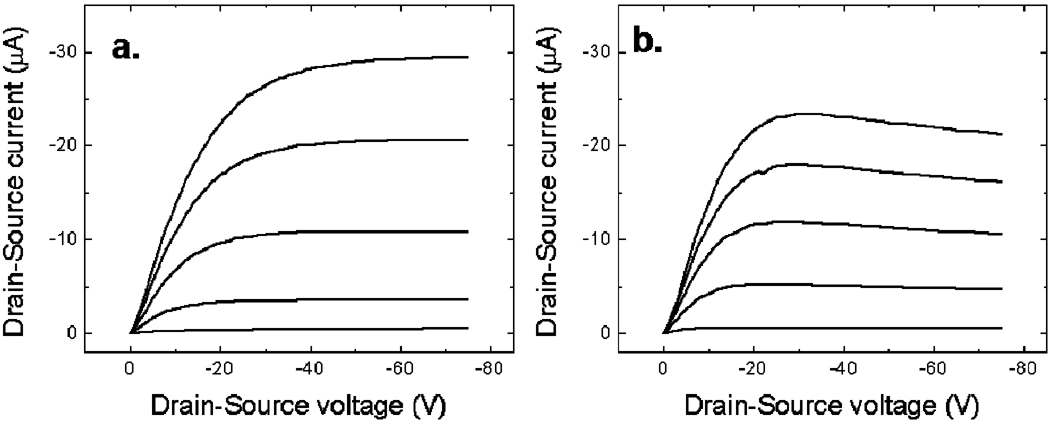

Figure VII.1.8. Output characteristics of OFET (a) without and (b) with polyterpenol interlayer. Applied voltage (*i.e.* V_{gs}–V_{th}) varies in range from –10 to –50 V for both OFETs.

In contrast to OFET with pentacene on bare SiO_2, whose behavior was already reported by many researchers, OFET with polyterpenol interlayer exhibits small drain-source current as well as very low value of pinch-off voltage (about –20 V) and very fascinatingly it is constant over a wide range of applied voltage. We have also observed an increase in the output hysteresis characteristics for the OFET with polyterpenol interlayer. For thorough understanding of the electric behavior of OFET we applied analysis based on the Maxwell–Wagner model [436]. If the injection time in comparison with the transit time is much smaller (*i.e.* hole injection energy barrier on the metal-organic interface is small), the drain-source current will exhibit a wide saturation region in the form:

$$I_{ds} = \mu C_g \frac{W}{2L}\left(V_{gs} - V_t\right)^2 \tag{2}$$

where C_g, W and L represent the gate capacitance per unit area, channel width and length. This relation denotes bulk-limited current because transport of the charge is determined by the space-charge limited conditions (SCLCs) [432,437]. It is important to focus on the injection limited conditions. Eq. (2) is applicable only in the saturated region of SCLC caused by the accumulation process. If the time required for carrier transition is lower than the accumulation time, injected carriers are drained out without accumulation on the interface. This also corresponds to the positive potential on the gate insulator surface, which restricts the charge accumulation. This condition is expressed using the relation:

$$I_{ds} = \mu C_g \frac{W}{L}\left(V_{gs} - V_t - \frac{V_{sat}}{2}\right)V_{sat} \tag{3}$$

where V_{sat} represents the pinch-off voltage when the current I_{ds} is saturated (approximately –20 V in this case). Knowledge about the charge transport limitation assists the precise evaluation of the mobility. Interestingly, addition of polyterpenol interlayer raises effective mobility from 0.012 to 0.210 cm^2/Vs. This increase can be assigned to lower charge accumulation on the pentacene-gate insulator interface and consequent contribution of the excess charge to the mobile charge.

VII.1.3.4.2 Injection properties

The displacement current measurement was performed in order to prove the charge injection phenomena in the OFET device. For this experiment top electrodes (source and drain) were electrically shorted and ramp voltage with amplitude of 50 V was applied to the gate electrode. The estimated normalized displacement current for selected frequencies was plotted in Figure VII.1.9.

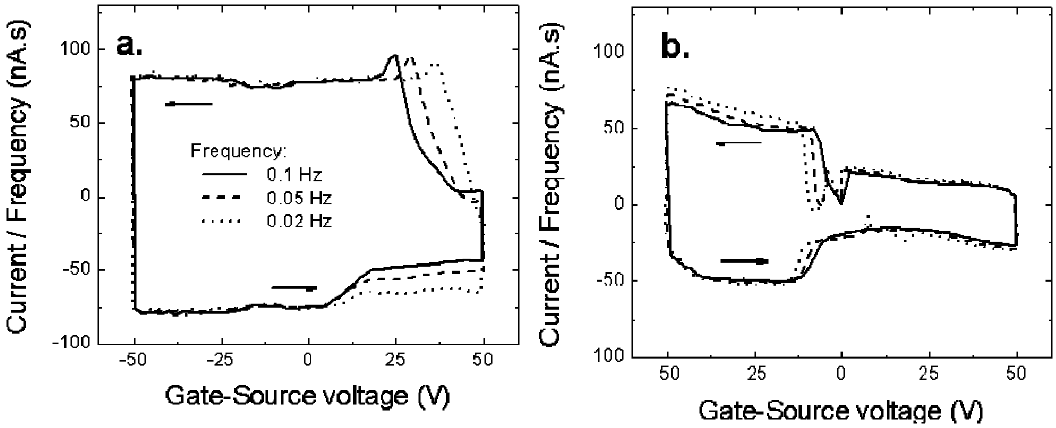

Figure VII.1.9. Displacement current measurement of OFET (a) without and (b) with polyterpenol interlayer.

In this experiment displacement current I_{disp} reflects the change of induced charge Q(t) on electrode given by CV(t) , where C is the capacitance of the investigated structure, and is usually expressed using:

$$I_{disp} = \frac{\partial Q(t)}{\partial t} = C\alpha V_0 \tag{4}$$

when C is a constant. Here, V_0 and α stand for voltage amplitude and sweeping rate ($\alpha = 4f$ where f is frequency). This shows that the displacement current is sensitive to the carrier position which determines the capacitance. If carriers are injected to the OFET and accumulated on the pentacene-gate insulator interface, the induced charge Q(t) changes and the total capacitance is represented by the gate insulator capacitance C_g. However, in the case of positive applied voltage on the gate electrode, we can expect exhaustion of pentacene film, and the induced charge Q(t) is given as the sum of the charge induced by total capacitance created by capacitances of pentacene film C_p and the gate capacitance connected in a series and mirror image of accumulated and trapped charge Q_s situated on the interface:

$$I_{disp} = \frac{\partial}{\partial t}\left(\frac{C_p C_g}{C_p + C_g} V(t) - \frac{C_p}{C_p + C_g} Q_s \right) \tag{5}$$

Application of this analysis on experimental data allows us to evaluate trapped charge on the pentacene-gate insulator interface. For bare SiO_2 surface the trapped charge flow is ~2 mC/m^2 and trapped charge was not present for polyterpenol interlayer. This supports our previous observation of the positively charged polyterpenol surface. It should be noted that small dip observed at the beginning of injection (at voltage of ~ 0 V) for OFET with polyterpenol interlayer has an origin in charge diffusion into the channel region, which actually decreases the current flowing the ammeter, that is, decreases the effective pentacene film capacitance in time. The carriers' diffusion-like motion is possible to observe due to polymer surface charge only, which reduces charge accumulation on pentacene-gate insulator interface. On the other hand, with bare SiO_2 surface the carriers are strongly attracted to gate insulator and therefore the flow to the channel region is restricted.

VII.1.4 Conclusion

Polyterpenol thin-films of thicknesses ranging from 30 nm to 500 nm were fabricated using RF plasma polymerization. The plasma polymerization is a clean process and therefore it is safe to use the polymerization technique for the fabrication of insulating layer. For the MIM and OFET 100 nm polyterpenol thin-films were used. The fabricated samples exhibited a very smooth surface with an average roughness less than 0.5 nm. The I-V characteristics were studied using the MIM structure and the thin-film showed insulating properties as expected. However, the dielectric constant of the material was higher than the conventional polymer materials used in the organic electronic devices. The polymer thin-film was incorporated as an insulating layer over the silicon dioxide layer to understand the influence of the material in electronic circuits. We have used this approach to keep all parameters same for comparison but we will use polyterpenol layer without SiO_2 in our future work. The addition of the polyterpenol interlayer in the OFET shifted the threshold voltage significantly; + 20 V to -3 V. The presence of trapped charge was not observed in the polyterpenol interlayer. This assisted in the improvement of effective mobility from 0.012 to 0.021 cm^2/Vs. This increase was assigned to lower charge accumulation on the pentacene-gate insulator interface and consequently the excess charge contribution to the mobile charge. The switching property of the polyterpenol based OFET was also improved; 10^7 compared to 10^4. Therefore polyterpenol is an excellent insulating material to improve the OFET output characteristics and is a potential candidate for full flexible organic electronic circuits.

VII.2 INTERFACIAL CHARGING AND DISCHARGING IN DOUBLE LAYER PENTACENE-BASED DEVICE WITH POLYTERPENOL BLOCKING LAYER

Abstract

Time-resolved electric field induced second harmonic generation technique was used to probe the carrier transients within double-layer pentacene-based MIM devices. Polyterpenol thin films fabricated from non-synthetic environmentally sustainable source were used as a blocking layer to assist in visualisation of single-species carrier transportation during charging and discharging under different bias conditions. Results demonstrated that carrier transients were comprised of charging on electrodes, followed by carrier injection and charging of the interface. Polyterpenol was demonstrated to be a sound blocking material and can therefore be effectively used for probing of double-layer devices using EFISHG.

Keywords: EFISHG; dielectric; pentacene; polyterpenol

As published in: Bazaka, K., Jacob, M. V., Taguchi, D., Manaka, T., Iwamoto, M., Investigation of interfacial charging and discharging in double-layer pentacene-based metal-insulator-metal device with polyterpenol blocking layer using electric field induced second harmonic generation. *Chemical Physics Letters* 2011, 503, 105-111.

VII.2.1 Introduction

Over the last two decades, organic materials and organic semiconducting devices have become a focus of intense research and advancement in academia and industry alike [438]. The significant commercial interest in organic electronics stems from their potential as building blocks for inexpensive and structurally flexible electronic devices, including radio frequency identification tags [439,440], smart cards [441], light emitting diodes [442,443], and flexible displays [444,445]. Organic field effect transistors (OFETs) have been demonstrated as a viable alternative to conventional devices for applications that require large area coverage, light weight, and low-temperature processing [446]. Recent improvements to the manufacturing process and modifications of the device structure allow for fabrication of OFETs with mobility comparable to that of amorphous silicon semiconductors. Mobilities over $1\,\mathrm{cm^2/V\,s}$ were recently reported for pentacene based OFETs [447] and others [448-450], with the former material being a popular choice for fabrication and performance evaluation of organic thin film devices.

Although some prototype organic electronics devices are nearing the market deployment stage [451], our understanding of the fundamental carrier behaviours within these materials and devices remains limited. In spite of years of intense investigation and experimental and theoretical efforts devoted to realisation of high-performance OFETs, our knowledge of the charge transport and emission properties of organic semiconductors is yet to be sufficient for effective optimisation of the organic devices [452]. Techniques frequently employed to investigate physics of OFET devices, including capacitance–voltage (*C*–*V*) and Hall-effect measurements to estimate carrier density and carrier polarity, Kelvin-probe approach to evaluate potential profile along the channel, and optical second harmonic generation measurement (SHG) for the determination of electric field distribution within the channel, revealed the behaviour of OFETs to be significantly different from that of Si-based devices [453]. For instance, OFET operation has been found to be largely influenced by carriers injected from source and drain electrodes, with the carrier injection into the OFET depending on the work function of the metal electrodes. Other studies reported ambipolar characteristics in a broad range of polymer semiconductor FETs based on trap-free gate dielectrics [438]. Importantly, due to high voltage required to operate the OFET device efficiently, i.e., a voltage corresponding to an energy gap between HOMO and LUMO of organic semiconductor materials, and a hysteresis behaviour induced in the FET characteristics due to trapping of carriers injected from the source electrode, the organic materials of the OFET display dielectric characteristics, and hence should be also investigated from the standpoint of dielectric physics.

Owing to the complex nature of the multicarrier transportation and accumulation within organic devices, detection and visualisation of carrier motion within OFET devices is challenging. In addition to being influenced by the chemical structure of the active layer, the carrier behaviour is strongly affected by the processing conditions, device architecture, choice of electrode, and significantly, by the choice of an appropriate gate dielectric material [438]. Recently, a time-resolved optical second harmonic generation (TR-SHG) has been demonstrated as an effective method for elucidation of carrier dynamics within OFET devices, including those based on pentacene. In this paper, in order to focus on the mechanism of carrier injection followed by accumulation at the interface between gate insulator and active layer of OFET devices, electron and hole transportation in a double-layer MIM device is investigated using the optical second harmonic generation approach. That is, in order to effectively resolve single carrier behaviour at the interface, particularly charge trapping and accumulation, a double-layer MIM with blocking layer (polyterpenol) is employed. Synthesised from non-synthetic terpinen-4-ol precursor using RF plasma polymerisation, polyterpenol thin films are smooth and defect free, with high spatial uniformity, good adhesion to substrates, and tunable chemical and physical properties. When used as a gate insulator, polyterpenol has been demonstrated to enhanced pentacene OFET effective mobility and improve the switching characteristics of the device [337]. As a transparent and stable coating with sound dielectric properties, polyterpenol is a suitable to be used as a blocking layer for the optical second harmonic generation measurement. It should be further noted that polyterpenol is an organic material fabricated from non-synthetic renewable sources using an environmentally responsible technique, RF plasma polymerisation, making these materials suitable for the advancements of contemporary electronics, while meeting the demands of the environmentally sustainable human life.

VII.2.2 Experimental

VII.2.2.1 Sample preparation

Samples used in this study are double layer MIM devices of indium zinc oxide (IZO)/polyterpenol/pentacene/Au, as depicted in Figure VII.2.1. A thin layer of polyterpenol is deposited onto the IZO surface using RF plasma polymerisation following the experimental procedure outlined elsewhere [336,337]. Briefly, samples are placed into a custom-built glass deposition reactor, which is then evacuated to 50 mTorr. RF energy (13.56 MHz) is delivered using two capacitively coupled copper electrodes. Terpinen-4-ol (Australian Botanical Products) vapours are released into the reactor at a constant rate. The deposition is performed at 15 W and a pressure of 100 mTorr. Subsequently, pentacene (Tokyo Kasei Kogyo Co., Japan) as-received without further purification is deposited onto the polyterpenol thin film using vacuum evaporation technique, under a pressure of 10^{-5} Torr and a deposition rate of approximately 1 nm/min, monitored using a quartz crystal microbalance. Gold or aluminium electrodes are then deposited onto the surface of the active layer using the aforementioned evaporation technique. Gold electrodes allow for the smooth hole carrier injection into organic materials, such as pentacene. All layers are approximately 100 nm in thickness as determined by spectroscopic ellipsometry (model M-2000D, J.A. Woollam Co. Inc.).

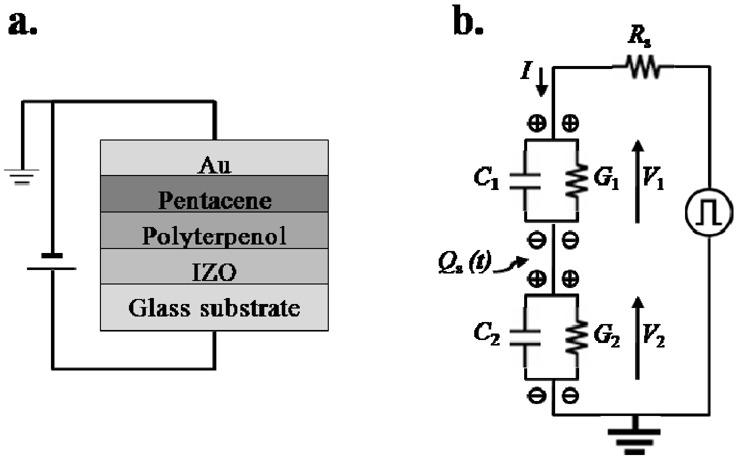

Figure VII.2.1. A schematic cross-sectional view of the double layer MIM device with polyterpenol as a blocking layer (a); and an equivalent circuit of the double layer MIM device (b).

Since carrier injection from electrode dominates the performance of OFET, and operation voltage of OFET is relatively high, the organic layers within the device can be treated as insulating materials [454]. Assuming that carrier accumulation at the pentacene-gate insulator interface is due to the Maxwell–Wagner effect, the OFET device is analysed as a system of Maxwell-Wagner elements, with the equivalent circuit presented in Figure VII.2.1b. Each organic layer is described as a parallel capacitance C_i and conductance G_i where i=1 and 2 represent blocking (polyterpenol) and active (pentacene) layers, respectively, and the resistance of the external measurement circuit is represented by $R_s = 180\ \Omega$. Upon application of external voltage (V_{ex}) to the double layer device, charges $\pm Q_m$ are induced on the electrodes with a response time $\tau_{RC} = R_s\ C^*$, where C^* is the total series capacitance of the OFET, $C^* = C_1C_2/(C_1+C_2)$. At time $t >> \tau_{RC}$, charge carriers are injected into the device and transported along the direction of the electric field. In accordance with Maxwell-Wagner effect, the accumulation of charge Q_s at the boundary between two adjacent dielectric layers 1 and 2 will take place when the respective relaxation times between the layers differ, that is $\tau_1 \neq \tau_2$. Charging Q_s at the active layer-blocking layer within the device takes a relaxation time $\tau_{MW} = (C_1+C_2)/(G_1+G_2)$, with τ_{MW}

>> τ_{RC}. Given that both organic layers are assumed to behave as dielectrics characterised by set C_i and G_i parameters, τ_{MW} and τ_{RC} are voltage independent constants. Since changes in the electric field distribution as a result of the injected charge modulate the intensity of the SHG signal, the technique can be employed to selectively probe the carrier transport mechanism and carrier behaviour within an OFET device. On the other hand, upon removal of external voltage (V_{ex}) from the double layer device, charges $\pm Q_m$ induced on the electrodes discharge with a response time $\tau_{RC} = R_s C^*$, and then accumulated charge Q_s at the boundary discharges. The charging and discharging should be reversal each other if charge Q_s merely discharges in the way as suggested from the linear equivalent circuit of Figure VII.2.1b.

VII.2.2.2 EFISHG measurement

The experimental optical setup employed to visualise carrier motion in the OFET devices has been described previously in [455-459], and is used in this study as portrayed in Figure VII.2.2, in which the double-layer MIM device is presented. An optical parametric oscillator (OPO: Continuum Surelite OPO) pumped by the third-harmonic light of a Q-switched Nd-YAG laser (Continuum: Surelite II-10, spatial resolution less than 1 μm) is used as the light source for the measurement; repetition rate 10 Hz, pulse duration 4 ns, average power 1 mW. The incidence light is *p*-polarised by passing it through a neutral density (ND) filter, prism polarizer and SH-cut filter. The samples are irradiated by the probing light from the substrate side, at an incident angle of 45° along the film thickness direction. The effective spot size of the focused light is less than 1 mm, an area significantly smaller than that of the working device. Filtered using an optical band pass filter and a monochromator to eliminate the reflected probing light, the SHG signal is detected by a photomultiplier tube (Hamamatsu photonics).

In these experiments, the wavelength of the probing light is set to 860 nm, with the SH light intensity $I(2\omega)$ generated at 430 nm [460]. The choice of the wavelength is important in order to effectively observe the SHG signal from the active layer (in this work, pentacene). Polyterpenol is transparent to the chosen wavelength of the probing light and the excited second harmonic light, and the SHG enhancement from IZO is very small [455]. Polyterpenol is also assumed to be an ideal blocking layer with the carriers being injected into the pentacene layer from the Au electrode (see Figure VII.2.1a). All measurements are carried out in laboratory ambient environment. A square wave voltage (frequency 10 Hz, duty time 50 ms) is applied to the OFET device, as demonstrated in Figure VII.2.2, to investigate the changing and discharging processes under varied bias conditions.

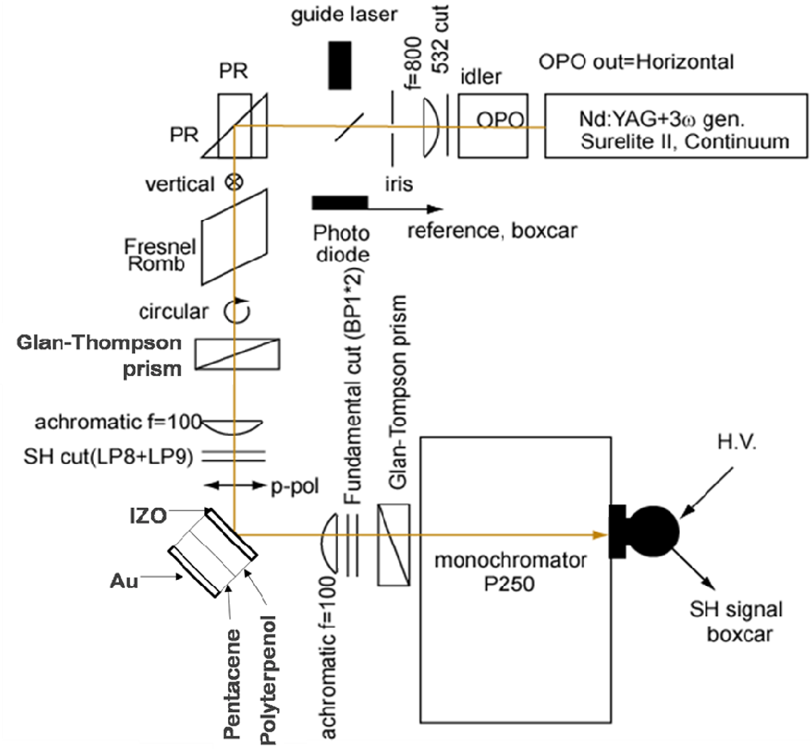

Figure VII.2.2. Experimental set-up for optical second harmonic generation measurement.

The electric field applied to the sample is on the order of 10^5 Vcm^{-1} (V_{ex} ~ 10 V) and is believed to be sufficient enough for carrier injection into the device. This field is also responsible for the generation of SH signal in pentacene. According to the SHG theory, within a noncentrosymmetric system, the enhancement of a SH signal is attributed to the quantum coupling of incident electromagnetic waves and electrons from the material. Since pentacene is a centrosymmetric material, the SHG enhancement is dipole-forbidden unless the electron distribution of the constituent molecules within the system is distorted, for instance by the application of a high external electric field and subsequent formation of a high space charge field [457]. The latter is attributed among other reasons to the displacement of excess charges within the system [459]. The generation of SH signals from centrosymmetric media including metals, semiconductors and organic materials, have been previously reported by numerous researchers [461-464]. The nature of SH generation in organic thin films of phthalocyanine [457,465], fullerene [466,467], and polydiacetylene [468] have been attributed to the electric quadrupole and magnetic dipole mechanisms, respectively. Considering the abundance of potential SHG sources, by choosing the appropriate wavelength of signals generated from centrosymmetric media, we can select electric-field induced second harmonic generation (EFISHG) signals that are useful for probing carrier motion as well as electric field distribution [469]. The EFISHG has a specific characteristic in that it is generated in proportion to the square of static electric field and this enables us to distinguish the EFISHG from other SHG sources. The intensity of the second harmonic light can be expressed as $I_{sh} \propto d^2 |P\ (2\omega)|^2$ where $P\ (2\omega) = \varepsilon_0\, \chi^{(2)} : E(\omega)E(\omega) + \varepsilon_0\, \chi^{(3)}\ \ E(0)E(\omega)E(\omega)$ and is the nonlinear polarisation wave, d the thickness of the layer being investigated, ε_0 the permittivity of vacuum, $E(0)$ the average electric field across the probed layer, $E(\omega)$ the electric field of the p-polarised light, and $\chi^{(n)}$ (n = 2, 3, …) the nth-order nonlinear susceptibility tensor, which is a material dependent parameter with ω. For pentacene, $\chi^{(2)} = 0$, and we may expect that the SH generation due to the second term contribution merely appears. In our EFISHG experiment, the square-root of SH intensity $(I_{sh})^{0.5}$ which can be defined as the square-root of the absolute difference between the SH intensity at zero and applied external voltage, is used for probing the electric field $E(0)$ formed in the pentacene layer in the direction of the layer thickness.

VII.2.3 Results and discussion

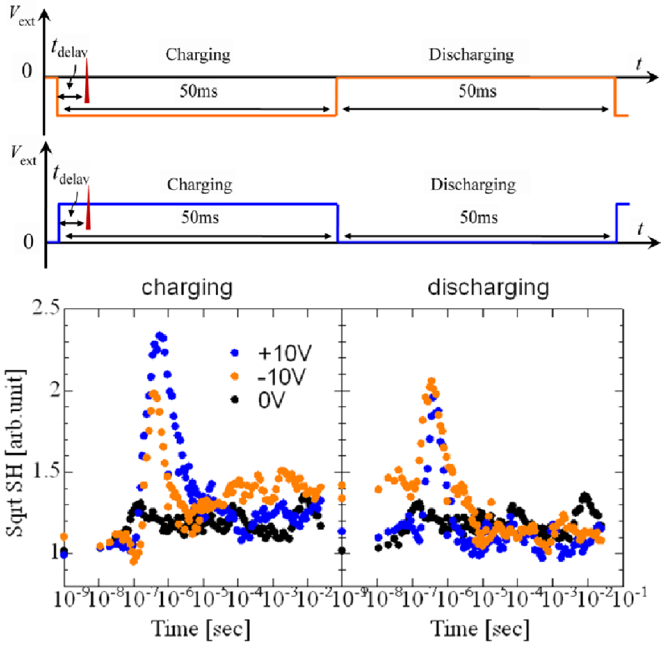

Figure VII.2.3. SH intensity for charging and discharging processes of IZO/polyterpenol/pentacene/Au device under forward bias (orange) and reverse bias (blue) conditions. Black line represents the baseline SH intensity at $V_{ex} = 0$.

The experimental results of time-resolved EFISHG of the double layer MIM device illustrating the charging and discharging mechanisms are demonstrated in Figure VII.2.3. The changes in the intensity of the SHG signal are interpreted in terms of the electric field distribution in pentacene layer under the presence of injected carriers [470]. Under forward bias conditions

(−10 V), holes are easily injected into pentacene layer from Au electrode, whereas electron injection from IZO is prohibited due to the presence of a polyterpenol blocking layer. Upon application of the external voltage, SH intensity increases from baseline level (at $V_{ex} = 0$) until it reaches its maximum value at around 10^{-7} s, the increase corresponding to charging of electrodes. The response time of the charging process agrees well with the calculated value for the equivalent circuit, $\tau_{\mathrm{RC}} = R_{\mathrm{s}} C^* \approx 4\times10^{-8}$ s. Smooth carrier injection follows, with holes being transported and accumulated at the pentacene/polyterpenol interface, as reflected by the rapid decrease in SH intensity commencing at ~ 5×10^{-6} s to its initial baseline level, which it reaches at approximately 10^{-5} s. Similar carrier injection behaviour has been reported for comparable pentacene-based device with polyimide blocking layer, where SH intensity was demonstrated to relax to the zero level at approximately 10^{-3} s under forward bias charging conditions [471]. According to the equivalent circuit model based on the Maxwell-Wagner effect, portrayed in Figure VII.2.1b, the plateau region representing the saturated potential should appear after reaching the SH intensity maximum when $\tau_{\mathrm{MW}} >> \tau_{\mathrm{RC}}$ [469]. However, merely a single sharp peak is observed in Figure VII.2.3, suggesting τ_{MW} is of the same order as τ_{RC} , but $\tau_{\mathrm{MW}} > \tau_{\mathrm{RC}}$, and carrier injection followed by charge accumulation at the interface proceeds almost simultaneously. In other words, the Poisson field formed by accumulated free carriers compensates the Laplace field from the $\pm\ Q_{\mathrm{m}}$ of the electrodes from the beginning of the charging process, i.e., upon applying the external voltage V_{ex} [454]. On the other hand, when device is short-circuited, the charges $+Q_{\mathrm{m}}$ and $-Q_{\mathrm{m}}$ induced on the electrodes are discharged through the external circuit with the relaxation time τ_{RC} of approximately 10^{-7} s, whereas positive charges accumulated at the interface remain. However, shortly the discharging commences at ~ 5×10^{-6} s, and as such the accumulated holes and the associated electric field decay, with SH intensity relaxing to its baseline value at approximately 10^{-5} s. Since the holes are believed to drift back to the Au electrode, the processes of interfacial charging and discharging of Q_s are reversal. In other words, the charging and discharging process proceed in a manner as predicted by the equivalent circuit of Figure VII.2.1b.

In the case of reverse bias conditions (+10 V), electrons are injected from Au electrode and hole injection is prohibited. Even though electron injection from Au electrode is more difficult due to high barrier height compared to holes, it has been reported for OFETs containing organic thin films. In addition, ambipolar carrier injection has been recognized in many OFETs from the ambipolar field-effect transistor (FET) characteristics [452]. Similarly to the forward bias case, an application of external voltage is followed by charging of the electrodes characterised by a single peak in SH intensity at 10^{-7} s. However, the magnitude of the SH peak is higher and the peak itself is broader in the case of electron injection compared to hole injection, indicating that electron injection from Au electrode into pentacene is slower and less smooth compared to hole injection, which is expected [472]. The injection commences at approximately 10^{-6} s, with SH intensity reaching its zero level at 10^{-4} s. During the discharge phase of the experiment, first the charges on the electrodes disappear at 10^{-7} s, while the accumulated electrons stay at the interface. Then, instead of electrons drifting back to the Au electrode, it is believed that holes are injected into pentacene from the Au electrode at ~ 5×10^{-6} s, driven by the electric field induced by the accumulated interfacial charges. In addition to low hole injection barrier from Au electrode, the intrinsic better hole transport properties of pentacene is thought to favour the proposed process. In terms of SH signal intensity, the discharging under the reverse bias conditions is very similar to the forward bias charging with regard to the magnitude and the position of the SH peak, arguing in favour of hole injection.

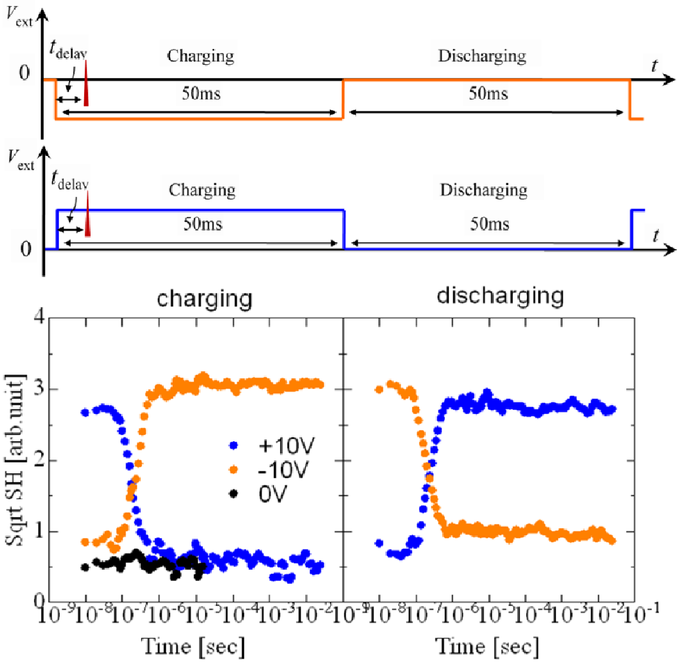

Figure VII.2.4. SH intensity for charging and discharging processes of IZO/polyterpenol/pentacene/Al device under forward bias (orange) and reverse bias (blue) conditions. Black line represents the baseline SH intensity at $V_{ex} = 0$.

The processes of interfacial charging and discharging of Q_s in the case of reverse bias conditions are clearly non-reversal. Non-reversal charging and discharging has also been reported for polyimide/pentacene double layer MIM structure, where the characteristic time at which the SH intensity returned to its ground level was longer at 10^{-2} s for charging compared to 10^{-3} for discharging under reverse bias conditions. Similarly, the forward bias charging and reverse bias discharging were reported to be very similar, with the latter being attributed to hole injection as a means of interfacial discharging. However, these discussions were merely assumptions, and a possibility remained that the SH behaviour was of reversal charging and discharging with electrons, in a manner similar to that observed under forward biasing condition (-10V).

In order to conclusively determine whether hole injection from Au dominated over electrons drifting back into Au electrode during the interface discharging, the Au was substituted with Al electrode material. The device was then investigated using time-resolved EFISHG technique under aforementioned experimental conditions, and the results are presented in Figure VII.2.4. There are notable differences in the charge carrier injection barriers between Au and Al electrodes, which have electron work functions of 5.1 and 4.28 eV, respectively. Lower work function of Al allows for more efficient injection of electrons into pentacene, whereas an approximately 2.0 eV energy difference between the LUMO of pentacene and Fermi level of Au makes electron injection rather difficult. Conversely, considering that the energy gap of pentacene is 2.5 eV and its ionization potential is 2.6 eV, the injection barrier for holes is negligible in the case of Au and prohibitive in the case of Al. The latter is phenomenon is being utilised to determine whether electrons accumulated at the polyterpenol/pentacene interface drift back during interfacial discharging.

Upon application of negative voltage (forward biasing, –10V), electron injection into the device from IZO electrode is disallowed by polyterpenol blocking layer, and the injection of holes into pentacene is prohibited due to high hole injection barrier of Al. Hence, only charging of electrodes takes place in the device with a response time τ_{RC} (around 10^{-7} s). The SH behaviour comprehensively describes such an account, with SH increasing from the baseline level to reach its maximum intensity at around 10^{-7} s and remains unchanged thereafter. During discharging, the charges on the electrodes disappear with the same relaxation time τ_{RC}, characterised by concomitant reduction in SH intensity of the signal. The charging and discharging process are of course reversal each other.

When positive voltage (+10 V) is applied to the device, electrons are injected from Al electrode, and the injection of holes into the device is disallowed due to the presence of polyterpenol. Following charging of the electrodes, electrons are injected into the pentacene around 10^{-7} s and transported to the interface where they accumulate, consequently reducing the SH signal to its baseline value at approximately 10^{-6} s. The injection of electrons is believed to be followed by carrier trapping at the interface, similar to previously reported results for pentacene [472]. Indeed, the SH signal remains activated even after the external bias voltage is turned off, due to the captured electrons working as excess charges and forming a space charge field. As demonstrated in Figure VII.2.5, initial intensity of activated SH signal indicates the formation of Poisson field by trapped carriers and is approximately equal to the Laplace field at positive bias application [454].

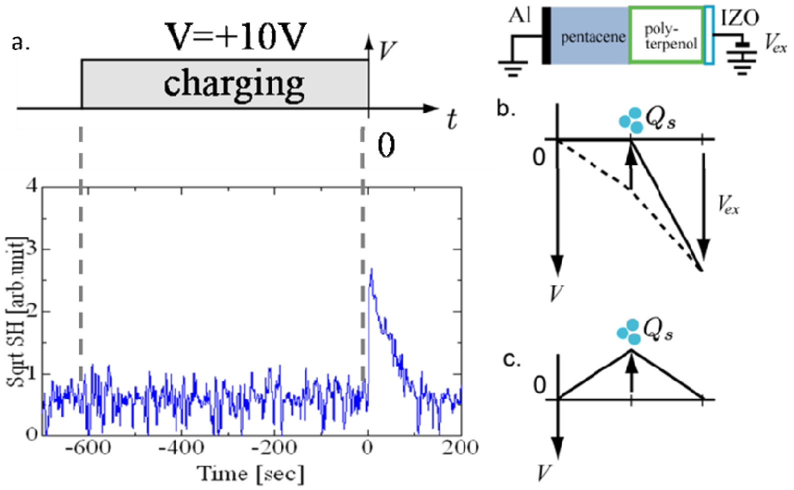

Figure VII.2.5. SH intensity (a) and the potential profile and injection conditions to pentacene for charging (b) and discharging (c) process. Dotted line represents a potential profile with the charges Q_m on the electrode and without the accumulated charges Q_s at the pentacene-polyterpenol interface.

Since the above described results indicated that the time required for interfacial discharging Q_s was considerably longer than the discharging time of 50 ms used in the experiment, additional experiments with extended charging/discharging time were conducted. Briefly, a d.c. voltage of +10 V was first applied to the IZO electrode for 10 min, time believed to be sufficiently long to fill electron traps. The external voltage was then removed (t = 0 s) and the device was short-circuited. Using EFISHG technique, the transients of the electric field in the pentacene layer were probed every 100 ms, with results presented in Figure VII.2.5a. In the region $t > 10^{-6}$ s, no EFISHG change was recorded within the limits of our experimental resolution of 10 ms, suggesting that electron injection and succeeding electron accumulation at the pentacene-polyterpenol interface proceeded rapidly, resulting in the cancelation of the electric field in the pentacene layer. As illustrated in Figure VII.2.5b, the electric field in the pentacene layer was nearly zero after charge Q_s was accumulated at the interface. As a result, the EFISHG intensity was very weak, approximating the baseline level. On the other hand, in the region $t > 0$, after short-circuiting the device, the EFISHG intensity immediately increased, owing to the space charge field from the remaining charge Q_s. The EFISHG intensity decayed with a relaxation time of 50 s, suggesting that the release of captured electrons from traps was slow. These results support the generation of SHG in the region t <0 in Figure VII.2.4, before a positive voltage +10 V was applied.

These findings confirm that in the case of reverse biased IZO/polyterpenol/pentacene/Au device, the single SH peak observed during the discharge phase of the experiment at approximately 10^{-7} s (Figure VII.2.3) cannot be due to the accumulated electrons drifting from the interface towards the Au electrode, but rather due to holes being injected into pentacene layer from the Au electrode. Figure VII.2.6 illustrates the proposed carrier motion during charging and discharging of the IZO/polyterpenol/pentacene/Au device.

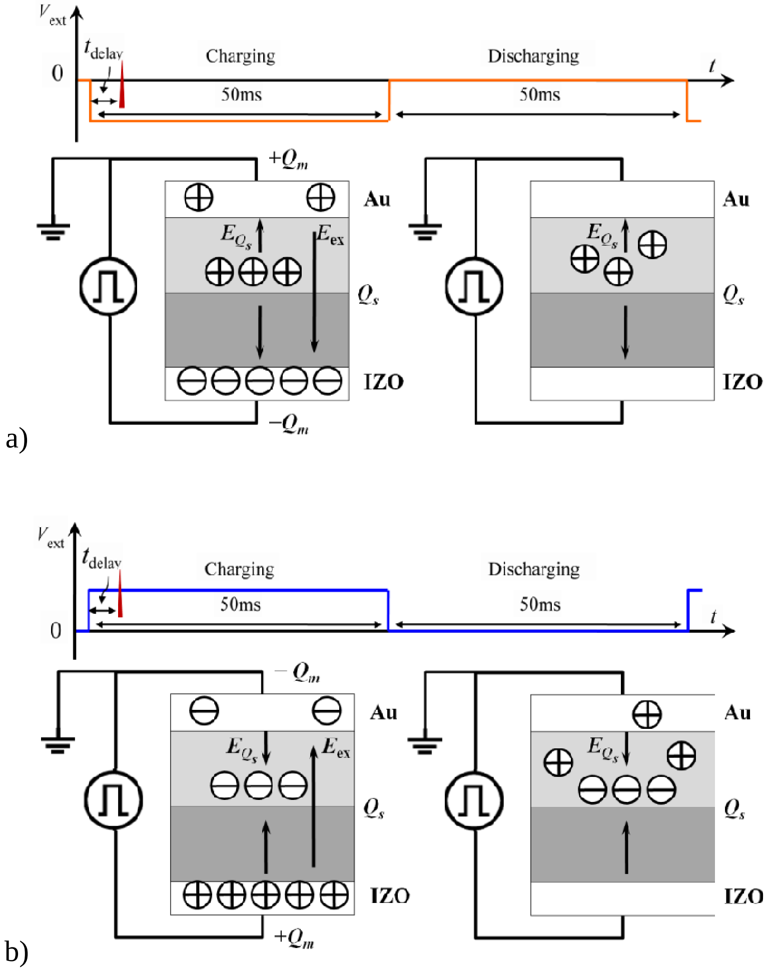

Figure VII.2.6. Carrier motion in IZO/polyterpenol/pentacene/Au devices under forward (a) and reverse (b) bias conditions during charging and discharging.

VII.2.4 Conclusions

EFISHG technique was used to probe the carrier transients within double-layer pentacene-based MIM devices during charging and discharging under different bias conditions. Given that pentacene is an ambipolar organic semiconductor, polyterpenol thin films fabricated from non-synthetic environmentally sustainable source, were used as a blocking layer to assist in visualisation of single-species carrier transportation. Time-resolved EFISHG demonstrated injection and accumulation at the interface of both holes and electrons under forward and reverse bias conditions, respectively. However, the nature of SH activity during the discharging differed between the two cases. Where holes were the injected carriers, the discharging of the interface involved the accumulated carriers drifting back into the Au electrode. However, when the accumulated charges were electrons, the discharging entailed an injection of holes from the Au electrode. Polyterpenol was demonstrated to be a sound blocking material and can therefore be used for probing of double-layer devices using EFISHG.

VII.3 EFFECT OF POLYTERPENOL MATERIAL PROPERTIES ON INTERFACIAL CHARGING AND DISCHARGING OF PENTACENE MIM DEVICE

Abstract

The effect of material properties of an environmentally friendly, optically transparent dielectric material, polyterpenol, on the carrier transients within the pentacene-based double-layer MIM device was investigated. Polyterpenol films were RF plasma polymerised under varied process conditions, with resultant films differing in surface chemistry and morphology. Independent of type of polyterpenol, time-resolved EFISHG study of IZO/polyterpenol/pentacene/Au structures showed similar transient behaviour with carriers injected into pentacene from Au electrode only, confirming polyterpenol to be a suitable blocking layer for visualisation of single-species carrier transportation during charging and discharging under different bias conditions. Polyterpenol fabricated under higher input power show better promise due to higher chemical and thermal stability, improved uniformity, and absence of defects.

Keywords: EFISHG; polyterpenol; polymer thin film; organic semiconductors

As published in: Bazaka, K., Jacob, M. V., Taguchi, D., Manaka, T., Iwamoto, M., Effect of organic gate dielectric material properties on interfacial charging and discharging of pentacene MIM device. *Physics Procedia* 2011, 14, 62-66.

VII.3.1 Introduction

Organic materials and organic semiconducting devices have attracted much attention from academia and industry for their potential as building blocks for inexpensive and structurally flexible electronic devices, including radio frequency identification tags, smart cards, light emitting diodes, and flexible displays. Organic field effect transistors (OFETs) are a particularly attractive alternative to conventional devices for applications that require large area coverage, light weight, and low-temperature processing. The performance of such a device is dependent on many factors, including the chemical structure of the active layer, processing conditions, device architecture, choice of electrode, and notably, the properties of gate dielectric material [438]. Furthermore, the composite nature of the carrier transportation and accumulation within organic devices renders detection and interpretation of carrier motion within OFET structures difficult. Time-resolved electric filed induced second harmonic generation (EFISHG) technique has been shown as a suitable method for elucidation of carrier dynamics within OFET devices [455]. Inclusion of a suitable transparent blocking layer into the structure of the device has been demonstrated to greatly assist in visualisation of single-carrier motion, particularly for those devices based on ambipolar semiconductors such as pentacene.

In our recently published work [353], we proposed using a newly synthesised environmentally friendly, organic insulating material, polyterpenol, as a blocking layer for probing of double-layer devices using EFISHG. Polyterpenol has been previously demonstrated to enhance the effective mobility and improve the switching characteristics of the pentacene based OFET device when used as a gate modification layer [337]. For polyterpenol, input power during fabrication has been demonstrated to be particularly significant as it influences the degree of fragmentation of the original monomer molecule, their recombination and film formation. Resultant thin films diverge chemically and structurally from the original monomer and each other, with implications for performance, degradation and stability of polyterpenol, as well as the manner in which these films interact with their ambient environment.

Surface properties of gate dielectrics (surface energy, roughness) are known to have a considerable effect on the active layer morphology. As an example, Lee and Wang recently reported on a discrepancy in the crystallinity and microstructure of pentacene and electrical properties of OTFT device incorporating gate dielectric layer with different surface characteristics [473]. Furthermore, since charges in OFETs are transported mainly within a very thin layer adjacent to the gate insulator, the field effect mobility does not only depend on the purity and order of the organic layer but also on the quality and nature of the insulator/semiconductor interface. For instance, SiO_2 commonly used as a gate insulator owing to its excellent insulating properties and sound thermodynamic stability exhibits a high density of hydroxyl groups at its surface. These groups give rise to a high surface free energy with a tendency for the material to form strongly adhering layers of adsorbed contaminants at its surface. Consequently, in this study, we seek to optimise the properties of polyterpenol to best fit its proposed application as a transparent insulating layer.

VII.3.2 Experimental

For material characterisation, polyterpenol was RF plasma polymerised onto glass, Si and KBr substrates under 15 W or 100 W RF power, the detailed experimental procedure is available elsewhere [336,337]. Briefly, wet cleaned substrates were placed into a custom-built glass deposition reactor, which was then evacuated to 50 mTorr, at which point terpinen-4-ol (Australian Botanical Products Pty Ltd, Australia) monomer vapours were gradually released into the reactor. RF energy (13.56 MHz) of 15 W or 100 W delivered using two capacitively coupled copper electrodes was used to initiate the plasma glow. Resultant films were characterised using AFM (NT-MDT), variable angle spectroscopic ellipsometer (model M-2000, J. A. Woollam Co., Inc.), Nicolet Maxim FT-IR Spectrometer, KSV 101 contact angle system, Axis Ultra spectrometer (Kratos Analytical Ltd., UK).

Device preparation involved RF plasma polymerisation of 100 nm polyterpenol thin film onto the IZO surface, followed by vacuum evaporation of 100 nm pentacene (Tokyo Kasei Kogyo Co., Japan) layer under a pressure of 10^{-5} Torr and a deposition rate of approximately 1 nm/min. Finally, Au electrodes were evaporated onto the surface of the active layer to allow for the smooth hole carrier injection into pentacene. The detailed account of the experimental EFISHG setup used to visualise carrier motion in the OFET devices can be found in [455-457]. For these experiments, the wavelength of the probing light was set to 860 nm, with the SH light intensity $I(2\omega)$ generated at 430 nm [460].

VII.3.3 Results and discussion

Elemental analysis of polyterpenol indicated that the material was composed primarily of carbon, hydrogen and oxygen. Higher deposition power conditions increased monomer dissociation and film cross-linking, yielding more hydro-carbon rich coatings with less oxygen containing moieties, as shown in Table VII.3.1.

Table VII.3.1. Elemental composition of polyterpenol thin films deposited at 15 and 100 W RF power.

Peaks	15 W		100 W	
	Binding energy, eV	Atomic fraction, %	Binding energy, eV	Atomic fraction, %
O 1s	533	23.1	533	12.2
N 1s	400	0.9	400	0.6
C 1s	286	76.0	286	87.2

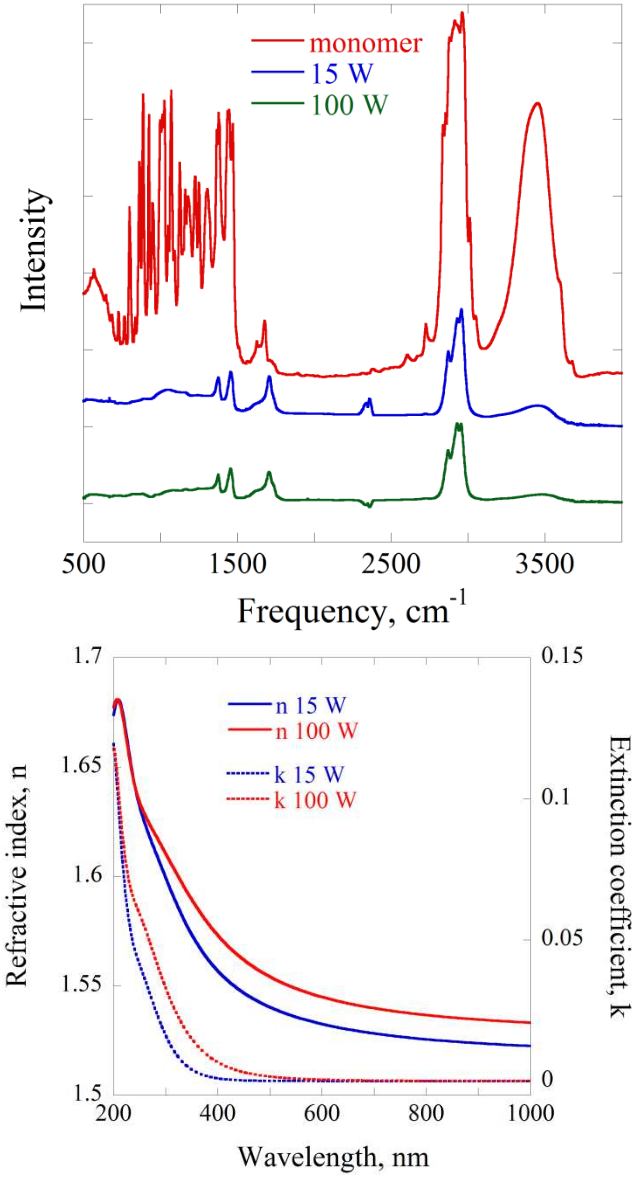

Figure VII.3.1. Chemical composition and optical properties of polyterpenol thin films.

FTIR spectra of the monomer and polymer films indicate that during polymerisation, bonds C(6)–OH and C(6)–C(7) of terpinen-4-ol molecule dissociate to form fragments, and the C(3)=C(4) double bond may become saturated to produce C(3)–C(4). As such, absorption frequencies associated with C=C–H unsaturation (between 3150 and 3000 cm^{-1}) seen on the monomer spectrum completely disappeared from the spectra for polyterpenol (Figure VII.3.1). On the other hand, a band indicative of a carbonyl group (C=O stretch at 1707 $cm\text{-}^{1}$) appeared as a result of polymerisation process. Bands at 1150 and 1050 cm-1 indicate C–O stretching of alkyl-substituted ether. Bands corresponding to methyl C-H asymmetric and symmetric stretching (~ 2955, 2930, and 2875 cm^{-1}) and bending (~ 1459 and 1380 cm^{-1}) decreased in magnitude with higher deposition power, as did the band associated with H-bonded O–H stretch.

Presence of high amount of C=C, C=O and –OH groups influences the dielectric constant of a material due to high polarizability of these moieties. Polyterpenol films deposited at lower RF power and hence containing higher portion of unsaturation and oxygen containing groups were characterised by notably higher dielectric constant compared to those fabricated at 100 W. Impedance spectroscopy was used to estimate the dielectric permittivity and breakdown strength of polyterpenol fabricated at 15 W and 100 W. Static relative permittivity ε_r for these materials was calculated from capacitance C value. At low frequency $f<10^5$, C value was constant. Calculated dielectric permittivity (V_{ac}=50 mV, f=1 kHz) decreased significantly as a function of deposition input power, from approximately 4.2 to 2.8 for 15 W and 100 W films, respectively. These results indicated that as an OFET gate insulator, 15 W polyterpenol may be more attractive in terms of low operations voltage and large breakdown strength. However, films fabricated at 100 W are characterised by higher stability, uniformity and absence of pin-holes.

Films produced under high input power conditions are more chemically and physically stable compared to those manufactured at 15 W, since the latter contains more of C–H and O–H bonds which are polar due to oxygen being more electronegative than C or H. Under ambient storage conditions, 15 W polyterpenol was reported to age via oxygen uptake via alkyl radical termination, whereas films fabricated at 100 W underwent molecular relaxation and gradual increase in density during an extended ageing process [347]. Thermal decomposition behaviour has also been shown to differ between the two materials, with films fabricated at lower RF power reported to commence loss of thickness via desorption of low molecular weight species at approximately 100 °C. Films fabricated at 100 W began to thermally decompose at significantly higher temperature of 205 °C, the shift in onset degradation temperature attributed to increased degree of cross-linking pertinent to these polymers. In addition, lower dissociation energy of hydroxyl and carboxyl groups abundant in 15 W films result in new reaction pathways being generated as the lone electron pairs undergo acid/base interactions.

All polyterpenol films were found to be optically transparent, pinhole free and smooth independent of deposition power. The average roughness decreased as a function of deposition power, from 0.4 nm to 0.2 nm for 15 W and 100 W coatings, respectively (Table VII.3.2). Polyterpenol films fabricated at lower RF input energy were characterised as more hydrophilic compared to those deposited at 100 W. Total surface free energy was also higher for the 15 W films, which was attributed to higher quantity of oxygen-containing moieties present at the surface of these films. Although both films were monopolar, manifesting mostly electron donor properties ($\gamma^+ << \gamma^-$), the electron donor fraction of surface energy decreased with fabrication power. Molecules of strongly monopolar material tend to repel each other when immersed in polar liquids. This allows the liquid to penetrate into the monopolar substance, resulting in pronounced solubility or dispersibility. Calculated from surface energy data, solvophobicity of polyterpenol material was demonstrated to increase with applied RF fabrication power for water, hexane, chloroform, ethanol, and acetone. Adhesion testing performed using nanoscratch test indicated significantly improved adhesion of 100 W polyterpenol to such substrates as glass, polystyrene, and polyethylene terephthalate.

Table VII.3.2. Physico-chemical surface attributes of polyterpenol films fabricated at different RF power.

	Contact angle, °			Surface free energy (mJ/m^2)				Roughness parameters, nm				
	θ_w	θ_E	θ_D	γ^{LW}	γ^+	γ^-	γ_{TOT}	R_{max}	R_a	R_q	R_{sk}	R_{kur}
15W	64	60	38	40.5	0.75	30.2	50	4.5	0.4	0.6	0.07	0.13
100W	76	59	38	40.7	0.16	11.7	43.4	2.93	0.3	0.4	0.05	0.2

Transient EFISHG behaviour was similar in devices using two types of blocking layer, as shown in Figure VII.3.2. The carrier behaviour within device containing 15 W polyterpenol was also consistent to previously reported observations [353]. Under forward bias conditions, charging of electrodes was followed by holes being injected from Au electrode into pentacene, whereas electron injection from IZO was prohibited owing to the presence of polyterpenol blocking layer. The EFISHG results revealed smooth and fast injection and almost simultaneous accumulation of holes at the pentacene-polyterpenol interface during charging, as indicated by the absence of considerable SH peak compared to SH base level (obtained at $V_{ex} = 0$). Once the external voltage was removed, the discharging of electrodes (at ~ 10^{-7} s) was followed by accumulated carriers drifting back into the Au electrode. The process was illustrated by SHG signal returning to its base line at approximately 10^{-5} s. Although there were no significant differences in charging/discharging between devices containing two types of polyterpenol, other material properties of the materials indicate 100 W films may be better due to their smooth uniform surfaces, absence of pinholes, improved adhesion to substrate and overall better thermal, physical and chemical stability.

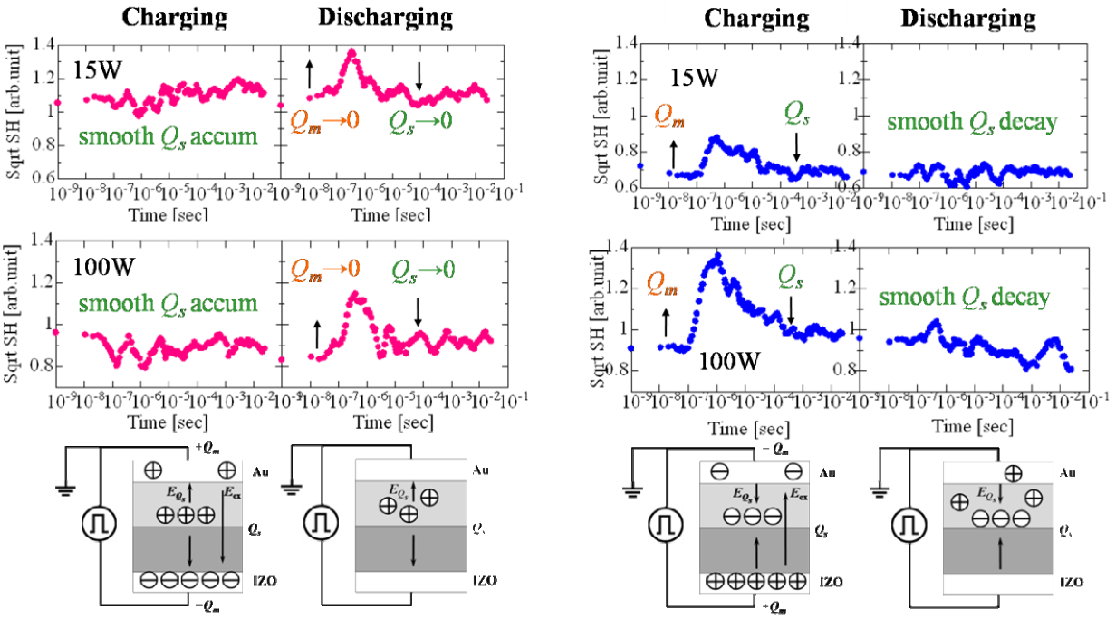

Figure VII.3.2. Transient behaviour of charge carriers in pentacene based device containing two types of polyterpenol blocking layer.

VII.3.4 Conclusion

Polyterpenol was demonstrated to be a sound blocking material and can therefore be used for probing of double-layer devices using EFISHG, with polyterpenol fabricated at higher RF power being a better suited material due to higher stability, particularly during pentacene deposition, improved uniformity, and absence of defects.

VII.4 ELECTRON-BLOCKING HOLE-TRANSPORT PROPERTY OF POLYTERPENOL THIN FILMS

Abstract

A carrier blocking property of polyterpenol thin films derived from non−synthetic precursor is studied using Electric Field Induced Optical Second Harmonic Generation technique that can directly probe carrier motion in organic materials. A properly biased double−layer MIM device with a structure of indium zinc oxide (IZO)/polyterpenol/C_{60}/Al shows that by incorporating the polyterpenol thin film, the electron transport can be blocked while the hole transport is allowed. The inherent electron blocking hole transport property is verified using Al/C60/Alq3/polyterpenol/IZO and Al/Alq3/polyterpenol/IZO structures. The rectifying property of polyterpenol is very promising and can be utilized in the fabrication of many organic devices.

Keywords: EFISHG; polyterpenol; polymer thin film; organic semiconductors

As submitted to: Jacob, M. V., Bazaka, K., Taguchi, D., Manaka, T., Iwamoto, M., Electron−blocking hole−transport polyterpenol thin films. *Chemical Physics Letters* (in review).

VII.4.1 Introduction

Recent progress in the area of organic electronic circuits, especially displays, demand new and improved materials for increasing the device efficiency. In electronics, the flexibility, light weight, and efficient integration of the organic materials-based electronic devices offer unique attractions [8]. Organic electronics present exciting possibilities for the realization of large-area self-illuminating displays based on organic light emitting diodes (OLED) and organic field effect transistors (OFET), low−cost organic solar cells and photovoltaic devices, sensors, and plastic electronics [16,474]. In OLEDs, holes and electrons are injected from opposite electrodes into an active molecular/macromolecular medium to produce, via exciton decay, light emission [475]. The efficiency of the OLEDs will be determined by the different layers used in the device; these include hole transport (HTL), emissive (EML), and electron-transport (ETL) layers. The HTL plays a significant role in the device performance by maximizing hole injection from the anode while blocking the efficiency-depleting electron overflow from the EML. A number of HTLs such as poly(3,4-ethylenedioxythiophene)-poly(styrenesulfonate) (PEDOTPSS) [476], polyaniline-camphorsulfonic acid (PANI-CSA) [477], and polypyrrole-dodecylbenzene sulfonic acid (Ppy-BDSA) [478] have been reported in the literature. The major detriments of many HTLs are only the annealing or ultraviolet photochemical processing requirement but also factors such as low durability and volume shrinkage, or microcracking resulting in leakage current.

Majority of the currently utilized HTL organic precursors pose an environmental hazard, an impediment, which can be overcome using non-synthetic environmentally-conscious alternatives. Polyterpenol is a polymer thin film of tepinen-4-ol, a monoterpene component of the essential oils of several plants, with demonstrated good electrical insulating performance. The developed material is characterized by transparency and stability over the environmental variations. Polyterpenol is used as an interfacial layer in the fabrication of a p-type OFET, substantially improving the mobility of the device [337]. The electrical insulating property of polyterpenol in terms of carrier blocking within double-layer MIM devices was further elucidated through time-resolved visualization of carrier motions using the electric field induced optical second harmonic generation (EFISHG) technique.

VII.4.2 Experimental

The fabrication of IZO/polyterpenol/C_{60}/Al double-layer diodes followed the previously outlined methodology [336,337]. A thin layer of polyterpenol was deposited onto the IZO surface using RF plasma polymerization at a pressure of 100 mTorr, RF frequency of 13.56

MHz, and 100 W RF power. Terpinen-4-ol (Australian Botanical Products) vapors were released into the reactor at a constant rate. The achieved film thickness was 100 nm. Then, a layer of C_{60} followed by Al electrode were deposited onto the polyterpenol thin film using vacuum evaporation technique, under a pressure of 10^{-5} Torr and a deposition rate of approximately 1 nm/min.

VII.4.3 Results and discussion

The I-V characteristics of the IZO/polyterpenol/C_{60}/Al diode were then collected, with Al acting as the reference electrode. As shown in Figure VII.4.1, the characteristics were comparable to those of a rectifying diode structure, and no hysteresis was observed. The magnitude of the current was similar to the pentacene-polyterpenol structure, which substantiated our previous findings regarding the insulating behavior of polyterpenol thin films. The results suggested that electron injection from Al electrode as well as hole injection from IZO electrode were probable, but electron injection from the IZO electrode and hole injection from the Al electrode were minor. Electron injection and transport through C_{60} and hole injection from IZO and transport through polyterpenol was therefore proposed as the mechanism behind the observed phenomenon. However, additional measurements on the structure had to be performed in order to eliminate other potential scenarios, such as electron injection from Al and successive transport through C_{60} and polyterpenol, or hole injection from IZO and successive transport through polyterpenol and C_{60} layers.

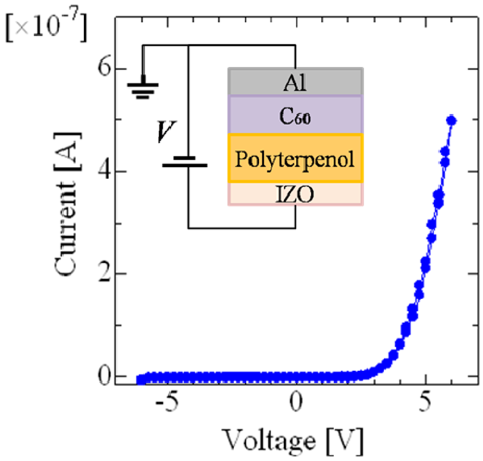

Figure VII.4.1. The I-V characteristics of the polyterpenol−C_{60} double layer device. Inset: The structure of the device.

Time-resolved EFISHG can directly probe the carrier motion within the double-layer diodes, providing direct experimental evidence necessary to verify the carrier behaviour within such a device. The experimental setup used in this study can be found elsewhere [455-459]. In the experiment, external voltage (V_{ex}) is applied to the double layer with capacitance C_i and conductance G_i and charges $\pm Q_m$ are induced on the electrodes with a response time $\tau_{RC} = R_s C^*$, where C^* is the total series capacitance of the diode. At time $t >> \tau_{RC}$, charge carriers are injected into the device and transported along the direction of the electric field. Should the respective relaxation times between the blocking and the active layers differ, $\tau_1 \neq \tau_2$, a charge Q_s is accumulated at the boundary between these layers with a relaxation time $\tau_{MW} = (C_1+C_2)/(G_1+G_2)$, $\tau_{MW} >> \tau_{RC,}$ due to the Maxwell-Wagner (MW) effect. The electric field distribution is directly correlated to the SHG signal changes [454,469].

The EFISHG is distinct in that it is generated in proportion to the square of static electric field, a characteristic that sets it apart from other SHG sources. The expression $I_{sh} \propto d^2 |P(2\omega)|^2$ can be used to describe the intensity of the second harmonic signal, with the nonlinear polarization wave $P(2\omega) = \varepsilon_0 \chi^{(2)} : E(\omega)E(\omega) + \varepsilon_0 \chi^{(3)}:E(0)E(\omega)E(\omega)$, the thickness of the centrosymmetric layer d, the permittivity of vacuum ε_0, the average electric field across the probed layer $E(0)$, the electric field of the *p*-polarized light $E(\omega)$, and the n^{th}-order nonlinear susceptibility tensor $\chi^{(n)}$ ($n = 2, 3, \ldots$), which is a material dependent parameter with ω. For C_{60}, $\chi^{(2)} = 0$, with only the SH generation due to the second term contribution expected to appear. The square-root of SH intensity $(I_{sh})^{0.5}$ is used for probing the electric field $E(0)$ which is the square-root of the absolute difference between the SH intensity at the baseline level and under applied external voltage. For C_{60}, the wavelength of the probing light is set to 1000 nm, with the SH light intensity $I(2\omega)$ generated at 500 nm [460].

The experimental results of time-resolved EFISHG of the double layer MIM device illustrating the charging and discharging mechanisms are presented in Figure VII.4.2(a). During charging, a step voltage was applied to the device, and it was removed in the discharging process. Figure VII.4.2a illustrates 3 conditions, namely 0 V, 3 V and 5 V on IZO with reference to Al electrode. The changes in the intensity of the SH signal were interpreted in terms of the electric field distribution in C_{60} layer under the presence of injected charge carriers [470]. The base line response was obtained for $V_{ex} = 0$. For the forward bias conditions of 3 V or 5 V, electron injection into C_{60} layer from Al electrode to the polyterpenol layer and/or hole injection into polyterpenol from IZO was suggested [469]. The decaying process during charging satisfied relaxation time dependence of applied voltage $1/V^2$. This suggested recombination of electrons and holes at the interface was probable, with the amount of positive charge less than that of negative charge. The SH intensity increased from the baseline and a maximum SH intensity was obtained at 10^{-6} s, on replying electrode charging with a response timeτ_{RC}. Smooth carrier injection followed, with electrons being transported and accumulated at the C_{60}/polyterpenol interface. This was reflected by the rapid decrease in SH intensity to its initial baseline level, which it reached at approximately 10^{-3} s, corresponding to the MW relaxation timeτ_{MW}. In this case, the electric field was relaxed since charges $\pm Q_m$ accumulated on electrodes at $t_{RC} = 440$ ns and the charges Q_s accumulated at C_{60}/polyterpenol.

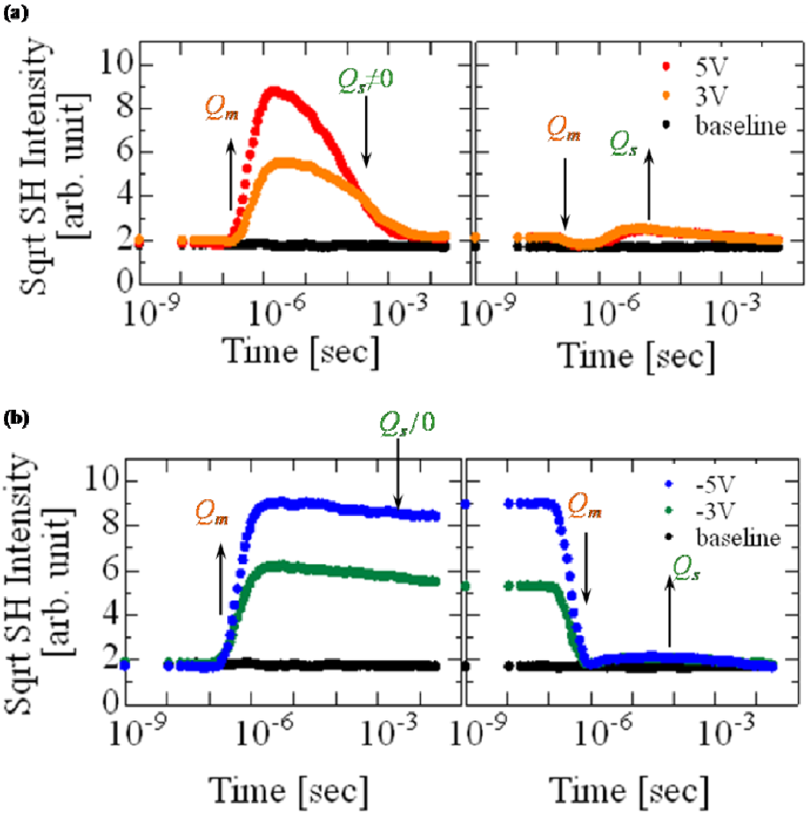

Figure VII.4.2. SH intensity for charging and discharging processes of IZO/polyterpenol/C_{60}/Al device under forward (a) and reverse (b) bias conditions, and the baseline for SH intensity at V_{ex} = 0.

In the case of reverse bias conditions, holes were candidates injected from Al electrode. As can be seen from Figure VII.4.2(b), the SH intensity for charging and discharging processes of the device under reverse bias conditions was a distinct feature in comparison with the forward bias. The charges $\pm Q_m$ accumulated on electrodes at t_{RC}=440 ns, but the Q_s accumulated at C_{60}/polyterpenol was very small. The SH peak was broader in the case of hole injection compared to electron injection, which was in agreement with our previous study [472]. The injection commenced at approximately 1µsec. During the discharge phase of the experiment, first the charges on the electrodes disappeared at 1µsec, while the accumulated electrons stayed at the interface. These results suggested that hole injection was blocked by the C_{60} layer, and electron injection was prohibited by the polyterpenol.

The inherent electron blocking hole transport property of the polyterpenol was further corroborated using Al/Alq3/polyterpenol/IZO and Al/C_{60}/Alq3/polyterpenol/IZO structures, schematics for which are presented in Figures VII.4.3(a) and VII.4.3(b). In the case of Al/Alq3/polyterpenol/IZO device, holes from IZO side were transported through the polyterpenol and recombined at the Alq3 layer with the electrons transmitted from the Al electrode. As a result of this recombination, electromagnetic radiation was emitted, as illustrated in Figure VII.4.3(c). Similar charge carrier behavior was observed for Al/C_{60}/Alq3/polyterpenol/IZO structure. This invention provides a new environmentally friendly electron blocking layer which can be used in between the active organic layers and anode.

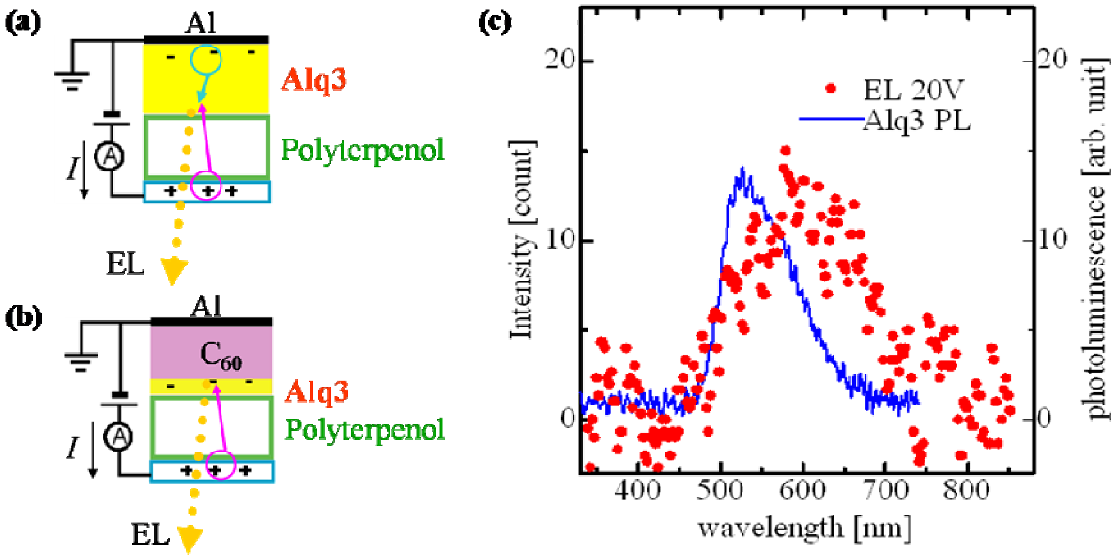

Figure VII.4.3. Experimental set-up and device structure (a) Al/C60/Alq3/polyterpenol/IZO, and (b) Al/Alq3/polyterpenol/IZO. (c) Observed electromagnetic radiation as a result of electron-hole recombination at Alq3 layer.

VII.4.4 Conclusion

In conclusion, the charge transport mechanism across plasma polymerized polyterpenol was studied by depositing C_{60} n-type organic semiconductor on the polyterpenol thin film and Al top electrodes. Using the EFISHG, charge accumulation under the steady state was demonstrated for electron injection from the Al/C_{60} ($V > 0$), whereas no charge accumulation was observed for hole injection (V < 0) from Al/C_{60}. Resulting from these observations, electron blocking property of polyterpenol was proposed as a likely mechanism. Results from electroluminescence spectrum measurement on the Al/C_{60}/Alq3/polyterpenol/IZO structure evidently confirmed the rectifying property of polyterpenol, with electron and hole recombination taking place in Alq3 and C_{60} layers, indicated by the EL wavelengths of the emitted light consistent with Alq3 and C_{60} photoluminescence spectra. This study substantiate that the environmentally friendly transparent polyterpenol thin film will be an excellent candidate to be used as a ‘hole transport electron blocking layer’ in organic electronic circuits and hence can be utilized in the fabrication of many organic devices, e.g., OLEDs.

CHAPTER VIII

POLYTERPENOL AS A BIOLOGICALLY ACTIVE ANTIFOULING COATING FOR MEDICALLY RELEVANT DEVICES

Chemical characterisation of polymer thin films fabricated under varied RF power conditions demonstrate that retention of monomer functionality can be achieved under low power conditions. A possibility of maintaining biological activity of liquid monomer within a solid polymer film is explored in this chapter.

In Section VIII.1, the performance of coatings deposited at higher and lower input powers in preventing adhesion and biofilm formation of pathogenic *Pseudomonas aeruginosa* are contrasted. The antifouling and antibacterial property of the material is investigated by means of scanning electron microscopy and confocal laser scanning microscopy, which allow for quantification of retained cells and the extracellular polymeric substances these bacteria produce. The findings are summarised in *Bazaka, K. et al., A study of retention of antimicrobial activity by plasma polymerized terpinen-4-ol thin films. Material Science Forum 2010, 654-656, 2261-2264* and expanded on in *Bazaka, K et al., Effect of plasma-enhanced chemical vapour deposition on the retention of antibacterial activity of terpinen-4-ol. Biomacromolecules 2010, 11, 2016-2026*. Subsequent studies involving different polyterpenol fabrication conditions and taxonomically distinct pathogenic bacteria were conducted to demonstrate the broad-spectrum activity of polyterpenol and optimise the coatings. Additional publications resulted but are not included into this thesis, namely *Bazaka, K. et al., Plasma polymerisation and retention of antibacterial properties of terpinen-4-ol, in: Mendez-Vilas, A. (Ed.), Science and technology against microbial pathogens. Research, development and evaluation. World Scientific Publishing Group 2011*, and *Bazaka, K. et al., Radio frequency plasma enhanced synthesis of antifouling polymeric coatings from monoterpene alcohols. IEEE TENCON Proceedings 2010, 1486-1491*.

In Section VIII.2, the respective contributions of surface chemistry and surface topography are identified. A combination of these two parameters determines hydrophobicity and the surface free energy of the material, which are important in controlling cell-surface interactions. The presence of specific chemical functionalities at the surface of the abiotic target may inhibit colonisation or provide sites for permanent attachment via covalent bonding. Similarly, surface features at different scales are known to affect the initial adherence and subsequent retention of bacterial cells. These finding are published as *Bazaka, K et al., The effect of polyterpenol thin film surfaces on bacterial viability and adhesion. Polymers 2011, 3, 388-404.*

VIII.1 SYNTHESIS OF BIOACTIVE COATINGS FROM MONOTERPENE ALCOHOLS: EXPERIMENTAL AND THEORETICAL STUDY

Abstract

This paper describes the synthesis and characterization of a novel organic polymer coating for the prevention of the growth of *Pseudomonas aeruginosa* on the solid surface of three-dimensional objects. Substrata were encapsulated with polyterpenol thin films prepared from terpinen-4-ol using radio frequency plasma enhanced chemical vapor deposition. Terpinen-4-ol is a constituent of tea-tree oil with known antibacterial properties. The influence of deposition power on the chemical structure, surface composition, and ultimately the antibacterial inhibitory activity of the resulting polyterpenol thin films was studied using X-ray photoelectron spectroscopy (XPS), water contact angle measurement, atomic force microscopy (AFM) and 3-D interactive visualization and statistical approximation of the topographic profiles. The experimental results were consistent with those predicted by molecular simulations. The extent of bacterial attachment and extracellular polymeric substances (EPS) production were analyzed using scanning electron microscopy (SEM) and confocal scanning laser microscopy (CSLM). Polyterpenol films deposited at lower power were particularly effective against P. aeruginosa due to the preservation of original terpinen-4-ol molecules in the film structure. The proposed antimicrobial and antifouling coating can be potentially integrated into medical and other clinically relevant devices to prevent bacterial growth and to minimize bacteria-associated adverse host responses.

Keywords: Bacterial adhesion; bacterial retention; plasma polymerization; *Pseudomonas aeruginosa*; thin films

As published in: Bazaka, K., Jacob, M. V., Truong, V. K., Wang, F., et al., Effect of plasma-enhanced chemical vapour deposition on the retention of antibacterial activity of terpinen-4-ol. *Biomacromolecules* 2010, 11, 2016-2026.

VIII.1.1 Introduction

The role of biologically active coatings in the etiology of surgical site infection has been the objective of discussion for decades, particularly in the case of indwelling medical devices [479-481]. The application of bioactive coatings is designed to prevent bacterial attachment and subsequent biofilm formation, the foremost cause of device related infections and device failure, while at the same time promoting host cell adhesion and tissue healing [161,162]. Biomaterial-associated infections can develop along several routes, with the most common route of introduction of the aetiological agents being direct contamination of the implant during surgery (peri-operative contamination) [115], or contamination during post-operative care [482]. Furthermore, microorganisms that originate from an infection site elsewhere in the body can spread through the blood causing late haematogenous infections of the implant, particularly in the case of medical devices directly exposed to the blood stream, such as artificial valves [117,118].

Passive coatings such as hydrophilic polyurethanes have been demonstrated to reduce the extent of bacterial attachment, however they are incapable of eradicating bacterial cells that can adhere to the surface [483,484]. Upon attachment, certain bacteria will secrete extracellular polymeric substances (EPS) and form a biofilm, an effective defence mechanism that protects bacteria from host immune response and systemic drugs [485]. Recently, active coatings capable of both preventing bacterial adhesion and eliminating the bacteria by means of releasing antibacterial agents have been receiving a great deal of attention [486-489]. Controlled-release coatings containing such antibiotics as vancomycin, amoxicillin and gentamicin have been shown to successfully inhibit bacterial growth [490,491]. However, with the rapidly diminishing effectiveness of many systemic antibiotics and antiseptics for the treatment and prevention of many common infections [492], alternative agents such as silver ions [493], nitric oxide [494], bioactive antibodies [495], and naturally occurring biocidal compounds are now being considered. Hence, there is a need to further develop an efficient coating that exhibits both a comprehensive biological activity together with long-lasting biocidal properties.

Some organic polymer materials have been shown to be effective alternative bioactive coatings [319]. The employment of plasma based polymerization techniques to synthesize high performance thin film materials has been investigated by many authors [85-88,90,320]. Polymer thin films fabricated by means of radio frequency plasma-enhanced chemical vapour deposition (RF-PECVD) have been shown to retain certain functionalities and a structure pertinent to the original monomer whilst gaining the structural advantages associated with the presence of the substratum [90,320]. Importantly, RF-PECVD allows smooth, pinhole free and uniform polymer thin films from organic composites to be produced that may not possess functionalities associated with conventional polymerization methods [96-98].

The antibacterial, antifungal and antiviral properties of *Melaleuca alternifolia* (tea tree oil, TTO) have been known to Indigenous Australians for centuries [386,496-499], yet commercial applications of essential oils are limited mainly to the formulation of food flavouring, fragrance/cosmetics, pharmaceuticals, and industrial solvents [386,500]. Terpinen-4-ol, a monocyclic terpene alcohol, is thought to be the major anti-bacterial constituent of tea tree oil [496,501-503]. Studies using liposome model systems have shown that cyclic terpene hydrocarbons accumulate in the cytoplasmic membrane of bacteria, causing a loss of membrane integrity which results in an increased passive flux of protons across the membrane and dissipation of the proton motive force [504]. Scanning electron microscopy of *S. aureus* cells treated with the terpinen-4-ol monomer have shown that the cell membrane is damaged by the action of the terpinen-4-ol, highlighted by the appearance of mesosomes and a loss of cytoplasmic material [505].

It is proposed that polymer thin films fabricated from tea tree oil and terpinen-4-ol monomers, using RF-PECVD under particular deposition conditions, may inherit the inhibitory and biocidal properties of their respective precursors, similar to plasma polymerized diethylene glycol dimethyl ether, which retained most of its original functional groups under low power deposition conditions [506]. This may make these films an appropriate protective coating for medical implants. Therefore, the primary goal of this study is to investigate whether the inhibitory properties of the terpinen-4-ol monomer are retained in the polyterpenol thin films deposited on the substrata, and to determine the deposition conditions under which these antibacterial characteristics may be retained. In order to do this, it is important to gain an understanding of the dissociation behaviour of the monomer, including the major elementary reactions and key radicals formed in the course of the polymerization process. The biochemical characteristics of the resulting polyterpenol film surfaces are assessed in terms of their chemical structure, film-solvent interactions, pattern of bacterial adhesion and inhibitory activity against selected human pathogenic bacteria, specifically *P. aeruginosa,* which may infect surgical wounds.

VIII.1.2 Experimental section

VIII.1.2.1 Polyterpenol thin film preparation

Polyterpenol thin films were deposited onto the substrata using the terpinen-4-ol monomer (Figure VIII.1.1) (Australian Botanical Products, Ltd) using RF-PECVD. The RF energy (13.56

MHz) was delivered into a custom-manufactured glass deposition chamber via two capacitively coupled copper electrodes (Supporting information, Figure VIII.1.1S: Schematic diagram of the plasma polymerization apparatus). Glass slides (BioLab Scientific, Ltd.) and KBr (International Crystal Laboratories) windows were employed as the substrata. The glass substrata were pre-washed in a 1:5 solution of Extran and distilled water. The substrata were then subjected to ultrasonic cleaning using distilled water heated to 50 °C for 30 min, then rinsed with propan-2-ol and air dried. The KBr substrata were not subjected to a wet cleaning procedure. To apply the film coatings, the substrata were placed into the deposition chamber, which was flushed with argon for 1 min to ensure that the substrata possessed an oxygen-free surface. The chamber was then evacuated to achieve a pressure of 50 mTorr. The terpinen-4-ol vapor was released gradually into the chamber and the glow was maintained by controlling the monomer flow [336]. Deposition was performed at room temperature and a pressure of 200 mTorr under 10 W and 25 W RF power for 10 min to achieve films of approximately the same thickness. Terpinen-4-ol monomer (1 mL) was used for each deposition cycle.

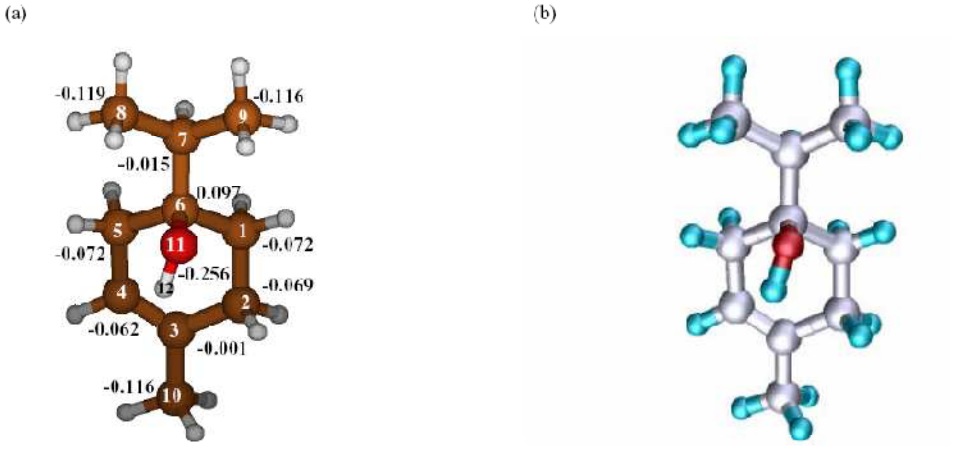

Figure VIII.1.1. Chemical structure of terpinen-4-ol molecule ($C_{10}H_{18}O$). Hirshfeld charges, which are based on the LB94/et-pVQZ//B3LYP/cc-pVTZ model, are marked on the non-hydrogen atoms. Molecular nomenclature is given in (a). Double click the structure in (b) on a computer or online will activate the embedded 3D-pdf.

VIII.1.2.2 Polyterpenol thin film surface characterization

FTIR. A single beam FTIR Spectrometer (Nicolet Maxim) was used to acquire the FTIR spectrum of the polyterpenol films. This spectrum for terpinen-4-ol was used as a reference, against which the degree of polymerization as a function of applied RF excitation signal was assessed. For each polyterpenol film sample, 32 scans were collected in transmission mode over the region of 4000 – 400 cm^{-1} at a resolution of approximately 2 cm^{-1}.

*Raman Scattering Spectroscopy***.** Raman spectra were collected with a WiTEC *alpha300R* Microscope in Raman mode using a 100× (Numerical Aperture 0.9) and 532 nm (E_{laser} = 2.33 eV) laser operating at constant power for each experiment up to ~ 60 mW. Raman data were collected by the WiTEC Control software and analysed in the WiTEC Project software with the surface perpendicular to the excitation source. Spectra were collected using an integration time of 1 s.

Contact Angle Measurements. Surface wetting studies were performed using a contact angle system (KSV 101) employing the sessile drop method [427,507,508]. The experimental procedure was verified by conducting water contact angle measurements on polytetrafluoroethylene (PTFE). Preceding each measurement, a CCD camera was employed to confirm the height of each water drop to ensure consistency in drop volume. Once the drop was placed on the surface of the sample by means of a one-touch dispenser system, KSV CAM software was automatically triggered to commence recording. Images were taken for 30 s at 1 s intervals and image processing software was employed to establish the contact angle by fitting the Young-Laplace equation to the measured drop profile. An average of ten measurements was obtained for each sample surface, using sterilized nanopure H_2O (18.2 M Ω cm^{-1}), diiodomethane (Sigma Aldrich) and ethylene glycol (Sigma Aldrich). The average contact angle for each liquid was used to calculate the surface free energy and its components, based on the Lewis acid/base method [427,507,508].

XPS Analysis. The elemental composition of the polyterpenol films was obtained using X-ray photoelectron spectroscopy (XPS). This was performed using an Axis Ultra spectrometer (Kratos Analytical Ltd., UK), equipped with a monochromatic X-ray source (Al Kα, hν = 1486.6 eV) operating at 150 W. The energy scale of the instrument was calibrated by measuring the Au $4f_{7/2}$ (E_b = 84.0 eV), Ag $3d_{5/2}$ (E_b = 368.3 eV), and Cu $2p_{3/2}$ (E_b = 932.7 eV) binding energies for pure metal foils. Samples were flooded with low-energy electrons during the analysis to counteract surface charging. The hydrocarbon component of the C 1s peak (binding energy 285.0 eV) was used as reference for charge correction. Photoelectrons emitted at 90° to the surface from an area of 700 × 300 μm^2 were analyzed with 160 eV survey spectra, 20 eV for region spectra. Survey spectra were recorded at 1 eV/step, region spectra at 0.1 eV/step. Peaks in the high-resolution regions of spectra were fitted with synthetic Gaussian-Lorentzian components after removal of a linear background (using the Kratos Vision II software).

Ellipsometry. The thickness and roughness of the polyterpenol films [336] were estimated from Ψ and Δ ellipsometric data collected for φ = 55º, 60º, and 65º angles of incidence over the 200 – 1000 nm wavelength range using a variable angle spectroscopic ellipsometer (model M-2000, J. A. Woollam Co., Inc.). Within the wavelength region of 500 - 1000 nm, the polyterpenol film was assumed to be optically transparent ($k \rightarrow 0$) and homogenous [327].

*AFM Analysis***.** The surfaces of the thin film samples were scanned using an atomic force microscope (AFM) (NT-MDT) in semi-contact (tapping) mode to observe the surface topography and to quantitatively estimate the extent of surface roughness. Semi-contact mode is commonly used for the characterization of soft materials such as polymer films and biological samples as the short intermittent contacts between the tip and the sample surface characteristics reduce the inelastic deformations to the surface of the sample compared to contact mode, where the high tip-to-surface forces can mechanically deform the surface under the investigation. The carbon "whisker" type silicon cantilevers (type NSC05, NT-MDT) with a spring constant of 11 N/m, tip radius of curvature of 10 nm, aspect ratio of 10:1 and resonance frequency of 150 KHz were used to obtain topographic resolution. Scanning was performed perpendicular to the axis of the cantilever at a rate of typically 1 Hz. The scan areas of 1 μm × 1 μm, 10 μm × 10 μm, and 100 μm × 100 μm were used to determine the extent to which changes in RF power affected the surface properties of the polymer film. Standard NT-MDT Image Analysis software was employed to process the raw topographical data and generate statistical values for surface roughness.

VIII.1.2.3 Computational details

The geometry of terpinen-4-ol was optimized using the B3LYP/cc-pVTZ model, incorporated in the GAMESS computational chemistry package [509], followed by harmonic vibrational frequency calculations using the Gaussian03 computational package (Figures VIII.1.1 and VIII.1.2, Table VIII.1.1, Supplementary Material Table VIII.1.S1) [510]. The optimized geometry is a true minimum configuration on the potential energy surface (PES), as any imaginary frequencies are found. An infrared (IR) spectrum and a Raman spectrum are simulated based on the optimized geometry using the same model, whereas the Hirshfeld charges [511], bond orders [512], and the XPS for O 1s and C 1s of the species are simulated using the LB94/et-pVQZ//B3LYP/cc-pVTZ model [513,514], which is incorporated in the Amsterdam Density Functional (ADF) computational chemistry package [515]. Orbital vertical ionization potentials (IPs) are produced using the "meta-Koopman's theorem" [516] without further modification and scaling. Detailed instructions on the generation of the interactive 3D-PDF structure given in Figure VIII.1.1 are provided in Selvam et al [517].

Table VIII.1.1. Bond orders of the monomer terpinen-4-ol produced using the LB94/Et-PVQZ model, indicating that the most likely break bond is the O(6) —C(6) bond, followed by C(5) — C(6).

bond	bond order	bond	bond order
O(6)—C(6)	0.4749	O(6)—H(12)	1.0802
C(6)—C(1)	0.8842		
C(1)—C(2)	0.9431	C(1)—H(13)	0.9791
		C(1)—H(14)	0.9075
C(2)—C(3)	1.1056	C(2)—H(15)	0.9126
		C(2)—H(16)	0.9479
C(3)—C(4)	1.9855		
C(4)—C(5)	0.9972	C(4)—H(20)	0.9139
C(5)—C(6)	0.8367	C(5)—H(21)	0.9074
		C(5)—H(22)	0.9375
C(6)—C(7)	0.9733		
C(7)—C(8)	0.8639	C(7)—H(26)	0.9312
C(7)—C(9)	0.8720		
		C(8)—H(23)	1.0336
		C(8)—H(24)	0.9711
		C(8)—H(25)	0.9747
		C(9)—H(27)	0.9739
		C(9)—H(28)	0.9693
		C(9)—H(29)	1.0272
C(3)—C(10)	0.8834	C(10)—H(17)	0.9656
		C(10)—H(18)	0.9596
		C(10)—H(19)	0.9810

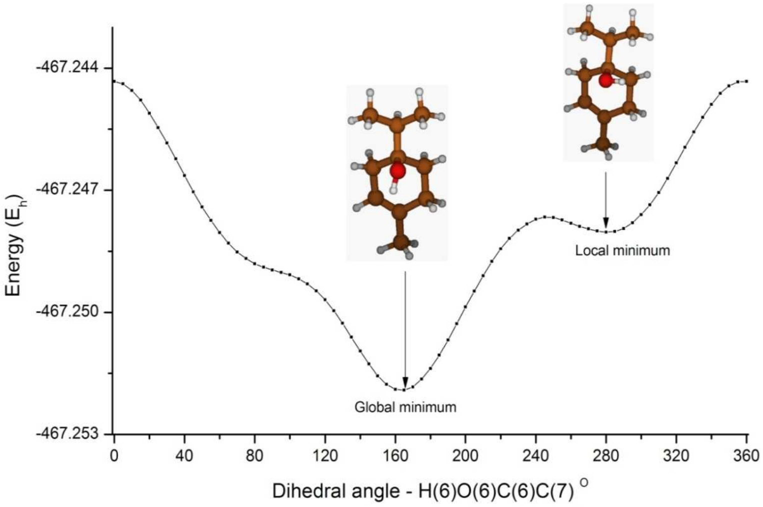

Figure VIII.1.2. Potential energy scan for terpinen-4-ol with respect to dihedral angle H(6)O(6)C(6)C(7). The calculation is based on B3LYP/cc-pVTZ model. Refer to Figure VIII.1.1 for atomic labels.

VIII.1.2.4 Bacterial strains, cultivation and sample preparation

P. aeruginosa ATCC 9025 used in this study was obtained from the American Type Culture Collection (ATCC, USA). Bacterial stock was stored at -80 °C in 20% glycerol nutrient broth (Oxoid) and was refreshed on nutrient agar (Oxoid) preceding each experiment.

In each experiment, a fresh bacterial suspension was prepared from bacterial cells gathered at the logarithmic stage of growth as described elsewhere [282]. To ensure consistency between bacterial suspensions used in the attachment study, the cell density of each batch was adjusted to OD_{600} = 0.3 with a haemocytometer employed to quantify the cell numbers in the suspensions according to the method described by Mather and Roberts [518].

An aliquot of 100 μL of bacterial suspension was deposited on the surface of each sample (in triplicate) of polyterpenol thin films. Unmodified glass substrata and sterile nutrient broth (100 μL) were also used as a negative control. After being subjected to 18 h incubation at temperature of 37 °C, the samples were gently rinsed with copious amounts of MilliQ water (18.2 M Ω cm^{-1}) to remove non-attached cells and left to dry at room temperature for 45 min at 55% humidity. Samples were handled under sterile conditions until just prior to imaging. The procedure allowed for the bacterial cells to remain in a semi-hydrated state, as confirmed by their morphological appearance, in order to maintain consistency between imaging experiments.

VIII.1.2.5 Visualization and quantification of viable cells and EPS

Simultaneous fluorescence staining was performed on the residual bacterial culture on the surface of the samples to monitor the level of production of extracellular substances and to enable the visualization of viable bacterial cells retained on the surfaces. Concanavalin Alexa Fluor 488 (Molecular Probes Inc.) dye was used as it selectively binds to α-mannopyranosyl and α-glucopyranosyl residues found in EPS and is commonly used in EPS visualization [519]. A mass of 5 mg of the dye was dissolved in 5 mL of 0.1 M sodium bicarbonate at pH 8.3 to produce the working dye solution. A ratio of 1 part of dye to 5 parts of suspension was used to stain the EPS. A 20 μL volume of the dye was added to the bacterial suspension, and incubated for 30 min to allow for the even distribution of the stain throughout the sample. After the 30 min incubation period, a Vybrant CFDA SE Cell Tracer Kit (Molecular Probe Inc.) was introduced into the suspension to stain viable cells. A working dye solution consisted of 1 µL of a 10 mM stock solution dissolved in 1000 µL of a 10 mM PBS solution (pH 7) warmed to 37 °C. As was the case for the Concanavalin Alexa Fluor 488 dye, a ratio of 1 part of dye to 5 parts of suspension was used to stain the live cells by adding 20 µL of working solution to 100 µL of suspension and incubating it for 15 min at 37 °C. Following the incubation period, the samples were re-suspended in fresh medium at 37 °C for 30 min and then rinsed with sterilized MilliQ water, then left to dry for 2 h at room temperature (*ca*. 22 ºC, humidity 55%) without additional fixation to prevent the deformation of the cells.

Images were acquired using a confocal scanning laser microscope Olympus FluorView FV1000 Spectroscopic Confocal System that included an inverted microscope OLYMPUS IX81 [with 20×, 40× (oil), 100× (oil) UIS objective lenses] operated with multiple Ar, He and Ne laser lines (458, 488, 515, 543, 633 nm) and Fluorview FV 6.0 and ImagePro imaging software. The volume of presumed EPS and viable cells was quantified by measuring and analyzing the intensity integration (counts per second, cps) of a fluorescent dye using FV10-ASW 1.6 software [520,521]. The total intensity of a biofilm was assumed to be the summation of respective EPS and viable cell intensities. For each sample, at least four random locations of approximately 126.7 µm × 126.7 µm areas were scanned.

To quantify 3D biofilm image stacks, the computer software COMSTAT was used [522]. Six typical biofilm areas of the bacterial strain on each type of polyterpenol surface were exported into a stack of grey-scale 8-bit images by Fluorview FV 7.0. At least ten representative images/areas on each type of the surfaces (in duplicate samples) were analyzed. Two quantitative parameters of biomass density were used to describe the biofilm formed on the polyterpenol surfaces [522]: (i) the biovolume, which encompasses both cells and EPS, i.e. the overall volume of the biofilm per unit area of substrate, and (ii) the average biofilm thickness.

SEM imaging. For scanning electron microscopy, a thin gold coating was coated on the polymer thin films using a Dynavac CS300 according to a previously described procedure [233,234]. FESEM (ZEISS SUPRA 40VP) was employed for high-resolution scanning of the film surfaces containing the adsorbed bacterial cells at 3 kV and 1000, 5000, and 20000× magnifications. In order to obtain a good statistical representation of the surface, a minimum of 5 areas of each sample were scanned and SPSS 17.0 software (SPSS Inc., Chicago, Illinois, USA) was used for the statistical analysis of the data.

VIII.1.3 Results

VIII.1.3.1 Polyterpenol thin film surface characterization

A comparative analysis of FTIR and Raman data for the monomer and polyterpenol films supported by molecular simulation data are presented in Figure VIII.1.3 and summarized in Table VIII.1.2. Analysis of the FTIR spectra for the monomer and resultant polymer films indicated that the number of absorption frequencies decreased significantly upon exposure to the plasma field.

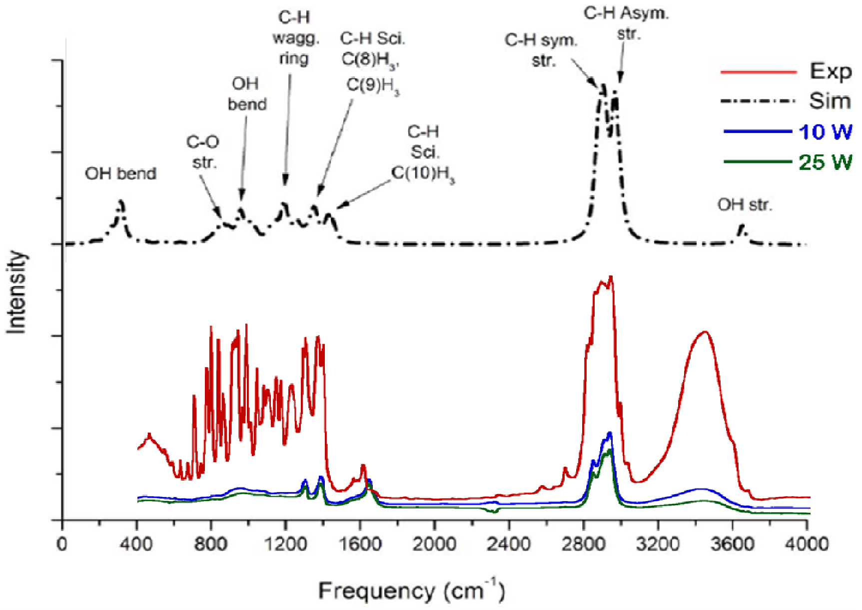

Figure VIII.1.3. Comparison of simulated infrared (IR) spectrum of terpinen-4-ol (gas phase, black, RF deposition power = 0 W) with experimental IR spectrum of terpinen-4-ol monomer (gas phase, red, RF deposition power = 0 W (control), and polyterpenol thin films fabricated at 10 W (blue) and 25 W (green) RF deposition power. The simulated IR spectrum is produced using the B3LYP/cc-pVTZ model. A scale factor of 0.96 has been applied.

Table VIII.1.2. Assignment of group frequencies for terpinen-4-ol monomer and polyterpenol films (experimental and simulation).

assignment	group frequency (cm^{-1})		
	monomer	polymer	simulation
IR spectra[a]			
Hydroxy group, H-bonded OH stretch	3450	~3460	3656
Medial, *cis*- or *trans* C-H stretch	3011		
Methyl asymmetric C-H stretch	2963, 2959	2955, 2930	2971, 2970
Methylene asymmetric C-H stretch			2964, 2961
Methyl symmetric C-H stretch	2880	2875	2886
Methylene symmetric C-H stretch	2851		2910
Alkenyl C=C stretch	1678, 1629	~1660	1660
Methylene C-H bend	1463		1460
Methyl C-H asymmetric bend	1444	1459	1434
Symmetric C-H bend	1376	1380	1354
Primary or secondary, OH in-plane bend	1303		958
Methylene skeletal C-C vibrations	1300-700		
C-O stretching of alkyl-substituted ether	1128, 1070,	1150, 1050	862
Tertiary alcohol, C-O stretch	1157		
Primary alcohol, C-O stretch	1050		
Cyclohexane ring vibrations	1050, 1026,		
Alcohol, OH out-of-plane bend	685		
Raman spectra			
C=C stretch	1640		1643
Methylene C-H bend	1450		1426

[a] The scaling factor for IR spectrum is 0.96and for Raman spectrum is 0.95

There was a substantial reduction in the magnitude of the H-bonded O–H stretch related band for all polymer spectra, with the peak size decreasing as the deposition power increased. Similarly, the absorptions corresponding to methyl C-H asymmetric and symmetric stretching (around 2955, 2930, and 2875 cm^{-1}) and bending (around 1459 and 1380 cm^{-1}) showed a diminution in magnitude with higher input RF power. Infrared bands associated with the unsaturated C=C–H moiety between 3150 and 3000 cm^{-1} disappeared even at the lowest of the deposition powers (10 W). A relatively strong experimental peak at 1707 cm^{-1} appeared, which was not found on the simulated monomer spectrum, and this indicates the presence of saturated carboxylic acid (C = O stretch). Bands at 1150 and 1050 cm^{-1} were characteristic of C – O stretching of an alkyl-substituted ether.

The Raman spectra (Figure VIII.1.4) confirmed the peak intensity shrinkage or disappearance of some peaks as the deposition power is increased suggesting that structural changes of the monomer were taking place and that the polyterpenol thin film is being confined on the surface.

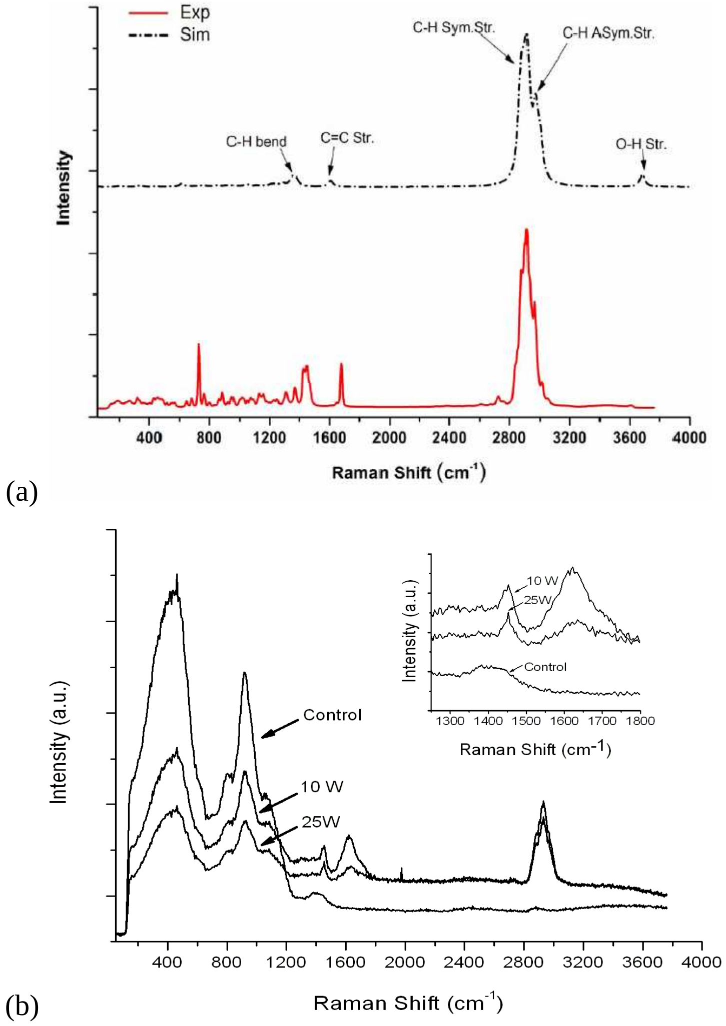

Figure VIII.1.4. a) Comparison of simulated Raman spectrum of terpinen-4-ol (gas phase, black) with experimental Raman spectrum (liquid, red). The simulated Raman spectrum is produced using the B3LYP/cc-pVTZ model. A scale factor of 0.96 has been applied. b) Comparison between experimental Raman spectra of terpenin-4-ol and polymer thin films fabricated from the monomer at 0 W (control), 10 and 25 W RF deposition power.

XPS analysis confirmed that carbon and oxygen dominated the surface of both films (up to 99 at. %), with Si, Zn and N present in trace amounts (below 1%) and regarded as negligible (Figure VIII.1.5). Simulated and experimental core ionization potentials are presented in Table VIII.1.3.

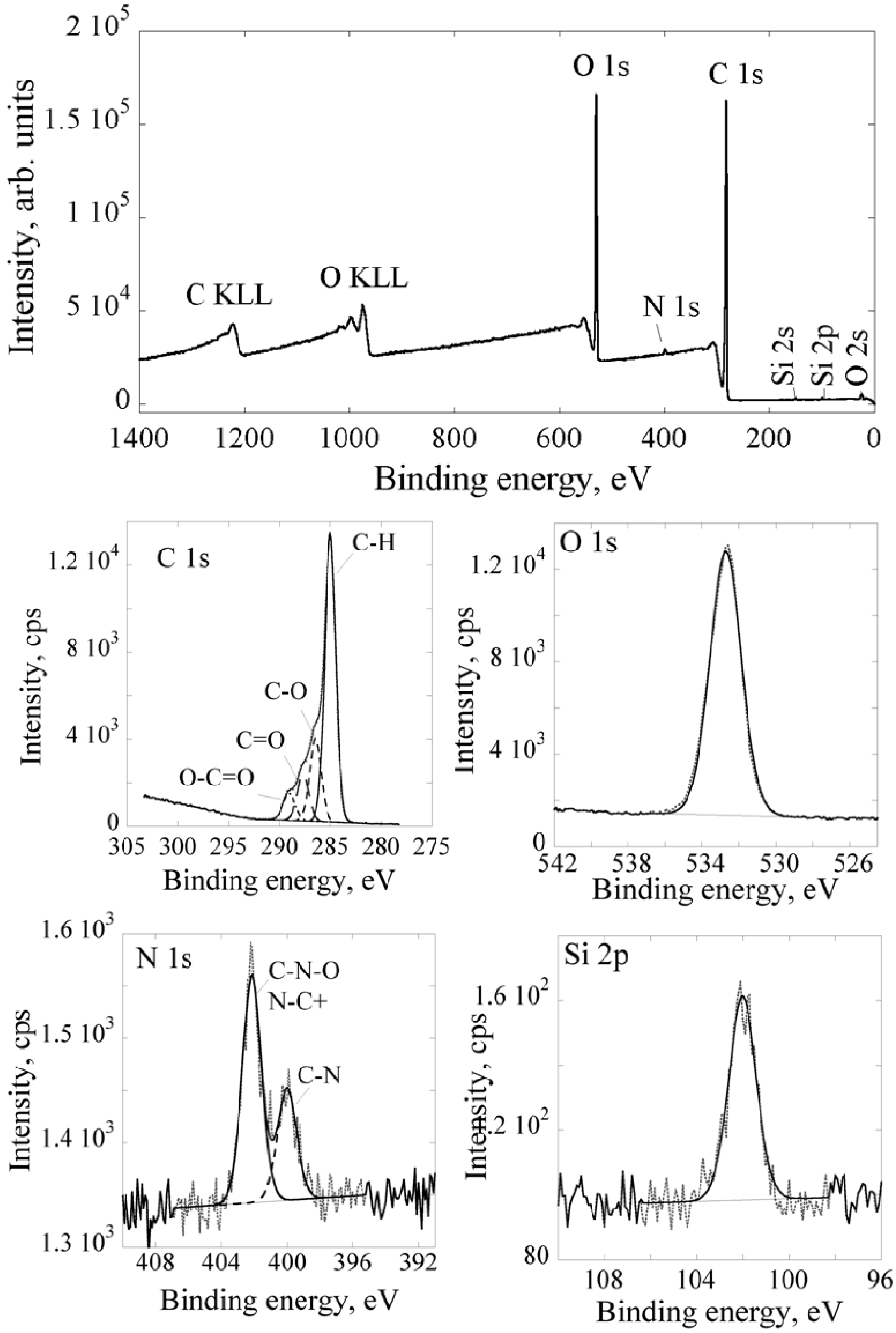

Figure VIII.1.5. A wide scan of XPS spectrum (top panel) and C 1s, O 1s, N 1s and Si 2p XPS spectra collected for polyterpenol film fabricated at 25 W RF power.

Table VIII.1.3. Comparison of simulated XPS vertical core ionization potentials (IPs) of terpinen-4-ol monomer (gas phase) with experiment (thin film under 25 W).

atomic site		IPs (eV)	IPs (eV) expt
O-K	O(6)	534.36	532.70
C-K	C(1)	289.27	285.0
	C(2)	289.50	285.0
	C(3)	289.55	285.0
	C(4)	289.15	285.0
	C(5)	289.41	285.0
	C(6)	291.05	285.0
	C(7)	289.54	286.4
	C(8)	288.84	285.0
	C(9)	288.82	285.0
	C(10)	289.36	285.0

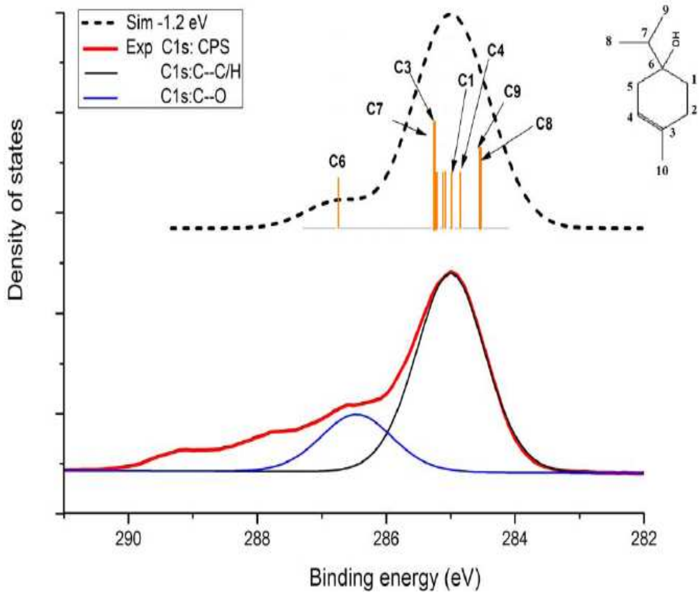

Figure VIII.1.6. Comparison of simulated and experimental X-ray photoelectron spectra (XPS) of C1s. The experimental XPS of C1s is in thin film with 25 W, whereas as the simulated XPS of C1s is in gas-phase without power. The simulated spectrum is based on the LB94/et-pVQZ//B3LYP/cc-pVTZ model. A global red shift of 4.30 eV is applied to the simulated to minimize the systematic energy shift due to the work function. The C1s XPS indicates that the chemical structure of the thin film under this condition is not very different from its gas phase monomer structure.

Contamination originating from the glass substrata and ambient air were determined to be the most likely contributors of Si, Zn, and N respectively. The high-resolution XPS C1s spectrum appears to be comprised of contributions from carbon atoms in at least four bonding environments (Figure VIII.1.6) with the most prominent peak attributable to a hydrocarbon species (BE = 285.0 eV). The remaining three peaks at binding energies of 286.4, 287.7, and 289.1 eV were assigned to functional groups with increasing bonding to oxygen, namely C – O, C = O and O – C = O species respectively.

The N1s spectrum has been fitted to two chemical states, with the peak at the lower binding energy (BE = 400.0 eV) attributed to nitrogen atoms bonded to carbon, in either amine or amide functional groups. The second component of N1s spectrum possesses a bonding energy (BE = 402.1 eV) between that observed for positively charged N atoms bonded to C, and for NO_2 species. It is assigned to nitrogen atoms bonded to a single oxygen atom, as few of such species that have been analyzed by XPS are reported to have BEs in the same region. The width of the O1s spectrum suggests that it is also made up of contributions from more than one chemical state of the element (Figure VIII.1.7). However, the spectrum appears as a single peak, with no obvious fine structure to assist fitting. Almost all of the contributions are likely to come from the various functional groups containing oxygen bonded to carbon, but there is a great deal of overlap in the O1s BEs reported for these species. The Si2p spectrum contains contributions from a single Si species at BE = 102.0 eV which is within the range observed for Si atoms bonded to O, as occurs not only in inorganic silica and silicates, but also in organic siloxanes.

A comparison of physico-chemical surface attributes of the two different polyterpenol films is presented in Table VIII.1.4. The water contact angle θ_W increased from approximately 63^o to 69^o for films deposited at 10 W and 25 W respectively, indicating the application of higher RF deposition power resulted in a more hydrophobic film surface compared to those prepared from lower power deposition. Although the differences in water contact angle for samples deposited at different powers are statistically significant ($p<0.05$), this is not the case for the ethylene glycol and diiodomethane. The glass substrata used in the study are highly hydrophilic, with prevalence of electron donor components due to hydroxyl groups (-OH) present on the glass surface [523]. For all polyterpenol film samples, $\gamma^- >> \gamma^+$ indicating the electron donor capability of the surface, with the 10 W samples displaying a higher electron donating tendency compared to the 25 W samples. The total surface free energy was found to be similar and independent of the deposition power.

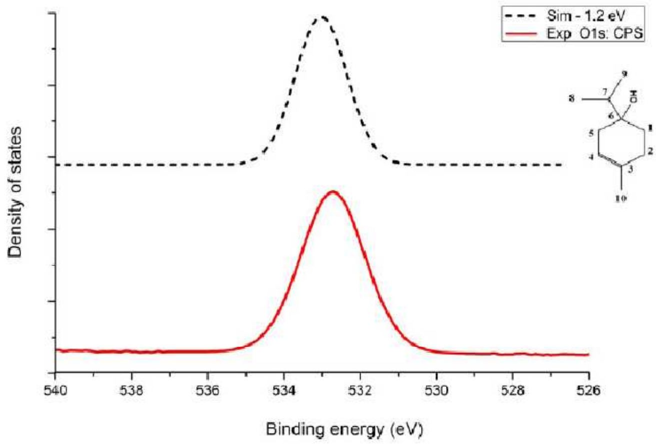

Figure VIII.1.7. Comparison of simulated and experimental X-ray photoelectron spectra (XPS) of O1s. The experimental XPS of O1s is in thin film with 25W, whereas as the simulated XPS of C1s is in gas-phase without power. The simulated spectrum is based on the LB94/et-pVQZ//B3LYP/cc-pVTZ model. A global red shift of 1.34 eV is applied to the simulated to minimize the systematic energy shift due to the work function.

Table VIII.1.4. Comparative evaluation of physico-chemical properties of polyterpenol thin films surfaces fabricated at different RF power and correspondent numbers of *P. aeruginosa* cells.

	Glass	10 W	25 W
contact angle (degrees)			
θ_W[a]	8.3±0.7	62.7±4.0	68.7±3.1
θ_{EG}	26.5±1.3	59.8±2.4	58.7±0.5
θ_D	43.8±0.8	38.2±0.8	38.1±0.8
surface free energy (mJ/m^2)			
γ^{LW}[b]	37.6	40.5	40.5
γ^{AB}	1.54	9.30	5.40
γ^+	0.01	0.7	0.4
γ^-	73.6	30	20.6
γ_{TOT}	39.2	49.8	45.9
percentage of attached cells, [%]	0.38 ±	0.040 ± 0.002	0.37 ± 0.11
retained cells[c] × 10^5, [number of cells per mm^2]	4.95 ±	0.50 ± 0.02	4.79 ± 1.41

[a] W water; EG ethylene glycol; D diiodomethane; [b] Surface free energies components: Lifshitz-van der Waals (γ^{LW}), acid/base (γ^{AB}), electron acceptor (γ^+) and electron donor (γ^-) components; [c] Cell densities have estimated errors of approximately 15-20% due to local variability in the surface coverage.

The surface topography of the polyterpenol films was investigated by means of AFM. Irrespective of deposition power, polymer films were found to be smooth, uniform and pinhole free (Figure VIII.1.8), suggesting that the polymerization occurred predominantly on the surface of the glass substratum rather than in the gas phase [326]. Surfaces of the films deposited at 25 W exhibited slightly higher average (R_a) and RMS (R_q) surface roughness parameters compared to those samples fabricated at 10 W; R_a increased from 0.39 to 0.42 nm and R_q from 0.51 to 0.52 nm. The values obtained as a result of this analysis were in agreement with the roughness estimates determined by means of ellipsometry. A similar trend was also noted for the maximum peak height (R_{max}), with an increase from 5.1 to 5.3 nm observed for samples deposited at 10 W and 25 W, respectively. A statistical analysis of the R_a and R_q data obtained for the polyterpenol thin films showed that there was no significant difference between the roughness of the films fabricated at 10 W and 25 W RF power ($p > 0.05$).

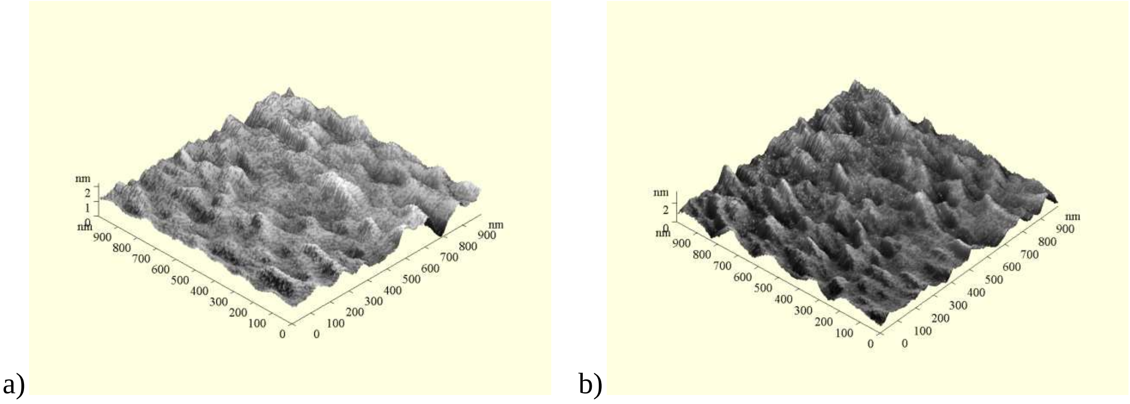

Figure VIII.1.8. Typical surface morphology of polyterpenol thin films deposited at 10 and 25 W RF fabrication power as inferred from 3D AFM images.

All polymer surfaces displayed a surface skewness (R_{skw}) greater than 0 and coefficient of kurtosis (R_{kur}) less than 3, i.e. the R_{skw} values highlight a disproportionate number of peaks pertinent to the polyterpenol surfaces; and the R_{kur} values indicate the surfaces with well spread out height distribution [359,360]. There was a subtle change in surface topography of the samples with films manufactured at lower RF powers, displaying broader, more rounded peaks and valleys while samples deposited at higher RF powers exhibiting narrower, sharper peaks. Such a change was reflected in the R_{skw} and R_{kur} values increasing from 0.54 to 0.60 and from 0.64 to 0.71 for samples deposited at 10 W and 25 W respectively, although it was not found to be statistically significant ($p > 0.05$).

VIII.1.3.2 Antibacterial activity of polyterpenol film

The *P. aeruginosa* cells attachment response on the polyterpenol films after 18 h incubation was visualized using SEM and CSLM imaging, and statistically analyzed (Table VIII.1.4, Figure VIII.1.9).

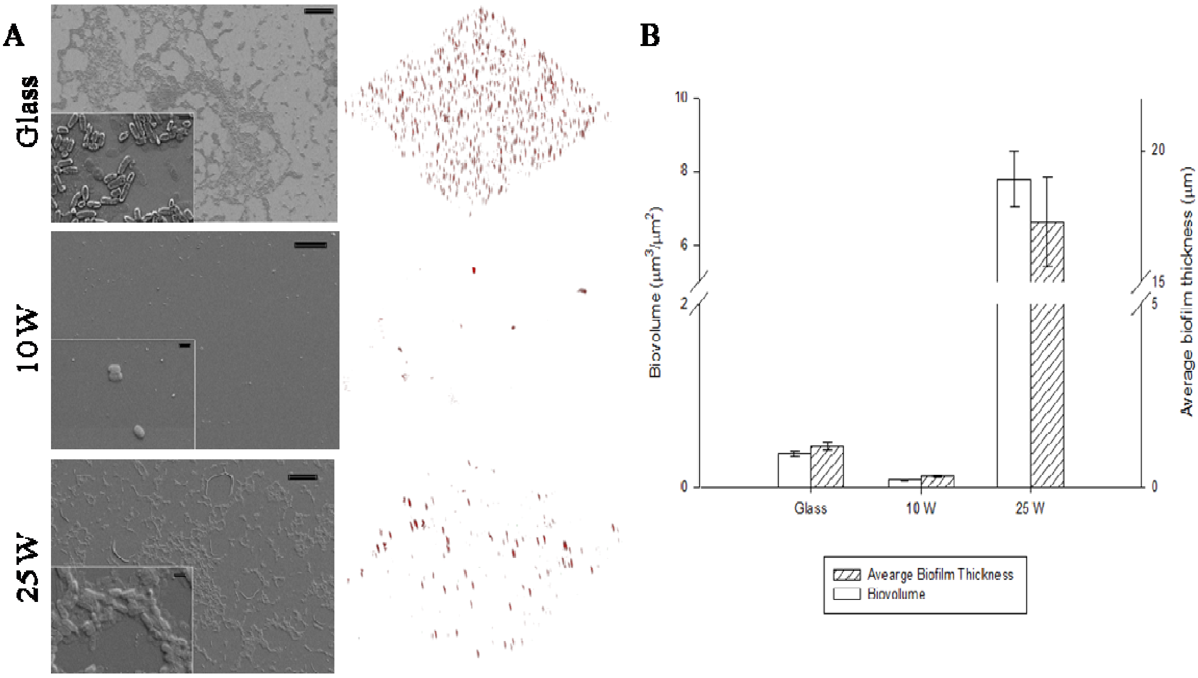

Figure VIII.1.9. **A.** *P. aeruginosa* growth on the glass and polyterpenol thin films fabricated at 10 and 25 W RF deposition power after 18 h incubation. SEM images (left) represent an overview of the attachment patterns taken at x500 magnification, bars = 20 µm; inserts are zoomed in areas taken at a x5000 magnification, bars = 1 µm. CSLM images (right) visualizing viable cells (stained red with SYTO® 17 Red) and the production of EPS (stained green with concanavalin A 488). **B.** *P. aeruginosa* biovolume and average biofilm thickness on the same surfaces presented in the graph was quantified using COMSTAT (n = 6, * if $p < 0.05$), indicate considerable inhibition of bacterial growth on polyterpenol thin films fabricated at 10 W RF deposition power.

The attachment pattern of *P. aeruginosa* was found to be markedly different on the two types of polyterpenol film. In particular, the polyterpenol films fabricated under 10 W RF power conditions exhibited antibacterial inhibitory properties; varying quantities of EPS were also detected around bacterial cells. The number of *P. aeruginosa* cells attached to the polyterpenol films fabricated under 10 W RF power conditions was significantly lower (Figure VIII.1.9) than those detected on glass or the polyterpenol films fabricated under 25 W RF power conditions. An examination of *P. aeruginosa* cells revealed the different cell morphology while the cells were undergoing attachment to the polyterpenol films surfaces, with larger *P. aeruginosa* cells being present on the surface of glass and the polyterpenol films fabricated under 25 W RF power conditions, most likely as a result of the lack of inhibitory effect. The *P. aeruginosa* cells also produced significantly more EPS when they attached to glass and the polyterpenol films fabricated under 25 W RF power conditions.

VIII.1.4 Discussion

The nature of the gas-phase and surface-related terpinen-4-ol plasma reactions depend on the plasma polymerization operating conditions used during the deposition process. In the course of plasma enhanced synthesis, the terpinen-4-ol monomer is fragmented, with the degree of fragmentation being closely related to the applied level of the RF input power. Electron-generated dissociation of the terpinen-4-ol, rather than thermal excitation or direct chemical reaction [322], produces the chemically reactive species that are involved in the polymerization process and subsequent polyterpenol thin film formation. Concurrently, a recombination process is taking place inside and outside plasma region. Since terpinen-4-ol possesses functionality associated with conventional polymerization (such as unsaturation), the molecule undergoes a more complex recombination process that combines the conventional polymerization with fragment-recombination mechanisms triggered by the plasma-created and surface-attached reactive species, such as ions and free radicals [320], the resultant polymer-like structure may possess chemical and physical properties notably different from those of its precursor, with a significant amount of incomplete bonds (free radicals trapped in a three dimensional network) being present [322].

Based on the chemical structure of terpinen-4-ol molecule, computer simulations were performed to predict the likely radicals that would form in the course of plasma-enhanced monomer decomposition. FTIR and Raman spectra and the XPS spectra for O1s and C1s of the species were simulated using the B3LYP/cc-pVTZ model, and the results of the modelling were compared to the respective FTIR, XPS and Raman spectra for the polyterpenol film surfaces. These results were then used to interpret the extended film properties, such as their chemical composition and surface characteristics, and these properties were correlated with the plasma deposition conditions.

Examination of the data obtained showed that the polyterpenol films fabricated at 10 W and 25 W RF power were predominantly hydrocarbon in nature, with oxygen-containing groups being present within the structure in the form of alcohol and carboxylic acid groups (Tables VIII.1.2-3, Figures VIII.1.3-7). As demonstrated by molecular simulation, under the RF plasma field conditions, the monocyclic alcohol of the original terpinen-4-ol monomer may undergo a transformation (Figures VIII.1.6 and Table VIII.1.1), whereby some bond structures associated with vertices C(6), C(7) and C(3), such as C(6)–OH and C(6)-C(7) may dissociate to form fragments, and the C(3)=C(4) double bond may become saturated to produce C(3)–C(4). These changes potentially alter the chemical and physical behaviour of the resulting polyterpenol films, and most importantly, the extent of the antibacterial activity. The differences in chemical composition of the resulting polyterpenol films, such as lower oxygen and higher hydrocarbon content for polymers fabricated at 25 W compared to that of the 10 W RF power can be attributed to a greater degree of fragmentation of the terpinen-4-ol molecule. Deposition at 10 W RF power resulted in a greater level of preservation of the configuration of functional groups, i.e. –OH, and double bonds, in the polymer film.

Such preservation of functionalities in plasma polymers deposited at low power has been widely described in literature and is attributed to the activation with lower fragmentation rates compared to films fabricated at higher input powers [340,524,525]. Using a similar capacitively coupled RF plasma reactor, Lopez and Ratner demonstrated that weakly ionized plasmas, and relatively low substrate temperature, encourage preferential condensation and adsorption of non-excited gaseous species and subsequent incorporation of increased number of non-fragmented molecules or slightly fragmented precursors in the growth region of the film [339]. It is believed that the above process is responsible for preservation of chemical functionalities in polyterpenol samples fabricated at lower input power. As carbon-oxygen and oxygen-hydrogen bonds are polar, polymer structures containing these functionalities are likely to exhibit greater hydrophilicity and hence biocompatibility compared to the more hydrophobic polymers that are hydrocarbon-rich [526].

Our analysis of surface wettability confirmed that the application of higher RF deposition power resulted in increased surface hydrophobicity (from $\theta_W = 63^o$ to $\theta_W = 69^o$). This reported tendency agrees with previously published results for polymer thin films deposited by means of RF plasma polymerization, and is attributed to a decrease in the oxygen content and thus the hydrophilicity of the fabricated polymers [526]. FTIR spectra further confirmed this observation, showing a significant decrease in the intensity of the peak attributed to the hydroxyl group. The values of the total surface free energy, however, remained similar ranging between 31 and 35 mJ/m^2 ($p > 0.05$). Also there was no significant difference in roughness parameters or surface topography between samples deposited at different RF powers. Morphological examination of polymer films revealed smooth, uniform and pinhole free surfaces [336].

VIII.1.5 Conclusions

The differences in growth of *P. aeruginosa* are most likely controlled by the differences in the surface chemistry of the respective polyterpenol films. The extent of bacterial attachment and EPS production increased as the polyterpenol films became more hydrocarbon dense, containing less hydroxyl groups. Since surface free energy values and surface topographic and morphological profiles did not appear different for the samples deposited at 10 W and 25 W RF power, such parameters cannot account for the difference in attachment behaviour of the studied bacterial strain. In the course of film deposition, plasma generated carbon-carbon scission leads to formation of a wide array of oxygen containing functional groups such as C–O, C=O or COOH at the surface of the polymer, with the 10 W sample possessing a significantly larger amount of oxygen containing functionalities compared to the sample deposited at 25 W. These functional groups can actively associate with functionalities present on the bacterial wall, suppressing cell biosynthesis, and disrupting the transport across the cell wall and causing a loss of membrane integrity. Such processes result in an increase in passive flux of protons across the membrane and consequent dissipation of the proton motive force, which accelerates the death of the pathogen.

The results of molecular modelling, confirmed by the experimental data, suggested that the hydroxyl group concentration may be the most affected during plasma treatment followed by the fragmentation of the monomer. The 10 W RF power deposition plasmas were likely to favour condensation and incorporation of monomer molecules with low degrees of fragmentation. Therefore, the preservation of the original terpinen-4-ol monomer structures in the bulk of the polyterpenol film matrix is responsible for the inhibitory effect of the polyterpenol films. Thus, RF power of 10 W can be employed for the fabrication of polyterpenol films of 500 nm thickness with an inhibitory effect on the growth of *P. aeruginosa.* The retention of the polyterpenol films’ antibacterial characteristics is due to the preservation of intact terpinen-4-ol on the surface of the polyterpenol thin films.

Supplementary Information

Table S1. Geometric properties of monomer terpinen-4-ol calculated using B3LYP/cc-pVTZ.

Properties	terpinen-4-ol
Ring perimeter R_6 (Å)	8.96
H-bond length (Å) – a	2.58
b	2.63
c	2.57
d	2.70
e	2.80
Dihedral angles	
∠C(6)C(1)C(2)C(3) (^{O})	44.04
∠C(6)C(5)C(4)C(3) (^{O})	-16.3
∠C(8)C(7)C(6)C(1) (^{O})	55.5
∠C(9)C(7)C(6)C(1) (^{O})	-58.8
∠C(10)C(3)C(2)C(1) (^{O})	167.72
∠H(12)O(11)C(6)C(7) (^{O})	162.6
Dipole moment (Debye)	1.75

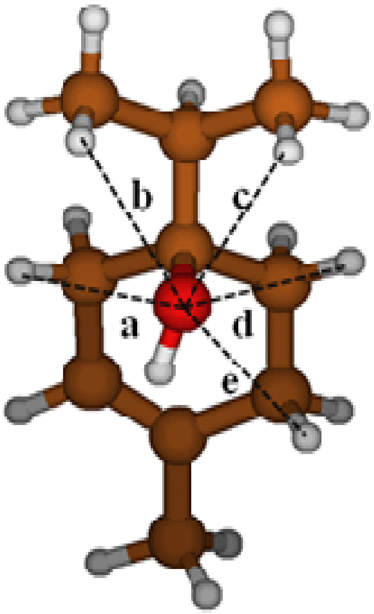

VIII.2 EFFECT OF SURFACE PROPERTIES OF POLYTERPENOL ON BACTERIAL VIABILITY AND ADHESION

Abstract

The nanometer scale surface topography of a solid substrate is known to influence the extent of bacterial attachment and their subsequent proliferation to form biofilms. As an extension of our previous work on the development of a novel organic polymer coating for the prevention of growth of medically significant bacteria on three-dimensional solid surfaces, this study examines the effect of surface coating on the adhesion and proliferation tendencies of *Staphylococcus aureus* and compares to those previously investigated tendencies of *Pseudomonas aeruginosa* on similar coatings. Radio frequency plasma enhanced chemical vapor deposition was used to coat the surface of the substrate with thin film of terpinen-4-ol, a constituent of tea-tree oil known to inhibit the growth of a broad range of bacteria. The presence of the coating decreased the substrate surface roughness from approximately 2.1 nm to 0.4 nm. Similar to *P. aeruginosa*, *S. aureus* presented notably different patterns of attachment in response to the presence of the surface film, where the amount of attachment, extracellular polymeric substance production, and cell proliferation on the coated surface was found to be greatly reduced compared to that obtained on the unmodified surface. This work suggests that the antimicrobial and antifouling coating used in this study could be effectively integrated into medical and other clinically relevant devices to prevent bacterial growth and to minimize bacteria-associated adverse host responses.

Keywords: nanoarchitecture; plasma polymerization; terpinen-4-ol

As published in: Bazaka, K., Jacob, M., Truong, V. K., Crawford, R. J., Ivanova, E. P., The effect of polyterpenol thin film surfaces on bacterial viability and adhesion. *Polymers* 2011, 3, 388-404.

VIII.2.1 Introduction

Biomaterial-associated infections remain a major hindrance to the long-term utilization of most implanted or intravascular devices, including orthopaedic prostheses, artificial valves, urinary tract and cardiovascular catheters, intraocular lenses and dentures [1,2]. Bacterial attachment and subsequent biofilm formation frequently results in indwelling device related infections and device failure [3,4]. In their biofilm state, bacteria are less susceptible to host defence mechanisms and systemic antibiotics, and also to detachment due to flow conditions. The presence of these biofilms can often cause an infection, often requiring the surgical removal of the infected device [5]. The mechanism of bacterial adhesion is complex, with initial reversible physicochemical interactions being followed by intricate irreversible molecular and cellular interactions. When the distance between the bacterial cell and other cells or abiotic surfaces is larger than 50 nm, the interactions between these two entities are nonspecific and are directly related to the distance and the dispersive component of free energy characteristics pertinent to these two surfaces [6]. The nature of these forces, *i.e.*, whether they are attractive or repulsive, will either facilitate the bacterial attachment or prevent the cell from engaging into the molecular or cellular phase of adhesion. When the distance separating these surfaces becomes less than 5 nm, chemical interactions such as hydrogen bonding, ionic and dipole interactions, hydration and/or hydrophobic interactions become significant, often resulting in a more stable adhesion between the microorganism and the surface [7]. Various polymeric structures such as capsules, fimbriae, pili, and slime that can be present on the surface of the bacterial cell engage in the molecular specific irreversible reactions with the chemical features of the tissue or abiotic surface. Therefore, in order to effectively control the attachment and adhesion of the cells to the surfaces, it is imperative to understand the surface properties and the physicochemical interactions associated with the initial events of cell adhesion. An obstacle to obtaining this understanding is that the relative contributions of the molecular and physical interactions that govern bacterial adhesion to biomaterials are yet to be fully interpreted.

There is much debate as to the extent to which the nanometer scale surface topography of a solid substrate influences bacterial adhesion and their subsequent proliferation to form biofilms [8,9]. Investigations on the adhesion of *Pseudomonas aeruginosa* to poly(methyl methacrylate) contact lenses identified that surfaces with a root-mean-square (RMS) roughness parameter of 14 nm or above tended to experience an increased extent of micro-organism attachment [10]. Other studies on the attachment preferences of human pathogens *P. fluorescens* and *Staphylococcus aureus* have demonstrated that the topography of micro-rough titanium surfaces can influence the extent of cell attachment and growth, with cells showing propensity for growth in the trenches of the surface in long rows [11,12], whilst the attachment response of these bacteria towards smooth surfaces did not follow a distinct pattern [11,13]. A few early studies reported that surface roughness was a 'minor factor' in the attachment mechanism of bacteria, in that the bacteria displayed no preference for adhesion to surface features such as scratches or grooves [8,9]. However, preferential adherence of bacteria to grooved and braided surfaces was found by Scheuerman *et al.*, who attributed this increased attachment propensity as being due to the presence of an increased surface area [13]. More specifically, in situations where the size of the surface features was comparable to the size of the bacterium, the bacteria-surface contact area is at a maximum and hence the binding potential of the bacteria was increased [14]. In cases where the surface features were significantly smaller than the bacterial size, the contact area was reduced, resulting in a reduced extend of binding [15]. The level of extracellular polymeric substance (EPS) production and bacterial cell morphology have also been shown to be affected by the surface architecture [11,16,17]. Nano-patterning of gold surfaces has been demonstrated to enhance the localized attachment of *P. fluorescens* in the trenches of the surfaces compared to that obtained using native gold surfaces, with cells showing limited EPS production and reduced cell size compare to those attached onto non-nano-patterned surfaces [11]. Our recent investigation on the effect of surface roughness on the attachment behaviour and production of extracellular polymeric substances for the Gram-positive coccoid pathogen, *S. aureus*, and Gram-negative rod shaped bacterium, *P. aeruginosa*, have shown that both pathogens exhibit a greater propensity for adhesion to glass and polymer surfaces that are smooth on the scale of nanometers, resulting in elevated cellular metabolic activity, augmented production of extracellular polymeric substances, and increased number of bacterial cells undergoing attachment [17-19].

Numerous surface modification techniques, such as radio frequency (RF) plasma modification, surface abrasion, chemical coating, and chemical grafting can be employed to change surface properties of the substrate so as to inhibit or promote bacterial adhesion and biofilm formation [20-26]. In this context, the present study is an extension of our previous work on the development of a novel organic polymer coating for the prevention of growth of medically significant bacteria on three-dimensional solid surfaces. In this study, the effect of surface coating with terpinen-4-ol on the adhesion and proliferation tendencies of *S. aureus* were examined and compared to those previously reported for *P. aeruginosa*. The surfaces of substrates were modified by the fabrication of a polyterpenol thin film derived from terpinen-4-ol using RF plasma enhanced chemical vapour deposition. Terpinen-4-ol is a constituent of tea-tree oil and its monomer (liquid) form is known to inhibit growth of a broad range of bacteria [27-30]. Surfaces of coatings produced from terpinen-4-ol are known to be smooth on the scale of nanometers and defect free, with good adhesion to the substrate and good stability [31-34]. Since previous studies have shown *S. aureus* and *P. aeruginosa* to preferentially attach and adhere to surfaces that are smooth on the nanometer scale, this study examines the influence of surface architecture on the antifouling properties of the polyterpenol coating.

VIII.2.2 Experimental

Modification of the surface of glass substrates was achieved using radio frequency plasma enhanced chemical vapour deposition (RF-PECVD) of a thin layer of polymer coating using terpinen-4-ol (Australian Botanical Products, Ltd.) as a precursor. The detailed account of the experimental set-up and deposition procedure is outlined elsewhere [31]. Briefly, the RF energy (13.56 MHz) was delivered into a custom-designed glass deposition chamber by means of two capacitively coupled copper electrodes. Glass substrates (BioLab Scientific, Ltd.) were pre-washed in a 1:5 solution of Extran and distilled water, ultrasonically cleaned using distilled water heated to 50 °C for 30 min, rinsed with propan-2-ol and dried. Cleaned substrates were then placed into the deposition reactor, which was then evacuated to 200 mTorr, flushed with argon for 1 min to ensure that the substrates possessed an oxygen-free surface. The chamber was then evacuated to achieve a pressure of 50 mTorr. The terpinen-4-ol vapour was released gradually into the chamber and the glow was maintained by controlling the monomer flow [32]. Deposition was performed in two stages at room temperature and pressure of 200 mTorr. First, to improve the strength of adhesion between the coating and the substrate, a 100 nm layer of polyterpenol thin film was deposited using input power of 75 W. Then, a functional coating was deposited from terpinen-4-ol under 10 W or 25 W RF power for 10 min to achieve films of approximately the same thickness.

The roughness parameters of both the native and coated glass surfaces were quantitatively analysed using an atomic force microscope (AFM) (NT-MDT) in semi-contact (tapping) mode, using (NSC05, NT-MDT) cantilevers with a spring constant of 11 N/m, tip radius of curvature of 10 nm, aspect ratio of 10:1 and resonance frequency of 150 KHz. 3-D interactive visualization and statistical approximation was used to analyse the topographic profiles of the surfaces. Scanning was performed perpendicular to the axis of the cantilever at a rate of typically 1 Hz, with the scan areas of 1 μm × 1 μm and 10 μm × 10 μm. At least five samples for the surfaces of each condition have been investigated.

In addition to the surface morphology, surface chemical characteristics were also determined. The chemical composition of the surface before and after coating was analysed by means of X-ray photoelectron spectroscopy (XPS). XPS was performed using an Axis Ultra spectrometer

(Kratos Analytical Ltd., UK), equipped with a monochromatic X-ray source (Al Kα, hν = 1,486.6 eV) operating at 150 W, as described elsewhere [34]. Using the Kratos Vision II software, peaks in the high-resolution regions of spectra were fitted with synthetic Gaussian-Lorentzian components. Surface wettability was determined from contact angle measurements using (KSV 101) employing the sessile drop method [51-54].

Prior to each experiment, a fresh bacterial suspension of $OD_{600\ nm}$ = 0.3 was prepared from *P. aeruginosa* ATCC 9025 and *S. aureus* CIP 68.5 cells grown in nutrient broth (Oxoid) at room temperature (~22 °C) for 24 h. A portion of 100 μL of bacterial suspension was deposited onto the surface of each sample (in triplicate). Sterile nutrient broth (100 μL) was used as a negative control. After incubation for 18 h at 37 °C, all of the samples were gently washed with copious amounts deionised water and left to dry at room temperature for 45 min at 55% humidity. A FeSEM-ZEISS SUPRA 40VP was used to obtain high-resolution images of the bacterial cells. Just before imaging, all slides were gold coated in order to achieve better conductivity. Separately, concanavalin A Alexa 488 dye (Molecular Probes Inc.) was used to label the extracellular polysaccharide (EPS) produced by the bacteria while attaching to the surfaces. After incubation, all samples were washed with sterilized nanopure water and carefully stored until being analysed at room temperature (~22 °C). The confocal scanning laser microscope (CSLM) Olympus Fluoview FV1000 Spectroscopic Confocal System was used [34]. Excitation and emission wavelengths for concanavalin A are 495 nm and 519 nm, respectively. Also, viability of attached bacterial cells was determined using Live/Dead® *Bac*Light™ Viability kit (L7007, Invitrogen). The staining was carried out according to the manufacturer's protocol.

Using a First Ten Angstroms (FTA200) instrument, sessile drop contact angle measurements were performed on the lawns of bacterial cells to estimate the surface wettability of the bacterial samples. Bacterial cells were washed three times and then suspended in a buffer (OD450 = 0.4). A bacterial lawn was formed by depositing the bacterial suspension onto cellulose acetate membrane filters (Sartorius, pore diameter 0.2 μm), which were then sufficiently dried at ambient temperature prior to measurement of the contact angle to reach "plateau state", whereby stable water contact angles can be measured over time. The contact angle of the water droplets deposited onto the bacterial lawns was recorded using a charge-coupled device (CCD) camera. Images were digitally saved and analysed using the image analysis software (v 1.961; Folio Instruments Inc.).

For the electrophoretic mobility measured using a zeta potential analyser (ZetaPALS, Brookhaven Instruments Corp.), the bacterial cells were harvested by centrifugation for 5 min at

5,000 rpm after 24 h of incubation. Harvested cell pellet was re-suspended in 10 mM potassium chloride (KCl) followed by further washing and centrifugation. This step was repeated four times and finally the cells were re-suspended in 10 mM KCl solution to OD (600 nm) = 1. The resultant solution of bacterial cells was further diluted 1,000 times in 5 mL of 10 mM KCl. Measurements were conducted in electric field 2.5 V cm^{-1} and 2 Hz. All measurements were done in triplicate and for each sample the final EPM quoted represented the average of five successive ZetaPALS readings, each of which consisted of 14 cycles per run.

VIII.2.3 Results

VIII.2.3.1 Surface Characterization

As indicated by the analysis of the high resolution atomic force microscope (AFM) images (Figure VIII.2.1), the surface topography of the glass substrates was altered at the nanometer scale by the application of thin polymer coating. The key parameters of the surface topography are summarized in Table VIII.2.1 and confirmed by a statistical analysis of the surface roughness parameters of polyterpenol thin films fabricated under 10 W and 25 W RF power conditions. The surfaces were described in terms of such roughness parameters as the average surface roughness (R_a) which is related to the average/absolute deviation of the surface irregularity from the mean line over one sampling length, the root-mean-square roughness (R_q) or RMS calculated as the standard deviation of the distribution of surface height, and the peak-to-peak roughness (R_{max}) which describes the vertical distance between the highest peak and the lowest valley along the assessment length of the surface profile.

Independent of deposition power, the average surface roughness (R_a), root mean square roughness (R_q), and peak-to-peak roughness (R_{max}) appeared to be statistically significantly lower ($p < 0.05$) on the coated glass substrates for both deposition conditions compared to unmodified glass (Table VIII.2.1). Notably, polyterpenol thin films deposited by means of RF plasma polymerization were confirmed to be smooth, defect free and homogenous, in agreement with a previously published report [32]. Amongst polyterpenol films, coatings fabricated at 25 W were characterized by lower average (R_a) and RMS (R_q) surface roughness parameters, and peak-to-peak roughness (R_{max}) compared to those deposited at 10 W, with the difference being statistically significant ($p < 0.05$). The observed reduction in roughness is expected for plasma polymer films deposited at higher RF power due to increased degree of fragmentation associated with higher energy of the plasma field. The surface skewness (R_{skw}) and coefficient of kurtosis (R_{kur}) values were determined to be independent of the input power during the coating of the substrate. Both types of polyterpenol coatings displayed a surface skewness (R_{skw})

of approximately or just above 0 and coefficient of kurtosis (R_{kur}) values of ~3, *i.e.*, the R_{skw} values describe a proportionate number of peaks and valleys pertaining to the polyterpenol surfaces; and the R_{kur} values signify the surfaces with well spread height distribution [35,36].

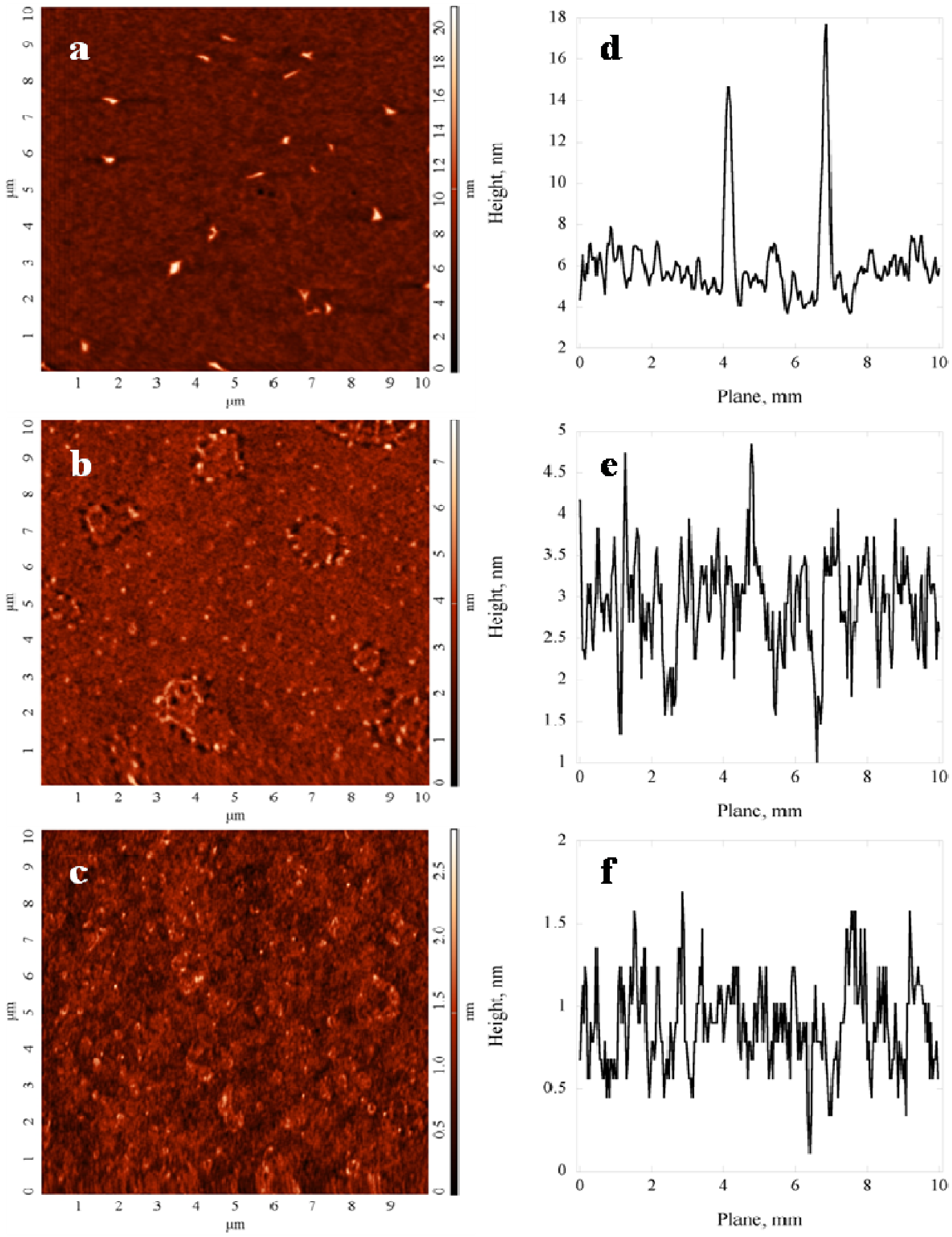

Figure VIII.2.1. Typical two-dimensional (2D) atomic force microscope (AFM) images and surface profiles of glass (**a** and **d**, respectively) and polyterpenol thin film surfaces fabricated at 10 W (**b** and **e**, respectively) and 25 W (**c** and **f**, respectively) from an approximately 10 µm × 10 µm scanned area.

Table VIII.2.1. Surface hydrophobicity, surface tension, surface free energy, and atomic force microscope (AFM) analysis of the roughness parameters for the modified and substrate (glass) surfaces.

	Substrate		Polyterpenol 10 W		Polyterpenol 25 W	
	Scanning areas (μm)					
Roughness parameters (nm) ± SD	1 × 1	10 × 10	1 × 1	10 × 10	1 × 1	10 × 10
Maximum peak height R_{max}	8.5 ± 1.0	30.5 ± 2.6	2.3 ± 0.2	17.5 ± 3.4	1.2 ± 0.2	3.6 ± 0.8
Average roughness R_a	0.4 ± 0.1	2.0 ± 0.1	0.3 ± 0.1	1.3 ± 0.3	0.1 ± 0.02	0.2 ± 0.03
Root Mean Square R_q	0.6 ± 0.1	2.1 ± 0.1	0.3 ± 0.1	1.6 ± 0.3	0.2 ± 0.03	0.4 ± 0.03
Surface skewness R_{skw}	3.2 ± 0.4	0.3 ± 0.1	−0.1 ± 0.1	−0.6 ± 0.1	0.1 ± 0.02	−0.04 ± 0.3
Coefficient of kurtosis R_{kur}	21.9 ± 1.7	5.3 ± 0.5	3.0 ± 0.3	3.1 ± 0.1	2.9 ± 0.1	3.4 ± 0.4
Contact angle (°)						
$\theta_W{}^a$	8.3 ± 0.7		62.7 ± 4.0		68.7 ± 3.1	
θ_{EG}	26.5 ± 1.3		59.8 ± 2.4		58.7 ± 0.5	
θ_D	43.8 ± 0.8		38.2 ± 0.8		38.1 ± 0.8	
Surface tension (mJ/m^2)						
γ^{LWb}	37.6		40.5		40.5	
γ^{AB}	1.54		9.3		5.4	
γ^+	0.01		0.7		0.4	
γ^-	73.6		30		20.6	
γ_{TOT}	39.2		49.8		45.9	

W, Water; EG, ethylene glycol; D, diiodomethane; Surface free energies components: Lifshitz-van der Waals (γ^{LW}), acid/base (γ^{AB}), electron acceptor (γ^+) and electron donor (γ^-) components.

Since the attachment of bacterial cells can be influenced by surface morphology of the substrate both on the nanometer and micrometer scale, for each sample type, the roughness data was estimated separately from 1 μm × 1 μm and 10 μm × 10 μm scanning areas, and the respective parameters were compared. For polyterpenol films deposited at 10 W, the value for the average (R_a) roughness estimated using 10 μm × 10 μm scanning data was approximately 5.25 times higher compared to R_a value obtained from 1 μm × 1 μm scans. At 1.58 nm, the RMS (R_q) roughness was also ~5 times higher when estimated from 10 μm × 10 μm scanning area than that determined using the data from 1 μm × 1 μm scans, at 0.32 nm. The maximum peak height *(R_{max})* surface parameter was also 7 times higher when inferred using 10 μm × 10 μm, at 17.5 nm, compared to 2.25 nm attained from 1 μm × 1 μm scans. Although to a lesser extent, similar variation in roughness values obtained from 1 μm × 1 μm and 10 μm × 10 μm scanning areas were observed for polyterpenol films fabricated at 25 W, with the values calculated from larger scanning areas ~1.8 and 2.4 times higher in the case of average (R_a) and RMS (R_q) roughness, respectively, and 2.9 times higher for maximum peak height (R_{max}) compared to those estimated from 1 μm × 1 μm scans. For both types of polyterpenol coating, the difference between surface skewness (R_{skw}) values from two scan sizes confirmed that over larger scanning areas, the chance of encountering a deep valley relative to the mean line is higher when compared to 1 μm × 1 μm scanning area. These findings indicate that polyterpenol films are smooth at the sub-nanometer scale.

For unmodified glass substrates, the values of average (R_a) and RMS (R_q) roughness, and the maximum peak height (R_{max}) were determined to be ~3.6–4.9 times higher when collected over larger scanning area of 10 μm × 10 μm compared to those of 1 μm × 1 μm area. Notably, both the coefficient of kurtosis (R_{kur}) and surface skewness (R_{skw}) were ~4 and 9 times lower, respectively, when calculated using data from the 10 μm × 10 μm scan area than the respective R_{kur} and R_{skw} values from the 1 μm × 1 μm data. At 0.34 for 10 μm × 10 μm scan, the smaller value of surface skewness (R_{skw}) indicates that over larger scanned areas, the height distribution is more uniform, with approximately equal number of high peaks to deep valleys. Similarly, the lower kurtosis (R_{kur}) coefficient over an increased sampling area indicates that on this scale, the roughness profile of the surface has less high peaks and low valleys [36], probably due to the lower resolution of the scan which may not allow for the detection of finer peaks and valleys.

The application of the polymer coating resulted in a significant increase in the substrate surface hydrophobicity, with the water contact angle increasing from 8° to 63° and 69° on the 10 W and 25 W polyterpenol coatings, respectively. The surface hydrophobicity/hydrophilicity and surface charge before and after the application of the polymeric coating are summarized in Table VIII.2.1. Independent of deposition power, application of the coating statistically significantly affected the contact angle values for all three probing liquid ($p < 0.05$). Among polyterpenol samples, the difference was significant only in the case of water, but not for ethylene glycol or diiodomethane solvents. The dispersive component of the surface tension γ^{LW} was not changed significantly by the application of the thin film coating, whilst the polar γ^{AB} component increased from 1.5 mJ/m^2 for the unmodified glass substrate to 9.3 mJ/m^2 and 5.4 mJ/m^2 for the 10 W and 25 W samples, respectively. All surfaces were identified as monopolar, with pronounced electron-donating capacity and negligible electron-accepting fraction γ^+. Total surface tension values remained relatively similar for all types of surfaces, ranging from 40 mJ m^{-2} to 50 mJ m^{-2} for unmodified and coated substrates, respectively.

Table VIII.2.2. Relative contributions of different chemical states on the surfaces of polyterpenol thin films assigned to the X-ray photoelectron spectroscopy (XPS) peaks.

Element/ transition	Assignment	Substrate		Polyterpenol 10 W		Polyterpenol 25 W	
		Binding energy (eV)	Relative Conc. (%)	Binding energy (eV)	Relative Conc. (%)	Binding energy (eV)	Relative Conc. (%)
O1s	C--O/C=O/Si--O			532.5	81	532.2	70
	*O--C=O			533.5	19	533.3	30
N1s	C–N	400.5	100			400.0	74
	C–N^+					401.9	26
Ca2p	Ca^{2+}	347.9	100				
C1s	C–C, C–H	285.0	80	285.0	77	284.9	60
	C–O, C–N	286.5	12	286.5	15	286.5	21
	CO_3	289.3	4	289.2	2	289.1	8
	C=O	288.1	4	287.8	6	287.9	12
Si2p	SiO_2	103.3	100				
	Si–O			102.2	100	102.0	100

An analysis of the surface chemistry of the native and coated substrates using X-ray photoelectron spectroscopy (XPS) revealed that appreciable differences existed between the surface chemical characteristics of these substrates, as summarized in Table VIII.2.2, where the relative concentration refers to the assignment of the element to a particular binding state (e.g., in 10 W sample, 81% of O is in C--O/C=O/Si—O, and 19% is in *O--C=O). In the case of the unmodified glass, the SEM analysis revealed the presence of predominantly Si and O, which is expected of glass surfaces. Examination of the C1s high-resolution spectra indicated the existence of hydrocarbons (C–C, C–H), carbon singly bonded to oxygen or nitrogen (C–O, C–N), carbon doubly bonded to oxygen (C=O) and carbonate species (CO_3). Modification of the glass substrate using polyterpenol resulted in a significant increase of carbon available on the surface of the substrate. Furthermore, polyterpenol coatings deposited at different RF input power differed in terms of their C and O ratio, with films fabricated at 10 W characterized with lower oxygen (17.2% *vs.* 27.5%) and higher carbon (80% *vs.* 68.4%) fractions compared to polymers deposited at 25 W. Silicon was present in small quantity (~3%) on both types of polyterpenol films, whilst some Na (0.4%) and N (1.0%) traces were detected on 25 W samples.

VIII.2.3.2 Bacterial Surface Properties

In addition to the surface properties of the substrates, bacterial surface characteristics such as hydrophobicity and surface charge were investigated. The *P. aeruginosa* cells have been characterized as moderately hydrophilic, with a water contact angle of ~43°, whilst *S. aureus* cells exhibited more hydrophobic characteristics, with a water contact angle of ~72°, most likely due to the presence of highly negatively charged and hydrophobic teichoic and lipoteichoic acid sites in the *S. aureus* cell walls [37,38]. The zeta potential of the bacterial cells (ζ) was estimated to be -14.4 ± 0.7 mV and -35.2 ± 1.0 mV for *P. aeruginosa* and *S. aureus*, respectively. These results were used to deduce the cell surface charge characteristics of the studied microorganisms. The *S. aureus* cells were more electronegative compared to those of *P. aeruginosa*, with the respective mobilities in the range of -2 (μm/s)/(V/cm) and -1.12(μm/s)/(V/cm). Negative charge is common for the majority of microbial cell surfaces, with the values given above being consistent with previously published results for these two bacterial species [40,41]. Given the estimated surface wettability and surface charge of the *P. aeruginosa* and *S. aureus* bacterial cells, these microorganisms may not have a strong affinity for the highly hydrophilic surface of the unmodified glass substrate [18].

VIII.2.3.3 Bacterial Attachment

The attachment patterns of *P. aeruginosa* and *S. aureus* cells after 18 h incubation were examined by means of high-resolution SEM and confocal scanning laser microscope (CLSM) imaging, followed by statistical analysis. The attachment patterns of the two bacterial species were seen to be markedly different, preserving, however, a similar response on two types of polyterpenol film, as shown in Figure VIII.2.2 and reported in [34]. Furthermore, inspection of the SEM images demonstrated notable differences in the cell morphology, production of EPSs, and the numbers of bacterial cells attaching to the three types of substrates, namely the unmodified glass, polymer film fabricated at 10 W and the coating deposited at 25 W input power.

Overall, the number of cells attached to the surface modified with 25 W polyterpenol thin films was found to be significantly higher when compared to the number of cells attaching to the unmodified glass and 10 W polyterpenol surfaces, despite the fact that surfaces of polyterpenol thin films fabricated under 10 W RF were smoother on nanometer scale than those of the unmodified glass (Figures VIII.2.2 and VIII.2.3). This is due to the antibacterial inhibitory properties exhibited by these surfaces, resulting in lower amounts of bacterial attachment. In the case of *S. aureus*, however, the SEM images clearly showed an increase in the number of attached cells for substrates modified with 25 W polyterpenol coating. Furthermore, the distribution of *S. aureus* cells on the surface changed from irregular to more uniform for 10 W and 25 W samples, respectively. Morphological examination of *S. aureus* revealed slight differences in cell size on the sample surfaces, with larger ~0.8–1 μm cells appearing on the surface of the unmodified glass and 25 W samples as opposed to the ~0.6 μm cells adhered to the surface of the 10 W polyterpenol coatings.

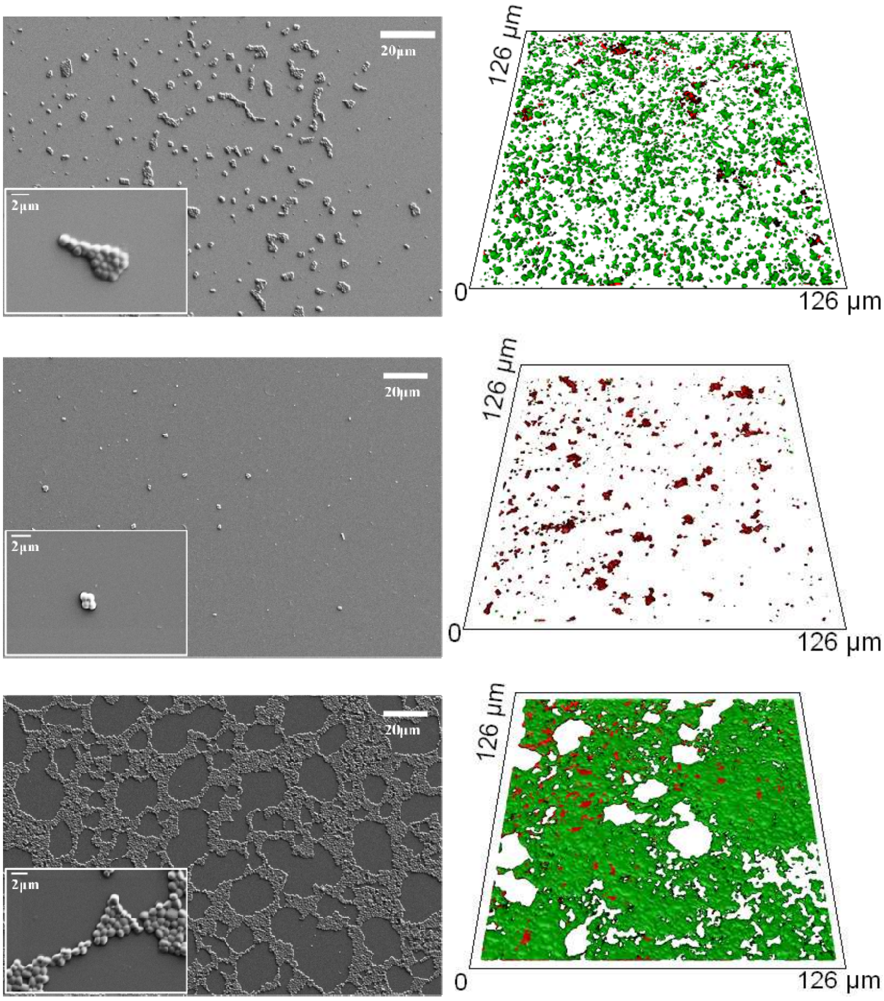

Figure VIII.2.2. Representative *S. aureus* attachment patterns on the unmodified (top panel) glass, modified with 10 W (middle panel), and 25 W (bottom panel) polyterpenol thin coating after 18 h incubation. Images on the top collected using SEM; (inset) SEM images showing typical cell morphologies of the attached microorganisms. Confocal scanning laser microscopy (CSLM) images (righ) visualize viable cells stained green and dead cells stained red with BacLight® Dead/Live Kit (Invitrogen), scanned areas of approximately 126 μm × 126 μm.

The amount of EPS produced by *S. aureus* cells was not significant for all of the samples examined, as confirmed by CLSM. The *S. aureus* attachment pattern on the polymer was further investigated using CLSM imaging, with the results confirming the observations made from the SEM data. The CLSM images of live cells (stained red with SYTO® 17 Red) and EPS (stained green with concanavalin A 488) produced by cells attached to the unmodified and polymer coated surfaces were statistically analyzed using the COMSTAT package. Figure VIII.2.3 shows the biovolume and average biofilm thickness of *S. aureus* on the surfaces of the unmodified glass and polymer coated substrates, calculated using the COMSTAT software.

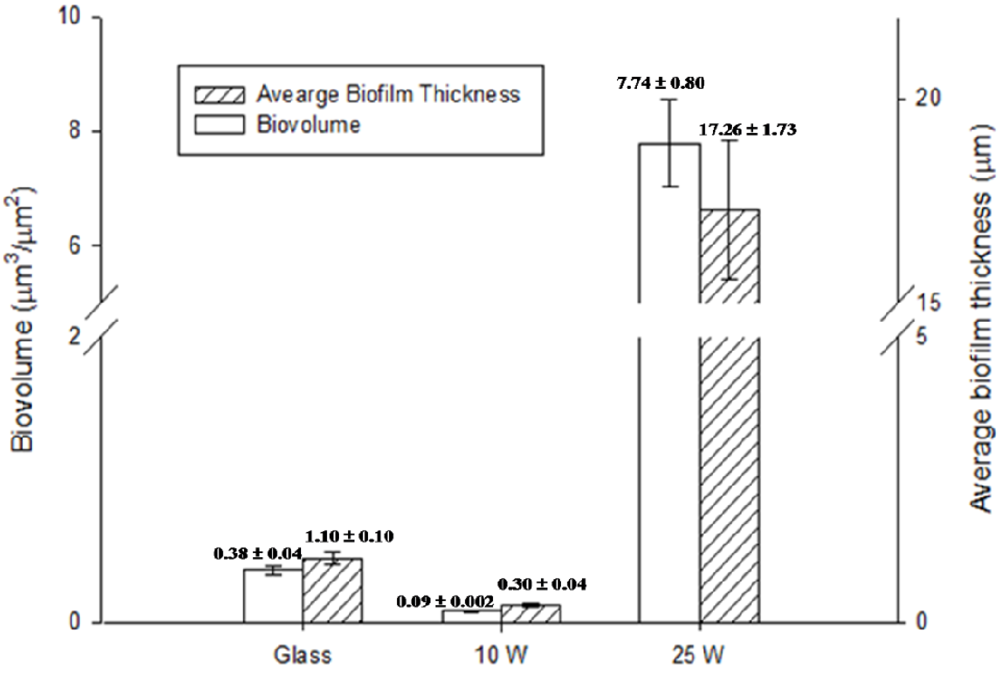

Figure VIII.2.3. Quantification of *S. aureus* biovolume and average biofilm thickness on the surfaces of the unmodified glass and polymer coated substrata.

An error of approximately 10–15% in the density values obtained for these samples can be attributed to the local variability in the surface coverage. A SEM analysis of the glass surface used as an experimental control revealed an even distribution of the attached cells across the surface of the substrate, with the attachment response being somewhat similar to that obtained for the surfaces of the 10 W deposition samples. However, the 3D CLSM imaging revealed a much higher number of cells attached to the glass surface compared to that of the 10 W coating, with an average biofilm thickness being approximately 4 times larger on glass than that on the 10 W polyterpenol films. The *S. aureus* cells exhibited a preference for attachment onto the 25 W polymer modified surface as evident from the SEM and 3D CLSM images. Analysis of CLSM images (Figure VIII.2.2) clearly indicated that above 90% of *S. aureus* cells retained on the surfaces of 10 W substrata were non-viable, in contrast to *S. aureus* cells retained on the unmodified glass and 25 W substrata.

These results for *S. aureus* are consistent with previously reported observations for *P. aeruginosa* [34], where the number of *P. aeruginosa* cells attaching to the 10 W polymer surface was found to be significantly lower than that obtained on the glass surfaces, with an average biofilm thickness of 0.47 ± 0.02 μm compared to thicknesses of 1.14 ± 0.22 μm and 23.09 ± 2.15 μm observed on glass and 25 W substrates, respectively. Furthermore, *P. aeruginosa* cells were found to be significantly larger and slightly thinner (~1.7–2 μm long and ~0.5–0.6 μm wide) when attached to the 25 W substrate and the glass reference sample compared to those attached to the 10 W samples (~1.2 μm long and ~0.7 μm wide). Similarly, the cells produced significantly more EPS when attached to the glass and 25 W substrates, with the biovolume increasing from 0.09 ± 0.005 $\mu m^2/\mu m^3$ on the 10 W surfaces to 0.61 ± 0.09 $\mu m^2/\mu m^3$ and 4.34 ± 0.39 $\mu m^2/\mu m^3$ on the glass and nanosmooth surfaces of 25 W samples, respectively.

VIII.2.4 Discussion

Our results showed that the presence of the polyterpenol thin films significantly altered the surface properties of the glass substrates, which resulted in a notable change in the adhesion behavior of both *P. aeruginosa* and *S. aureus* cells. The difference in surface architecture was reflected in the surface roughness parameters of polyterpenol coatings applied under different deposition power. This was attributed to the degree of monomer fragmentation resulting from the increased intensity of the plasma field. The lower deposition rate and higher substrate temperature associated with the increased RF power conditions allowed for a faster relaxation of film fragments within the growth region prior to deposition of the next layer of the film, resulting in a smoother surface [22]. This observation is clearly supported by the notable differences in roughness parameters of the two polyterpenol surfaces examined, particularly when the data from 10 μm × 10 μm scanning area sizes are compared. The higher peaks observed on the surfaces of the 10 W samples can be also explained by the presence of large fragments of terpinen-4-ol molecule that are loosely bound to the surface of the polymer matrix.

Modification of the surface properties using polyterpenol not only altered the surface architecture, but also the surface chemistry. The combined effect of these two parameters can strongly influence the extent of bacterial adhesion and proliferation while preserving the material properties inherent to the substrate, such as the mechanical properties [39]. Alterations of the functional groups present on the surface of the substrate change the surface hydrophobicity and surface energy. These parameters not only directly affect the interactions between the cells and the substrate, but also the manner in which the surface interacts with its immediate environment, such as the liquid medium [40]. Previously published *S. aureus* adhesion studies showed that bacterial cells tended to attach more effectively to surfaces bearing carboxylic and methyl functional groups than those containing hydroxyl functionality [41]. Other studies reported a reduction in bacterial adhesion for negatively charged poly(methyl methacrylate)/acrylic acid functional groups, whilst the presence of positively charged methyl methacrylate/ dimethylaminoethyl methacrylate groups resulted in an increased level of bacterial cell attachment [14]. In this study, the modification of the surface chemistry of the substrates resulted in a significant increase in the amount of carbon available on the surface. The higher oxygen concentration observed in the case of the 25 W polymer films can be attributed to the oxidation of the top layer of the film, which is part of the post-degradation ageing reaction occurring in the film. Due to the nature of the fabrication process, films manufactured at higher input energy tend to contain a higher number of radicals compared to those deposited at lower power settings, as the lower power conditions favour the preservation of original molecular structure of the monomer precursor [31].

Comparison of the attachment preferences of *S. aureus* to unmodified glass surfaces and 25 W polymer coated substrates showed that the presence of the polyterpenol film resulted in a significant increase in the number of the attached bacterial cells, their size and the quantity of EPS these cells produced. *P. aeruginosa* was also found to attach more readily to the 25 W samples compared to the unmodified glass substrates, a behavior similar to that previously reported for *P. aeruginosa* on topographically dissimilar glass surfaces and on polyterpenol samples [34,42]. There is much debate and controversies concerning the extent to which surface free energy and its polar component affect bacterial adhesion [43,44]. In the case of *S. aureus*, the thermodynamically predicted preference of hydrophobic cells for hydrophobic substrates can partially account for the reduced cell adhesion to the more hydrophilic surface of the unmodified glass substrate, as reported elsewhere [45]. The 25 W polymer layer is smooth on the sub-nano-scale roughness level compared to unmodified substrate; therefore the current “attachment point” theory [46-47] that suggests that bacterial cells prefer microscopic surface irregularities as the starting point for their attachment as these provide shelter from unfavourable environmental influences clearly also cannot explain the attachment behaviour. Our recent studies found that nano-scale surface roughness may have a notable effect on bacterial attachment and adhesion, with nano-scale fluctuations in roughness exerting a significant influence on the cellular response to certain surfaces [18,42,48]. The results presented here show that a higher number of bacterial cells were able to colonize the nanosmooth 25 W polymer coated substrates, whereas less smooth, unmodified glass substrates sustained a significantly lower level of cellular attachment. This adhesion tendency was observed for both strains used in this study, regardless of their taxonomic affiliation and their cell surface characteristics. Further studies on polyterpenol coatings fabricated at even higher RF powers showed a similar trend [49].

Glass substrates modified with a 10 W polyterpenol coating exhibited the least number of bacterial cells adhering to the surface. In its monomer form, terpinen-4-ol has been characterized as a nonspecific membrane active biocide that possesses adequate hydrophilicity to diffuse through liquid medium to the bacterial cytoplasmic membrane and hydrophobicity necessary to diffuse through the bacterial cytoplasmic membrane [28], where it accumulates causing a loss of membrane integrity [50]. Previous studies have demonstrated that it is possible to preserve certain functionalities and hence the biological activity of terpinen-4-ol in polyterpenol thin films by using relatively low deposition power conditions [33,34]. Hence, the significant reduction in the attachment of bacterial cells observed on these surfaces could be due to the preservation of chemical activity rather than the reduction in the surface irregularities or an increase in the hydrophobicity of the surface compared to the unmodified substrate.

VIII.2.5 Conclusions

High resolution AFM studies showed that application of a polyterpenol coating significantly altered the surface topography of the substrates, decreasing the substrate average surface roughness (R_a) from approximately 0.4 nm to 0.25 nm and 0.13 nm for 10 W and 25 W polyterpenol coatings, respectively (scan size 1 μm × 1 μm). A statistical analysis of the roughness parameters showed that there was a statistically significant difference in the surfaces roughness parameters for each of the coated and unmodified substrates used in this study. The extent of bacterial attachment and EPS production was then analysed using SEM and CSLM. The CSLM and SEM analyses clearly demonstrated that *S. aureus* and *P. aeruginosa* presented notably different patterns of attachment onto surfaces of polyterpenol thin films fabricated under the two conditions. The smooth on the scale of nanometers 25 W polyterpenol coating resulted in enhanced attachment and adherence of two taxonomically different bacterial strains, the behaviour previously described in our recent works. However, bacterial attachment can be further controlled by changing the surface chemical functionality, by, for example, coating the substrate with terpinen-4-ol, a compound with known bacterial inhibitory activity. Despite being characterized as smoother on a nanometer scale than glass surfaces, the degree of attachment, EPS production, and cell proliferation on the polyterpenol thin films fabricated under 10 W was found to be greatly reduced compared to that obtained on the unmodified surface or on the polyterpenol thin films fabricated under 25 W deposition power conditions. The added advantages of this coating include uniform coverage, good adhesion to the substrate, and film stability. Furthermore, the antibacterial efficacy is based on the presence of a natural antimicrobial compound with no use of antibiotics. Thus, this work suggests that such an antimicrobial and antifouling coating could be effectively integrated into medical and other clinically relevant devices to prevent bacterial growth, thus minimizing bacteria-associated adverse host responses.

CHAPTER IX

CONCLUSIONS AND RECOMMENDATIONS FOR FUTURE WORK

The development of novel organic polymers with properties equivalent to or superseding those of existing materials is an area of intense research investigation and commercial investment. Development of novel and enhancement of existing technologies are heavily reliant on the ongoing advancement of materials required for these applications. Recent progress in the field of organic thin films and coatings has already supported significant advancement of flexible optoelectronics and complex biomaterial devices. Yet, there are many avenues along which a noticeable improvement is necessary to bring such a technology from laboratory settings to a commercially viable product. The aim of this work was to develop a range of high−performance thin film polymer structures from non-synthetic monomer, terpinen−4−ol, using RF plasma polymerisation for application in emerging technologies. Terpinen−4−ol is a major constituent of *Melaleuca alternifolia* (tea tree) essential oil attributed with strong broad-spectrum antimicrobial and anti-inflammatory activities. RF plasma polymerisation is a ‘green’ fabrication method that requires minimal use of harmful chemicals and produces no hazardous by−products. As such, the choice of precursor material and fabrication methodology addresses a current global interest in environmentally responsible development.

IX.1 Polyterpenol thin film fabrication and fundamental characterisation

Plasma polymer thin films were fabricated using a custom made reactor under a range of processing parameters to achieve materials with distinct material (physical, chemical, optical, electrical), biological and degradation characteristics. Film deposition was performed using low−temperature plasma, which allowed for use of temperature sensitive substrates, such as plastics and thin film devices, in addition to metals, glasses, and ceramics. External capacitively coupled copper electrodes were used to deliver RF energy to the cylindrical polymerisation chamber. The experimental arrangement, including deposition time and pressure, use of additional gases, electrode spacing, placement of electrodes and substrate holder, were optimised to ensure uniformity and improve properties of the resultant thin film structures. Deposition time was found to significantly affect film thickness, with minimal influence over material properties of polyterpenol. Input RF power, on the other hand, was demonstrated to be a significant determinant of material properties of polyterpenol thin films. Therefore, properties of polyterpenol films deposited at various RF powers were investigated using the characterisation facilities available at James Cook University and collaborating national and international institutions. A summary of the major findings are presented below.

IX.1.1 Chemical properties

Chemical characteristics of bulk polyterpenol thin films were investigated using FTIR, Raman and XRR. Exposure to RF plasma field notably altered the chemical structure of terpinen−4−ol monomer, with polymer films retaining only some of the original monomer functionalities. Polyterpenol thin films were characterised as hydrocarbon rich structures, with variable oxygen content. Lower RF deposition powers favoured preservation of the high polarizability moieties, such as hydroxy group, and therefore was found to be more appropriate for fabrication of insulating films. These conditions also promoted condensation and incorporation of unfragmented or slightly fragmented terpinen−4−ol molecules into the matrix of the film, thus increasing the likelihood of such materials to retain the biological activity of the precursor. Application of higher RF deposition powers resulted in higher degree of monomer fragmentation, with the resultant films being highly cross-linked and brunched, and characterised by shorter polymer chains. XPS characterisation of chemical composition and structure of polyterpenol surfaces confirmed the hydrocarbon nature of the material, with oxygen moieties present in the form of hydroxy and carboxylic acid functional groups. The availability of oxygen containing functionalities varied with power of deposition. Trace amounts of N, Si and Zn were also detected, attributed to contamination during deposition.

Surface tension and solubility parameters of polyterpenol thin films as a function of the deposition RF power were also examined using six different solvents. For solvents such as water, glycerol, DIM and formamide, reactions between the solid-liquid interface and evaporation were taking place; in the case of ethylene glycol and DMSO, the reorientation of functionalities at the solid-liquid interface occurred. Improved stability was observed for films fabricated at higher RF powers due to the increased degree of cross linking and the decrease in the oxygen content associated with the higher deposition power; the decrease in oxygen containing functional groups was responsible for the increased hydrophobicity of the polymer surface, from 62.7° for the 10 W samples to 76.3° for the films deposited at 100 W. Polyterpenol films manifested mostly electron donor properties with hardly any electron acceptor properties. Polymers were determined to be not water soluble due to the extensive intermolecular and intramolecular hydrogen bonds present. Polyterpenol films fabricated at higher RF powers were less soluble for all test liquids as well as other solvents commonly used in electronics and biomedical processing, namely hexane, chloroform, acetone and ethanol. Solubility and wettability results obtained for polyterpenol confirmed that thin films deposited from terpinen−4−ol using RF plasma deposition can be used for applications where the polymer must resist solubilisation, i.e. if it is used as a protective coating; a thermally degradable sacrificial material in IC fabrication where wet etching procedure is used; or an antifouling coating for implantable medical devices.

IX.1.2 Surface properties

Independent of deposition power, the surface topography of the polymers was shown to be smooth, uniform and defect free. Smooth surface of polyterpenol films indicates that the polymerization reactions took place predominantly on the surface of the glass substrate rather than in the gas phase. Analyses of surface features obtained using AFM in semi−contact mode showed a small change in surface architecture with deposition power. The maximum peak height, average and RMS roughness parameters decreased for films deposited at higher RF power. These roughness estimates were in agreement with roughness values derived using spectroscopic ellipsometry. Deposition power did not have an effect on surface skewness or coefficient of kurtosis, with all polyterpenol thin films characterised by a disproportionate number of peak and a well spread out height distribution pertaining to the polyterpenol surfaces.

IX.1.3 Optical properties

UV-Vis spectroscopy and spectroscopic ellipsometry were utilised for optical characterisation of polyterpenol thin films. Independent of deposition power, all films were optically transparent, as confirmed by an examination of UV-Vis spectra. The main absorption peak occurred outside the visible region of the spectrum. Application of higher RF power did not produce a shift and/or broadening of the absorption peak. Transmission measurement using spectroscopic ellipsometry confirmed the optical transparency of polyterpenol. The refractive index of polyterpenol was similar to that of glass, increasing slightly for films fabricated at higher RF power. Independent of deposition power, the extinction coefficient approximated zero at wavelengths above 500 nm. The optical band gap values declined with increase in RF deposition power, from 2.95 eV for 10 W to 2.64 eV for 100 W.

IX.4 Electrical properties

At optical frequencies, the real part of permittivity (k) was determined using spectroscopic ellipsometry. It was found to be between 2.34 and 2.65 in the wavelength region 400 nm to 1100 nm indicating a potential low-k material. These permittivity values were confirmed at microwave frequencies determined by means of split post dielectric resonators operating at frequencies of 10 GHz and 20 GHz. Employing full wave electromagnetic theory, permittivity and dielectric loss tangent were derived from the observed shift in measured resonant frequency and Q-factor of resonator with bare substrate and of resonator with coated substrate.

Permittivity increased for samples deposited at higher RF energy − from 2.65 (25 W) to 2.83 (75 W) measured by 20 GHz resonator and from 2.32 (25 W) to 2.53 (100 W) obtained using 10 GHz resonator. At low frequencies, the dielectric constant was determined from current−voltage characteristics of Al−polyterpenol−Al devices. At frequencies between 1 Hz and 100 kHz, the dielectric constant varied with RF power, from 3.86 (10 W) to 4.42 (100 W) at 1 kHz.

The current density–voltage characteristics of polyterpenol films of different thickness were investigated at room temperature. In higher applied voltage region, DC conduction was dominated by Schottky conduction mechanism, whereas up to 2.5 V an approximately ohmic conduction prevailed. The resistivity of the polyterpenol were found to decrease for films deposited at higher RF power, attributed to the change in the chemical composition and structure of the polymer. The resistivity for all samples are in the order of 10^8-10^9 Ωm (calculated at 6 V), confirming the insulating nature of polyterpenol material.

In situ iodine doping was demonstrated to increase the conductivity of polyterpenol, from 5.05×10^{-8} S/cm to 1.20×10^{-6} S/cm (at 20 V). The change was attributed to changes in the chemical structure of polyterpenol, via incorporation of iodine into the backbone of the polymer and consequent reduction in the methyl and methylene functionalities and an appearance of C=C bond, as determined by FTIR. XPS confirmed that reduction in oxygen and an increase in carbon atomic fractions, indicating abstraction of H being a likely process. Although increasing the conductivity most, higher levels of doping were detrimental to optical transparency of the doped films, owing to the strong absorption of light characteristic of iodine species. Higher levels of doping notably increased the refractive index of the thin films, from 1.54 to 1.70 (at 500 nm). Introduction of iodine impurity reduced the band gap of polyterpenol, from 2.8 eV to 1.64 eV, by extending the density of states more into the visible region of the electromagnetic spectrum and an increase in C=C bonds in the iodine doped film layers compared to pristine polyterpenol. While doping did not affect surface morphology of the film, increased hydrophilicity of doped samples was attributed to a significantly larger number of polar functional groups exposed to the top of the polymer surface. Iodine doped samples were found to be monopolar in nature, largely manifesting electron-donor properties, although the electron-acceptor fraction of the surface tension for iodine doped samples was significantly higher than that of pristine polyterpenol, due to the presence of iodine atoms. Annealing to 100 °C for 5 hours resulted in the band gap of doped polyterpenol increased slightly, the increase was attributed to desorption of loosely bonded iodine atoms from the surface of the film, and remained stable thereafter.

IX.5 Mechanical properties and adhesion

Mechanical and tribological properties of polyterpenol thin films were examined using nanoindentation and nanoscratch analyses. Coatings fabricated at higher deposition power were characterised by improved hardness and enhanced wear resistance. The hardness increased from 0.33 GPa for 10 W to 0.51 GPa for 100 W at 500 μN load. The elastic recovery was estimated to be between 0.1 and 0.14. Absence of significant fluctuations in the friction coefficient indicates no considerable damage, cracking or delamination of the coating occurred. Coatings deposited at higher RF powers showed less mechanical deformation attributed to increased degree of cross-linking associated with higher input power and hence are likely to be more stable and less susceptible to wear. Potential for damage and delamination of polyterpenol coatings was also qualitatively assessed using a standardised cross-hatch test. Independent of the substrate, the quality of adhesion is improved for samples deposited at higher RF power; the results consistent with those obtained using nanoindentation system. This study substantiate that the polyterpenol, which adheres well to many commonly used substrates, is a potential candidate for thin film applications which require smooth and uniform surfaces.

IX.6 Stability of polyterpenol

Optical parameters, thickness and chemical structure of polyterpenol thin films prepared at different deposition powers were observed over the period of 1128 h. Under ambient conditions, the bulk of ageing occurred within first 150 h after deposition and was attributed to oxidation and volumetric relaxation. Changes of under 0.58 and 0.37 % in refractive index and thickness respectively were insignificant confirming the polyterpenol films were stable when in contact with ambient environment and therefore can potentially be used as an encapsulating layer in circuitry. The chemical characterisation established that the aging of polymers deposited at lower RF power occurred via oxidation, as observed by a slight increase in the −OH stretch assigned to alcohol.

Thermal ageing studies were conducted *in situ* using the heat stage attachment for the ellipsometer and *ex situ* using FTIR. The results indicated thermal stability increased for the films manufactured at higher RF powers. The refractive index was found to undergo a large change between 200 and 300 ºC, indicating the material undergoes a phase change within this temperature region. Heating up to 150 ºC had minimal effect on chemical composition and refractive index of the material, whereas thickness reduced due to desorption of low molecular weight species. The onset temperature at which decomposition begins was lower in the case of polymer films fabricated at lower RF power. Above 250 ºC, peaks associated with C−H bonding reduced, whereas bands assigned to C−O stretches and C=C increased in intensity. Hydrogen abstraction and radical transfer to the tertiary carbon atom followed by the scission of a C–C bond in the β–position have been identified as the likely processes to transform the original polyterpenol film into a less hydrocarbon dense structure. Annealing the films to 405 °C resulted in full degradation, with retention between 0.29 and 0.99 %. Films deposited at lower RF powers showed most promising decomposition outcomes due to their less cross−linked structure compared to the films fabricated at higher RF power. Polyterpenol films are therefore believed to have great potential for use as sacrificial material in air gap fabrication due to their controllable degradation onset temperature and minimal residue levels.

IX.2 Applications of polyterpenol in electronics and biomaterial coatings

Given the outcomes of the fundamental characterisation, a number of potential applications for polyterpenol have been identified. The tunable permittivity and loss tangent properties of polyterpenol suggest the material can be used as a low permittivity dielectric in fabrication of integrated circuit fabrication. The flexible nature of the polyterpenol films further substantiates the material's potential as an insulating layer in plastic electronics. Optical transparency and variable optical band gap indicate polyterpenol can find potential applications in optoelectronics. Sound adhesion, good chemical and physical stability, and low temperature of fabrication suggest polyterpenol can be used for encapsulation of photovoltaic devices. Encapsulation of biomedical devices is also proposed, given that under favourable conditions, the original chemical and biological functionality of terpinen−4−ol molecule can be preserved. Furthermore, polymers fabricated from non-synthetic precursors are likely to be biocompatible with human tissues, and therefore can potentially be used to promote eukaryotic cell adhesion and proliferation. Depending on their reactivity, these coatings can also be used to encapsulate metals, such as magnesium, to control their biodegradation *in vivo*.

IX.2.1 Polyterpenol as a gate insulating layer

Favourable material characteristics of polyterpenol, particularly its permittivity and loss tangent characteristics have identified the material as a potential dielectric layer for fabrication of flexible OFET devices. Implementation of polyterpenol as a surface modification of the gate insulator in pentacene-based field effect transistor resulted in significant improvements. The addition of the polyterpenol interlayer in the OFET shifted the threshold voltage significantly, from + 20 V to –3 V. No trapped charges were observed in the polyterpenol interlayer, which assisted in the improvement of effective mobility of the device, from 0.012 to 0.021 cm^2/Vs. The switching property of the polyterpenol based OFET was also improved, from 10^7 to 10^4.

The results showed that the non-synthetic polyterpenol polymer film is a promising candidate of insulators in electronic devices.

Time-resolved electric field induced second harmonic generation technique was then used to probe the carrier transients within double−layer pentacene−based MIM devices, where polyterpenol thin film was used as a blocking layer. Given that pentacene is an ambipolar organic semiconductor, a blocking layer is used to assist in visualisation of single−species carrier transportation during charging and discharging under different bias conditions. Time−resolved measurement demonstrated injection and accumulation at the interface of both holes and electrons under forward and reverse bias conditions, respectively. However, the nature of SH activity during the discharging differed between the two cases. Where holes were the injected carriers, the discharging of the interface involved the accumulated carriers drifting back into the Au electrode. However, when the accumulated charges were electrons, the discharging entailed an injection of holes from the Au electrode. Polyterpenol was demonstrated to be a sound blocking material and can therefore be used for probing of double−layer devices using this technique. Polyterpenol fabricated at higher RF power were identified as being a better suited material due to higher stability, particularly during pentacene deposition, improved uniformity, and absence of defects.

The charge transport mechanism across plasma polymerised polyterpenol was also studied by depositing C_{60} n-type organic semiconductor on the polyterpenol thin film and Al top electrodes. Charge accumulation under the steady state was demonstrated for electron injection from the Al/C_{60}, whereas no charge accumulation was observed for hole injection from Al/C_{60}. Resulting from these observations, electron blocking property of polyterpenol was proposed as a likely mechanism. Electroluminescence spectrum measurement using Al/C_{60}/Alq3/polyterpenol/IZO structures evidently confirmed the rectifying property of polyterpenol, with electron and hole recombination taking place in Alq3 and C_{60} layers, indicated by the EL wavelengths of the emitted light consistent with Alq3 and C_{60} photoluminescence spectra. This study substantiate that the environmentally friendly transparent polyterpenol thin film will be an excellent candidate to be used as a ‘hole transport electron blocking layer’ in organic electronic circuits and hence can be utilized in the fabrication of many organic devices, such as organic light emitting diodes.

IX.2.2 Polyterpenol as a bioactive coating

Polyterpenol thin films fabricated at varied RF power have also been investigated as potential antifouling and antibacterial coatings for biomaterials. The extent of bacterial attachment and extracellular polymeric substances (EPS) production were analyzed using scanning electron microscopy (SEM) and confocal scanning laser microscopy (CSLM). The CSLM and SEM analyses clearly demonstrated that *Pseudomonas aeruginosa*, *Staphylococcus aureus*, and *Streptococcus epidermidis* presented notably different patterns of attachment onto surfaces of polyterpenol thin films fabricated under different RF power. Such differences in attachment behaviour were attributed to a combination of species−specific cell morphology, cell structure and surface properties, and the extracellular substances bacteria produce. Cell−polyterpenol surface interactions were significantly affected by the chemical functionality of polyterpenol. However, independent of the species, the number of retained cells was greatly reduced on 10 W polyterpenol coated surfaces. Films deposited at low RF power were shown to successfully prevent adhesion and retention of several important human pathogens, including *P. aeruginosa*, *S. aureus*, and *S. epidermidis*. On the other hand, films deposited at higher RF power promoted cell adhesion, proliferation and EPS production. Furthermore, cells adhered to 25 W polyterpenol were found to conform to a 3D architecture, indicating the formation of biofilm. The nanotopography of polyterpenol coating was also demonstrated to affect the attachment and adherence of taxonomically different bacterial strains. The proposed antimicrobial and antifouling coating can be potentially integrated into medical and other clinically relevant devices to prevent bacterial growth and to minimize bacteria-associated adverse host responses.

IX.3 Recommendation for future work

It is evident that polyterpenol is a promising candidate for applications in organic electronics. However, further investigation into polyterpenol degradation of the material under various environmental conditions and long-term performance are required. For instance, some stages of IC fabrication may require high−temperature processing, for which polyterpenol may need to be modified to increase the thermal stability of the material. Similarly, polyterpenol behaviour when in contact with solutions used in IC wet processing need to be controlled. Polyterpenol performance upon long-term exposure to UV light would require further investigation to assess the polymer’s potential as an encapsulating layer for organic photovoltaics. Performance of polyterpenol−incorporated electronic devices also necessitates detailed exploration to demonstrate improvement. Low temperature annealing should also be pursued to assess the influence of this treatment onto electrical properties of polyterpenol. Doping using other agents, in addition to iodine, need to be considered to further enhance conductivity of polyterpenol.

Additional work is also expected to confirm biomedical applicability of polyterpenol. Preliminary investigations into *in vitro* biocompatibility of polyterpenol demonstrated the coating to be non−toxic for several types of eukaryotic cells. Balb/c mice macrophage and human monocytes (HTP−1 non-adherent) cells showed similar attachment, cell morphology and viability when in contact with polyterpenol coated and unmodified glass slides. Furthermore, when applied to magnesium substrates, polyterpenol encapsulating layer significantly slowed down *in vitro* biodegradation of the metal, thus increasing the viability and growth of HTP−1 cells. Recently, applied to varied nanostructured titanium surfaces, polyterpenol thin films successfully reduced attachment, growth, and viability of *P. aeruginosa* and *S. aureus*. This experiment demonstrated that polyterpenol retains its bactericidal activity when deposited over commercially used biomaterials. Yet, more work is needed to explain the nature of the material's bioactivity. The stability and biodegradation of polyterpenol under *in vitro* and *in vivo* conditions also warrants further research.

Tunable thermal degradation with low residue rates demonstrated polyterpenol as a potential sacrificial material for fabrication of nanofluidic channels in chip based bio/chemical analysis, air gap fabrication and in semiconductor devices to produce ultra low permittivity dielectrics. A study comparing performance of polyterpenol to conventional sacrificial materials is needed to determine material's applicability for this application.

IX.4 Conclusion

Environmentally−friendly polyterpenol thin films were successfully fabricated from non−synthetic terpinen−4−ol using plasma polymerisation. Table IX.1 shows the summary of polyterpenol material properties:

Table IX.1. Material properties of polyterpenol fabricated at different RF powers.

Property	Deposition RF power			
	10 W	25 W	50 W	100 W
Refractive index n (500 nm)	1.537	1.544	1.548	1.554
Extinction coefficient k (500 nm)	2.67×10^{-5}	8.25×10^{-5}	75.01×10^{-5}	160.7×10^{-5}
Optical band gap E_g, eV	2.95	2.83	2.81	2.64
Permittivity (<100 kHz)	15.2-3.75	17.3-4.15	18.4-4.15	17.3-4.30
Permittivity at high frequencies	2.84	2.80	2.81	2.81
Conductivity σ, S/cm	8.21×10^{-10}	1.12×10^{-9}	1.47×10^{-9}	1.52×10^{-9}
Average roughness R_a, nm	0.44	0.40	0.40	0.33
Water contact angle θ_w, °	60.3	62.5	64.4	75.2
Surface tension, mJ/m^2	29.4-46.2	30.0-42.5	30.1-41.6	29.9-41.5
Thermal degradation onset temperature, °C	~150	~150	~170	~190
Hardness, GPa (at 500 μN)	0.32	0.35	0.42	0.51
Friction coefficient	0.46	0.35	0.29	0.26
Antimicrobial activity against common pathogens	Active	Not active	Not active	Not active
Cytocompatibility	Compatible	Compatible	Compatible	Compatible

Property variability was achieved by varying deposition conditions, as demonstrated by extensive polymer characterisation. In the course of this work, several potential applications in the fields of biomaterials and electronics have been identified. Extensive testing was conducted to show applicability of polyterpenol as an insulating layer in organic electronics devices and as bioactive layer for encapsulation of biomaterials.

BIBLIOGRAPHY

[1] C. Cen, S. Thiel, J. Mannhart, J. Levy, Science 323 (2009) 1026.

[2] J.V. Barth, G. Costantini, K. Kern, Nature 437 (2005) 671.

[3] J.D. Meindl, Q. Chen, J.A. Davis, Science 293 (2001) 2044.

[4] D.R. Steinke, J. Piccirillo, S.C. Gausepohl, S. Vivekand, M.P. Rodgers, J.U. Lee, Solid-State Electron. 68 (2012) 51.

[5] L. Ding, Z. Wang, T. Pei, Z. Zhang, S. Wang, H. Xu, F. Peng, Y. Li, L.-M. Peng, ACS Nano 5 (2011) 2512.

[6] A.J. Heinrich, C.P. Lutz, J.A. Gupta, D.M. Eigler, Science 298 (2002) 1381.

[7] M. Halik, A. Hirsch, Adv. Mater. 23 (2011) 2689.

[8] G. Gelinck, Nature 445 (2007) 268.

[9] W.-Y. Wong, B.Z. Tang, Macromol. Chem. Phys. 211 (2010) 2460.

[10] D. Gendron, P.-O. Morin, P. Berrouard, N. Allard, B.R. Aïch, C.N. Garon, Y. Tao, M. Leclerc, Macromolecules 44 (2011) 7188.

[11] S. Wang, P. Gao, I. Liebewirth, K. Kirchhoff, S. Pang, X. Feng, W. Pisula, K. Müllen, Chem. Mater. 23 (2011) 4960.

[12] T.-Y. Chu, J. Lu, S. Beaupré, Y. Zhang, J.-R.m. Pouliot, S. Wakim, J. Zhou, M. Leclerc, Z. Li, J. Ding, Y. Tao, J. Am. Chem. Soc. 133 (2011) 4250.

[13] T.R. Andersen, T.T. Larsen-Olsen, B. Andreasen, A.P.L. Bőttiger, J.E. Carlé, M. Helgesen, E. Bundgaard, K. Norrman, J.W. Andreasen, M. Jørgensen, F.C. Krebs, ACS Nano 5 (2011) 4188.

[14] J.-J. Kim, M.-K. Han, Y.-Y. Noh, Semicond. Sci. Technol. 26 (2011) 030301.

[15] W. Chen, D.C. Qi, H. Huang, X. Gao, A.T.S. Wee, Adv. Funct. Mater. 21 (2011) 410.

[16] A. Facchetti, Mater. Today 10 (2007) 28.

[17] M. Kitamura, Y. Arakawa, J. Phys.: Condens. Matter 20 (2008) 184011.

[18] W.W.H. Wong, T.B. Singh, D. Vak, W. Pisula, C. Yan, X. Feng, E.L. Williams, K.L. Chan, Q. Mao, D.J. Jones, C.-Q. Ma, K. Müllen, P. Bäuerle, A.B. Holmes, Adv. Funct. Mater. 20 (2010) 927.

[19] K.H. Lee, P.E. Schwenn, A.R.G. Smith, H. Cavaye, P.E. Shaw, M. James, K.B. Krueger, I.R. Gentle, P. Meredith, P.L. Burn, Adv. Mater. (Weinheim, Ger.) 23 (2011) 766.

[20] C. Ababei, S. Yuvarajan, D.L. Schulz, Sol. Energy 84 (2010) 1111.

[21] Q. Peng, X. Liu, D. Su, G. Fu, J. Xu, L. Dai, Adv. Mater. 23 (2011) 4554.

[22] S. Chen, L. Deng, J. Xie, L. Peng, L. Xie, Q. Fan, W. Huang, Adv. Mater. 22 (2010) 5227.

[23] B. Cho, S. Song, Y. Ji, T.-W. Kim, T. Lee, Adv. Funct. Mater. 21 (2011) 2806.

[24] D.T. Simon, K.C. Larsson, M. Berggren, A. Richter-Dahlfors, J. Biomech. Sci. Eng. 5 (2010) 208.

[25] M. Zhang, Y. Sun, X. Guo, C. Cui, Y. He, Y. Li, Macromolecules 44 (2011) 7625.

[26] R.M. Westervelt, Science 320 (2008) 324.

[27] A.K. Geim, Science 324 (2009) 1530.

[28] H. Park, P.R. Brown, V. Bulović, J. Kong, Nano Lett. (2011).

[29] C. Ramanan, A.L. Smeigh, J.E. Anthony, T.J. Marks, M.R. Wasielewski, J. Am. Chem. Soc. (2011).

[30] H.U. Khan, M.E. Roberts, W. Knoll, Z. Bao, Chem. Mater. 23 (2011) 1946.

[31] S. Yu, C. Klimm, P. Schäfer, J.P. Rabe, B. Rech, N. Koch, Org. Electron. 12 (2011) 2180.

[32] K.H. Lee, H.S. Lee, K. Lee, T. Ha, J.H. Kim, S. Im, Adv. Mater. 23 (2011) 1231.

[33] D.Y. Shu, G. Tarabella, N. Coppede, S. Iannotta, L. Lutterotti, F. Cicoira, J.E. Anthony, C. Santato, Appl. Phys. Lett. 99 (2011) 023304.

[34] M. Saito, T. Yamamoto, I. Osaka, E. Miyazaki, K. Takimiya, H. Kuwabara, M. Ikeda, ChemInform 42 (2011) no.

[35] M.J. Kang, I. Doi, H. Mori, E. Miyazaki, K. Takimiya, M. Ikeda, H. Kuwabara, Adv. Mater. 23 (2011) 1222.

[36] W. Li, M. Uno, Y. Hirose, T. Uemura, K. Takimiya, J. Takeya, Mol. Cryst. Liq. Cryst. 539 (2011) 58/[398].

[37] J.E. Northrup, Appl. Phys. Lett. 99 (2011) 062111.

[38] K. Nakayama, Y. Hirose, J. Soeda, M. Yoshizumi, T. Uemura, M. Uno, W. Li, M.J. Kang, M. Yamagishi, Y. Okada, E. Miyazaki, Y. Nakazawa, A. Nakao, K. Takimiya, J. Takeya, Adv. Mater. 23 (2011) 1626.

[39] H. Tanaka, M. Kozuka, S.-i. Watanabe, H. Ito, Y. Shimoi, K. Takimiya, S.-i. Kuroda, Phys. Rev. B 84 (2011) 081306.

[40] Y. Wen, Y. Liu, Adv. Mater. 22 (2010) 1331.

[41] Q. Wu, R. Li, W. Hong, H. Li, X. Gao, D. Zhu, Chem. Mater. 23 (2011) 3138.

[42] Z. Wu, B. Fan, A. Li, F. Xue, J. Ouyang, Org. Electron. 12 (2011) 993.

[43] V. Kamm, G. Battagliarin, I.A. Howard, W. Pisula, A. Mavrinskiy, C. Li, K. Müllen, F. Laquai, Adv. Energy Mater. 1 (2011) 137.

[44] H. Wonneberger, N. Pschirer, I. Bruder, J. Schöneboom, C.-Q. Ma, P. Erk, C. Li, P. Bäuerle, K. Müllen, Chem.- Asian J. 6 (2011) 1744.

[45] Z. Liang, R.A. Cormier, A.M. Nardes, B.A. Gregg, Synth. Met. 161 (2011) 1014.

[46] T.W. Chamberlain, E.S. Davies, A.N. Khlobystov, N.R. Champness, Chem.- Eur. J. 17 (2011) 3759.

[47] X. Zhan, A. Facchetti, S. Barlow, T.J. Marks, M.A. Ratner, M.R. Wasielewski, S.R. Marder, Adv. Mater. 23 (2011) 268.

[48] C.-W. Liang, W.-F. Su, L. Wang, Appl. Phys. Lett. 95 (2009) 133303.

[49] Y. Vaynzof, D. Kabra, L. Zhao, L.L. Chua, U. Steiner, R.H. Friend, ACS Nano 5 (2010) 329.

[50] A.K.-Y. Jen, J. Mater. Chem. 20 (2010) 2491.

[51] H. Ma, H.-L. Yip, F. Huang, A.K.Y. Jen, Adv. Funct. Mater. 20 (2010) 1371.

[52] D.M. DeLongchamp, R.J. Kline, D.A. Fischer, L.J. Richter, M.F. Toney, Adv. Mater. 23 (2011) 319.

[53] K. Hong, J.-L. Lee, Electron. Mater. Lett. 7 (2011) 77.

[54] A. Pron, P. Gawrys, M. Zagorska, D. Djurado, R. Demadrille, Chem. Soc. Rev. 39 (2010) 2577.

[55] X.-Y. Deng, Int. J. Mol. Sci. 12 (2011) 1575.

[56] Y. Sun, S.-C. Chien, H.-L. Yip, Y. Zhang, K.-S. Chen, D.F. Zeigler, F.-C. Chen, B. Lin, A.K.Y. Jen, Chem. Mater. 23 (2011) 5006.

[57] C.-Y. Chen, K.-Y. Wu, Y.-C. Chao, H.-W. Zan, H.-F. Meng, Y.-T. Tao, Org. Electron. 12 (2011) 148.

[58] S.-Y. Yu, D.-C. Huang, Y.-L. Chen, K.-Y. Wu, Y.-T. Tao, Langmuir (2011).

[59] N. Yong-Young, C. Xiaoyang, T. Marta, L. Mi-Jung, S. Henning, Semicond. Sci. Technol. 26 (2011) 034003.

[60] J. Park, W.H. Lee, S. Huh, S.H. Sim, S.B. Kim, K. Cho, B.H. Hong, K.S. Kim, J. Phys. Chem. Lett. 2 (2011) 841.

[61] K.-J. Baeg, J. Kim, D. Khim, M. Caironi, D.-Y. Kim, I.-K. You, J.R. Quinn, A. Facchetti, Y.-Y. Noh, ACS Appl. Mater. Interfaces 3 (2011) 3205.

[62] H. Zhang, X. Guo, J. Hui, S. Hu, W. Xu, D. Zhu, Nano Lett. 11 (2011) 4939.

[63] N.B. Ukah, J. Granstrom, R.R.S. Gari, G.M. King, S. Guha, Appl. Phys. Lett. 99 (2011) 243302.

[64] Y. Tian, C. Hu, Q. Wu, X. Wu, X. Li, M. Hashim, Appl. Surf. Sci. 258 (2011) 321.

[65] P. Chen, Y.-W. Lo, T.-L. Chou, J.-M. Ting, J. Electrochem. Soc. 158 (2011) H1252.

[66] J.E. Allen, C.T. Black, ACS Nano 5 (2011) 7986.

[67] M.D. Irwin, J.D. Servaites, D.B. Buchholz, B.J. Leever, J. Liu, J.D. Emery, M. Zhang, J.-H. Song, M.F. Durstock, A.J. Freeman, M.J. Bedzyk, M.C. Hersam, R.P.H. Chang, M.A. Ratner, T.J. Marks, Chem. Mater. 23 (2011) 2218.

[68] A. Kumar, Z. Hong, S. Sista, Y. Yang, Adv. Energy Mater. 1 (2011) 124.

[69] S.B. Jo, J.H. Lee, M. Sim, M. Kim, J.H. Park, Y.S. Choi, Y. Kim, S.-G. Ihn, K. Cho, Adv. Energy Mater. 1 (2011) 690.

[70] C. Schlenker, M. Thompson. Springer Berlin / Heidelberg, 2011, p. 1.

[71] H. Yan, Z. Chen, Y. Zheng, C. Newman, J.R. Quinn, F. Dotz, M. Kastler, A. Facchetti, Nature 457 (2009) 679.

[72] A. Dodabalapur, Nature 434 (2005) 151.

[73] H. Yasuda: Luminous Chemical Vapour Deposition, Marcel Dekker, 2005.

[74] R.D. Short, D.A. Steele, Plasma Processes Polym. 7 (2010) 366.

[75] K. Vasilev, A. Michelmore, H.J. Griesser, R.D. Short, Chem. Commun. (2009) 3600.

[76] H.K. Yasuda, Plasma Processes and Polymers 2 (2005) 293.

[77] A. Hiratsuka, I. Karube, Electroanalysis 12 (2000) 695.

[78] K. Ostrikov, A.B. Murphy, J. Phys. D: Appl. Phys. 40 (2007) 2223.

[79] M.H. Yoon, H. Yan, A. Facchetti, T.J. Marks, J. Am. Chem. Soc. 127 (2005) 10388.

[80] M. Halik, H. Klauk, U. Zschieschang, G. Schmid, C. Dehm, M. Schutz, S. Malsch, F. Effenberger, M. Brunnbauer, F. Stellacci, Nature 431 (2004) 963.

[81] C.D. Dimitrakopoulos, S. Purushothaman, J. Kymissis, A. Callegari, J.M. Shaw, Science 283 (1999) 822.

[82] D.K. Hwang, C.S. Kim, J.M. Choi, K. Lee, J.H. Park, E. Kim, H.K. Baik, J.H. Kim, S. Im, Adv. Mater. 18 (2006) 2299.

[83] T. Desmet, R. Morent, N.D. Geyter, C. Leys, E. Schacht, P. Dubruel, Biomacromolecules 10 (2009) 2351.

[84] J.E. Raynor, J.R. Capadona, D.M. Collard, T.A. Petrie, A.J. Garcia, Biointerphases 4 (2009) FA3.

[85] H. Biederman, D. Slavínská, Surf. Coat. Technol. 125 (2000) 371.

[86] F.S. Denes, S. Manolache, Prog. Polym. Sci. 29 (2004) 815.

[87] E.E. Johnston, B.D. Ratner, J. Electron Spectrosc. Relat. Phenom. 81 (1996) 303.

[88] M. Muccini, Nat. Mater. 5 (2006) 605.

[89] F.F. Shi, Surf. Coat. Technol. 82 (1996) 1.

[90] H. Yasuda, J. Polym. Sci., Part D: Macromol. Rev. 16 (1981) 199.

[91] M. Korachi, C. Gurol, N. Aslan, J. Electrost. 68 (2010) 508.

[92] F. Sohbatzadeh, A. Hosseinzadeh Colagar, S. Mirzanejhad, S. Mahmodi, Appl. Environ. Microbiol. 160 (2010) 1978.

[93] A. Sureshkumar, R. Sankar, M. Mandal, S. Neogi, Int. J. Pharm. 396 (2010) 17.

[94] S. Roth, J. Feichtinger, C. Hertel, J. Appl. Microbiol. 108 (2010) 521.

[95] S.K. Zaaba, T. Akitsu, H. Ohkawa, K. Katayama-Hirayama, M. Tsuji, N. Shimizu, Y. Imanishi, IEEJ Trans. Fundam. Mater. 130 (2010) 355.

[96] M.C. Kim, S.H. Cho, J.G. Han, B.Y. Hong, Y.J. Kim, S.H. Yang, J.H. Boo, Surf. Coat. Technol. 169-170 (2003) 595.

[97] J. Lahann, Polym. Int. 55 (2006) 1361.

[98] U. Sajeev, C. Mathai, S. Saravanan, R. Ashokan, S. Venkatachalam, M. Anantharaman, Bull. Mater. Sci. 29 (2006) 159.

[99] C.J. Bettinger, Z. Bao, Polym. Int. 59 (2010) 563.

[100] C.P. Yoganand, V. Selvarajan, V. Cannillo, A. Sola, E. Roumeli, O.M. Goudouri, K.M. Paraskevopoulos, M. Rouabhia, Ceram. Int. 36 (2010) 1757.

[101] C.P. Yoganand, et al., J. Phys.: Conf. Ser. 208 (2010) 012099.

[102] G. Wang, F. Meng, C. Ding, P.K. Chu, X. Liu, Acta Biomater. 6 (2009) 990.

[103] A.B. Nawale, N. Kulkarni, S. Karmakar, A.K. Das, S.V. Bhoraskar, V.L. Mathe, J. Phys.: Conf. Ser. 208 (2010) 012121.

[104] G.Y. Dautov, J. Eng. Phys. Thermophys. 53 (1987) 1434.

[105] S. Inbakumar, R. Morent, N. De Geyter, T. Desmet, A. Anukaliani, P. Dubruel, C. Leys, Cellulose 17 (2010) 417.

[106] Z. Yang, X. Wang, J. Wang, Y. Yao, H. Sun, N. Huang, Plasma Processes Polym. 6 (2009) 498.

[107] L. Denis, P. Marsal, Y. Olivier, T. Godfroid, R. Lazzaroni, M. Hecq, J. Cornil, R. Snyders, Plasma Processes Polym. 7 (2010) 172.

[108] A. Geissler, M.-F. Vallat, L. Vidal, J.-C. Voegel, J. Hemmerle, P. Schaaf, V. Roucoules, Langmuir 24 (2008) 4874.

[109] V. Nelea, et al., J. Phys. D: Appl. Phys. 42 (2009) 225208.

[110] S. Swaraj, U. Oran, A. Lippitz, J.E. Friedrich, W.E.S. Unger, Plasma Processes Polym. 2 (2005) 572.

[111] R. Gristina, E. D'Aloia, G.S. Senesi, A. Milella, M. Nardulli, E. Sardella, P. Favia, R. d'Agostino, J. Biomed. Mater. Res., Part B 88B (2009) 139.

[112] S. Liu, M.M.L.M. Vareiro, S. Fraser, A.T.A. Jenkins, Langmuir 21 (2005) 8572.

[113] A.N. Chifen, R. Forch, W. Knoll, P.J. Cameron, H.L. Khor, T.L. Williams, A.T.A. Jenkins, Langmuir 23 (2007) 6294.

[114] D.T.K. Kwok, L. Tong, C.Y. Yeung, C.G.d. Remedios, P.K. Chu, Surf. Coat. Technol. 204 (2010) 2892.

[115] G. Subbiahdoss, R. Kuijer, D.W. Grijpma, H.C. van der Mei, H.J. Busscher, Acta Biomater. 5 (2009) 1399.

[116] H.J. Busscher, R.J. Ploeg, H.C. van der Mei, Biomaterials 30 (2009) 4247.

[117] A.D. Hanssen, J. Arthroplasty 17 (2002) 98.

[118] L. Montanaro, D. Campoccia, C.R. Arciola, Biomaterials 28 (2007) 5155.

[119] B. Gottenbos, H.C. van der Mei, F. Klatter, P. Nieuwenhuis, H.J. Busscher, Biomaterials 23 (2002) 1417.

[120] P.M. Merritt, T. Danhorn, C. Fuqua, J. Bacteriol. 189 (2007) 8005.

[121] P. Velasco-Casal, L.Y. Wick, J.-J. Ortega-Calvo, Environ. Sci. Technol. 42 (2008) 1131.

[122] U. Jenal, R.E. Silversmith, L. Sogaard-Andersen, L. Sockett, EMBO Rep. 6 (2005) 615.

[123] S.M. Kirov, FEMS Microbiol. Lett. 224 (2003) 151.

[124] R.B. Dickinson, R.T. Tranquillo, J. Math. Biol. 31 (1993) 563.

[125] D. Pavithra, D. Mukesh, Biomed. Mater. 3 (2008) 034003.

[126] R.M. Donlan, Emerging Infect. Dis. 8 (2002) 881.

[127] H.C. Flemming, J. Wingender, Water Sci. Technol. 43 (2001) 1.

[128] C. Mayer, R. Moritz, C. Kirschner, W. Borchard, R. Maibaum, J. Wingender, H.-C. Flemming, Int. J. Biol. Macromol. 26 (1999) 3.

[129] C. Dong, K. Beis, J. Nesper, A.L. Brunkan-LaMontagne, B.R. Clarke, C. Whitfield, J.H. Naismith, Nature 444 (2006) 226.

[130] E.B. Roberson, M.K. Firestone, Appl. Environ. Microbiol. 58 (1992) 1284.

[131] P. Jayaratne, W.J. Keenleyside, P.R. MacLachlan, C. Dodgson, C. Whitfield, J. Bacteriol. 175 (1993) 5384.

[132] T.J. Beveridge, L.L. Graham, Microbiol. Mol. Biol. Rev. 55 (1991) 684.

[133] C. Bruno, F. Yves, Colloids Surf B: Biointerfaces 23 (2002) 173.

[134] A.W. Decho, Oceanogr. Mar. Biol. 28 (1990) 73.

[135] H.C. Flemming, Chem. Ingnieur Technik. 67 (1995) 1425.

[136] D.R. Absoiom, F.V. Lamberti, Z. Policova, W. Zingg, D.J. Van Oss, A.W. Neumann, Appl. Environ. Microbiol. 46 (1983) 90.

[137] T.J. Beveridge, W.S. Fyfe, Can. J. Earth Sci. 22 (1985) 1893.

[138] S.S. Cheng, K.K. Chittur, C.N. Sukenik, L.A. Culp, K. Lawrence, J. Colloid Interface Sci. 162 (1994) 135.

[139] J.L. Ong, K.K. Chittur, L.C. Lucas, J. Biomed. Mater. Res. 28 (1994) 1337.

[140] C.W. Hoge, B. Schwartz, D.F. Talkington, R.F. Breiman, E.M. Macneill, S.J. Englender, JAMA, J. Am. Med. Assoc. 269 (1993) 1638.

[141] R. Kaul, A. McGeer, D.E. Low, K. Green, B. Schwartz, A.E. Simor, Am. J. Med. 103 (1997) 18.

[142] C. Cywes, I. Stamenkovic, M.R. Wessels, J. Clin. Invest. 106 (2000) 995.

[143] C.D. Ashbaugh, T.J. Moser, M.H. Shearer, G.L. White, R.C. Kennedy, M.R. Wessels, Cell. Microbiol. 2 (2000) 283.

[144] I.W. Sutherland, Crit. Rev. Microbiol. 10 (1983) 173.

[145] M.C. Veiga, M.K. Jain, W.W. Wu, R.I. Hollingsworth, J.G. Zeikus, Appl. Environ. Microbiol. 63 (1997) 403.

[146] T.A. Camesano, B.E. Logan, Environ. Sci. Technol. 34 (2000) 3354.

[147] M.C.M. van Loosdrecht, W. Norde, J. Lyklema, A.J.B. Zehnder, Aquat. Sci. 53 (1990) 103.

[148] V. Williams, M. Fletcher, Appl. Environ. Microbiol. 62 (1996) 100.

[149] P. Cescutti, H. Otto, J.B. Patrick, I. Mark von, Microbial Glycobiology. Academic Press, San Diego, 2010, p. 93.

[150] A. Omoike, J. Chorover, Biomacromolecules 5 (2004) 1219.

[151] M.R. Wessels, M.S. Bronze, Proc. Natl. Acad. Sci. U. S. A. 91 (1994) 12238.

[152] M. Fletcher, in M. Fletcher (Ed.), Bacterial Adhesion: Molecular and Ecological Diversity. Wiley-Liss, New York, 1996, p. 1.

[153] J. Strauss, N.A. Burnham, T.A. Camesano, J. Mol. Recognit. 22 (2009) 347.

[154] N.I. Abu-Lail, T.A. Camesano, Environ. Sci. Technol. 37 (2003) 2173.

[155] H. Sheng, J.Y. Lim, M.K. Watkins, S.A. Minnich, C.J. Hovde, Appl. Environ. Microbiol. 74 (2008) 5015.

[156] J.W. Costerton, K.J. Cheng, G.G. Geesey, T.I. Ladd, J.C. Nickel, M. Dasgupta, T.J. Marrie, Annu. Rev. Microbiol. 41 (1987) 435.

[157] I.W. Sutherland, Microbiology 147 (2001) 3.

[158] E. van Hullebusch, M. Zandvoort, P. Lens, Rev. Environ. Sci. Biotechnol. 2 (2003) 9.

[159] A. Romaní, K. Fund, J. Artigas, T. Schwartz, S. Sabater, U. Obst, Microb. Ecol. 56 (2008) 427.

[160] T. Das, P.K. Sharma, H.J. Busscher, H.C. van der Mei, B.P. Krom, Appl. Environ. Microbiol. (2010) AEM.03119.

[161] X. Liu, P.K. Chu, C. Ding, Mater. Sci. Eng., R 47 (2004) 49.

[162] N. Stobie, B. Duffy, D.E. McCormack, J. Colreavy, M. Hidalgo, P. McHale, S.J. Hinder, Biomaterials 29 (2008) 963.

[163] J.W. Costerton, P.S. Stewart, E.P. Greenberg, Science 284 (1999) 1318.

[164] T.-F. Mah, B. Pitts, B. Pellock, G.C. Walker, P.S. Stewart, G.A. O'Toole, Nature 426 (2003) 306.

[165] I. Sadovskaya, E. Vinogradov, J. Li, A. Hachani, K. Kowalska, A. Filloux, Glycobiology 20 (2010) 895.

[166] A.W. Decho, Cont. Shelf Res. 20 (2000) 1257.

[167] K.J. Lauderdale, C.L. Malone, B.R. Boles, J. Morcuende, A.R. Horswill, J. Orthop. Res. 28 (2010) 55.

[168] J. van Heerden, M. Turner, D. Hoffmann, J. Moolman, J. Plast. Reconstr. Aesthetic Surg. 62 (2009) 610.

[169] J.-H. Lee, H. Wang, J.B. Kaplan, W.Y. Lee, Tissue Eng., Part C 17 (2011) 39.

[170] L.S. Dorobantu, S. Bhattacharjee, J.M. Foght, M.R. Gray, Langmuir 25 (2009) 6968.

[171] B. Cappella, G. Dietler, Surf. Sci. Rep. 34 (1999) 5.

[172] B.A. Jucker, H. Harms, A.J.B. Zehnder, Colloids Surf B: Biointerfaces 11 (1998) 33.

[173] H.H.M. Rijnaarts, W. Norde, E.J. Bouwer, J. Lyklema, A.J.B. Zehnder, Appl. Environ. Microbiol. 59 (1993) 3255.

[174] K.G. Davies, P. Afolabi, P. O'Shea, Parasitology 112 (1996) 553.

[175] B. Song, L.G. Leff, Microbiol. Res. 161 (2006) 355.

[176] V. Hancock, M. Dahl, P. Klemm, Appl. Environ. Microbiol. 76 (2010) 3836.

[177] C. Perrin, R. Briandet, G. Jubelin, P. Lejeune, M.-A. Mandrand-Berthelot, A. Rodrigue, C. Dorel, Appl. Environ. Microbiol. 75 (2009) 1723.

[178] M. Radzig, O. Koksharova, I. Khmel’, Mol. Genet. Microbiol. Virol. 24 (2009) 194.

[179] Y. Hong, D.G. Brown, Biotechnol. Bioeng. 105 (2009) 965.

[180] H.J. Busscher, W. Norde, P.K. Sharma, H.C. van der Mei, Curr. Opin. Colloid Interface Sci. 15 (2010) 510.

[181] S.S. Andrews, Phys. Biol. 6 (2009) 046015.

[182] J. Piglowski, I. Gancarz, J. Staniszewska-Kus, D. Paluch, M. Szymonowicz, A. Konieczny, Biomaterials 15 (1994) 909.

[183] R. Bos, H.C. Van Der Mei, H.J. Busscher, FEMS Microbiol. Rev. 23 (1999) 179.

[184] Y.H. An, R.J. Friedman, R.A. Draughn, E.A. Smith, J.H. Nicholson, J.F. John, J. Microbiol. Methods 24 (1995) 29.

[185] G. Subbiahdoss, B. Pidhatika, G. Coullerez, M. Charnley, R. Kuijer, H.C. van der Mei, M. Textor, H.J. Busscher, Eur. Cells Mater. 19 (2010) 205.

[186] J.-H. Lee, H. Wang, J.B. Kaplan, W.Y. Lee, Acta Biomater. 6 (2010) 4422.

[187] R.A M. Donlan, Clin. Infect. Dis. 33 (2001) 1387.

[188] L. Hao, J. Lawrence, L. Li, Appl. Surf. Sci. 247 (2005) 453.

[189] J.M. Schakenraad, H.J. Busscher, C.R.H. Wildevuur, J. Arends, J. Biomed. Mater. Res. 20 (1986) 773.

[190] P.B. van Wachem, T. Beugeling, J. Feijen, A. Bantjes, J.P. Detmers, W.G. van Aken, Biomaterials 6 (1985) 403.

[191] Y. Tamada, Y. Ikada, Polymer 34 (1993) 2208.

[192] L. Ponsonnet, K. Reybier, N. Jaffrezic, V. Comte, C. Lagneau, M. Lissac, C. Martelet, Mater. Sci. Eng., C 23 (2003) 551.

[193] C.C. Annarelli, J. Fornazero, R. Cohen, J. Bert, J.L. Besse, J. Colloid Interface Sci. 213 (1999) 386.

[194] I. Pashkuleva, A. Marques, F. Vaz, R. Reis, J. Mater. Sci.: Mater. Med. 21 (2010) 21.

[195] A.L. Hook, H. Thissen, J. Quinton, N.H. Voelcker, Surf. Sci. 602 (2008) 1883.

[196] R.A.N. Pertile, F.K. Andrade, C. Alves Jr, M. Gama, Carbohydr. Polym. 82 (2010) 692.

[197] I.W. Wang, J.M. Anderson, M.R. Jacobs, R.E. Marchant, J. Biomed. Mater. Res. 29 (1995) 485.

[198] V. Kumar, H. Rauscher, F. Bretagnol, F. Arefi-Khonsari, J. Pulputel, P. Colpo, F. Rossi, in H. Rauscher, M. Perucca, G. Buyle (Eds.), Plasma technology for hyperfunctional surfaces: Food, biomedical, and textile applications. Wiley, Weinheim, 2010.

[199] K. Schröder, A. Meyer-Plath, D. Keller, W. Besch, G. Babucke, A. Ohl, Contrib. Plasma Phys. 41 (2001) 562.

[200] K. Bazaka, M.V. Jacob, V.K. Truong, F. Wang, W.A. Pushpamali, J. Wang, A. Ellis, C.C. Berndt, R.J. Crawford, E.P. Ivanova, Biomacromolecules 11 (2010) 2016.

[201] B. Gottenbos, D.W. Grijpma, H.C. van der Mei, J. Feijen, H.J. Busscher, J. Antimicrob. Chemother. 48 (2001) 7.

[202] N.P. Boks, H.J. Kaper, W. Norde, H.C. van der Mei, H.J. Busscher, J. Colloid Interface Sci. 331 (2009) 60.

[203] R. Kugler, O. Bouloussa, F. Rondelez, Microbiology 151 (2005) 1341.

[204] Y. Hong, D.G. Brown, Appl. Environ. Microbiol. 75 (2009) 2346.

[205] K.N. Timmis, H.J. Heipieper, S. Cornelissen, M. Pepi, Handbook of Hydrocarbon and Lipid Microbiology. Springer Berlin Heidelberg, 2010, p. 1615.

[206] D.J. Balazs, K. Triandafillu, Y. Chevolot, B.O. Aronsson, H. Harms, P. Descouts, H.J. Mathieu, Surf. Interface Anal. 35 (2003) 301.

[207] K. Triandafillu, D.J. Balazs, B.O. Aronsson, P. Descouts, P. Tu Quoc, C. van Delden, H.J. Mathieu, H. Harms, Biomaterials 24 (2003) 1507.

[208] F.R. Marciano, L.F. Bonetti, N.S. Da-Silva, E.J. Corat, V.J. Trava-Airoldi, Appl. Surf. Sci. 255 (2009) 8377.

[209] T. Kaufmann, B.J. Ravoo, Polym. Chem. 1 (2010) 371.

[210] M. Katsikogianni, E. Amanatides, D. Mataras, Y.F. Missirlis, Colloids Surf B: Biointerfaces 65 (2008) 257.

[211] F. Hamadi, H. Latrache, M. Zekraoui, M. Ellouali, J. Bengourram, Mater. Sci. Eng., C 29 (2009) 1302.

[212] R. Atkin, V.S.J. Craig, P.G. Hartley, E.J. Wanless, S. Biggs, Langmuir 19 (2003) 4222.

[213] H. Schonherr, M.T. van Os, R. Forch, R.B. Timmons, W. Knoll, G.J. Vancso, Chem. Mater. 12 (2000) 3689.

[214] H. Chen, L. Yuan, W. Song, Z. Wu, D. Li, Prog. Polym. Sci. 33 (2008) 1059.

[215] P. Déjardin, T. Pompe, L. Renner, C. Werner, Proteins at solid-liquid interfaces. Springer Berlin Heidelberg, 2006, p. 175.

[216] R. Förch, A.N. Chifen, A. Bousquet, H.L. Khor, M. Jungblut, L.Q. Chu, Z. Zhang, I. Osey-Mensah, E.K. Sinner, W. Knoll, Chem. Vap. Deposition 13 (2007) 280.

[217] J.E. Gray, P.R. Norton, R. Alnouno, C.L. Marolda, M.A. Valvano, K. Griffiths, Biomaterials 24 (2003) 2759.

[218] D.J. Balazs, K. Triandafillu, P. Wood, Y. Chevolot, C. van Delden, H. Harms, C. Hollenstein, H.J. Mathieu, Biomaterials 25 (2004) 2139.

[219] M. Haïdopoulos, S. Turgeon, G. Laroche, D. Mantovani, Plasma Processes Polym. 2 (2005) 424.

[220] V. Sevast’yanov, V. Vasilets, Russ. J. Gen. Chem. 79 (2009) 596.

[221] N.R. Choudhury, A.G. Kannan, N.K. Dutta, F. Klaus, K.S. Alois, Tribology and Interface Engineering Series. Elsevier, 2008, p. 501.

[222] P. Hale, S. Turgeon, P. Horny, F.o. Lewis, N. Brack, G. Van Riessen, P. Pigram, D. Mantovani, Langmuir 24 (2008) 7897.

[223] F. Lewis, et al., J. Phys. D: Appl. Phys. 41 (2008) 045310.

[224] A.L. Cordeiro, R. Zimmermann, S. Gramm, M. Nitschke, A. Janke, N. Schafer, K. Grundke, C. Werner, Soft Matter 5 (2009) 1367.

[225] L.K. Ista, S. Mendez, G.P. Lopez, Biofouling 26 (2010) 111

[226] A. Cordeiro, M. Pettit, M. Callow, J. Callow, C. Werner, Biotechnol. Lett. 32 (2010) 489.

[227] T.R. Scheuerman, A.K. Camper, M.A. Hamilton, J. Colloid Interface Sci. 208 (1998) 23.

[228] M. Katsikogianni, Y.F. Missirlis, Eur. Cells Mater. (2004) 37.

[229] K.J. Edwards, A.D. Rutenberg, Chem. Geol. 180 (2001) 19.

[230] K.A. Whitehead, J. Colligon, J. Verran, Colloids Surf B: Biointerfaces 41 (2005) 129.

[231] L.G. Harris, S. Tosatti, M. Wieland, M. Textor, R.G. Richards, Biomaterials 25 (2004) 4135.

[232] C. Diaz, M.C. Cortizo, P.L. Schilardi, S.G.G. de Saravia, M.A.F.L. de Mele, Mater. Res. 10 (2007) 11.

[233] V.K. Truong, S. Rundell, R. Lapovok, Y. Estrin, J.Y. Wang, C.C. Berndt, D.G. Barnes, C.J. Fluke, R.J. Crawford, E.P. Ivanova, Appl. Environ. Microbiol. 83 (2009) 925.

[234] N. Mitik-Dineva, J. Wang, V.K. Truong, P. Stoddart, F. Malherbe, R.J. Crawford, E.P. Ivanova, Curr. Microbiol. 58 (2009) 268.

[235] N. Mitik-Dineva, J. Wang, R.C. Mocanasu, P.R. Stoddart, R.J. Crawford, E.P. Ivanova, Biotechnol. J. 3 (2008) 536.

[236] E.P. Ivanova, N. Mitik-Dineva, J. Wang, D.K. Pham, J.P. Wright, D.V. Nicolau, R.C. Mocanasu, R.J. Crawford, Micron 39 (2008) 1197.

[237] M. Clauss, A. Trampuz, O. Borens, M. Bohner, T. Ilchmann, Acta Biomater. 6 (2010) 3791.

[238] N. Qureshi, B. Annous, T. Ezeji, P. Karcher, I. Maddox, Microb. Cell Fact. 4 (2005) 24.

[239] M. Shafahi, AIP Conf. Proc. 1254 (2010) 193.

[240] T.J. Kinnari, J. Esteban, N.Z. Martin-de-Hijas, O. Sanchez-Munoz, S. Sanchez-Salcedo, M. Colilla, M. Vallet-Regi, E. Gomez-Barrena, J. Med. Microbiol. 58 (2009) 132.

[241] G.E. Kapellos, T.S. Alexiou, A.C. Payatakes, Adv. Water Resour. 30 (2007) 1648.

[242] R.J. Covert, R.D. Ott, D.N. Ku, Wear 255 (2003) 1064.

[243] A.J.S.P. Coury, MN), Cahalan, Patrick T. (Stein, NL), Di Domenico Jr., Edward D. (Anoka, MN), Keeney, Kenneth W. (Forest Lake, MN), Swoyer, John M. (Coon Rapids, MN), Radio frequency glow discharge surface treatment of silicone tubing used as covering for electrical leads to improve slip properties thereof. Medtronic, Inc. (Minneapolis, MN), United States, 1992.

[244] A. Almaguer-Flores, L.A. Ximénez-Fyvie, S.E. Rodil, J. Biomed. Mater. Res., Part B 92B (2009) 196.

[245] A. Kugel, B. Chisholm, S. Ebert, M. Jepperson, L. Jarabek, S. Stafslien, Polym. Chem. 1 (2010) 442.

[246] W.P. Meier, W. Knoll, K. Bender, R. Förch, C. Frank, H. Götz, C. Heibel, T. Jenkins, U. Jonas, A. Kibrom, R. Kügler, C. Naumann, R. Naumann, A. Reisinger, J. Rühe, S. Schiller,

E.-K. Sinner, in W.P. Meier, W. Knoll (Eds.), Polymer Membranes/Biomembranes. Springer, Berlin, 2010, p. 87.

[247] P. Majumdar, E. Lee, N. Patel, S. Stafslien, J. Daniels, B. Chisholm, J. Coat. Technol. Res. 5 (2008) 405.

[248] S.N. Jampala, M. Sarmadi, E.B. Somers, A.C.L. Wong, F.S. Denes, Langmuir 24 (2008) 8583.

[249] Y. Song, J. Wang, G. Li, Q. Sun, X. Jian, J. Teng, H. Zhang, Polymer 49 (2008) 724.

[250] S. Pinto, P. Alves, C.M. Matos, A.C. Santos, L.R. Rodrigues, J.A. Teixeira, M.H. Gil, Colloids Surf B: Biointerfaces 81 (2010) 20.

[251] A. Asadinezhad, I. Novák, M. Lehocký, V. Sedlaík, A. Vesel, I. Junkar, P. Sáha, I. Chodák, Colloids Surf B: Biointerfaces 77 (2010) 246.

[252] Y. Dong, X. Li, R. Sammons, H. Dong, J. Biomed. Mater. Res., Part B 93B (2010) 185.

[253] M. Miola, S. Ferraris, S. Di Nunzio, P. Robotti, G. Bianchi, G. Fucale, G. Maina, M. Cannas, S. Gatti, A. Massé, C. Vitale Brovarone, E. Verné, J. Mater. Sci.: Mater. Med. 20 (2009) 741.

[254] W. Zhang, P.K. Chu, J. Ji, Y. Zhang, X. Liu, R.K.Y. Fu, P.C.T. Ha, Q. Yan, Biomaterials 27 (2006) 44.

[255] N. Huang, P. Yang, Y.X. Leng, J. Wang, H. Sun, J.Y. Chen, G.J. Wan, Surf. Coat. Technol. 186 (2004) 218.

[256] P.K. Chu, Surf. Coat. Technol. 201 (2007) 8076.

[257] N. Huang, Y.X. Leng, P. Yang, J.Y. Chen, H. Sun, G.J. Wan, J. Wang, P.K. Chu, I.G. Brown, Plasma surface modification of biomaterials applied for cardiovascular devices, The 30th International Conference on Plasma Science., 2003, p. 439.

[258] V. Brunetti, G. Maiorano, L. Rizzello, B. Sorce, S. Sabella, R. Cingolani, P.P. Pompa, Proc. Natl. Acad. Sci. U. S. A. 107 (2010) 6264.

[259] E. Fadeeva, V.K. Truong, M. Stiesch, B.N. Chichkov, R.J. Crawford, J. Wang, E.P. Ivanova, Langmuir 27 (2011) 3012.

[260] C. Baum, W. Meyer, R. Stelzer, L.G. Fleischer, D. Siebers, Mar. Biol. 140 (2002) 653.

[261] K.K. Chung, J.F. Schumacher, E.M. Sampson, R.A. Burne, P.J. Antonelli, A.B. Brennan, Biointerphases 2 (2007) 89.

[262] A.J. Malkin, M. Plomp, in S.V. Kalinin, A. Gruverman (Eds.), Scanning probe microscopy of functional materials. Springer New York, 2011, p. 39.

[263] K. Anselme, P. Davidson, A.M. Popa, M. Giazzon, M. Liley, L. Ploux, Acta Biomater. 6 (2010) 3824.

[264] R.N. Wenzel, J. Phys. Colloid Chem. 53 (1949) 1466.

[265] B. Bhushan, K. Koch, Y.C. Jung, Soft Matter 4 (2008) 1799.

[266] P.F. Rios, H. Dodiuk, S. Kenig, S. McCarthy, A. Dotan, J. Adhes. Sci. Technol. 21 (2007) 399.

[267] P.F. Rios, H. Dodiuk, S. Kenig, S. McCarthy, A. Dotan, J. Adhes. Sci. Technol. 20 (2006) 563.

[268] H. Dodiuk, P.F. Rios, A. Dotan, S. Kenig, Polym. Adv. Technol. 18 (2007) 746.

[269] A.J. Scardino, H. Zhang, D.J. Cookson, R.N. Lamb, R.d. Nys, Biofouling 25 (2009) 757

[270] R. De Nys, P.D. Steinberg, Curr. Opin. Biotechnol. 13 (2002) 244.

[271] M. Salta, J.A. Wharton, P. Stoodley, S.P. Dennington, L.R. Goodes, S. Werwinski, U. Mart, R.J.K. Wood, K.R. Stokes, Philos. Trans. R. Soc., A 368 (2010) 4729.

[272] L.D. Chambers, K.R. Stokes, F.C. Walsh, R.J.K. Wood, Surf. Coat. Technol. 201 (2006) 3642.

[273] A. Whelan, F. Regan, J. Environ. Monit. 8 (2006) 880.

[274] J. Lee, I.S. Kim, Desalination 273 (2011) 118.

[275] E. Almeida, T.C. Diamantino, O. de Sousa, Prog. Org. Coat. 59 (2007) 2.

[276] V.J.D. Rascio, Corros. Rev. 18 (2000) 133.

[277] C.M. Grozea, G.C. Walker, Soft Matter 5 (2009) 4088.

[278] D.M. Yebra, S. Kiil, K. Dam-Johansen, Prog. Org. Coat. 50 (2004) 75.

[279] C. Baum, F. Simon, W. Meyer, L.G. Fleischer, D. Siebers, J. Kacza, J. Seeger, Biofouling 19 (2003) 181.

[280] C. Baum, L.G. Fleischer, D. Roessner, W. Meyer, D. Siebers, Biorheology 39 (2002) 703.

[281] R. Ganguli, V. Mehrotra, B. Dunn, Smart Mater. Struct. 18 (2009).

[282] E.P. Ivanova, V.K. Truong, J. Wang, C.C. Berndt, T.R. Jones, I.I. Yusuf, I. Peake, H.W. Schmidt, C. Fluke, D. Barnes, R.J. Crawford, Langmuir 26 (2010) 1973.

[283] K. Bazaka, M.V. Jacob, V.K. Truong, F. Wang, W.A.A. Pushpamali, J.Y. Wang, A.V. Ellis, C.C. Berndt, R.J. Crawford, E.P. Ivanova, Biomacromolecules 11 (2010) 2016.

[284] N.S.H. Lim, K.J. Everuss, A.E. Goodman, K. Benkendorff, Aquat. Microb. Ecol. 47 (2007) 275.

[285] J. Guenther, R. De Nys, Biofouling 23 (2007) 419.

[286] R.A. Pareta, A.B. Reising, T. Miller, D. Storey, T.J. Webster, Biotechnol. Bioeng. 103 (2009) 459.

[287] H.J. Lee, D.N. Kim, S. Park, Y. Lee, W.G. Koh, Acta Biomater. 7 (2011) 1281.

[288] A. Ranjan, T.J. Webster, Nanotechnol. 20 (2009).

[289] Y. Estrin, E.P. Ivanova, A. Michalska, V.K. Truong, R. Lapovok, R. Boyd, Acta Biomater. 7 (2011) 900.

[290] B.B. Mandal, S. Das, K. Choudhury, S.C. Kundu, Tissue Eng., Part A 16 (2010) 2391.

[291] Y. Shen, G. Wang, L. Chen, H. Li, P. Yu, M. Bai, Q. Zhang, J. Lee, Q. Yu, Acta Biomater. 5 (2009) 3593.

[292] A. Ranella, M. Barberoglou, S. Bakogianni, C. Fotakis, E. Stratakis, Acta Biomater. 6 (2010) 2711.

[293] A.I. Hochbaum, J. Aizenberg, Nano Lett. 10 (2010) 3717.

[294] L. Ploux, K. Anselme, A. Dirani, A. Ponche, O. Soppera, V. Roucoules, Langmuir 25 (2009) 8161.

[295] C. Díaz, P.L. Schilardi, R.C. Salvarezza, M. Fernández Lorenzo de Mele, Langmuir 23 (2007) 11206.

[296] S. Rozhok, Z. Fan, D. Nyamjav, C. Liu, C.A. Mirkin, R.C. Holz, Langmuir 22 (2006) 11251.

[297] B. Rowan, M.A. Wheeler, R.M. Crooks, Langmuir 18 (2002) 9914.

[298] E.P. Ivanova, D.K. Pham, J.P. Wright, D.V. Nicolau, FEMS Microbiol. Lett. 214 (2002) 177.

[299] H.K. Webb, R.J. Crawford, T. Sawabe, E.P. Ivanova, Microbes Environ. 24 (2009) 39.

[300] L. Boulangé-Petermann, J. Rault, M.N. Bellon-Fontaine, Biofouling 11 (1997) 201.

[301] E. Medilanski, K. Kaufmann, L.Y. Wick, O. Wanner, H. Harms, Biofouling 18 (2002) 193.

[302] B. Li, B.E. Logan, Colloids Surf B: Biointerfaces 36 (2004) 81.

[303] K.A. Whitehead, D. Rogers, J. Colligon, C. Wright, J. Verran, Colloids Surf B: Biointerfaces 51 (2006) 44.

[304] F. Gentile, L. Tirinato, E. Battista, F. Causa, C. Liberale, E.M. di Fabrizio, P. Decuzzi, Biomaterials 31 (2010) 7205.

[305] N. Mitik-Dineva, J. Wang, V.K. Truong, P.R. Stoddart, F. Malherbe, R.J. Crawford, E.P. Ivanova, Biofouling 25 (2009) 621.

[306] C. Díaz, R.C. Salvarezza, M.A. Fernández Lorenzo De Mele, P.L. Schilardi, ACS Appl. Mater. Interfaces 2 (2010) 2530.

[307] C. Díaz, P.L. Schilardi, R.C. Salvarezza, M. Fernández Lorenzo de Mele, Colloids Surf B: Biointerfaces 82 (2011) 536.

[308] D.B. Weibel, W.R. DiLuzio, G.M. Whitesides, Nat. Rev. Microbiol. 5 (2007) 209.

[309] Y.J. Oh, N.R. Lee, W. Jo, W.K. Jung, J.S. Lim, Ultramicroscopy 109 (2009) 874.

[310] K. Anselme, P. Davidson, A.M. Popa, M. Giazzon, M. Liley, L. Ploux, Acta Biomater. 7 (2011) 1936.

[311] N. Mitik-Dineva, J. Wang, V.K. Truong, P.R. Stoddart, M.R. Alexander, D.J. Albutt, C. Fluke, R.J. Crawford, E.P. Ivanova, Biofouling 26 (2010) 461

[312] S.D. Puckett, E. Taylor, T. Raimondo, T.J. Webster, Biomaterials 31 (2010) 706.

[313] G. Colon, B.C. Ward, T.J. Webster, J. Biomed. Mater. Res., Part A 78 (2006) 595.

[314] L. Ploux, A. Ponche, K. Anselme, J. Adhes. Sci. Technol. 24 (2010) 2165.

[315] V.K. Truong, R. Lapovok, Y. Estrin, S. Rundell, J.Y. Wang, C.J. Fluke, D.G. Barnes, R.J. Crawford, E.P. Ivanova, Biomaterials 31 (2010) 3674.

[316] J.Y. Wang, M.K. Ghantasala, R.J. McLean, Thin Solid Films 517 (2008) 656.

[317] Y.L. Jeyachandran, B. Karunagaran, S.K. Narayandass, D. Mangalaraj, T.E. Jenkins, P.J. Martin, Mater. Sci. Eng., A 431 (2006) 277.

[318] S. Sirinrath, et al., Nanotechnol. 22 (2011) 085101.

[319] S.R. Forrest, Nature 428 (2004) 911.

[320] F.F. Shi, Surface and Coatings Technology 82 (1996) 1.

[321] H. Yasuda, T. Hsu, J. Polym. Sci., Polym. Chem. Ed. 15 (1977) 81.

[322] H. Yasuda, Q. Yu, Plasma Chem. Plasma Process. 24 (2004) 325.

[323] H. Biederman, Y. Osada: Plasma Polymerization Processes, Elsevier Science Publications, New York, 1992.

[324] I.S. Bae, S.J. Cho, W.S. Choi, B.Y. Hong, Y.J. Kim, Y.M. Kim, J.H. Boo, Thin Solid Films 516 (2008) 3577.

[325] M.V. Jacob, C.D. Easton, G.S. Woods, C.C. Berndt, Thin Solid Films 516 (2008) 3884.

[326] X. Hu, X. Zhao, A. Uddin, C.B. Lee, Thin Solid Films 477 (2005) 81.

[327] R. Rochotzki, M. Arzt, F. Blaschta, E. Kreyig, H.U. Poll, Thin Solid Films 234 (1993) 463.

[328] J. Jaglarz, T. Wagner, J. Cisowski, J. Sanetra, Opt. Mater. 29 (2007) 908.

[329] M. Campoy-Quiles, P.G. Etchegoin, D.D.C. Bradley, Synth. Met. 155 (2005) 279.

[330] J.G.E. Jellison, F.A. Modine, Appl. Phys. Lett. 69 (1996) 371.

[331] J.A. Woollam Co. Inc, Guide to Using WVASE32, 2001.

[332] J. Tauc, A. Menth, D.L. Wood, Phys. Rev. Lett. 25 (1970) 749.

[333] M. Mujahid, D.S. Srivastava, S. Gupta, D.K. Avasthi, Radiat. Phys. Chem. 74 (2005) 118.

[334] E.A. Davis, N.F. Mott, Philos. Mag. 22 (1970) 903

[335] J. Tyczkowski, R. Ledzion, J. Appl. Phys. 86 (1999) 4412.

[336] K. Bazaka, M.V. Jacob, Mater. Lett. 63 (2009) 1594.

[337] M.V. Jacob, K. Bazaka, M. Weis, D. Taguchi, T. Manaka, M. Iwamoto, Thin Solid Films 518 (2010) 6123.

[338] X.-Y. Zhao, M.-Z. Wang, B.-Z. Zhang, L. Mao, Polym. Int. 56 (2007) 630.

[339] G.P. Lopez, B.D. Ratner, Langmuir 7 (1991) 766.

[340] T.B. Casserly, K.K. Gleason, Chem. Vap. Deposition 12 (2006) 59.

[341] K.J. Miller, J. Am. Chem. Soc. 112 (1990) 8533.

[342] M.R. Alexander, T.M. Duc, Polymer 40 (1999) 5479.

[343] S. Takeda, K. Yamamoto, Y. Hayasaka, K. Matsumoto, J. Non-Cryst. Solids 249 (1999) 41.

[344] B. Eraiah, S.G. Bhat, J. Phys. Chem. Solids 68 (2007) 581.

[345] D.K. Basa, Thin Solid Films 406 (2002) 75.

[346] C. Oppedisano, A. Tagliaferro, Appl. Phys. Lett. 75 (1999) 3650.

[347] K. Bazaka, M.V. Jacob, Polym. Degrad. Stab. 95 (2010) 1123.

[348] B.D. Beake, S. Zheng, M.R. Alexander, J. Mater. Sci. 37 (2002) 3821.

[349] V. Cech, IEEE Trans. Plasma Sci. 34 (2006) 1148.

[350] K. Bazaka, M.V. Jacob, B.F. Bowden, J. Mater. Res. 26 (2011) 1018.

[351] K. Bazaka, M.V. Jacob, Mater. Sci. Forum 654-656 (2010) 1764.

[352] K. Bazaka, M.V. Jacob, E.P. Ivanova, Mater. Sci. Forum 654-656 (2010) 2261.

[353] K. Bazaka, M.V. Jacob, D. Taguchi, T. Manaka, M. Iwamoto, Chem. Phys. Lett. 503 (2011) 105.

[354] W.C. Oliver, G.M. Pharr, J. Mater. Res. 7 (1992) 1564.

[355] F. Abbes, et al., J. Micromech. Microeng. 20 (2010) 065003.

[356] Y. Chen, S.R. Bakshi, A. Agarwal, Surf. Coat. Technol. 204 (2010) 2709.

[357] S.b. Lafaye, M. Troyon, Wear 261 (2006) 905.

[358] C. Brechignac, P. Houdy, M. Lahmani (Ed.)^(Eds.), Nanomaterials and nanochemistry. Springer, Berlin, 2008.

[359] S.F. Lamolle, M. Monjo, M. Rubert, H.J. Haugen, S.P. Lyngstadaas, J.E. Ellingsen, Biomaterials 30 (2009) 736.

[360] E.S. Gadelmawla, M.M. Koura, T.M.A. Maksoud, I.M. Elewa, H.H. Soliman, J. Mater. Process. Technol. 123 (2002) 133.

[361] M. Pelliccione, T.-M. Lu: Evolution of thin film morphology, Springer, New York, 2008.

[362] G.W. Collins, S.A. Letts, E.M. Fearon, R.L. McEachern, T.P. Bernat, Phys. Rev. Lett. 73 (1994) 708.

[363] R.N. Wenzel, Ind. Eng. Chem. 28 (1936) 988.

[364] J.M. Kranenburg, C.A. Tweedie, K.J. van Vliet, U.S. Schubert, Adv. Mater. 21 (2009) 3551.

[365] C.A. Tweedie, G. Constantinides, K.E. Lehman, D.J. Brill, G.S. Blackman, K.J. Van Vliet, Adv. Mater. 19 (2007) 2540.

[366] V. Cech, B. Cechalova, R. Trivedi, J. Studynka, Thin Solid Films 517 (2009) 6034.

[367] I.S. Bae, S.J. Cho, W.S. Choi, H.J. Cho, B. Hong, H.D. Jeong, J.H. Boo, Prog. Org. Coat. 61 (2008) 245.

[368] E.C. Rangel, N.C. Cruz, C.M. Lepienski, Nucl. Instrum. Methods Phys. Res., Sect. B 191 (2002) 704.

[369] F. Benítez, E. Martínez, J. Esteve, Thin Solid Films 377-378 (2000) 109.

[370] Z.V. Vardeny, A.J. Heeger, A. Dodabalapur, Synth. Met. 148 (2005) 1.

[371] T.R. Gengenbach, H.J. Griesser, Polymer 40 (1999) 5079.

[372] P.A. Kohl, D.M. Bhusari, M. Wedlake, C. Case, F.P. Klemens, J. Miner, L. Byung-Chan, R.J. Gutmann, R. Shick, IEEE Electron Device Lett. 21 (2000) 557.

[373] W. Li, J.O. Tegenfeldt, L. Chen, R.H. Austin, S.Y. Chou, P.A. Kohl, J. Krotine, J.C. Sturm, Nanotechnol. 14 (2003) 578.

[374] B. Shieh, K.C. Saraswat, J.P. McVittie, S. List, S. Nag, M. Islamraja, R.H. Havemann, IEEE Electron Device Lett. 19 (1998) 16.

[375] H.A. Al-Attar, A.D. Telfah, Opt. Commun. 229 (2004) 263.

[376] Y. Huang, D.R. Paul, Macromolecules 39 (2006) 1554.

[377] D.D. Burkey, K.K. Gleason, Chem. Vap. Deposition 9 (2003) 65.

[378] B.J. Holland, J.N. Hay, Polymer 42 (2001) 4825.

[379] A. Nelson, B.W. Muir, J. Oldham, C. Fong, K.M. McLean, P.G. Hartley, S.K. Øiseth, J. James, Langmuir 22 (2006) 453.

[380] J.R. White, C. R. Chimie 9 (2006) 1396.

[381] A. Hollander, J. Thome, in H. Biederman (Ed.). Imperial Collage Press, London, 2004, p. 252.

[382] H. Yasuda, L. Ledernez, F. Olcaytug, G. Urban, Pure Appl. Chem. 80 (2008) 1883.

[383] J.-Y. Lai, C.-W. Tseng, S.-L. Huang, J. Polym. Res. 1 (1994) 361.

[384] S. Turmanova, M. Minchev, K. Vassilev, G. Danev, J. Polym. Res. 15 (2008) 309.

[385] J. Tegenfeldt, C. Prinz, H. Cao, R. Huang, R. Austin, S. Chou, E. Cox, J. Sturm, Anal. Bioanal. Chem. 378 (2004) 1678.

[386] C.F. Carson, K.A. Hammer, T.V. Riley, Clin. Microbiol. Rev. 19 (2006) 50.

[387] V. Linder, B.D. Gates, D. Ryan, B.A. Parviz, G.M. Whitesides, Small 1 (2005) 730.

[388] R.R. Deshmukh, A.R. Shetty, J. Appl. Polym. Sci. 107 (2008) 3707.

[389] F.M. Fowkes, Ind. Eng. Chem. 56 (2002) 40.

[390] D.K. Owens, R.C. Wendt, J. Appl. Polym. Sci. 13 (1969) 1741.

[391] R.J. Good, Nature 212 (1966) 276.

[392] C.J. van Oss, M.K. Chaudhury, R.J. Good, Adv. Colloid Interface Sci. 28 (1987) 35.

[393] C.J. Van Oss, M.K. Chaudhury, R.J. Good, Chem. Rev. 88 (1988) 927.

[394] A.W. Neumann, R.J. Good, C.J. Hope, M. Sejpal, J. Colloid Interface Sci. 49 (1974) 291.

[395] S. Wu, J. Polym. Sci., Part C: Polym. Symp. 34 (1971) 19.

[396] S. Wu, R.A. Shanks, J. Appl. Polym. Sci. 93 (2004) 1493.

[397] M. Lampin, R. Warocquier-Clérout, C. Legris, M. Degrange, M.F. Sigot-Luizard, J. Biomed. Mater. Res. 36 (1997) 99.

[398] J.H. Lee, H.W. Jung, I.-K. Kang, H.B. Lee, Biomaterials 15 (1994) 705.

[399] H. Nakae, R. Inui, Y. Hirata, H. Saito, Acta Mater. 46 (1998) 2313.

[400] T. Ueda-Yukoshi, T. Matsuda, Langmuir 11 (1995) 4135.

[401] J. Krupka, W.-T. Huang, M.-J. Tung, Ferroelectrics 335 (2006) 89

[402] C.D. Easton, M.V. Jacob, J. Krupka, Meas. Sci. Technol. 18 (2007) 2869.

[403] S.-J. Cho, J.-H. Boo, Microelectron. Eng. 89 (2012) 19.

[404] W.-J. Yoon, D. Bhattacharyya, R.B. Timmons, P.R. Berger, Org. Electron. 11 (2010) 1767.

[405] H. Biederman, Surf. Coat. Technol. 205, Supplement 2 (2011) S10.

[406] L.J. Anderson, M.V. Jacob, Mater. Sci. Eng., B.

[407] H. Akther, A.H. Bhuiyan, New J. Phys. 7 (2005) 173.

[408] S. Sajeev, M.R. Anantharaman, J. Phys. D: Appl. Phys. 43 (2010) 055403.

[409] R.B. Sarker, A.H. Bhuiyan, Thin Solid Films 519 (2011) 5912.

[410] S. Majumder, A. Bhuiyan, Polym. Sci., Ser. A 53 (2011) 85.

[411] H.M. Chenari, H. Sedghi, M. Talebian, M.M. Golzan, A. Hassanzadeh, J. Nanomater. 2011 (2011).

[412] R. Matin, A.H. Bhuiyan, Thin Solid Films 519 (2011) 3462.

[413] J. John, S. Sivaraman, S. Jayalekshmy, M.R. Anantharaman, J. Phys. Chem. Solids 71 (2010) 935.

[414] A.B.M. Shah Jalal, S. Ahmed, A.H. Bhuiyan, M. Ibrahim, Thin Solid Films 295 (1997) 125.

[415] D.S. Kumar, N. Kenji, N. Satoko, N. Hiromichi, I. Shigeru, K. Kunihiro, Y. Yasuhiko, J. Appl. Polym. Sci. 90 (2003) 1102.

[416] S.D. Kumar, K.M.G. Pillai, Thin Solid Films 353 (1999) 249.

[417] J.L. Brédas, B. Thémans, J.G. Fripiat, J.M. André, R.R. Chance, Phys. Rev. B 29 (1984) 6761.

[418] S. Chand, N. Kumar, J. Mater. Sci. Lett. 8 (1989) 1009.

[419] K. Bazaka, M.V. Jacob, J. Polym. Eng. 31 (2011) 73.

[420] K. Bazaka, M.V. Jacob, J. Mater. Res. (2012).

[421] K. Bazaka, M.V. Jacob, D. Taguchi, T. Manaka, M. Iwamoto, Phys. Procedia 14 (2011) 62.

[422] J. Coates, in R.A. Meyers (Ed.), Encycl. Anal. Chem. Wiley and Sons, Chichester, 2000, p. 1.

[423] A. Sharma, Deepak, S. Kumar, M. Katiyar, A.K. Saxena, A. Ranjan, R.K. Tiwari, Synth. Met. 139 (2003) 835.

[424] H. Bässler, Phys. Status Solidi B 175 (1993) 15.

[425] V.I. Arkhipov, P. Heremans, E.V. Emelianova, G.J. Adriaenssens, H. Bässler, J. Non-Cryst. Solids 338-340 (2004) 603.

[426] C.J. Mathai, S. Saravanan, M.R. Anantharaman, S. Venkitachalam, S. Jayalekshmi, J. Phys. D: Appl. Phys. 35 (2002) 2206.

[427] C.J. Van Oss, R.J. Good, M.K. Chaudhury, Langmuir 4 (1988) 884.

[428] M.-H. Yoon, H. Yan, A. Facchetti, T.J. Marks, J. Am. Chem. Soc. 127 (2005) 10388.

[429] M. Halik, H. Klauk, U. Zschieschang, G. Schmid, C. Dehm, M. Schatz, S. Malsch, F. Effenberger, M. Brunnbauer, F. Stellacci, Nature 431 (2004) 963.

[430] C.D. Dimitrakopoulos, S. Purushothaman, J. Kymissis, A. Callegari, J.M. Shaw, Science 283 (1999) 822.

[431] D.K. Hwang, C.S. Kim, J.M. Choi, K. Lee, J.H. Park, E. Kim, H.K. Baik, J.H. Kim, S. Im, Adv. Mater. 18 (2006) 2299.

[432] S.M. Sze: Physics of semiconducting devices, Wiley, New York, 1981.

[433] S. Gross, D. Camozzo, V. Di Noto, L. Armelao, E. Tondello, Eur. Polym. J. 43 (2007) 673.

[434] A. Ramazan, B. Geist, W.B.J. Spillman, R. O Claus, Smart Mater. Struct. 14 (2005) 1493.

[435] E.T. Lagally, R.A. Mathies, J. Phys. D: Appl. Phys. 37 (2004) R245.

[436] R. Tamura, E. Lim, T. Manaka, M. Iwamoto, J. Appl. Phys. 100 (2006) 7.

[437] M.A. Lampert, P. Mark: Current injection in solids., Academic Press, New York, 1970.

[438] J. Zaumseil, H. Sirringhaus, Chem. Rev. 107 (2007) 1296.

[439] K. Myny, S. Steudel, S. Smout, P. Vicca, F. Furthner, B. van der Putten, A.K. Tripathi, G.H. Gelinck, J. Genoe, W. Dehaene, P. Heremans, Org. Electron. 11 (2010) 1176.

[440] K. Myny, S. Steudel, P. Vicca, M.J. Beenhakkers, N.A.J.M. van Aerle, G.H. Gelinck, J. Genoe, W. Dehaene, P. Heremans, Solid-State Electron. 53 (2009) 1220.

[441] D. Praca, C. Barral, Comput. Networks 36 (2001) 381.

[442] Y.-J. Li, H. Sasabe, S.-J. Su, D. Tanaka, T. Takeda, Y.-J. Pu, J. Kido, Chem. Lett. 39 (2010) 140.

[443] H.H. Chou, C.H. Cheng, Adv. Mater. (Weinheim, Ger.) 22 (2010) 2468.

[444] M.C. Choi, J.C. Hwang, C. Kim, S. Ando, C.S. Ha, J. Polym. Sci., Part A: Polym. Chem. 48 (2010) 1806.

[445] Y. Leterrier, A. Pinyol, D. Gilliéron, J.A.E. Månson, P.H.M. Timmermans, P.C.P. Bouten, F. Templier, Eng. Fract. Mech. 77 (2010) 660.

[446] E. Lim, T. Manaka, R. Tamura, M. Iwamoto, J. Appl. Phys. 101 (2007) 094505.

[447] Y. Kato, S. Iba, R. Teramoto, T. Sekitani, T. Someya, H. Kawaguchi, T. Sakurai, Appl. Phys. Lett. 84 (2004) 3789.

[448] T. Uemura, Y. Hirose, M. Uno, K. Takimiya, J. Takeya, Appl. Phys. Express 2 (2009).

[449] X. Zhan, Z.a. Tan, B. Domercq, Z. An, X. Zhang, S. Barlow, Y. Li, D. Zhu, B. Kippelen, S.R. Marder, J. Am. Chem. Soc. 129 (2007) 7246.

[450] M. Mas-Torrent, M. Durkut, P. Hadley, X. Ribas, C. Rovira, J. Am. Chem. Soc. 126 (2004) 984.

[451] S.E. Burns, K. Reynolds, W. Reeves, M. Banach, T. Brown, K. Chalmers, N. Cousins, M. Etchells, C. Hayton, K. Jacobs, A. Menon, S. Siddique, P. Too, C. Ramsdale, J. Watts, P. Cain, T. von Werne, J. Mills, C. Curling, H. Sirringhaus, K. Amundson, M.D. McCreary, J. Soc. Inf. Disp. 13 (2005) 583.

[452] Y. Ohshima, H. Kohn, E. Lim, T. Manaka, M. Iwamoto, Jpn. J. Appl. Phys. 47 (2008) 1297.

[453] R. Tamura, E. Lim, S. Yoshita, T. Manaka, M. Iwamoto, Thin Solid Films 516 (2008) 2753.

[454] T. Manaka, H. Kohn, Y. Ohshima, E. Lim, M. Iwamoto, Appl. Phys. Lett. 90 (2007) 171119.

[455] E. Lim, Y. Shibata, T. Manaka, M. Iwamoto, Thin Solid Films 518 (2009) 893.

[456] I.A. Mir, T. Ahuja, D. Kumar, D. Taguchi, T. Manaka, M. Iwamoto, Synth. Met. 160 (2010) 2116.

[457] D. Yamada, T. Manaka, E. Lim, R. Tamura, M. Iwamoto, J. Appl. Phys. 103 (2008) 084118.

[458] T. Manaka, E. Lim, R. Tamura, M. Iwamoto, Appl. Phys. Lett. 87 (2005) 222107.

[459] T. Manaka, Y. Suzue, M. Iwamoto, Jpn. J. Appl. Phys. 44 (2005) 2818.

[460] T. Manaka, M. Nakao, D. Yamada, E. Lim, M. Iwamoto, Opt. Express 15 (2007) 15964.

[461] G.J. Ashwell, G. Jefferies, D.G. Hamilton, D.E. Lynch, M.P.S. Roberts, G.S. Bahra, C.R. Brown, Nature 375 (1995) 385.

[462] B. Kaminski, M. Lafrentz, R.V. Pisarev, D.R. Yakovlev, V.V. Pavlov, V.A. Lukoshkin, A.B. Henriques, G. Springholz, G. Bauer, E. Abramof, P.H.O. Rappl, M. Bayer, Phys. Rev. B 81 (2010) 155201.

[463] K. Koshino, T. Ishihara, Nonlinear Opt. 29 (2002) 357

[464] M. Maymó, J. Martorell, A. Molinos-Gómez, F. López-Calahorra, Opt. Express 14 (2006) 2864.

[465] K. Kumagai, G. Mizutani, H. Tsukioka, T. Yamauchi, S. Ushioda, Phys. Rev. B 48 (1993) 14488.

[466] X.K. Wang, T.G. Zhang, W.P. Lin, S. Liu, G.K. Wong, Appl. Phys. Lett. 60 (1992) 810.

[467] B. Koopmans, A.-M. Janner, H.T. Jonkman, G.A. Sawatzky, F. van der Woude, Phys. Rev. Lett. 71 (1993) 3569.

[468] T. Manaka, T. Yamada, H. Hoshi, K. Ishikawa, H. Takezoe, A. Fukuda, Synth. Met. 84 (1997) 963.

[469] D. Taguchi, L. Zhang, J. Li, M. Weis, T. Manaka, M. Iwamoto, J. Phys. Chem. C 114 (2010) 15136.

[470] T. Manaka, M. Nakao, E. Lim, M. Iwamoto, Appl. Phys. Lett. 92 (2008) 142106.

[471] L. Zhang, D. Taguchi, J. Li, T. Manaka, M. Iwamoto, J. Appl. Phys. 108 (2010) 093707.

[472] E. Lim, T. Manaka, R. Tamura, M. Iwamoto, Thin Solid Films 516 (2008) 2513.

[473] W.-H. Lee, C.-C. Wang, J. Nanosci. Nanotechnol. 10 (2010) 762.

[474] W. Chen, D.-C. Qi, H. Huang, X. Gao, A.T.S. Wee, Adv. Funct. Mater. 21 (2011) 410.

[475] H. Yan, P. Lee, N.R. Armstrong, A. Graham, G.A. Evmenenko, P. Dutta, T.J. Marks, J. Am. Chem. Soc. 127 (2005) 3172.

[476] L. Groenendaal, F. Jonas, D. Freitag, H. Pielartzik, J.R. Reynolds, Adv. Mater. (Weinheim, Ger.) 12 (2000) 481.

[477] S.A. Carter, M. Angelopoulos, S. Karg, P.J. Brock, J.C. Scott: Polymeric anodes for improved polymer light-emitting diode performance, AIP, 1997.

[478] A. Elschner, F. Bruder, H.W. Heuer, F. Jonas, A. Karbach, S. Kirchmeyer, S. Thurm, R. Wehrmann, Synth. Met. 111-112 (2000) 139.

[479] M.C. Hudson, W.K. Ramp, K.P. Frankenburg, FEMS Microbiol. Lett. 173 (1999) 279.

[480] R.O. Darouiche, N. Engl. J. Med. 350 (2004) 1422.

[481] Y.-L. Ong, A. Razatos, G. Georgiou, M.M. Sharma, Langmuir 15 (1999) 2719.

[482] H.J. Busscher, R.J. Ploeg, H.C. van der Mei, Biomaterials 30 (2009) 4247.

[483] E.M. Hetrick, M.H. Schoenfisch, Biomaterials 28 (2007) 1948.

[484] J.A. Nagel, R.B. Dickinson, S.L. Cooper, J. Biomater. Sci., Polym. Ed. 7 (1996) 769.

[485] A.W. Smith, Adv. Drug Delivery Rev. 57 (2005) 1539.

[486] J. Fu, J. Ji, W. Yuan, J. Shen, Biomaterials 26 (2005) 6684.

[487] M. Zilberman, J.J. Elsner, J. Controlled Release 130 (2008) 202.

[488] G.J. Gabriel, A. Som, A.E. Madkour, T. Eren, G.N. Tew, Mater. Sci. Eng., R 57 (2007) 28.

[489] P.A. Norowski, J.D. Bumgardner, J. Biomed. Mater. Res., Part B 88B (2009) 530.

[490] M. Stigter, J. Bezemer, K. de Groot, P. Layrolle, J. Controlled Release 99 (2004) 127.

[491] J.S. Price, A.F. Tencer, D.M. Arm, G.A. Bohach, J. Biomed. Mater. Res. 30 (1996) 281.

[492] A.E. Madkour, G.N. Tew, Polym. Int. 57 (2008) 6.

[493] R. Kumar, H. Münstedt, Biomaterials 26 (2005) 2081.

[494] B.J. Nablo, T.-Y. Chen, M.H. Schoenfisch, J. Am. Chem. Soc. 123 (2001) 9712.

[495] I.A. Rojas, J.B. Slunt, D.W. Grainger, J. Controlled Release 63 (2000) 175.

[496] F. Mondello, F. De Bernardis, A. Girolamo, A. Cassone, G. Salvatore, BMC Infect. Dis. 6 (2006) 158.

[497] M. Minami, M. Kita, T. Nakaya, T. Yamamoto, H. Kuriyama, J. Imanishi, Microbiol. Immunol. 47 (2003) 681.

[498] S. Chao, D. Young, C. Oberg, J. Essent. Oil Res. 12 (2000) 639.

[499] P. Schnitzler, K. Schön, J. Reichling, Pharmazie 64 (2001) 343.

[500] T. Nuryastuti, H.C. van der Mei, H.J. Busscher, S. Iravati, A.T. Aman, B.P. Krom, Appl. Environ. Microbiol. 75 (2009) 6850.

[501] A. Brady, R. Loughlin, D. Gilpin, P. Kearney, M. Tunney, J. Med. Microbiol. 55 (2006) 1375.

[502] R. Loughlin, B.F. Gilmore, P.A. McCarron, M.M. Tunney, Lett. Appl. Microbiol. 46 (2008) 428.

[503] F. Mondello, F. De Bernardis, A. Girolamo, G. Salvatore, A. Cassone, J. Antimicrob. Chemother. 51 (2003) 1223.

[504] D. Belsito, D. Bickers, M. Bruze, P. Calow, H. Greim, J.M. Hanifin, A.E. Rogers, J.H. Saurat, I.G. Sipes, H. Tagami, Food Chem. Toxicol. 46 (2008) S1.

[505] C.F. Carson, B.J. Mee, T.V. Riley, Antimicrob. Agents Chemother. 46 (2002) 1914.

[506] T.C.A.M. Azevedo, A.M.A. Algatti, A.R.P. Mota, A.R.Y. Honda, A.M.E. Kayama, A.K.G. Kostov, A.R.S. Fernandes, A.N.C. Cruz, A.E.C. Rangel, J. Phys.: Conf. Ser. 012053 (2009).

[507] C.J. Van Oss, R.J. Good, M.K. Chaudhury, J. Colloid Interface Sci. 111 (1985) 378.

[508] D. Öner, T.J. McCarthy, Langmuir 16 (2000) 7777.

[509] M.W. Schmidt, K.K. Baldridge, J.A. Boatz, S.T. Elbert, M.S. Gordon, J.H. Jensen, S. Koseki, N. Matsunaga, K.A. Nguyen, S. Su, T.L. Windus, M. Dupuis, J. Montgomery, J.A., J. Comput. Chem. 14 (1993) 1347.

[510] M.J. Frisch, G.W. Trucks, H.B. Schlegel, G.E. Scuseria, M.A. Robb, J.R. Cheeseman, J. Montgomery, J. A., T. Vreven, K.N. Kudin, J.C. Burant, J.M. Millam, S.S. Iyengar, J. Tomasi, V. Barone, B. Mennucci, M. Cossi, G. Scalmani, N. Rega, G.A. Petersson, H. Nakatsuji, M. Hada, M. Ehara, K. Toyota, R. Fukuda, J. Hasegawa, M. Ishida, T. Nakajima, Y. Honda, O. Kitao, H. Nakai, M. Klene, X. Li, J.E. Knox, H.P. Hratchian, J.B. Cross, V.

Bakken, C. Adamo, J. Jaramillo, R. Gomperts, R.E. Stratmann, O. Yazyev, A.J. Austin, R. Cammi, C. Pomelli, J.W. Ochterski, P.Y. Ayala, K. Morokuma, G.A. Voth, P. Salvador, J.J. Dannenberg, V.G. Zakrzewski, S. Dapprich, A.D. Daniels, M.C. Strain, O. Farkas, D.K. Malick, A.D. Rabuck, K. Raghavachari, J.B. Foresman, J.V. Ortiz, Q. Cui, A.G. Baboul, S. Clifford, J. Cioslowski, B.B. Stefanov, G. Liu, A. Liashenko, P. Piskorz, I. Komaromi, R.L. Martin, D.J. Fox, T. Keith, M.A. Al-Laham, C.Y. Peng, A. Nanayakkara, M. Challacombe, P.M.W. Gill, B. Johnson, W. Chen, M.W. Wong, C. Gonzalez, J.A. Pople, Gaussian 03, Revision C.02. Gaussian, Inc., Wallingford CT, 2004.

[511] F.L. Hirshfeld, Theor. Chim. Acta 44 (1977) 129.

[512] A. Michalak, R.L. DeKock, T. Ziegler, J. Phys. Chem. A 112 (2008) 7256.

[513] D.P. Chong, E.V. Lenthe, S.V. Gisbergen, E.J. Baerends, J. Comput. Chem. 25 (2004) 1030.

[514] R. van Leeuwen, E.J. Baerends, Phys. Rev. A 49 (1994) 2421.

[515] E. Baerends, J. Autschbach, A. Bérces, C. Bo, P. Boerrigter, L. Cavallo, D. Chong, L. Deng, R. Dickson, D. Ellis, M. van Faassen, L. Fan, T. Fischer, C. Guerra, S. van Gisbergen, J. Groeneveld, O. Gritsenko, M. Grüning, F. Harris, P. Van den Hoek, H. Jacobsen, L. Jensen, G. van Kessel, F. Kootstra, E. Van Lenthe, D. McCormack, A. Michalak, V. Osinga, S. Patchkovskii, P. Philipsen, D. Post, C. Pye, W. Ravenek, P. Ros, P. Schipper, G. Schreckenbach, J. Snijders, M. Solà, M. Swart, D. Swerhone, G. te Velde, P. Vernooijs, L. Versluis, O. Visser, F. Wang, E. van Wezenbeek, G. Wiesenekker, S. Wolff, T. Woo, A. Yakovlev, T. Ziegler, Theo Chem ADF 2006.01, SCM. Vrije Universiteit: Amsterdam, Amsterdam, The Netherlands, 2006.

[516] O.V. Gritsenko, R. van Leeuwen, E.J. Baerends, Phys. Rev. A 52 (1995) 1870.

[517] L. Selvam, V. Vasilyev, F. Wang, J. Phys. Chem. B 113 (2009) 11496.

[518] J. Mather, P. Roberts: Introduction to cell and tissue culture: theory and technique, Plenum Press, 1998.

[519] I.J. Goldstein, C.E. Hollerman, E.E. Smith, Biochemistry 4 (1964) 876.

[520] B.E. Feller, J.T. Kellis Jr, L.G. Cascão-Pereira, W. Knoll, C.R. Robertson, C.W. Frank, Langmuir 24 (2008) 12303.

[521] T.R. Neu, J.R. Lawrence, FEMS Microbiol. Ecol. 24 (1997) 11.

[522] A. Heydorn, A.T. Nielsen, M. Hentzer, C. Sternberg, M. Givskov, B.K. Ersboll, S. Molin, Microbiology 146 (2000) 2395.

[523] Y. Gu, D. Li, J. Colloid Interface Sci. 226 (2000) 328.

[524] S. Myung, H. Choi, Korean J. Chem. Eng. 23 (2006) 505.

[525] J.F. Evans, G.W. Prohaska, Thin Solid Films 118 (1984) 171.

[526] Z.X. Jiang, Y.D. Huang, L. Liu, High Perform. Polym. 21 (2009) 79.